Tampere University

YI LU

Millimeter Wave Positioning and Location-Aware Communications for 5G-Empowered Industrial IoT

Tampere University Dissertations 492

Tampere University Dissertations 492

YI LU

Millimeter Wave Positioning and Location-Aware Communications for 5G-Empowered Industrial IoT

ACADEMIC DISSERTATION
To be presented, with the permission of
the Faculty of Information Technology and Communication Sciences
of Tampere University,
for public discussion at Tampere University,
on 26 November 2021, at 13 o'clock.

ACADEMIC DISSERTATION
Tampere University, Faculty of Information Technology and Communication Sciences
Finland

Responsible supervisor and Custos	Professor Mikko Valkama Tampere University Finland	
Supervisors	Professor Elena Simona Lohan Tampere University Finland	Dr. Jukka Talvitie Tampere University Finland
Pre-examiners	Professor Jesus Ureña University of Alcala Spain	Professor Jari Iinatti University of Oulu Finland
Opponent	Professor Jyri Hämäläinen Aalto University Finland	

The originality of this thesis has been checked using the Turnitin OriginalityCheck service.

Cover design: Roihu Inc.

ISBN 978-952-03-2150-5 (print)
ISBN 978-952-03-2151-2 (pdf)
ISSN 2489-9860 (print)
ISSN 2490-0028 (pdf)
http://urn.fi/URN:ISBN:978-952-03-2151-2

PunaMusta Oy – Yliopistopaino
Joensuu 2021

To Mom, *Meiju Hou* for unconditional and unlimited love and support.

Research is like a spiritual dance, when the mind is fueled with inspirations.

Simulation may be theoretical, but the pain and the joy are real.

Life is like positioning, both need anchors.

PREFACE

From Spring 2018 to Autumn 2021, this unbelievable life-changing journey as a doctoral researcher at Tampere University has eventually come to the end. The works herein won't be possible without the invaluable help/guidance kindly offered by my supervisors, my colleagues and my family. Therefore, at the point of writing the final thesis, I would like to express my sincere gratitude to those incredible people in my life.

Prof. Mikko Valkama. An authentic Finnish professor with high work efficiency, who is always able to provide me (and everyone) with the precise right amount of supervision and sufficient flexibility. Both serve as the keys to make full use of the creativity of each student, which in turn lays the foundation of high-quality works and publications. Thank You Mikko.

Prof. Elena Simona Lohan. An enthusiastic and energetic professor who influences me using her own hard-working spirit, and motivates me to push myself towards a higher level, to work harder and to offer more. Thank you for providing me a fresh start and embracing my wavering trajectory with abundant degrees of freedom. Undoubtedly, having the latter is a luxury, and I have been lucky enough to have you, thank You Simona.

Dr. Jukka Talvitie. A kind, humble and high-capability researcher who has provided me both technical and non-technical help since 2018. Many thanks to your insightful and valuable comments and suggestions. Your warm welcome on my first day in Tampere will always live in my memory. Your humbleness and professions are my life-long targets. Thank You Jukka.

Dr. Mike Koivisto. A true Doctor and my Cramér-Rao lower bound (CRLB). I have read Mike's work before meeting him in person. Honestly, both the work and the person are very impressive, which is a fairly rare phenomenon. Thereafter, I have been benefiting from the very many fruitful and mind-blowing discussions with him. Meeting with Mike is therefore never enough. Additionally, Mike is the person who

not only gets the job done but also with high quality, and that is why Mike is my CRLB, whose level I will always try to approach as close as possible, but never be able to go beyond. Thank You Mike.

In addition, I would like to thank all the colleagues that I have met, your presence has made my life colorful and unpredictable, the names are not listed in any particular order: Prof. J. Nurmi, Dr. J. Kangas, Dr. O-P. Lundén, Dr. M. Allen, Dr. J. Säe, Prof. T. Riihonen, Dr. B. Tan, Dr. P. Richter (vielen dank), Mr. R. Morales, Mr. W. Wang and all the Russian folks.

Furthermore, there are plenty of lovely friends and teachers from Universitat Autonoma de Barcelona (UAB) whom I would like to thank. First of all, *Prof. Jose Antonio Lopez Salcedo*. If Barcelona is the place where my dream started, Jose has to be the mentor who taught me the skills to build my own boat, such that I am able to sail and live my dream. His patient guidance and encouragement empowered me and made me a better version of myself. Muchas gracias Jose! Second of all, *Prof. Josep Parron Granados*. Josep has witnessed my ups and downs when I worked at UAB. Thank you for supporting me the entire time, thank you for sharing the very many good lessons with me, which helped me see the world clearer. Muchas gracias Josep! Thirdly, *Dr. Alfred Giménez Bonastre*. Alfred is like the brother I have never had. Thanks to Alfred, I have spent all the Christmas time from 2014 to 2017 at his home with his family. The routine was rather simple, we ate, talked and slept (separately) then we came back and ate again for three successive days and nights. The food and drink just kept getting better. Besides the spiritual and appetite satisfaction, I do realize what a big heart it takes to offer me all of those joy, meanwhile, without asking me for anything in return. From Alfred, I have learnt that the best things in the world are free. I am extreme lucky to have the opportunity to embrace all of it. Muchas gracias Alfred! Additionally, I would like to thank a few other colleagues at UAB, they are: Dr. A. Crespo, Dr. J. A. De Peral, Dr. D. Egea, Dr. S. Locubiche, Dr. D. Gomez, Mr. V. Lucas, Prof. G. Seco, Prof. P. De Paco and Mr. G. Junkin.

Finally, I sincerely express my gratitude to the pre-examiners, Prof. Jesus Ureña and Prof. Jari Iinatti, and the opponent, Prof. Jyri Hämäläinen for your great considerations and efforts, and for being an indispensable part of this memorable journey of mine!

Yi Lu

Tampere, Finland, Autumn 2021

ABSTRACT

With the fast technological development in the future generation wireless systems, known as the fifth generation of cellular networks (5G) and beyond, radio positioning steadily serves as one of the key enablers to the industrial Internet of things (IoT), where the location information of all the user equipment (UE), such as smart phones, wearables, and the ground/aerial robots can be obtained via millimeter wave (mmWave) connectivity and measurements. The obtained knowledge of the location via positioning can thereafter be exploited for enhanced communications and location-based services, further improving, e.g., the situational awareness and spectral efficiency for the industrial IoT use cases. Aiming at developing and exploiting the radio positioning technologies, the first objective is to achieve the location awareness via positioning in the industrial IoT systems. Particularly, several 3D positioning and tracking algorithms are developed, their performance is evaluated with the potential challenges existed in the context of the industrial environment. The second objective is to exploit the location awareness for enhanced communications. By utilizing the obtained location awareness, the attainable performance gain in terms of communications is investigated. In particular, a network-centric positioning-aided beamforming (PA-BF) strategy and a device-centric location-aware handover (LHO) scheme are respectively presented and assessed.

In essence, this thesis provides a conceptual and technical journey from positioning to location-aware communications. First of all, by targeting the industrial IoT systems where the anchors' locations are not perfectly known, several approaches, such as weighted centroid geometric (WCG) and a joint positioning and tracking framework based on the extended Kalman filter (EKF) are proposed to achieve accurate and reliable 3D positioning. Second of all, in terms of location-aware communications, a network-centric positioning-aid communication framework (positioning + BF) is proposed and employed to take advantage of the achieved location awareness within the networks. It is demonstrated that the PA-BF strategy in general

outperforms the standardized BF strategy with respect to the inital access latency and spectral efficiency, especially for UE with velocity higher than normal human walking speed (≈ 0.6m/s). Third of all, by utilizing a multi-radio access technology (RAT) robotic platform, the feasibility of the LHO is explored and investigated in a multi-radio environment. With WiFi and mmWave RAT (WiGig) connectivities as well as the available environmental awareness, our experimental results show that the applied LHO is capable of maintaining an enhanced link robustness while enjoying an augmented throughput compared with channel state information (CSI)-based handover.

In conclusion, the proposed algorithms and framework are built based on mathematical formulation, simulation, and experiments, demonstrating the improvement and/or the trade-off among the performance metrics in terms of both positioning and communications, such as positioning accuracy in both 2D and vertical direction, initial access latency, and spectral efficiency. Therefore, it is expected that the corresponding formulations and framework presented in this thesis could lay the foundation for the integration of communications and positioning solutions, further advancing the proposed framework and concepts beyond industrial IoT, towards an intelligent and universal wireless ecosystem with versatile functions and capabilities.

CONTENTS

1 Introduction 1

1.1 Background and motivation 1

1.2 Objectives and scope of the thesis 2

1.3 Main outcomes and contributions 4

1.4 Thesis structure 6

2 Opportunities and challenges for communications and positioning in 5G mmWave system 9

2.1 Abundant spectrum — mmWave 10

2.2 Network densification — SCNs 12

2.3 Large antenna array — MIMO 14

2.4 Spatial multiplexing/reuse — BF 16

2.5 Summary 18

3 Achieving the location awareness — Positioning 21

3.1 Proposed network-centric positioning framework 22

3.2 Location-related measurements 23

3.2.1 Signal and mmWave channel models 24

3.2.2 Characterization of LRMs' accuracy 26

3.2.2.1 ToA measurements 26

3.2.2.2 AoA measurements 27

3.3 Positioning algorithms 29

3.3.1 Snapshot positioning — WCG 29

3.3.2 Sequential positioning I — SLAT EKF 31

3.3.3 Sequential positioning II — normal EKF 36
3.4 Considered industrial IoT scenario for positioning 37
3.5 Performance evaluation and analysis 38
3.5.1 Algorithm initialization 38
3.5.2 Positioning performance 39
3.5.2.1 Accuracy of the LRMs 39
3.5.2.2 WCG vs SLAT EKF vs normal EKF 41
3.5.2.3 Performance under different number of targets and anchors 42
3.6 Summary 45
4 Exploiting the location awareness — A network-centric positioning-aided beamforming strategy 47
4.1 A cloud-oriented mmWave mobile network 48
4.1.1 System overview 48
4.1.2 UL positioning engine 49
4.1.2.1 Utilized LRMs 50
4.1.2.2 Positioning error bound 51
4.1.3 DL positioning-aided communications 51
4.2 Benchmark strategy and performance metric 52
4.2.1 The benchmark strategy 53
4.2.2 Performance metric — Spectral efficiency 53
4.2.2.1 The proposed PA-BF 55
4.2.2.2 The benchmark EX-BF 56
4.3 Scenarios and simulations 57
4.3.1 Scenario deployment 57
4.3.2 Simulation evaluations and analysis 58
4.4 Summary 63
5 Exploiting the location awareness — A device-centric location-aware handover scheme 65

5.1 System overview 65
5.2 Scenario deployment 66
5.3 Enabling the handover with location awareness 67
5.3.1 From environmental awareness to mmWave LoS coverage . . 67
5.3.2 Proposed positioning solution 68
5.3.3 Proposed handover scheme 69
5.4 Handover performance and analysis 71
5.5 Summary 74
6 Conclusions and future perspectives 75
6.1 Conclusions 75
6.2 Future perspectives 77
References 79
Publication I 95
Publication II 103
Publication III 113
Publication IV 129
Publication V 153
Publication VI 163

1.1 Positioning-aided location-aware communication system — a block diagram illustration. 3

2.1 An illustration of two available bands as frequency range (FR) [3] and potential applications. 10

2.2 An illustration of the concept of SCNs in heterogeneous networks (HetNets), employing the control/user plane seperation (CUPS) under non-standalone architecture [106]. 12

2.3 An illustration of multiple-input multiple-output (MIMO) and beamforming (BF). In particular, this graph portrays a multi-user MIMO scenario with a centralized array configuration [68], [22, Ch. 2]. . . . 15

3.1 In the envisioned network-centric positioning framework, the mobile vehicles or robots (as *targets*) are the Tx while the *anchors* represent the Rx that estimated the location-related measurements (LRMs), e.g., time of arrival (ToA) and/or angle of arrival (AoA). Positioning is carried out at the edge/cloud server, where the location estimates of both targets and anchors are steadily available at the network side for further actions, such as scheduling, mobility management and proactive resource allocation. 22

3.3 Joint positioning and tracking via millimeter wave (mmWave) device-to-device (D2D) (sidelink) communications — a network-centric scheme. 37

3.4 An indoor industrial warehouse environment for the industrial Internet of things (IoT) systems. The ray-tracing feature is enabled in the environment [129]. 38

3.5 The accuracy of Cramér-Rao lower bounds (CRLB)-based LRMs. . . 40

3.6 The positioning performance comparison among weighted centroid geometric (WCG), simultaneous localization and tracking (SLAT) extended Kalman filter (EKF) and normal EKF. 41

3.7 Positioning performance of *ToA* based SLAT EKF at $\sigma_{\mathrm{AT}} = 4$ m under various number of target user equipment (UE) and anchor UE. . 43

3.8 Positioning performance of *AoA* based SLAT EKF at $\sigma_{\mathrm{AT}} = 4$ m under various number of target UE and anchor UE. 44

3.9 Positioning performance of *ToA+AoA* based SLAT EKF at $\sigma_{\mathrm{AT}} =$ 4 m under various number of target UE and anchor UE. 44

4.1 A cloud-oriented mmWave mobile network, facilitating the positioning-aided communications. 48

4.2 Demonstration of two different schemes for initial access and data transmission. (a) A standardized procedure [11] when both transmitter and receiver (Tx & Rx) equip directional antennas. (b) The proposed positioning-aided communication scheme. 54

4.3 The top view illustration of a spatial correlated received signal strength (RSS) distribution with respect to the access point (AP) in red circle. 58

4.4 The effective transmit ratio $1 - T_{\mathrm{IA}}/T_f$ as a function of Doppler velocity V_d. 59

4.5 The positioning error bound (PEB) in 3D obtained on the UE height using the time difference of arrival (TDoA) measurements under the same AP deployment of Fig. 4.3. 60

4.6 The spectral efficiency by positioning-aided beamforming (PA-BF) (aided by different positioning accuracy) and exhaustive beamforming (EX-BF) at **0.6 m/s** Doppler velocity over the considered area. . . 62

4.7 The spectral efficiency by PA-BF (aided by different positioning accuracy) and EX-BF at **2.0 m/s** Doppler velocity over the considered area. 62

5.1 A conceptual illustration of the location-aware handover (LHO) scheme in an industrial multi-radio environment. 66

5.2 Test scenario 3D model and layout. (a) The 3D view of the corridor from the wireless Gigabit alliance (WiGig) perspective. The red line represents an exemplified robot trajectory; (b) The top view of floor plan with the coordinates used in simulation. The yellow shadow refers to the line-of-sight (LoS) coverage of WiGig. 67

5.3 The geometric relationships between the robot and mmWave AP from side view and top view. 68

5.4 Procedures of the proposed location-aware handover (LHO) scheme. 70

5.5 Simulation-based numerical characterization as a function of time along the simulated robot trajectory (see Figure 5.2b)). 72

5.6 Positioning and handover performance via simulations. 72

5.7 The handover frequency as a function of AoA accuracy for two considered tracks. 73

6.1 From the complement of technologies and use cases towards the ultimate merging of the physical world, the digital world and the virtual world. 77

List of Tables

1.1 RQ (research question) versus P. (publication) 4

2.1 Opportunities and challenges for *communications* in the fifth generation of cellular networks (5G) system 19
2.2 Opportunities and challenges for *positioning* in 5G system 20

3.1 The number of available LRMs as a function of the number of targets K and anchors M for each considered measurement choice 33
3.2 Utilized parameters in the simulation 40

4.1 Simulation parameters 61
4.2 Considered 3D positioning accuracies based on the positioning accuracy requirement in [2] 61

5.1 Parameter table for simulation 72

ABBREVIATIONS

3GPP	the 3rd generation partnership project
5G	the fifth generation of cellular networks
ADoA	angle difference of arrival
AoA	angle of arrival
AoD	angle of departure
AP	access point
B-RSRP	beam reference signal received power
BF	beamforming
CDF	cumulative density function
CI	context-information
cmWave	centimeter wave
CoMP	coordinated multi-point
CRLB	Cramér-Rao lower bounds
CSI	channel state information
CUPS	control/user plane separation
D2D	device-to-device
DFT	discrete Fourier transform
DL	downlink
EKF	extended Kalman filter
eMBB	enhanced mobile broadband
eNB	evolved node B

EX-BF	exhaustive beamforming
FDD	frequency-division duplex
FIM	Fisher information matrix
FR	frequency range
GBP	geometry-based positioning
gNB	next generation node B
GNSS	globe navigation satellite system
H2H	human-to-human
H2M	human-to-machine
HetNets	heterogeneous networks
IMU	inertial measurement unit
IoT	Internet of things
LHO	location-aware handover
LoS	line-of-sight
LRMs	location-related measurements
LTE	long term evolution
M2M	machine-to-machine
MIMO	multiple-input multiple-output
MISO	multiple-input single-output
mMTC	massive machine-type communications
mmWave	millimeter wave
NLoS	non line-of-sight
NR	new radio
OFDM	orthogonal frequency division multiplex
OFDMA	orthogonal frequency division multiple access
PA-BF	positioning-aided beamforming
PEB	positioning error bound

QoE	quality of experiences
QoS	quality of services
RAT	radio access technology
RF	radio frequency
RSS	received signal strength
RWP	random waypoint
SCNs	small cell networks
SDMA	space-division multiple access
SIMO	single-input multiple-output
SINR	signal-to-interference-plus-noise ratio
SLAM	simultaneous localization and mapping
SLAT	simultaneous localization and tracking
SNR	signal-to-noise ratio
TDD	time-division duplex
TDoA	time difference of arrival
ToA	time of arrival
Tx & Rx	transmitter and receiver
UE	user equipment
UL	uplink
ULA	uniform linear array
URA	uniform rectangular array
URLLC	ultra-reliable low-latency communications
UWB	ultra-wide-band
WCG	weighted centroid geometric
WiGig	wireless Gigabit alliance
XR	extended reality

ORIGINAL PUBLICATIONS

Publication I Y. Lu, P. Richter and E. S. Lohan. Opportunities and Challenges in the Industrial Internet of Things based on 5G Positioning. *2018 8th International Conference on Localization and GNSS (ICL-GNSS)*. 2018, 1–6. DOI: 10.1109/ICL-GNSS.2018.8440903.

Publication II Y. Lu, M. Koivisto, J. Talvitie, M. Valkama and E. S. Lohan. EKF-based and Geometry-based Positioning under Location Uncertainty of Access Nodes in Indoor Environment. *2019 International Conference on Indoor Positioning and Indoor Navigation (IPIN)*. 2019, 1–7. DOI: 10.1109/IPIN.2019.8911785.

Publication III Y. Lu, M. Koivisto, J. Talvitie, M. Valkama and E. S. Lohan. Positioning-Aided 3D Beamforming for Enhanced Communications in mmWave Mobile Networks. *IEEE Access* 8 (2020), 55513–55525. DOI: 10.1109/ACCESS.2020.2981815.

Publication IV Y. Lu, M. Gerasimenko, R. Kovalchukov, M. Stusek, J. Urama, J. Hosek, M. Valkama and E. Lohan. Feasibility of Location-Aware Handover for Autonomous Vehicles in Industrial Multi-Radio Environments. *Sensors* 20.21 (2020). DOI: 10.3390/s20216290.

Publication V Y. Lu, M. Koivisto, J. Talvitie, E. Rastorgueva-Foi, M. Valkama and E. S. Lohan. Cooperative Positioning System for Industrial IoT via mmWave Device-to-Device Communications. *2021 IEEE 93rd Vehicular Technology Conference (VTC2021-Spring)*. 2021, 1–7. DOI: 10.1109/VTC2021-Spring51267.2021.9448644.

Publication VI Y. Lu, M. Koivisto, J. Talvitie, E. Rastorgueva-Foi, T. Levanen, E. S. Lohan and M. Valkama. Joint Positioning and Tracking via

NR sidelink in 5G-Empowered Industrial IoT. *Submitted to IEEE Internet of Things Magazine* (2021). DOI: arxiv.org/abs/2101.06003.

Author's contribution

This thesis includes overall *six* articles (five published ones and one submitted paper) with the author as the key contributor. Prof. Elena Simona Lohan provided valuable comments and suggestions on the idea, text and results for all the articles.

Publication I — The original ideas were proposed by the Author who wrote 95% of the manuscript for this publication. 90% of the simulation code was developed by the Author based on the map data provided by Dr. Philipp Richter.

Publication II — The problem being tackled in this publication was originally identified by Prof. Elena Simona Lohan and the Author. The proposed geometry-based positioning algorithm was developed and implemented by the Author. The Kalman filter based method was discussed with Dr. Mike Koivisto and Dr. Jukka Talvitie, then implemented by the Author. More than 95% of the manuscript for this publication was written by the Author, and reviewed by other co-authors.

Publication III — The original idea, simulation code and the overall manuscript of this publication were completed by the Author. The development of the proposed idea and strategy, and obtained results were discussed with Dr. Mike Koivisto and Dr. Jukka Talvitie. Prof. Mikko Valkama offered comments on the manuscript's structure and technical ingredients.

Publication IV — The original idea and objective of this publication were discussed and identified by Dr. Mikhail Gerasimenko and the Author. In addition, the Author produced the state of the art review, proposed and evaluated the positioning method that was then applied in the experiment. More than 80% of the manuscript was

prepared and written by the Author. Besides, a video demonstration of the experiment was created by the Author with the assistant of Mr. Jani Urama.

Publication V — The research problem was identified by Prof. Elena Simona Lohan and the Author. The idea of the proposed positioning algorithm was inspired by Dr. Mike Koivisto, then further extended by the Author based on the discussion with Dr. Jukka Talvitie. The Author programmed and evaluated the positioning algorithm, created video demonstrations and wrote the whole manuscript, which was reviewed by all the co-authors.

Publication VI — As an extension work of the previous publication, the Author envisioned and broaden the concept and use case towards the industrial use case with connected vehicles and IoT devices. The whole manuscript was produced by the Author, while part of the simulation code was assisted by Dr. Jukka Talvitie. The final manuscript was reviewed and updated by all the co-authors.

1 INTRODUCTION

In this chapter, a brief introduction of the background and motivation of the chosen topic and research area are provided, followed by a description of the scope and objective of the thesis. Thereafter, the main contributions of the conducted research work are summarized with the overall outline being given in the end.

1.1 Background and motivation

Over the past few decades, information technology and mobile devices have become an integral part of our daily life. Wireless technology, as an augmented digital dimension, has profoundly transformed our way of working, living as well as thinking. In particular, wireless communications have been fundamentally integrated into all the business sectors to serve not only human-to-human (H2H), but also human-to-machine (H2M) and further machine-to-machine (M2M) communications [102], forever revolutionizing how the world connects, communicates and computes [90]. With more tangible forms of services/use cases, there comes various types of mobile devices, e.g., tablets, watches, glasses and ground/aerial vehicles. As such, the mobile device has evolved from a uni-function equipment supporting voice/text services, to a multi-function gear providing all sorts of infotainment, such as healthcare, extended reality (XR), video chatting and mobile gaming. With a rapid growth of the number of such mobile devices, Internet of things (IoT) has therefore been realized with the support of the wireless networks.

Furthermore, the arrival of the millimeter wave (mmWave)-enabled wireless system, namely the fifth generation of cellular networks (5G) and beyond, brings fresh ingredients [23], such as high carrier frequencies with flexible bandwidth, large antenna array and beamforming (BF). Such ingredients unveil unprecedented challenges and opportunities for both communications and positioning. Meanwhile, as a natural evolution of the IoT, the industrial IoT comes along with various applications for

different industry verticals, covering from manufacturing and automation to logistics and transportation [84]. Without a doubt, the industrial IoT use cases not only pose a higher requirement for seamless communications in terms of initial access latency and throughput, but also introduce certain difficulties for high-accuracy 3D (radio) positioning [138, Ch. 1], which, if accurate enough, can be exploited to empower various industry-oriented applications [57, 72]. Hence, the investigation and development of accurate 3D positioning algorithms and advanced communication schemes that exploit the novel ingredients while satisfying the industry IoT applications serve as primary objective of this thesis as well as one of the most rigorous and interesting research directions that call for continuous and substantial research efforts in the coming time.

1.2 Objectives and scope of the thesis

The broad scope of this thesis consists of developing mmWave positioning techniques[1] and location-aware communication schemes in 5G-empowered industrial IoT systems. Hence, the objective of the conducted research is twofold. The first objective is to develop and evaluate the positioning algorithms in industrial IoT based on the radio network measurements taking into account the 5G ingredients. Throughout this thesis, we define the radio network measurements as the location-related measurements (LRMs) which can be measured either by the access point (AP) at the network edge or by the user equipment (UE) at the device side. The typical LRMs consists of received signal strength (RSS), time of arrival (ToA) and angle of arrival (AoA) [38, 44, 87]. As the complementary positioning scenario to the globe navigation satellite system (GNSS), the indoor situations, such as an industrial warehouse/factory are our main focus. However, it is noteworthy that, there are no limitations in applying the proposed methods in this thesis to the outdoor scenarios under a similar context.

Regarding the second objective, this thesis investigates and proposes both framework and solutions to realize the location-aware communications scheme based on the achieved location awareness (estimated locations) via positioning. Towards this

[1]Here, positioning refers particularly to the wireless techniques that provide location estimates via the transmission and reception of mmWave signals. Therefore, positioning and mmWave positioning are considered as synonyms, and used interchangeably throughout the thesis.

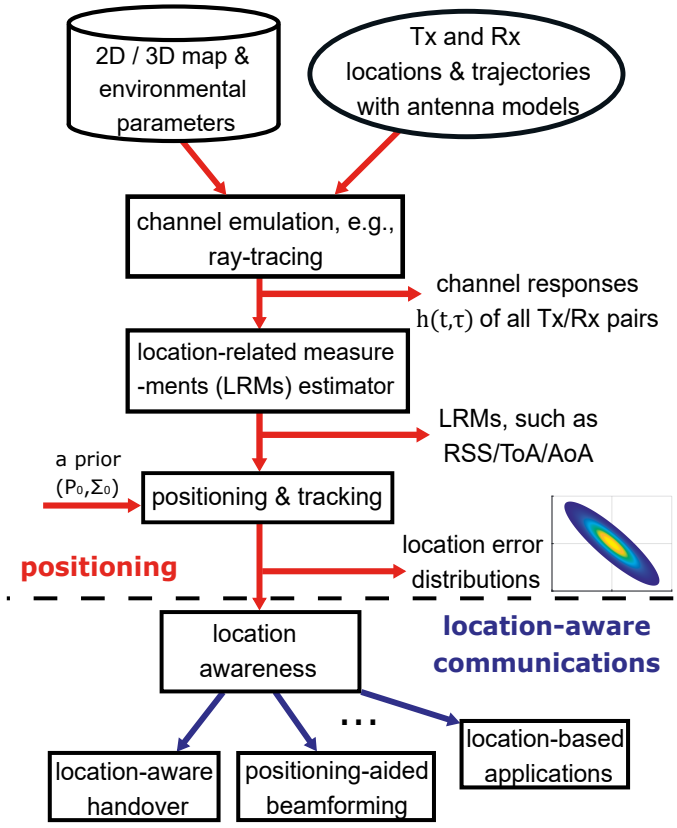

Figure 1.1 Positioning-aided location-aware communication system — a block diagram illustration.

objective, there are in total two location-aware communications schemes being investigated. i) With the knowledge of the UE locations, a positioning-aided communications framework (positioning + BF) is proposed and evaluated to enhance the communications performance in mmWave networks. Due to a vastly reduced initial access latency, the proposed framework can be employed for the latency-sensitive industrial IoT applications. ii) The feasibility of location-aware handover (LHO) in an indoor multi-radio environment is designed and assessed to jointly achieve both improved throughput and enhanced link reliability. The block diagram that describes overall abstraction of positioning and location-aware communications is depicted in Fig. 1.1.

The key research questions which further elaborate our objective and scope of this thesis are outlined as follows.

1. With the key ingredients of the mmWave-enabled 5G system, what are the

Table 1.1 RQ (research question) versus P. (publication)

	P. I	P. II	P. III	P. IV	P. V	P. VI
RQ 1	×		×			
RQ 2	×	×			×	×
RQ 3			×	×		

opportunities and challenges for communications & positioning?

2. What is the main difficulty of positioning in the industrial environment? how to resolve it? — Positioning algorithm development for industrial IoT.
3. How can communications benefit from the obtained location awareness? — Exploring the feasibility and benefits of the location-aware communications.

Furthermore, each research question has been addressed by different articles on the publication list. In order to present a clear structure, the relationships between the research questions and included publications are summarized in Table 1.1. Specifically, the research question 1 is addressed by publication I & III, while research question 2 and 3 are elaborated by publication I, II, V & VI and publication III & IV, respectively.

1.3 Main outcomes and contributions

The main contributions of this thesis are briefly summarized as follows:

- With the representative ingredients i.e., mmWave, small cell networks (SCNs), multiple-input multiple-output (MIMO) and BF in the context, a systematic overview and analysis is provided, discussing the opportunities and challenges for communications and positioning in 5G system towards the industrial IoT.

From positioning perspective,

- an analytical model for the RSS and ToA is proposed under both line-of-sight (LoS) and non line-of-sight (NLoS) conditions in an indoor multi-floor envi-

ronment[2]. The benefits to positioning under mmWave, SCNs and MIMO are demonstrated.

- Unlike most of the positioning works, in which the locations of anchors, e.g., APs are assumed perfectly known, different positioning approaches are proposed and examined by taking into account the location uncertainty of the APs, which is a typical problem in the industrial environments. The proposed geometry-based positioning method, i.e., weighted centroid geometric (WCG) has shown a better accuracy and a lower computational complexity compared with a generic extended Kalman filter (EKF)-based approach.
- Furthermore, via the device-to-device (D2D) communications, a joint positioning and tracking framework is presented and formulated to better addresses the location uncertainty of the anchors. In other words, the locations of both the anchors (e.g., the AP) and the target (e.g., the UE) are jointly estimated via the proposed EKF-based approach, forming a simultaneous localization and mapping (SLAM)-alike positioning framework that we refer to as simultaneous localization and tracking (SLAT) EKF. It is shown that the SLAT EKF outperforms the other two methods (i.e., WCG and normal EKF) in terms of the achieved accuracy especially when the anchor location uncertainty is larger than 1 m.

From location-aware communications perspective,

- a cloud-oriented positioning-aided communications framework is presented. In particular, the network-centric positioning is first carried out, such that the location awareness is obtained and available at the network side. The corresponding positioning accuracy is characterized by theoretical positioning error bound (PEB). Thereafter, the proposed communications framework is completed by performing positioning-aided beamforming (PA-BF) in the downlink (DL). Moreover, the performance in terms of achieved spectral efficiency and initial access latency is validated via the comparison with the codebook-based BF strategies. Additionally, the impact of positioning accuracy on the PA-BF performance is also studied under various system parameters. The results could assist the design of future location-based systems.

[2]Due to the structure and main scope of this thesis, this perspective is not reflected in the introductory part. Further details can be found in publication I.

- Aiming at empowering and exploiting a location-aware network, an efficient handover scheme based on the location awareness, i.e., LHO is designed and carried out in an indoor multi-radio environment. Via an conducted experiment, the feasibility of the proposed LHO is validated using a multi-radio access technology (RAT) enabled robotic platform. In addition, our experiment results[3] manifest that LHO outperforms the RSS-based handover in terms of achieved throughout and link robustness along the whole considered robot trajectory.

1.4 Thesis structure

The overall doctoral thesis consists of an introductory part with six chapters appended by *six* publications. The remainder of the introductory part is organized as follows.

Chapter 2 starts with the representative ingredients that are adopted in 5G systems. The corresponding opportunities and challenges for communications and positioning are then discussed and analyzed from a general context towards the industrial IoT.

Chapter 3 extends the technical details of *positioning*, illustrated in the upper part of Fig. 1.1. Specifically, this chapter begins by presenting the considered network-centric positioning system, which is followed by the discussion on the typical difficulty for positioning in the considered industrial scenario. The approach of estimating the LRMs is then presented with the support of a ray-tracing engine. Finally, the studied and proposed positioning algorithms for achieving the location awareness are formulated with simulation-based evaluations being given in the end.

The following two chapters, Chapter 4 and Chapter 5, provide the conducted studies and proposed schemes on *location-aware communications*, which is shown in the lower part of Fig. 1.1. Specifically, Chapter 4 describes and assesses the proposed positioning-aided communication framework in a cloud-oriented network. Via the achieved location awareness via uplink (UL) positioning, a positioning-aided BF strategy is presented. Thereafter, the corresponding performance is evaluated

[3]In order to control the overall length of this thesis and avoid overlapping similar results, only the representative outcomes on LHO are shown in this introductory part, whereas the experiment-based handover performance with multi-RAT can be found in publication IV.

and compared with other standardized BF methods.

Chapter 5 introduces and presents the proposed device-centric LHO scheme, i.e., handover based on the location awareness in an indoor multi-radio environment. With the available wireless measurements, the location estimates for handover prediction are calculated at the device side using a geometry-based approach. The corresponding performance in both positioning accuracy and handover frequency is tested and demonstrated.

Finally, Chapter 6 concludes this thesis with a discussion that consolidates the major outcomes and insights obtained from the research. Possible future research directions are pointed out.

2 OPPORTUNITIES AND CHALLENGES FOR COMMUNICATIONS AND POSITIONING IN 5G MMWAVE SYSTEM

With the advent of future generation wireless systems and technology, the mmWave band will undoubtedly be utilized to co-operate with the current sub-6 GHz band in order to enable various user-driven services that meet both flexible and stringent requirements in various industrial IoT use cases. Although the high carrier frequencies come with a wider available signal bandwidth, a major challenge of mmWave communications lies in the fact that the corresponding radio signals experience a higher path-loss as well as a bigger penetration/absorption loss than centimeter wave signals [89], thus yielding weaker radio links. Therefore, several other key features such as SCNs, MIMO and BF are being incorporated as the ingredient technologies [23] to cope with such challenges, gradually forming a robust and versatile wireless mobile network as a fundamental enabler for industrial IoT.

As the process of network densification continues, SCNs certainly bring numerous benefits to both communications [29] and positioning [64]. Besides SCNs, BF is also incorporated as another enabling technology to cope with the severe signal attenuation and to take advantage of the classic spatial reuse [22]. Together with MIMO [68, 96], the transmission and reception within the mmWave network become inherently directional. On one hand, a high directivity can indeed be employed to improve the maximum propagation distance. On the other hand, the directional transmission might result in a high-probability of beam misalignment, yielding poor wireless coverage. Nevertheless, such problem can be compensated by SCNs [123] to a certain extent. Therefore, the aforementioned key features gracefully complement each other. In this chapter, the opportunities and challenges for both communications and positioning are examined and analyzed in the presence of

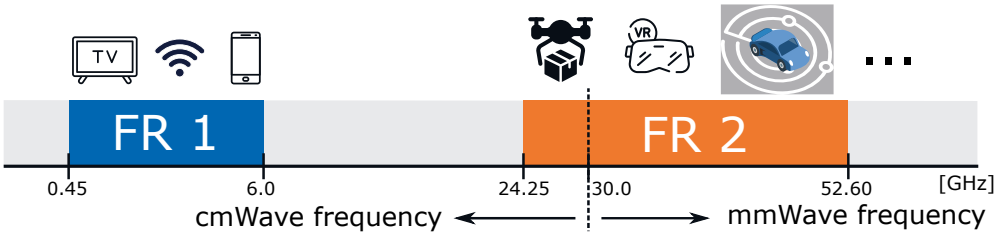

Figure 2.1 An illustration of two available bands as frequency range (FR) [3] and potential applications.

the key ingredients in 5G system.

2.1 Abundant spectrum — mmWave

As the natural evolution from earlier generations to future generations wireless/cellular systems, the access and usage towards a higher carrier band serve as the root ingredient. In order to support the upcoming standalone mode as well as the cooperation with other available RATs [3, 9], two ranges of spectrum have been regulated by the 3rd generation partnership project (3GPP) as the frequency range (FR). As illustrated in Fig. 2.1, the FR 1 (i.e., sub-6 GHz band) within the centimeter wave (cmWave) frequency has been and will be greatly favored by nearly all the available wireless interfaces, including the initial deployment of 5G [47, Ch. 4]. Nevertheless, it can be foreseen that the FR 1 spectrum gradually and eventually becomes overwhelmed, which leads to the exploration of high-frequency band with more available spectrum, as the key asset. So far, the FR 2 (from 24.25 GHz to 52.60 GHz) frequencies are in general utilized for the short-range and high-rate applications [111, 125]. In the context of industrial IoT, the integration of both FRs [28, Ch. 17] remains a key solution in support of many versatile communication schemes, especially in private new radio (NR) networks operating on unlicensed spectrum [34, 91].

The opportunities brought by mmWave to communications mainly stem from the wider available bandwidth compared with that in cmWave band. From information theory perspective, the signal bandwidth refers to the total complex dimensions that a signal can represent, which means that any continuous signal with bandwidth B_{w} conveys information with approximately B_{w} complex dimensions per second [118, Ch. 2]. From the Rx point of view, B_{w} essentially reflects the number of complex symbols which can be reliably distinguished [20, Ch. 1]. Therefore, a wider

signal bandwidth in general corresponds to a higher throughput. Additionally, NR supports a scaleable frame structure by adjusting the slot duration through different sub-carrier spacing of the orthogonal frequency division multiplex (OFDM) signals, that is, $f_{\text{sc}} = 2^{\mu} \times 15$ kHz, $\mu = [0, 1, \cdots, 5]$. The choice of numerology μ depends on the FR as well as the required bandwidth. As a result, slots (e.g., transmission intervals) enjoy more flexible configurations than long term evolution (LTE), which greatly supports the dynamic scheduling in both UL and DL [18, 25, 51]. More importantly, such a flexible frame structure can better control the transmission latency [28, Ch. 14], which serves as the key enabler for ultra-reliable low-latency communications (URLLC) in delay-sensitive applications. Last but not least, both communications and sensing technologies can be unified via mmWave air interface, i.e., the radio frequency (RF) convergence [88], where the sensing functionality facilitates a vigorous mmWave networking [111, 126, 143] via directional beams, which will be discussed in Section 2.3. Although creating plenty of attractive opportunities, there are several challenged coming along with mmWave that are needed to be addressed before mmWave can be fully applied to support, e.g., the enhanced mobile broadband (eMBB) or other industrial IoT use cases, especially in the UL.

According to the properties of mmWave propagation and channels [6, 77, 110], the mmWave radio signals travel typically short distance due to a high loss in propagation, reflection and diffraction, which limits the maximum cell size down to 200 m with the LoS probability less than 20% [5, 92, 100]. Network densification (to be discussed in the next section) is therefore one of the most fundamental transformations in 5G. In addition, the overall performance of the networks become blockage-limited rather than bandwidth/capacity-limited [52]. In other words, the continuity of the wireless connectivity strongly depends on the propagation environment. The UE quality of services (QoS) in the mmWave networks will be mainly affected and driven by the blockage due to static and moving blockers (e.g., buildings and vehicles), whereas the available bandwidth acts as the secondary deciding factor.

Furthermore, the mobility support becomes another significant bottleneck for the mmWave systems [15], the key reason lies in a much shorter channel coherence time that is inversely proportional to the carrier frequency and the relative velocity [107]. As such, mmWave communications typically thrive in a low-mobility scenario with eMBB for local coverage. However, due to the enhanced capacity of mmWave communications, the short channel coherence time does not necessarily

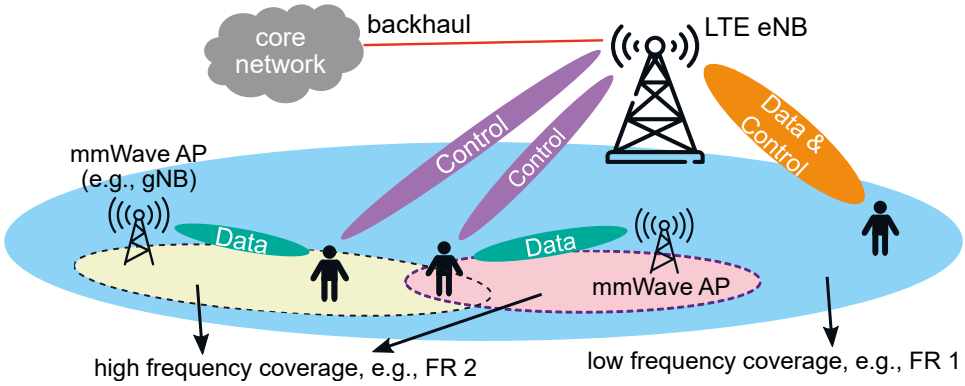

Figure 2.2 An illustration of the concept of SCNs in heterogeneous networks (HetNets), employing the control/user plane seperation (CUPS) under non-standalone architecture [106].

pose severe challenges because of another concept to be introduced in Section 2.4, the beam coherence bandwidth [119].

From positioning perspective, mmWave boosts the ToA estimation accuracy [138, Ch. 6 and Ch. 7] [101, Ch. 3] thanks to a wide bandwidth, which in turn improves the positioning accuracy for any lateration-based approaches. Essentially, the wide bandwidth, e.g., in ultra-wide-band (UWB) systems, leads to high temporal solution in the delay domain. Such feature not only promotes the LoS estimation accuracy, but also facilitates the exploitation of the multipath components for positioning as well as mapping, conditional on the availability of the prior information, such as the 2D/3D floor plan [66, 67, 69, 127, 130]. However, the rich-scattering has been proved not to be a valid characterization for the channels measured in 60 GHz [133], therefore, mmWave may not be particularly suitable for multipath-based positioning approaches. Rather, mmWave-based positioning is generally carried out in the LoS condition [81, 122]. However, in situations where the LoS paths with respect to all the anchors (e.g., APs) are blocked, multipath parameters can be estimated and integrated to provide location estimates [69, 78]. In this thesis, we mainly focus on positioning solutions utilizing the LoS measurements.

2.2 Network densification — SCNs

In addition to mmWave, network densification, i.e., the SCNs acts as the second ingredient during the transformation towards 5G and beyond. By "densification" and

"small cell", the terms indicate the deployment of many mmWave APs on top of the overlaid macro layer of LTE [28, Ch. 17]. At the beginning of the 5G era, non-standalone mode [106] shall still play the major role in providing radio services and co-existence with LTE, thus forming heterogeneous networks (HetNets). A major advantage of the HetNets is illustrated in Fig. 2.2, i.e., control/user plane separation (CUPS) [10], where the control plane signal is handled by the evolved node B (eNB) to maintain the link robustness and reliability while the user plane signal is transmitted by the next generation node B (gNB) to take advantage of the wider available bandwidth in FR 2 for a higher throughput [28, Ch. 5]. The co-existence and cooperation of FR 1 and FR 2 are generally referred to as Spectrum Heterogeneity [104].

In term of communications, SCNs not only offers several favorable opportunities/benefits, but also provides solutions to the challenges composed by mmWave. Specifically, the severe path-loss and reflection/diffraction loss can be alleviated since the end-to-end propagation distance becomes in general short. In addition, the transmit power at both ends, i.e., AP and UE, can be vastly eased especially with directional antenna, which will be discussed in Section 2.3. Furthermore, SCNs can also effectively reduce the potential coverage holes within the macro cells [123] and enable the flexible frequency reuse strategies [101, Ch. 9]. With proper design and deployment, both the signal-to-interference-plus-noise ratio (SINR) that reflects the interference level and the area spectral efficiency (i.e., sum of normalized throughput) scale linearly with the AP (cell) density.

Nevertheless, there are fundamental limits, such as resource allocation and interference management [112, 115] needing to be properly addressed. In particular, as the number of APs outgrow a certain threshold, neither the *SINR invariance* nor *cell splitting gain* continue holding [17], the network therefore changes from noise-limited to interference-limited. From economy perspective, SCNs indicate a much higher deployment cost together with an added complexity on cell cooperation [74]. Aiming at reliving the deployment cost and at improving the system flexibility, a fresh and adaptive concept, namely drone cell [71, 139, 140], has been proposed and is gaining its momentum in terms of multi-access scheme, interference management and data harvest, for instance. Despite many advantages, such approach suffers from various major limitations, such as, limited battery life, weather conditions and serving environments/scenarios, therefore, needs further investigation and validation.

Meanwhile, SCNs offer numerous opportunities for better positioning. First of

all, a high AP density yields a high probability of having LoS connections among all transmitter and receiver (Tx & Rx) pairs. With the locations of AP as a prior, high accuracy (sub-meter level) positioning is proved to be achievable [63, 64]. Furthermore, a higher LoS probability suggest a larger number of LoS APs, which guarantees that more LRMs become available for positioning, and more available LRMs in general assure higher positioning accuracy [54]. Not least of all, in the cases when the only available measurement from the APs is the cell-ID information, positioning can be realized by calculating the intersection of all the cell (AP) coverage [101, Ch. 2], SCNs can therefore minimize the upper bound of positioning error. However, there are a few challenges needing attentions. For instance, the selection/filtering of all the available LRMs may raise the complexity of positioning algorithm and delay the location estimation outputs. Sometimes such task remains infeasible without the measurements statistics. Although applying all the LRMs could be a rule-of-thumb, the existence of one outlier can seriously degrade the positioning performance [99].

2.3 Large antenna array — MIMO

Thanks to the short wavelength of carriers at mmWave frequencies, antenna elements up to the order of hundreds can be packed and installed at both AP and UE, forming large antenna arrays [96]. Such configuration comes with several interesting features, such as directional transmission/reception, spatial multiplexing/diversity and BF [60]. As graphically depicted in Fig. 2.3, MIMO and BF inherently accompany each other [109]. It is seen that, with a centralized antenna array configuration, directional beams can be formed sequentially or simultaneously via either analog/digital/hybrid BF scheme [83, 124] for wireless connections. In addition to the centralized configuration, the distributed system, namely cell-free MIMO [85, 117] possesses good potential as well, which is out of the scope of this thesis.

To date, two types of MIMO schemes have been widely investigated: single-user MIMO (also known as point-to-point MIMO) and multi-user MIMO [47, Ch. 3]. The former scheme is capable of supporting multiple parallel steams simultaneously conditional on a rich multipath environment in the condition of a similar number of antenna elements and the perfect channel state information (CSI) at both Tx & Rx to perform the transmit precoding and receive combining [118, Ch. 7 and Ch. 8]. However, requiring an array size at the UE that is approximately equal to that at the

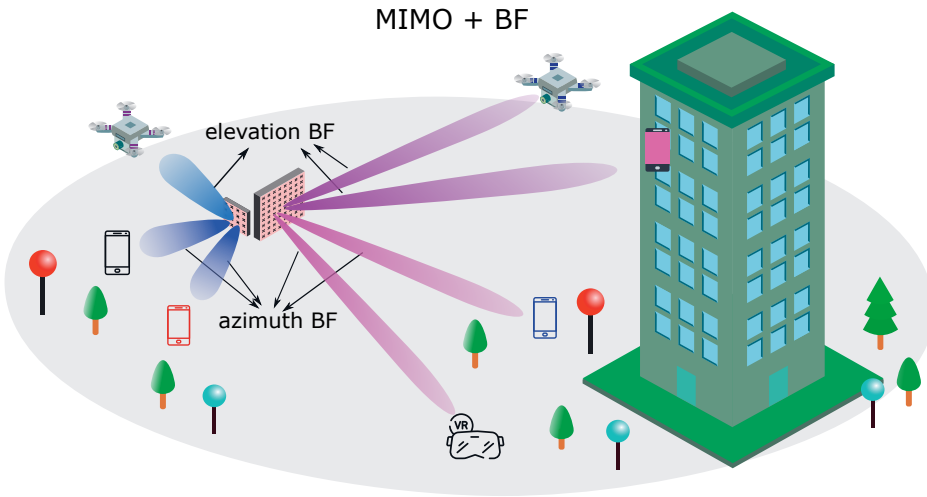

Figure 2.3 An illustration of MIMO and BF. In particular, this graph portrays a multi-user MIMO scenario with a centralized array configuration [68], [22, Ch. 2].

AP could be rather challenging, therefore, typically infeasible. Furthermore, as discussed in Section 2.1, mmWave communications basically rule out a rich multipath propagation condition. As such, the studies of multi-user MIMO is in general much more applicable since single or few-antenna UE are considered and rich multipath propagation is not required [68]. More importantly, multi-user MIMO serves as an excellent framework to study and exploit the space-division multiple access (SDMA), scalability to large number of UE, and to derive and analyze the spatial channel correlation property [22, Ch. 2], which ultimately determines the overall performance of the mmWave MIMO systems.

In terms of the strategies that amplify the power of MIMO for different scenarios and use cases, various schemes were studied, such as [19, 74, 102, 117]. In particular, with a massive number of antenna elements at the APs, a random fading channel acts nearly deterministically, and the communication performance is almost independent of the small-scale fading. The two aforementioned phenomenons refer to channel hardening and favorable propagation [132], [22, Ch. 2]. That being said, the random channel looks deterministic from the Rx point of view, the impact of small-scale fading then vanishes, the SINR merely relies on the large-scale fading. In summary, the corresponding benefits contain an improved SINR, a reduced link latency and a boosted link stability, which are all favored in the industrial IoT scenarios.

However, there are several challenges coming along with the large antenna array

configuration. First of all, due to the limited physical size of the UE, especially the wearables, the benefits of massive MIMO where the number of antenna elements approach infinity can never be realized practically. In addition, pilot contamination (i.e., interference from other cells) and channel reciprocity (i.e., time and resources spent on reciprocity calibration) [96, 121] are the limiting factors. Moreover, channel aging effect [116] becomes even more severe in mmWave networks due to the short effective duration of the CSI, i.e., short channel coherence time. Nonetheless, different BF strategies can be utilized to reliably resolve some of the aforementioned limits, which will be discussed in Section 2.4 together with the opportunities and challenges for positioning.

2.4 Spatial multiplexing/reuse — BF

BF technique enabled by MIMO refers to the fourth ingredient to be discussed in this section. Under certain BF capabilities [104], directional beams with high array gain can be steered towards a desired spatial direction in both azimuth and elevation plane, i.e., azimuth BF and elevation BF, as depicted in Fig. 2.3. In particular, the achievable array gain and capacity by BF largely depends on the overall number of antenna elements as well as the number of Tx branches [47, Ch. 3]. That is, more beams can be generated simultaneously with more Tx branches, while higher array gain can be achieved with larger number of antenna elements. In the meantime, the array gain is normally characterized by the beamwidth, that is, a narrower beam comes with a higher array gain, whereas a wider beam suggests a lower array gain.

More importantly, BF empowers the elegant spatial reuse and multiplexing that are beneficial to communications from several aspects. Specifically, in the condition of beam alignment, spectral efficiency is improved due to a high SINR, meanwhile, energy efficiency can also be enhanced due to the fact that most of the energy is radiated towards a small spatial area through a beamformed signal [68, 120]. In terms of different use cases in 5G, such as eMBB, massive machine-type communications (mMTC) and URLLC, BF gain can be effectively utilized to support and enhance the IoT connectivities [19]. Furthermore, the spatial information of the UE serves as the enabler of the coordinated multi-point (CoMP) scheme in order to improve the reliability and minimize the latency, especially for industrial IoT systems [90]. However, taking advantage of the spatial information requires the acquisition and

estimation of the desired UE direction, e.g., angle of departure (AoD) [37, 59] or the UE locations [93], known as the location-based BF. As discussed in the previous section, the performance of MIMO system can be maximized especially when the CSI is known at the Tx (AP side). Such information is generally acquired via two classical methods, channel reciprocity and feedback, which can be adopted in either time-division duplex (TDD) or frequency-division duplex (FDD) systems [109].

Nevertheless, some potential challenges of BF, such as the increased complexity due to beam management and potential deafness because of beam misalignment have to be carefully addressed before fully exploiting the benefits of BF. In NR system, beam management has been defined and included in the specifications [11], it consists of at least four steps: beam sweeping, beam measurement, beam reporting and beam determination [42]. As such, the initial access BF latency that is proportional to the overall number of antenna elements could occupy most of the channel coherence time, leaving no time for actual data transmission. In order to reduce such latency, various BF strategies have been proposed to replace the CSI-based BF strategies, for instances, the codebook-based BF or the location-based BF[1]. In particular, compressive-sensing based approaches have been investigated to reduce the initial access latency by taking advantage of the sparseness of mmWave channel [26, 82], however, such algorithms inevitably yield a higher latency and higher complexity [19].

Despite the fast channel variation, the mmWave transmission can actually be maintained longer than the channel coherence time without beam realignment, a concept known as "long-term BF" [73]. In other words, the path information, such as AoD and AoA that are associated with the aligned beam between any pair of Tx and Rx varies in a much slower manner than the channel coherence time. That is, the coherence time of the beams, i.e., the beam coherence time [119] is in fact longer than the channel coherence time. Therefore, BF can be more effectively implemented to profit from a longer time for data transmission, the overhead of beam realignment is also vastly minimized. However, such concept highly depends on the operating environments, it can only be fully exploited for a low-mobility UE or static scatters with strong enough multipath components. Additionally, the deafness described in [27] refers to another challenge of BF, in which case, UE cannot hear any signal stronger than the minimum detection threshold because of the beam misalignment,

[1]Interesting readers may refer to Chapter 4 (PA-BF) and [41] for a more detailed discussion on different BF strategies.

resulting link outage event. However, such situation can be ruled out with more frequent beam sweeping, beam reporting and feedback.

From positioning perspective, BF serves as one of the key technical components enabling high-accuracy location estimates, mainly for the following reasons. First, the ability of recognizing directional beams via BF empowers the estimation/tracking of both AoD and AoA [55, 93, 141]. Compared with the ToA-only based positioning system, like GNSS and UWB, this angle-domain information provides additional degree-of-freedom for accurate location estimates especially when fused with ToA measurements, which are to be demonstrated in Chapter 3. Furthermore, the achievable high SINR in the condition of beam alignment improves the accuracy of both time-domain and angle-domain LRMs. Therefore, positioning can be efficiently and effectively carried out with as few as one AP [61], which is not possible for most of the current existing positioning systems. Although angle-domain LRMs brings extra profits for positioning, the major challenges of utilizing them lies in the uncertainty of the array orientation [79, 103]. The absence of accurate knowledge of the orientation could result a huge positioning error, turning the angular LRMs from a friend to a foe. Possible solutions include the joint positioning and orientation tracking using Bayesian filters, and employment of angle difference of arrival (ADoA) for the cancellation of such uncertainty [101, Ch. 4]. Last but not least, there involves a trade-off between communication performance and positioning accuracy, which depends on the utilized array size [31].

2.5 Summary

In this chapter, the opportunities and challenges for both communications and positioning were discussed based on the key ingredients in 5G system towards industrial IoT. In addition to what were presented, other ingredients/features, such as network slicing [1], [28, Ch. 6], edge computing [12], M2M/D2D communications [23], full-duplex radio [76] and network architecture transformation [49], can also be seen as vital technical components, which are reserved for the future investigation.

Finally, this chapter ends with a summary of the potential opportunities and challenges brought by the 5G ingredients to both communications and positioning in Table 2.1 and Table 2.2, respectively.

Table 2.1 Opportunities and challenges for *communications* in 5G system

Ingredients	Opportunities	Challenges
mmWave	• abundant spectrum with wide signal bandwidth => high degrees of freedom [118, Ch. 2] and high channel capacity/throughput [46, 124] • flexible numerology for bandwidth adaptation [51] • unifying both communications and sensing, i.e., RF convergence [88, 111, 125, 126, 143]	• outstanding loss in propagation, diffraction and reflection [75] and high sensitivity to blockage, from both human and objects (e.g., buildings, vehicles) [52] • difficult to provide continuous connectivity especially for high mobility UEs [15]
SCNs	• ease on the transmit power at both Tx and Rx ends owing to short end-to-end propagation distance • reduce coverage holes within macro cells [123] • flexible frequency reuse strategies [101, Ch. 9]	• complexity of resource allocation and interference management increased as the number of small cells [112, 115] • large deployment cost as well as extra cost on cell-wise coordinations [74]
MIMO	• high diversity gain and spatial multiplexing gain [118, Ch. 7] • small scale fading vanishes thanks to channel hardening and favorable propagation [132], [22, Ch. 2] • improved interference mitigation thanks to spatial signature, yielding high SINR [22, Ch. 4 and Ch. 7]	• increased hardware/signal processing complexity and energy consumption [96] • pilot contamination and channel reciprocity [68] are limiting factors • channel aging effects result in frequent sounding and channel prediction [116]
BF	• directional beams with high array gain [118, Ch. 5] • BF gain with maximum ratio processing for IoT connectivity [19] • spatial reuse is enabled and enhanced for better CoMP transmission and reception [90]	• extra cost for beam management [41] • certain BF strategies yield high complexity and latency [19], a trade-off between complexity and performance [31] • possible deafness [27] due to potential beam-misalignment

Table 2.2 Opportunities and challenges for *positioning* in 5G system

Ingredients	Opportunities	Challenges
mmWave	• clean propagation channel dominant by LoS and few multipath [86] • wide bandwidth => high temporal resolution => accurate ToA estimation [101, Ch. 3] • unifying both positioning and sensing via mmWave communications	• acquisition of LoS LRMs can be disabled by blockage [98], yielding high positioning error • utilization of multipath ToAs needs to map the correct virtual anchors [66, 67, 69], it requires precise knowledge of the environment and more computational resources
SCNs	• high probability of LoS connection among Tx & Rx pairs [64] • more available LRMs due to a dense deployment of APs -> higher positioning accuracy [54] • lower upper bound of positioning error (cell ID based positioning [101, Ch. 2],[135])	• increased complexity for AP selection/filtering [142] in order to apply good quality LRMs for positioning • the maximum number of reliably detected signal sources, i.e., potential pilot contamination
MIMO & BF	• directional beams enable AoD/AoA estimation & tracking [59] • high SINR enhanced by MIMO further reduces the ToA estimation uncertainty • with both ToA and AoA available, positioning can be done with as few as one AP [79] • beam-sweep technique is facilitated for joint estimation of ToA and AoA [Mike's trans SP] • geometric BF enabled in both UL and DL[a]	• knowledge on array orientation is required to have sensible AoD/AoA • uncertainty on array orientation increases the error distribution of AoD/AoA

[a]A multimedia demonstration of geometric BF can be found online at: http://www.tut.fi/prisma/Video.htm, Video 1

3 ACHIEVING THE LOCATION AWARENESS — POSITIONING

Today, positioning has become an indispensable key technology that enables not only the commercial but also the industrial use cases, such as personal navigation and autonomous guided robotics [39, 76]. Via the transmission and reception of the ubiquitous radio signals, the location information of the connected mobile robots/devices can be estimated and obtained via processing the available LRMs, i.e., positioning. Therefore, the positioning performance (e.g., the accuracy and reliability) plays a significant role in enabling the location-based services [8] as well as the location-aware communications [32]. In general, positioning can be divided into two stages as depicted in the upper part of Fig. 1.1 as follows:

1. Generation/estimation of the LRMs, such as RSS, ToA and AoA according to the signal parameters, antenna models as well as the path information obtained from the propagation environments;
2. Positioning and tracking via Bayesian and/or non-Bayesian approaches[1].

Aiming at resolving the potential challenges for positioning in the industrial environments, i.e., the location uncertainty of the anchors, as described in research question 2 in Section 1.2, this chapter introduces and demonstrates the methods of achieving the location awareness of all the connected entities in a mmWave positioning system. First, an overall description of the proposed network-centric positioning framework is provided. Then, the approach of characterizing/estimating the LRMs are outlined and analyzed. Thereafter, the proposed 3D positioning algorithms (both snapshot and sequential methods) are formulated and presented. Fi-

[1] In some literature, the Bayesian approach is referred to as a sequential estimation method, whereas the non-Bayesian approach is also known as snapshot method, both types of approaches will be discussed further in the later sections.

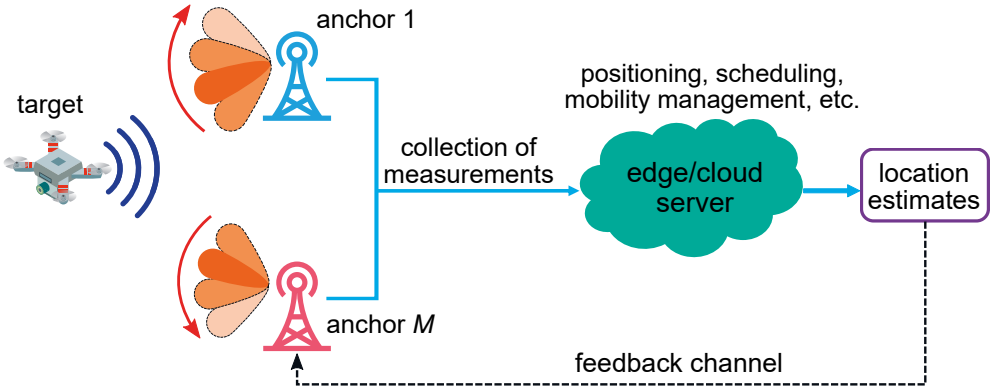

Figure 3.1 In the envisioned network-centric positioning framework, the mobile vehicles or robots (as *targets*) are the Tx while the *anchors* represent the Rx that estimated the LRMs, e.g., ToA and/or AoA. Positioning is carried out at the edge/cloud server, where the location estimates of both targets and anchors are steadily available at the network side for further actions, such as scheduling, mobility management and proactive resource allocation.

nally, this chapter is concluded with the numerical characterization and discussion on the achieved positioning performance.

3.1 Proposed network-centric positioning framework

With the industrial IoT in the context, a network-centric positioning framework is envisioned and illustrated in Fig. 3.1, in which one or several industrial robots/vehicles, which we refer to as *targets* transmit reference signals through different air interfaces (e.g., the access link or sidelink) towards the *anchors* (AP) whose locations are typically known. Throughout this chapter, the locations of neither the targets nor the anchors are precisely known, therefore remain to be estimated. The positioning algorithm will be presented in Section 3.3.

Furthermore, the transmitted signals employ the form of an OFDM signal transmitted periodically from the omni-directional targets, while moving along certain trajectory (e.g., the random waypoint trajectory). Such configuration yields a single-input multiple-output (SIMO) model for each pair of Tx & Rx in the wireless system, thus forming a multi-user MIMO scenario for positioning. Additionally, the uniform rectangular array (URA) arrays[2] are assumed to be employed at all the anchors to facilitate 3D BF technique. One of the procedures in beam management [11],

[2]In addition to URA, other types of antenna can also be employed, such as uniform circular array.

beam sweeping technique is employed and involved in the estimation of LRMs that are then fused together and uploaded to a edge/cloud server, where positioning is carried out. With the support of network slicing and virtualization, the edge/cloud server can be thought of as a data center in proximity [49], such that the feedback latency for communicating the location estimates back to the targets is minimized.

Finally, the estimated locations are sent back to the network edge via a feedback channel facilitating the positioning-aided communications (discussed in the next chapter) and other location-based services.

3.2 Location-related measurements

At the first stage of positioning, the LRMs are to be acquired or estimated. Therefore, the property of typical LRMs that can be utilized for positioning is first discussed in this section. Thereafter, the method of characterizing their accuracy is formulated and presented together with applied channel model.

RSS. Owing to its cost-efficiency, RSS-based positioning has maintained constant interests in the positioning community. Nevertheless, the multipath and spatial-correlated shadowing remain as the two major error sources that hinder the obtainable positioning accuracy [97]. Although fingerprinting based methods can vastly boost the performance, the corresponding positioning accuracy is not good enough to meet the requirement of the specified positioning use cases in [2, 7]. Additionally, the required database as well as the complexity for interpolation and extrapolation of the fingerprints makes RSS a less attractive option [128]. The RSS-based positioning is out of the research interests of this thesis.

ToA. Similar to the RSS, the ToA is seen as the range-based LRMs, but obtained by estimating the arrival time of the LoS component [45]. In general, there are two major error sources for ToA measurements as well, i.e., multipath/NLoS impairment [14, 81] and synchronization error [35]. The integration of FR2 bands in 5G NR allows for a high temporal resolution for mmWave positioning, yielding low impact from the multipath components. Furthermore, with the assistance of virtual anchors, ToA-based positioning is capable of achieving high positioning accuracy using both LoS and multipath components [66, 130]. As to the second error source, the time-varying clock offsets typically exist between any Tx & Rx pairs. Therefore, the ToA measurements remain useless without proper synchronization scheme. Such

problem can be resolved by joint tracking the locations and clock offsets as [65] or utilizing the time difference of arrival (TDoA) measurements.

AoA. As a directional measurements, AoA provides positioning information that is complementary to the other two range-based LRMs [80, 103]. However, a potential problem remains before this angular information can be properly employed for positioning, that is, the uncertainty of array orientations. Such problem can be tackled by several means. For a network-centric system, a Bayesian filter can be applied to jointly track both the locations and the orientations [94]. As of the device-centric positioning, the ADoA measurements [101, Ch. 4] can be performed the same way as the TDoA to eliminate the orientation offsets. Moreover, an inertial measurement unit (IMU) can be employed to provide the orientation estimates [126, 143].

3.2.1 Signal and mmWave channel models

This section presents the mathematical formulation of the applied signal under the LoS-dominant mmWave radio channel. More specifically, the transmitted OFDM symbol at the pth sub-carrier is denoted as $s[p,i] \in \mathbb{C}$ at any time instant i. For the sake of notation simplicity, the index of targets is omitted. After passing through a LoS-dominate mmWave multipath channel, the anchors acquire the radio signals via a beam sweeping process that is associated with multiple beamformers (beam-steering vectors). From the perspective of the mth anchor, the received frequency-domain complex symbol at the ith time instant and the pth sub-carrier through the qth beamformer is denoted as

$$r_m^{(q)}[p,i] = \left(\boldsymbol{w}_m^{(q)}[i]\right)^{\mathrm{H}} (\boldsymbol{\Lambda}_m[p] s[p,i] + \boldsymbol{n}[p,i]), \tag{3.1}$$

where $\boldsymbol{n}[p,i] \sim \mathscr{CN}\left(0, \sigma_n^2 \mathbf{I}_{N_R}\right)$, referring to the complex-Gaussian white noise with a power density of σ_n^2 imposed on overall N_R antenna elements, and the Hermitian transpose is denoted as $^{\mathrm{H}}$. Moreover, the qth analog beamformer $\boldsymbol{w}_m^{(q)}[i] \in \mathbb{C}^{N_R \times 1}$ can be constructed, but not limited to, via phase-shifter according to certain spatial angles. Due to the omni-directional transmission, the channel matrix for each sub-carrier $\boldsymbol{\Lambda}_m[p] \in \mathbb{C}^{N_R \times 1}$ (otherwise, $\boldsymbol{\Lambda}_m[p] \in \mathbb{C}^{N_R \times N_T}$ where $N_T = 1$) can be

written as

$$\begin{aligned}\boldsymbol{\Lambda}_m[p] &= \boldsymbol{A}_R[p]\boldsymbol{\Gamma}[p] \\ &= \sum_{l=0}^{L-1} \boldsymbol{b}_{\mathrm{URA}}(\phi_l)\gamma_l e^{-j2\pi f_{\mathrm{sc}} p \tau_l},\end{aligned} \tag{3.2}$$

where $\boldsymbol{A}_R[p] \in \mathbb{C}^{N_R \times L} = \left[\boldsymbol{b}_{\mathrm{URA}}(\phi_0), \cdots, \boldsymbol{b}_{\mathrm{URA}}(\phi_{L-1})\right]$ represents the array response and $\boldsymbol{\Gamma}[p] \in \mathbb{C}^{L\times 1} = \left[\gamma_0 e^{-j2\pi f_{\mathrm{sc}} p \tau_0}, \cdots, \gamma_{L-1} e^{-j2\pi f_{\mathrm{sc}} p \tau_{L-1}}\right]^T$ is the channel state vector. Specifically, $\boldsymbol{b}_{\mathrm{URA}}(\phi_l) \in \mathbb{C}^{N_R \times 1}$ refers to the URA response at the spatial angle $\phi_l \triangleq (\varphi_l, \theta_l)$, γ_l is the complex channel coefficient including the path-loss of the lth path with a time delay of τ_l and f_{sc} is the sub-carrier spacing. Furthermore, $\boldsymbol{b}_{\mathrm{URA}}(\phi_l)$ can be modeled as a combination of two uniform linear array (ULA) responses

$$\boldsymbol{b}_{\mathrm{URA}}(\phi_l) = \sqrt{\beta_0(N_R, \phi_l)}\boldsymbol{a}_{\mathrm{ULA}}(\varphi_l) \otimes \boldsymbol{a}_{\mathrm{ULA}}(\theta_l|\varphi_l), \tag{3.3}$$

where $\otimes$ denotes the Kronecker product and the scaling factor $\beta_0(N_R, \phi_l)$ represents the antenna pattern which decides the array gain that is a function of the total number of antenna elements N_R as well as the spatial angle pair ϕ_l. Basically, more antenna elements allow for a narrower beamwidth, which yields a higher array gain β_0. In addition, the angle pair ϕ that consists of the azimuth angle θ as well as the co-elevation angle φ slightly varies the corresponding array gain depending on the radiation pattern of each antenna element. Assuming a half-wavelength antenna element interval, the individual normalized ULA responses are given as

$$\begin{aligned}\boldsymbol{a}_{\mathrm{ULA}}(\varphi_l) &= \frac{1}{\sqrt{N_{\mathrm{el}}}} e^{-j\pi \sin(\varphi_l)\left[-\frac{N_{\mathrm{el}}-1}{2}, \cdots, \frac{N_{\mathrm{el}}-1}{2}\right]^T}, \\ \boldsymbol{a}_{\mathrm{ULA}}(\theta_l|\varphi_l) &= \frac{1}{\sqrt{N_{\mathrm{az}}}} e^{-j\pi \cos(\varphi_l)\sin(\theta_l)\left[-\frac{N_{\mathrm{az}}-1}{2}, \cdots, \frac{N_{\mathrm{az}}-1}{2}\right]^T},\end{aligned} \tag{3.4}$$

where N_{el} and N_{az} are the number of antenna elements in the vertical (elevation) and horizontal (azimuth) directions, respectively, and $N_R = N_{\mathrm{el}} N_{\mathrm{az}}$. For example, $N_{\mathrm{el}} = N_{\mathrm{az}} = 16$ for a 16×16 URA.

Last but not least, the qth beamformer $\boldsymbol{w}_m^{(q)}$ without the time index is constructed in a similar fashion as (3.3) as

$$\boldsymbol{w}_m^{(q)} = \boldsymbol{a}_{\mathrm{ULA}}(\varphi_q) \otimes \boldsymbol{a}_{\mathrm{ULA}}(\theta_q|\varphi_q), \tag{3.5}$$

in which $\left(\varphi_q, \theta_q\right) \triangleq \phi_q$ represents the corresponding spatial angle defined in the applied codebook. In addition, it is presumed that the whole beam sweeping process (i.e., the duration of all the beamformers combined) takes less or equal time as the channel coherence time. That is, the channel matrix in frequency domain (3.2) remains nearly constant during one beam sweeping process.

3.2.2 Characterization of LRMs' accuracy

In this section, the achievable accuracy of LRMs via the ubiquitous Cramér-Rao lower bounds (CRLB) based on the beam-based observations, i.e., beam reference signal received power (B-RSRP) is examined.

3.2.2.1 ToA measurements

The ToA measurements that reflect the distance observations between the anchors and the target is expressed as

$$\hat{\tau}[i] = \boldsymbol{b}[i] + \boldsymbol{f}_{\tau}(\mathbf{P}_{\mathrm{T}}[i]) + \boldsymbol{n}_{\tau}[i], \tag{3.6}$$

where $\boldsymbol{b}[i] \in \mathbb{R}^{M\times 1}$ refers to the bias vector caused by several factors, such as NLoS transmission, the clock offsets [62], or the location uncertainty of the anchors. While the effects of NLoS and clock offsets have been studied and investigated by the earlier works [35, 45], the solution to the anchor locations' uncertainty has not been widely analyzed. The proposed solutions are to be provided in Section 3.3. Furthermore, the ToA observation function $\boldsymbol{f}_{\tau}(\mathbf{P}_{\mathrm{T}}[i])$ is expressed as

$$\begin{aligned} \boldsymbol{f}_{\tau}(\mathbf{P}_{\mathrm{T}}[i]) &= [\tau_1[i], \cdots, \tau_M[i]]^T \\ &= \left[||\mathbf{P}_{\mathrm{T}}[i] - \mathbf{P}_{\mathrm{A},1}||, \cdots, ||\mathbf{P}_{\mathrm{T}}[i] - \mathbf{P}_{\mathrm{A},M}||\right]^T / c, \end{aligned} \tag{3.7}$$

where c is the speed of light, $\mathbf{P}_{\mathrm{T}} = [x_{\mathrm{T}}, y_{\mathrm{T}}, z_{\mathrm{T}}]^T$ refers to any arbitrary target location and $\mathbf{P}_{\mathrm{A},m} = [x_{\mathrm{A},m}, y_{\mathrm{A},m}, z_{\mathrm{A},m}]^T$ represents the location of the mth anchor (e.g., AP). Furthermore, the variable $\boldsymbol{n}_{\tau}$ represents the noise vector that reflects the measurement accuracy. It is worth noting that $\boldsymbol{n}_{\tau}$ remains zero-mean under the LoS and NLoS scenario as the bias is modeled separately in $\boldsymbol{b}[i]$ (3.6). Since the LoS is a typical situation in 5G SCNs [16], the noise vector $\boldsymbol{n}_{\tau}[i]$ is modelled

as a zero-mean Gaussian variable with a time-dependent noise covariance matrix $\mathbf{R}_{\tau}[i] = \mathrm{diag}\left(\sigma^2_{\tau,1}[i], \cdots, \sigma^2_{\tau,M}[i]\right)$. The noise variance of the mth ToA measurement, $\sigma^2_{\tau,m}[i]$, is bounded by the following CRLB for OFDM signals [101, Ch.3]

$$\sigma^2_{\tau,m}[i] \geq \frac{3}{8\pi^2 f_{\mathrm{sc}}^2 \mathrm{SNR}_m[i] M_p(M_p+1)(2M_p+1)}, \tag{3.8}$$

where f_{sc} refers to the sub-carrier spacing, and $M_p = \frac{N_p-1}{2}$, N_p is the overall number of sub-carriers. It is noteworthy that (3.8) applies only for OFDM with *uniformly distributed* energy among all the active sub-carriers. Furthermore, the linear scale signal-to-noise ratio (SNR) at the ith time instant with respect to the mth anchor is denoted as

$$\mathrm{SNR}_m[i] = \max(\mathbf{B}_m[i])/P_n = \mathrm{B}_m^{(\hat{q})}[i]/P_n, \tag{3.9}$$

where P_n is the noise power over the considered signal bandwidth $B_{\mathrm{w}} = f_{\mathrm{sc}} N_p$, and $\mathrm{B}_m^{(\hat{q})}[i]$ refers to the maximum B-RSRP among the beam power vector $\mathbf{B}_m[i] \in \mathbb{R}^{Q\times 1}$, where Q is the overall number of the beamformers in the codebook. Each B-RSRP can be computed by averaging the power over all the active sub-carriers of the received OFDM signals[3], defined in (3.1)

$$\mathrm{B}_m^{(q)}[i] = \frac{1}{N_p}\sum_{p=1}^{N_p} |r_m^{(q)}[p,i]|^2, \tag{3.10}$$

where the index of beamformer $q \in \mathcal{Q} = \{1, \cdots, Q\}$. Normally, the ToA and AoA associated with such beamformer corresponds to the information of the LoS path if unblocked or the strongest multipath when the LoS path is blocked.

3.2.2.2 AoA measurements

In any typical 3D environments, the AoA measurements consist of the elevation and the azimuth angles. Taking the array orientation into account, the AoA measurement vector with respect to a single target is expressed as

$$\hat{\boldsymbol{\phi}}[i] = \boldsymbol{f}_{\phi}(\mathbf{P}_{\mathrm{T}}[i]) + \boldsymbol{\alpha} + \boldsymbol{n}_{\phi}[i], \tag{3.11}$$

[3] In practical systems, the B-RSRP measurements are normally taken from certain reference or pilot sub-carriers, where the transmitted signal is known.

where $\hat{\boldsymbol{\phi}}[i] \in \mathbb{R}^{2M\times 1}$ contains the elevation AoA $\hat{\varphi}[i] \in \mathbb{R}^{M\times 1}$ as well as the azimuth AoA $\hat{\theta}[i] \in \mathbb{R}^{M\times 1}$. In addition, the angular offset due to the specific array orientations is denoted as $\boldsymbol{\alpha} = [\boldsymbol{\alpha}_\varphi^T, \boldsymbol{\alpha}_\theta^T]^T \in \mathbb{R}^{2M\times 1}$, which contains the angular offsets along both elevation domain and azimuth domain, $\boldsymbol{\alpha}_\varphi \in \mathbb{R}^{M\times 1}$ and $\boldsymbol{\alpha}_\theta \in \mathbb{R}^{M\times 1}$, respectively. It is noteworthy that the angular offset $\boldsymbol{\alpha}$ can be considered as known or unknown, depending on the available information to the system. Herein, the angular offset $\boldsymbol{\alpha}$ is assumed to be known. Furthermore, the AoA noise vector $\boldsymbol{n}_\phi[i] \sim \mathcal{N}\left(\mathbf{0}_{2M}, \mathbf{R}_\phi[i]\right)$ is a zero-mean Gaussian process, in which, $\mathbf{R}_\phi[i] \in \mathbb{R}^{2M\times 2M}$ is described as

$$\mathbf{R}_\phi[i] = \begin{bmatrix} \mathbf{R}_\varphi[i] & \mathbf{0} \\ \mathbf{0} & \mathbf{R}_\theta[i] \end{bmatrix}, \tag{3.12}$$

where the noise covariance of elevation AoA $\mathbf{R}_\varphi[i] = \mathrm{diag}\left(\sigma^2_{\varphi,1}[i], \cdots, \sigma^2_{\varphi,M}[i]\right)$ and the noise covariance of azimuth AoA $\mathbf{R}_\theta[i] = \mathrm{diag}\left(\sigma^2_{\theta,1}[i], \cdots, \sigma^2_{\theta,M}[i]\right)$.

The AoA observation function $\boldsymbol{f}_\phi(\cdot)$ in (3.11) consists of two parts, the observation function for elevation angles that is denoted as $\boldsymbol{f}_\varphi(\cdot)$, and the observation function for azimuth angles that is denoted as $\boldsymbol{f}_\theta(\cdot)$. Therefore, the AoA observation function is expressed as $\boldsymbol{f}_\phi(\mathbf{P}_\mathrm{T}[i]) = \left[\boldsymbol{f}_\varphi^T(\mathbf{P}_\mathrm{T}[i]), \boldsymbol{f}_\theta^T(\mathbf{P}_\mathrm{T}[i])\right]^T$, where

$$\boldsymbol{f}_\varphi(\mathbf{P}_\mathrm{T}[i]) = \begin{bmatrix} \arcsin(\Delta z_1[i]/d_1[i]) \\ \vdots \\ \arcsin(\Delta z_M[i]/d_M[i]) \end{bmatrix}, \quad \boldsymbol{f}_\theta(\mathbf{P}_\mathrm{T}[i]) = \begin{bmatrix} \mathrm{atan}_2(\Delta y_1[i], \Delta x_1[i]) \\ \vdots \\ \mathrm{atan}_2(\Delta y_M[i], \Delta x_M[i]) \end{bmatrix}, \tag{3.13}$$

in which $\Delta x_m[i] = x[i] - x_m$, $\Delta y_m[i] = y[i] - y_m$, and $\Delta z_m[i] = z[i] - z_m$ for all $m = 1, \ldots, M$. Additionally, arcsin and atan_2 denote the inverse sine function and four-quadrant inverse tangent function, respectively.

Further, the measurement noise variance of the mth azimuth AoA measurement, $\sigma^2_{\theta,m}[i]$, is bounded by the CRLB that is derived based on [101, Ch.3] as

$$\sigma^2_{\theta,m}[i] \geq \frac{6}{N_\mathrm{az}\left(N_\mathrm{az}^2 - 1\right)\mathrm{SNR}_m[i](\pi\cos\theta_m)^2}, \tag{3.14}$$

where N_az and $\mathrm{SNR}_m[i]$ refer to the same variables defined in (3.4) and (3.8), respec-

tively. The number of antenna element along the azimuth plane N_{az} actually represents the angular resolution, the same applies to the co-elevation plane. As such, a higher resolution (more antenna elements) yields a higher accuracy. Throughout this thesis, we consider the URA to be square, i.e., $N_{\text{az}} = N_{\text{el}}$. Such configuration yields the same angular resolution in both elevation and azimuth direction. Hence, the noise statistics of the elevation AoA measurements, $\sigma^2_{\varphi,m}$, shares the same expression as (3.14). Additionally, un-squared URA with $N_{\text{az}} \neq N_{\text{el}}$ can certainly be employed for applications that do not equally value the vertical accuracy and the horizontal accuracy, such as the ground vehicles-oriented positioning system [70].

Furthermore, it is seen that the angular CRLB also depends on the relative geometry (reflected by both θ_m and φ_m) between the target and the anchor, judging from the mathematical property of cosine function. That being said, any AoA approaching $\pm\pi/2$ leads the variance in (3.14) approaching infinity as, in which case, the effective array aperture vanishes leaving no visible angular resolution. Moreover, it is noteworthy that, compared to the applied individual characterization as (3.14), the AoA accuracy in both elevation and azimuth directions should be further reduced when jointly utilizing measurements from all the antenna elements of URA.

3.3 Positioning algorithms

As the second stage of positioning, different approaches are introduced in this section to acquire location estimates based on available LRMs. The corresponding performance is evaluated in ray-tracing based simulations. Herein, the focus will be given to perform positioning with the location uncertainties of the anchors, which have not been widely investigated in the earlier works of positioning. Specifically, there are three algorithms proposed and evaluated, one refers to the geometry-based positioning approach, whereas the other two belong to the Bayesian framework, both build on the ubiquitous EKF.

3.3.1 Snapshot positioning — WCG

As the first approach, the proposed geometry-based positioning solution, WCG, is derived based on the fusion of the measurements from both delay and angular domains (i.e., the ToA and AoA) and the geometric relationship. The specific il-

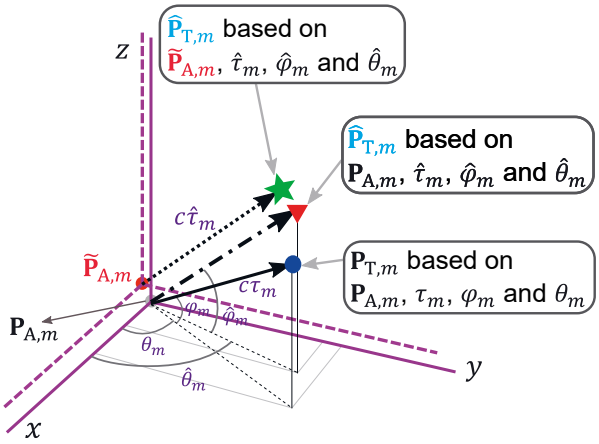

Figure 3.2 The geometric relationship between the mth anchor and the target with measurement errors as well as the location uncertainty of the anchors.

lustrations are given in Fig. 3.2. The time instant is skipped since WCG is a snapshot estimation method, i.e., the current estimate depends only on the current available information/measurements. With a perfect location of the mth anchor where $m \in \mathcal{M} = \{1, \ldots, M\}$ and the corresponding true ToA and AoA, the target location obtained via the mth anchor $\mathbf{P}_{\mathrm{T},m}$ can be computed as

$$\mathbf{P}_{\mathrm{T},m} = \begin{bmatrix} x_{\mathrm{T},m} \\ y_{\mathrm{T},m} \\ z_{\mathrm{T},m} \end{bmatrix} = \begin{bmatrix} x_{\mathrm{A},m} + c\tau_m \cos\varphi_m \cos\theta_m \\ y_{\mathrm{A},m} + c\tau_m \cos\varphi_m \sin\theta_m \\ z_{\mathrm{A},m} + c\tau_m \sin\varphi_m \end{bmatrix}. \tag{3.15}$$

Note that the calculated location in (3.15) is the ground truth of the target, which is illustrated by the blue dot marker in Fig. 3.2.

In practice, not only the LRMs are in general erroneous, but there also exists certain uncertainty in the assumed locations of the anchors, in which case, (3.15) can be re-written as

$$\hat{\mathbf{P}}_{\mathrm{T},m} = \begin{bmatrix} \hat{x}_{\mathrm{T},m} \\ \hat{y}_{\mathrm{T},m} \\ \hat{z}_{\mathrm{T},m} \end{bmatrix} = \begin{bmatrix} \tilde{x}_{\mathrm{A},m} + c\hat{\tau}_m \cos\hat{\varphi}_m \cos\hat{\theta}_m \\ \tilde{y}_{\mathrm{A},m} + c\hat{\tau}_m \cos\hat{\varphi}_m \sin\hat{\theta}_m \\ \tilde{z}_{\mathrm{A},m} + c\hat{\tau}_m \sin\hat{\varphi}_m \end{bmatrix}, \tag{3.16}$$

in which, the location of the mth anchor known to the network is denoted as $\tilde{\mathbf{P}}_{\mathrm{A},m} =$

$\left[\tilde{x}_{\mathrm{A},m}, \tilde{y}_{\mathrm{A},m}, \tilde{z}_{\mathrm{A},m}\right]^T$. The green star marker in Fig. 3.2, that is acquired by applying (3.16), is the location estimate based on erroneous anchor location as well as the noisy measurements. Therefore, overall M location estimates are obtained from M pairs of anchors, denoted as $\hat{\mathbf{P}}_{\mathrm{T}} = \left[\hat{\mathbf{P}}_{\mathrm{T},1}, \cdots, \hat{\mathbf{P}}_{\mathrm{T},M}\right]$. To fuse the obtained M location estimates into the final location estimate, a weight vector is formed based on the channel quality (which reflects the measurement quality) of each anchor as

$$\boldsymbol{w} = [w_1, \cdots, w_M]^T = [\mathrm{SNR}_1, \cdots, \mathrm{SNR}_M]^T, \tag{3.17}$$

where the SNR are defined and calculated in (3.9).

In the end, the location estimate by the WCG is the product of the estimate target location matrix $\hat{\mathbf{P}}_{\mathrm{T}}$ and the normalized weight vector $\tilde{\boldsymbol{w}}$ such that

$$\hat{\mathbf{P}}_{\mathrm{WCG}} = \hat{\mathbf{P}}_{\mathrm{T}} \tilde{\boldsymbol{w}}, \tag{3.18}$$

where $\tilde{\boldsymbol{w}} = \boldsymbol{w} / \sum_{m=1}^{M} w_m$. The weight vector can certainly be constructed in different manners, and the performance largely relies on the applied scenarios. Additionally, it is noteworthy that the most attractive feature of WCG lies in the computational efficiency especially compared to the EKF-based solutions that are introduced next.

3.3.2 Sequential positioning I — SLAT EKF

As one of the major contributions of this thesis, the second proposed positioning solutions, namely SLAT EKF is introduced in this section. Since it is a SLAT-based approach, the most significant feature is the capability of tracking the locations of the mobile targets, while mapping the static anchors' location, further enhancing the positioning capability and performance for the industrial IoT systems.

Exploiting the flexibility in dealing with the non-linear measurement or state transition models, the proposed SLAT EKF is formulated according to [105] as

$$\begin{aligned} \text{state transition model}: \mathbf{s}[i] &= \mathbf{F}\mathbf{s}[i-1] + \mathbf{u}[i] \\ \text{measurement model}: \mathbf{y}[i] &= \mathbf{h}(\mathbf{s}[i]) + \mathbf{w}[i], \end{aligned} \tag{3.19}$$

where $\mathbf{y}[i]$ represents the LRMs which are facilitated as the measurements in the

EKF, and $\mathbf{s}[i]$ refers to the time-varying state vector[4] that contains the information of both targets and anchors such as

$$\mathbf{s} = \left[\mathbf{s}_{\mathrm{T},1}^T, \cdots, \mathbf{s}_{\mathrm{T},K}^T, \mathbf{P}_{\mathrm{A},1}^T, \cdots, \mathbf{P}_{\mathrm{A},M}^T\right]^T, \tag{3.20}$$

in which, the state vector of the kth target is given as

$$\mathbf{s}_{\mathrm{T},k} = \left[\mathbf{P}_{\mathrm{T},k}^T, \mathbf{v}_{\mathrm{T},k}^T, \mathbf{a}_{\mathrm{T},k}^T\right]^T, \tag{3.21}$$

where $\mathbf{v}_{\mathrm{T},k}^T = \left[v_x^{(\mathrm{T},k)}, v_y^{(\mathrm{T},k)}, v_z^{(\mathrm{T},k)}\right]$ and $\mathbf{a}_{\mathrm{T},k}^T = \left[a_x^{(\mathrm{T},k)}, a_y^{(\mathrm{T},k)}, a_z^{(\mathrm{T},k)}\right]$ are the target velocity and acceleration vector, respectively. The index of targets $k \in \mathcal{K} = \{1, \cdots, K\}$. Although only the locations of the anchors are considered in the state vector, their velocity and acceleration can also be included to track the movements of the anchors.

Furthermore, the process noise vector is denoted as $\mathbf{u} \sim \mathcal{N}\left(\mathbf{0}_{9K+3M}, \mathbf{Q}\right)$ where $\mathbf{0}_{9K+3M}$ is a zero-vector with a dimension of $9K+3M$, which are expressed as follows together with the linear state transition matrix $\mathbf{F}$ and the state covariance matrix $\mathbf{\Sigma}$

$$\mathbf{Q} = \begin{bmatrix} \mathbf{Q}_{\mathrm{T}} & \mathbf{0} \\ \mathbf{0} & \mathbf{Q}_{\mathrm{A}} \end{bmatrix}, \mathbf{F} = \begin{bmatrix} \mathbf{F}_{\mathrm{T}} & \mathbf{0} \\ \mathbf{0} & \mathbf{F}_{\mathrm{A}} \end{bmatrix}, \mathbf{\Sigma} = \begin{bmatrix} \mathbf{\Sigma}_{\mathrm{T}} & \mathbf{0} \\ \mathbf{0} & \mathbf{\Sigma}_{\mathrm{A}} \end{bmatrix}, \tag{3.22}$$

where $\mathbf{Q}_{\mathrm{T}} \in \mathbb{R}^{9K\times 9K}$, $\mathbf{Q}_{\mathrm{A}} \in \mathbb{R}^{3M\times 3M}$, $\mathbf{F}_{\mathrm{T}} \in \mathbb{R}^{9K\times 9K}$, $\mathbf{F}_{\mathrm{A}} \in \mathbb{R}^{3M\times 3M}$, $\mathbf{\Sigma}_{\mathrm{T}} \in \mathbb{R}^{9K\times 9K}$ and $\mathbf{\Sigma}_{\mathrm{A}} \in \mathbb{R}^{3M\times 3M}$ are the process noise covariance matrix, the linear state transition matrix and state covariance matrix of the considered targets and anchors, respectively. In particular, both $\mathbf{Q}_{\mathrm{T}}$ and $\mathbf{F}_{\mathrm{T}}$ are block diagonal matrices that consist of the corresponding matrix of each individual target, i.e., $\mathbf{Q}_{\mathrm{T}} = \mathrm{blkdiag}\left(\mathbf{Q}_{\mathrm{T},1}, \cdots, \mathbf{Q}_{\mathrm{T},K}\right)$ and $\mathbf{F}_{\mathrm{T}} = \mathrm{blkdiag}\left(\mathbf{F}_{\mathrm{T},1}, \cdots, \mathbf{F}_{\mathrm{T},K}\right)$, the individual $\mathbf{F}_{\mathrm{T},k}$ and $\mathbf{Q}_{\mathrm{T},k}$ are written as

$$\mathbf{F}_{\mathrm{T},k} = \begin{bmatrix} 1 & \Delta t & \frac{\Delta t^2}{2} \\ 0 & 1 & \Delta t \\ 0 & 0 & 1 \end{bmatrix} \otimes \mathbf{I}_{3\times 3}, \ \mathbf{Q}_{\mathrm{T},k} = \sigma_{q,k}^2 \begin{bmatrix} \frac{\Delta t^5}{20} & \frac{\Delta t^4}{8} & \frac{\Delta t^3}{6} \\ \frac{\Delta t^4}{8} & \frac{\Delta t^3}{3} & \frac{\Delta t^2}{2} \\ \frac{\Delta t^3}{6} & \frac{\Delta t^2}{2} & \Delta t \end{bmatrix} \otimes \mathbf{I}_{3\times 3}, \tag{3.23}$$

where Δt represents the update time-step between two successive time instants, and $\sigma_{q,k}^2$ denotes the process noise variance of the acceleration of the kth target. For the

[4]The time index i is dropped thereafter for the notation's simplicity.

Table 3.1 The number of available LRMs as a function of the number of targets K and anchors M for each considered measurement choice

Measurement	**Number of available LRMs**, N
ToA, τ	MK
TDoA, $\Delta\tau$	$(M-1)K$
AoA, ϕ	$2MK$
ToA+AoA, $\tau+\phi$	$3MK$
TDoA+AoA, $\Delta\tau+\phi$	$(3M-1)K$

anchors, $\mathbf{F}_{\mathrm{A}} = \mathbf{I}_{3M\times 3M}$ and $\mathbf{Q}_{\mathrm{A}} = \mathbf{I}_{3M\times 3M}\sigma^2_{q,\mathrm{A}}$. Similarly, the covariance matrices of the initial state for both targets and anchors are (block) diagonal as well, in which $\mathbf{\Sigma}_{\mathrm{T}} = \mathrm{blkdiag}\big(\mathbf{\Sigma}_{\mathrm{T},1},\cdots,\mathbf{\Sigma}_{\mathrm{T},K}\big)$, where $\mathbf{\Sigma}_{\mathrm{T},k} = \mathrm{blkdiag}\big(\mathbf{\Sigma}_{\mathrm{P},k},\mathbf{\Sigma}_{\mathrm{v},k},\mathbf{\Sigma}_{\mathrm{a},k}\big)$ and for the anchors $\mathbf{\Sigma}_{\mathrm{A}} = \mathrm{blkdiag}\big(\mathbf{\Sigma}_{\mathrm{A},1},\cdots,\mathbf{\Sigma}_{\mathrm{A},M}\big)$, where $\mathbf{\Sigma}_{\mathrm{A},m} = \mathrm{diag}\big(\sigma_x^2,\sigma_y^2,\sigma_z^2\big)$.

Moreover, the measurement noise vector that reflects the accuracy of $\mathbf{y}$ is denoted as $\mathbf{w}\sim\mathcal{N}(\mathbf{0}_N,\mathbf{R})$ where N is the overall number of available LRMs, $\mathbf{R} = \mathrm{blkdiag}\big(\mathbf{R}^{(1)},\cdots,\mathbf{R}^{(K)}\big)$ and $\mathbf{y} = \big[\mathbf{y}_1^T,\cdots,\mathbf{y}_K^T\big]^T$. For instance, the number of LRMs is equal to the number of anchors, i.e., $N = M$ when only the ToA measurements are available. As such, the measurement noise covariance matrix $\mathbf{R}_\tau \in \mathbb{R}^{MK\times MK} = \mathrm{blkdiag}\big(\mathbf{R}_\tau^{(1)},\cdots,\mathbf{R}_\tau^{(K)}\big)$ in which, $\mathbf{R}_\tau^{(k)} = \mathrm{diag}\big(\sigma^2_{\tau,1,k},\cdots,\sigma^2_{\tau,M,k}\big)$. The overall number of LRMs is essentially a function of the number of targets and anchors, given in Table 3.1. It can be seen that when utilizing both time- and angle-domain LRMs, the number of available LRMs becomes larger, which could be beneficial to the achievable positioning performance, as will be shown in Section 3.5.

Additionally, the measurement function $\mathbf{h}(\cdot)$ in (3.19) for all considered LRMs is outlined in (3.6) and (3.11) from which the Jacobian matrix is evaluated. As a concrete example, when only the ToA measurements are utilized, the Jacobian matrix $\mathbf{H}_\tau \in \mathbb{R}^{MK\times(9K+3M)}$ can be constructed as

$$\mathbf{H}_\tau = \begin{bmatrix} \mathbf{H}^{(1)}_{\tau,\mathrm{T}} & \mathbf{0} & \cdots & \mathbf{0} & \mathbf{H}^{(1)}_{\tau,\mathrm{A}} \\ \mathbf{0} & \mathbf{H}^{(2)}_{\tau,\mathrm{T}} & & \vdots & \mathbf{H}^{(2)}_{\tau,\mathrm{A}} \\ \vdots & & \ddots & \mathbf{0} & \vdots \\ \mathbf{0} & \cdots & \mathbf{0} & \mathbf{H}^{(K)}_{\tau,\mathrm{T}} & \mathbf{H}^{(K)}_{\tau,\mathrm{A}} \end{bmatrix}, \tag{3.24}$$

where $\mathbf{H}^{(k)}_{\tau,\mathrm{T}} \in \mathbb{R}^{M\times 9}$ and $\mathbf{H}^{(k)}_{\tau,\mathrm{A}} \in \mathbb{R}^{M\times 3M}$ refer to the Jacobian matrix of the kth

target, where the partial derivatives are taken with respect to the variables of targets and anchors, respectively. In a similar manner, $\mathbf{H}_{\Delta\tau}$, $\mathbf{H}_{\phi}$, $\mathbf{H}_{\tau+\phi}$ and $\mathbf{H}_{\Delta\tau+\phi}$ are constructed as (3.24), and evaluated at the a prior mean $\hat{\mathbf{s}}^{-}$ which is shown in Algorithm 1 where the proposed SLAT EKF is briefly summarized. Furthermore, the specific Jacobian matrices with respect to the ToA, $\mathbf{H}^{(k)}_{\tau,\mathrm{T}}$ and the AoA, $\mathbf{H}^{(k)}_{\phi,\mathrm{T}} \in \mathbb{R}^{2M\times 9}$can then be expressed as

$$\mathbf{H}^{(k)}_{\tau,\mathrm{T}} = \begin{bmatrix} \dfrac{\Delta\hat{x}_1^{(k)}}{c\hat{d}_1^{(k)}} & \dfrac{\Delta\hat{y}_1^{(k)}}{c\hat{d}_1^{(k)}} & \dfrac{\Delta\hat{z}_1^{(k)}}{c\hat{d}_1^{(k)}} & \mathbf{0}_{1\times 6} \\ \vdots & \vdots & \vdots & \vdots \\ \dfrac{\Delta\hat{x}_M^{(k)}}{c\hat{d}_M^{(k)}} & \dfrac{\Delta\hat{y}_M^{(k)}}{c\hat{d}_M^{(k)}} & \dfrac{\Delta\hat{z}_M^{(k)}}{c\hat{d}_M^{(k)}} & \mathbf{0}_{1\times 6} \end{bmatrix}, \tag{3.25}$$

$$\mathbf{H}^{(k)}_{\phi,\mathrm{T}} = \begin{bmatrix} -\dfrac{\Delta\hat{x}_1^{(k)}\Delta\hat{z}_1^{(k)}}{\left(\hat{d}_1^{(k)}\right)^2 \hat{d}_{\mathrm{2D},1}^{(k)}} & -\dfrac{\Delta\hat{y}_1^{(k)}\Delta\hat{z}_1^{(k)}}{\left(\hat{d}_1^{(k)}\right)^2 \hat{d}_{\mathrm{2D},1}^{(k)}} & \dfrac{\hat{d}_{\mathrm{2D},1}^{(k)}}{\left(\hat{d}_1^{(k)}\right)^2} & \mathbf{0}_{1\times 6} \\ \vdots & \vdots & \vdots & \vdots \\ -\dfrac{\Delta\hat{x}_M^{(k)}\Delta\hat{z}_M^{(k)}}{\left(\hat{d}_M^{(k)}\right)^2 \hat{d}_{\mathrm{2D},M}^{(k)}} & -\dfrac{\Delta\hat{y}_M^{(k)}\Delta\hat{z}_M^{(k)}}{\left(\hat{d}_M^{(k)}\right)^2 \hat{d}_{\mathrm{2D,M}}^{(k)}} & \dfrac{\hat{d}_{\mathrm{2D},M}^{(k)}}{\left(\hat{d}_M^{(k)}\right)^2} & \mathbf{0}_{1\times 6} \\ -\dfrac{\Delta\hat{y}_1^{(k)}}{\hat{d}_{\mathrm{2D},1}^{(k)}} & \dfrac{\Delta\hat{x}_1^{(k)}}{\hat{d}_{\mathrm{2D},1}^{(k)}} & 0 & \mathbf{0}_{1\times 6} \\ \vdots & \vdots & \vdots & \vdots \\ -\dfrac{\Delta\hat{y}_M^{(k)}}{\hat{d}_{\mathrm{2D},M}^{(k)}} & \dfrac{\Delta\hat{x}_M^{(k)}}{\hat{d}_{\mathrm{2D},M}^{(k)}} & 0 & \mathbf{0}_{1\times 6} \end{bmatrix}, \tag{3.26}$$

where $\Delta\hat{x}_m^{(k)} = \hat{x}_{\mathrm{T},k} - \hat{x}_{\mathrm{A},m}$, $\Delta\hat{y}_m^{(k)} = \hat{y}_{\mathrm{T},k} - \hat{y}_{\mathrm{A},m}$, $\Delta\hat{z}_m^{(k)} = \hat{z}_{\mathrm{T},k} - \hat{z}_{\mathrm{A},m}$, $\hat{d}_m^{(k)} = ||\hat{\mathbf{P}}_{\mathrm{T},k} - \hat{\mathbf{P}}_{\mathrm{A},m}||$ and the 2D distance between the kth target and the mth anchor is denoted as $\hat{d}_{\mathrm{2D},m}^{(k)}$. In terms of the Jacobian matrix of anchors in (3.24), they can be conveniently constructed by taking the opposite sign of each entry in (3.25) and (3.26). Nevertheless, since the matrix dimension changes from $M \times 9$ to $M \times 3M$ (for ToA-based formulation) or $2M \times 3M$ (for AoA-based formulation), the non-zero entries

Algorithm 1: SLAT EKF

At time index $i=0$, initialize the state $\mathbf{s}$, covariance $\mathbf{\Sigma}$, process noise covariance $\mathbf{Q}$
for $i=1,\cdots,N_T$ **do**
  Generate the LRMs vector $\mathbf{y}[i]$ and compute the corresponding measurement noise covariance matrix $\mathbf{R}[i]$
  Calculate the Jacobian matrix according to, e.g., (3.24)
  Implement the EKF equations [105]
  Prediction:
    state $\hat{\mathbf{s}}^{-}[i]=\mathbf{F}\hat{\mathbf{s}}[i-1]$
    state covariance $\hat{\mathbf{\Sigma}}^{-}[i]=\mathbf{F}\hat{\mathbf{\Sigma}}[i-1]\mathbf{F}^{T}+\mathbf{Q}[i]$
  Kalman gain:
    $\mathbf{K}[i]=\hat{\mathbf{\Sigma}}^{-}[i]\mathbf{H}^{T}[i]\Big(\mathbf{H}[i]\hat{\mathbf{\Sigma}}^{-}[i]\mathbf{H}^{T}[i]+\mathbf{R}[i]\Big)^{-1}$
  Correction/update:
    $\hat{\mathbf{s}}[i]=\hat{\mathbf{s}}^{-}[i]+\mathbf{K}[i]\big(\mathbf{y}[i]-\mathbf{h}\big(\hat{\mathbf{s}}^{-}[i]\big)\big)$
    $\hat{\mathbf{\Sigma}}[i]=(\mathbf{I}-\mathbf{K}[i]\mathbf{H}[i])\hat{\mathbf{\Sigma}}^{-}[i]$
end

are to be shifted accordingly. An example of $\mathbf{H}^{(k)}_{\tau,\mathrm{A}}\in\mathbb{R}^{M\times 3M}$ is provided as

$$\mathbf{H}^{(k)}_{\tau,\mathrm{A}}=\begin{bmatrix}\mathbf{H}^{(k)}_{\tau,\mathrm{A},1} & \mathbf{0}_{1\times 3} & \cdots & \mathbf{0}_{1\times 3}\\ \mathbf{0}_{1\times 3} & \mathbf{H}^{(k)}_{\tau,\mathrm{A},2} & & \vdots\\ \vdots & & \ddots & \\ \mathbf{0}_{1\times 3} & \mathbf{0}_{1\times 3} & \cdots & \mathbf{H}^{(k)}_{\tau,\mathrm{A},M}\end{bmatrix}, \tag{3.27}$$

where $\mathbf{H}^{(k)}_{\tau,\mathrm{A},m}\in\mathbb{R}^{1\times 3}$ is

$$\mathbf{H}^{(k)}_{\tau,\mathrm{A},m}=\left[\frac{\Delta\hat{x}^{(k)}_{m}}{c\hat{d}^{(k)}_{m}},\frac{\Delta\hat{y}^{(k)}_{m}}{c\hat{d}^{(k)}_{m}},\frac{\Delta\hat{z}^{(k)}_{m}}{c\hat{d}^{(k)}_{m}}\right]. \tag{3.28}$$

Meanwhile, the Jacobian matrix of anchors when utilizing the AoA $\mathbf{H}^{(k)}_{\phi,\mathrm{A}}\in\mathbb{R}^{2M\times 3M}$ can be computed and obtained in the same way as (3.27). In the next section, another EKF-based but different positioning approach is formulated.

3.3.3 Sequential positioning II — normal EKF

Instead of joint positioning of both targets and anchors as the proposed SLAT EKF, another EKF-based solution is presented, namely the normal EKF, where only the location of targets are estimated, however, with the statistics of anchor location uncertainty being taken into account. One advantage of the normal EKF lies in the reduced computational complexity compared to the SLAT EKF due to a much shorter state vector. Specifically, the normal EKF is formulated as

$$\begin{aligned} \text{state transition model}: \mathbf{s}_{\mathrm{T},k}[i] &= \mathbf{F}_{\mathrm{T},k}\mathbf{s}_{\mathrm{T},k}[i-1] + \mathbf{u}_{\mathrm{T},k}[i] \\ \text{measurement model}: \mathbf{y}_k[i] &= \mathbf{h}\left(\mathbf{s}_{\mathrm{T},k}[i]\right) + \tilde{\mathbf{w}}_k[i], \end{aligned} \tag{3.29}$$

where the noise noise $\mathbf{u}_{\mathrm{T},k} \sim \mathcal{N}\left(\mathbf{0}_K, \mathbf{Q}_{\mathrm{T},k}\right)$. The state vector becomes

$$\mathbf{s}_{\mathrm{T},k} = \left[x_{\mathrm{T},k}, y_{\mathrm{T},k}, z_{\mathrm{T},k}, v_x^{\mathrm{T},k}, v_y^{\mathrm{T},k}, v_z^{\mathrm{T},k}, a_x^{\mathrm{T},k}, a_y^{\mathrm{T},k}, a_z^{\mathrm{T},k}\right]^T. \tag{3.30}$$

The major difference between normal EKF and SLAT EKF lies in the modelling of the measurement noise in (3.29) that is denoted as $\tilde{\mathbf{w}}_k \sim \mathcal{N}\left(\mathbf{0}, \mathbf{C}^{(k)}\right)$, the covariance matrix of which is denoted as

$$\mathbf{C}^{(k)} = \mathbf{R}^{(k)} + \tilde{\mathbf{R}}^{(k)}. \tag{3.31}$$

It is observed that the measurement covariance now consists of two components: $\mathbf{R}^{(k)}$ that represents the measurement noise coming from LRMs as in Algorithm 1, and $\tilde{\mathbf{R}}^{(k)}$ that refers to the extra noise coming from the anchors' location uncertainty. The specific way of calculating this extra noise component $\tilde{\mathbf{R}}^{(k)}$ differs slightly when considering different LRMs, which are expressed as

$$\tilde{\mathbf{R}}_\tau^{(k)} = \mathbf{H}_{\tau,\mathrm{A}}^{(k)} \Sigma_\mathrm{A} \left(\mathbf{H}_{\tau,\mathrm{A}}^{(k)}\right)^T, \;\; \tilde{\mathbf{R}}_\phi^{(k)} = \mathbf{H}_{\phi,\mathrm{A}}^{(k)} \Sigma_\mathrm{A} \left(\mathbf{H}_{\phi,\mathrm{A}}^{(k)}\right)^T, \tag{3.32}$$

where $\tilde{\mathbf{R}}_\tau^{(k)}$ and $\tilde{\mathbf{R}}_\phi^{(k)}$ are the considered extra noise when utilizing ToA and AoA, respectively. In addition, Σ_A was given in (3.22) and $\mathbf{H}_{\tau,\mathrm{A}}^{(k)}$, $\mathbf{H}_{\phi,\mathrm{A}}^{(k)}$ can be constructed as (3.27). In such way, the anchor location uncertainty is integrated and mapped into the measurement model and processed by the normal EKF procedure.

It is noteworthy that, although the target index k has been employed in the for-

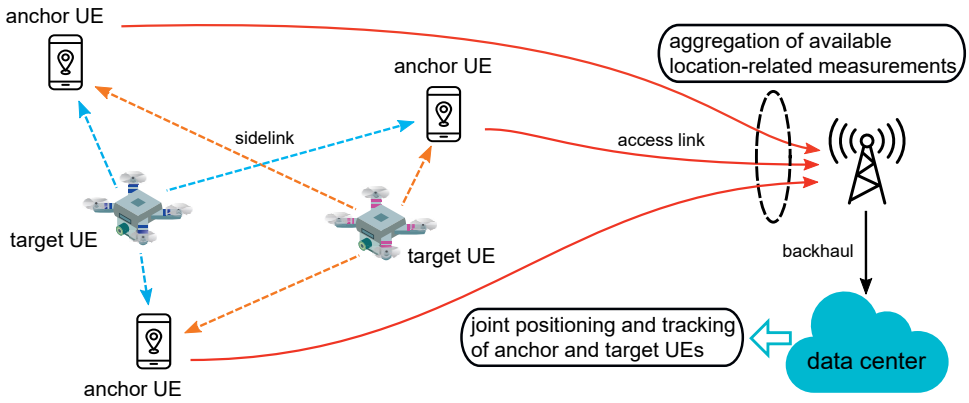

Figure 3.3 Joint positioning and tracking via mmWave D2D (sidelink) communications — a network-centric scheme.

mulation, the positioning for each target when applying the normal EKF is independent from each other since the obtained LRMs are statistically independent for each pair of target-anchor. This evidence is also applied to the WCG algorithm. However, due to the joint estimation of both targets and anchors in the SLAT EKF, the consideration of different number of targets possesses certain impact, which we will take a close look at in Section 3.5.

3.4 Considered industrial IoT scenario for positioning

In the previous section, one geometry-based and two EKF-based positioning algorithms have been proposed and formulated to cope with the difficulty/challenge of positioning in the industrial environment, i.e., the location uncertainty of the anchors. The proposed algorithms can be considered as the answers to research question 2 (see Section 1.2 and Table 1.1).

In this section, the considered industrial IoT scenario based on NR sidelink for positioning is presented as in Fig. 3.3, where various mobile vehicles and sensor devices coexist in an industrial environment, e.g., an outdoor harbor and an indoor warehouse. As such, an improved location awareness can be beneficial for the enhancement of the overall situational awareness [78], which in turn reinforce the operational efficiency and safety in the industrial system [21]. Since a D2D network is considered, all the involved vehicles and sensor devices are referred to as UE, which are categorized into two kinds, the *target UE* and the *anchor UE*. Specifically, the

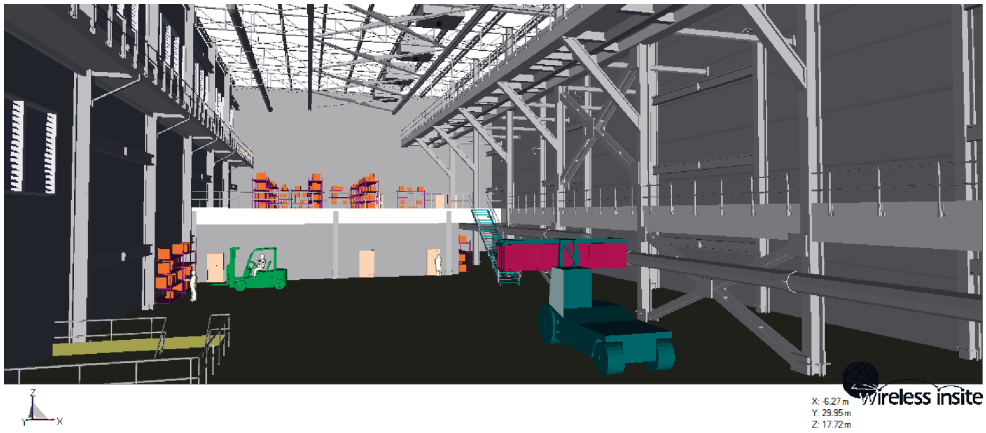

Figure 3.4 An indoor industrial warehouse environment for the industrial IoT systems. The ray-tracing feature is enabled in the environment [129].

target UE, such as the ground or aerial vehicles, in general possesses high mobility in order to perform certain tasks, such as environment monitoring and video surveillance. On the other hand, the anchor UE, e.g., the sensor devices or ground machinery normally maintains low mobility. They are deployed at certain locations serving as anchors. Thereafter, the LRMs estimation as well as the positioning are carried out as specified in Section 3.1. Last but not least, the ray-tracing enabled industrial environment, on which the channel emulation is carried out, is illustrated in Fig. 3.4 [129].

3.5 Performance evaluation and analysis

This section presents and compares the achievable positioning performance within a mmWave D2D network using the three proposed positioning algorithms.

3.5.1 Algorithm initialization

The initialization of the proposed SLAT EKF is to be done for two entities: the target UE and the anchor UE, as expressed in (3.20). In terms of the target UE locations, the proposed WCG approach is applied, however, with the available LoS APs or gNBs as the anchors. The rationale of doing so is to control the initial uncertainty of the overall positioning system, such that the uncertainty of initialized target UE is not

correlated with the location uncertainty of the anchor UE. Moreover, the locations of all the anchor UE are initialized based on a prior knowledge (that can be acquired from the available database, such as the fingerprinting records) as the following form

$$\mathbf{\Sigma}_{\mathrm{A},m} = \mathrm{diag}\left(\sigma_{\mathrm{AT}}^2, \sigma_{\mathrm{AT}}^2, \frac{\sigma_{\mathrm{AT}}^2}{\beta^2} \right), \tag{3.33}$$

where σ_{AT} refers to the location uncertainty in x- and y-direction and $\beta = 10$, $\forall m \in \mathcal{M}$. That said, there exists a roughly 7.1 m uncertainty in 3D when $\sigma_{\mathrm{AT}} = 5$ m, and such parameter σ_{AT} is varied in the simulation in order to obtain the corresponding positioning performance under different levels of anchor location uncertainty.

Furthermore, the process noise variance $\sigma_{q,k}^2$ (for the targets) is tuned according to the maximum acceleration $|a_{\max}|$ such that $\sigma_{q,k}^2 = (|a_{\max}|/(6\Delta t))^2$. Since all the anchor UE are assumed to be static, the $\sigma_{q,\mathrm{A}}^2$ is set to 0. The initialization for normal EKF is the same as the part for target UE in the SLAT EKF. There is no requirement on the initialization for the WCG approach, which can be seen as another advantage of the snapshot positioning method.

3.5.2 Positioning performance

The positioning performance of three proposed approaches are to be presented in this section. The radio channel is emulated in the ray-tracing environment shown in Fig. 3.4. The LoS region where the industrial vehicles and robots (i.e., target UE) move occupies a horizontal space of 70 m×25 m, with a 18 m height in the vertical direction. In addition, all target UE's trajectories have been generated using a random waypoint (RWP) model [50] that last for 200 seconds. Moreover, the signal parameters (the carrier and the bandwidth) outlined in Table 3.2 are selected mainly according to the NR sidelink specifications [4] for mmWave D2D communications. The antenna system is configured as 8×8 URA under the consideration of a reasonable physical size and acceptable angular resolutions.

3.5.2.1 Accuracy of the LRMs

Prior to the positioning performance of the proposed algorithms, the obtained accuracy of the LRMs is presented, including ToA, TDoA, azimuth and elevation AoA.

Table 3.2 Utilized parameters in the simulation

Parameter	Value
carrier frequency	26 GHz
sub-carrier spacing	60 kHz
signal bandwidth	10 MHz
transmit power	10 dBm
receive beamforming gain	20 dBi
EKF update time-interval	100 ms
anchor UE antenna	8×8 URA
target UE antenna	omni-directional
anchor UE height	1 - 11 m
avg. target UE velocity	1.1 m/s

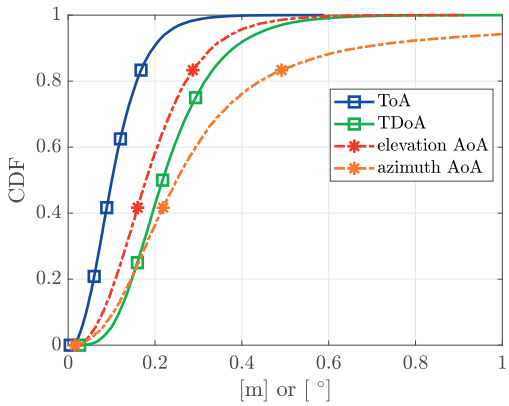

Figure 3.5 The accuracy of CRLB-based LRMs.

As discussed in Section 3.2, the accuracy of ToA, azimuth and elevation AoA is evaluated based on the derived CRLB as expressed in (3.8) and (3.14) while that of TDoA measurements can be calculated by summing the estimation uncertainty of two ToA statistics (4.6). Assuming a Gaussian error in each ToA estimate, the TDoA is inevitably less accurate than the ToA, as shown in Fig. 3.5.

In the same figure, the AoA measurement accuracy is plotted with the unit of degree (instead of radian). It can be observed that, the majority of the angle errors is less than 0.9 degree, while the azimuth AoA measurements remain in general more uncertain compared to the elevation AoA. This phenomenon has been indirectly explained in Section 3.2.2.2, where the AoA uncertainty depends on the signal level

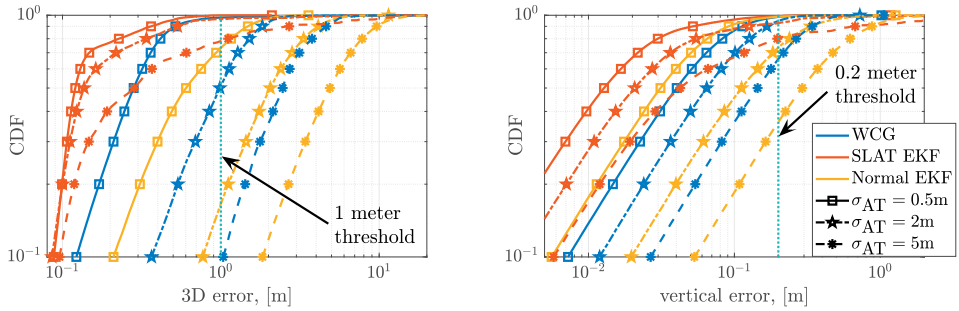

(a) The 3D performance

(b) The vertical performance

Figure 3.6 The positioning performance comparison among WCG, SLAT EKF and normal EKF.

(SNR), angular resolution (number of antenna elements), and the geometry (true AoA). Thus, for either azimuth or elevation AoA, the corresponding measurement uncertainty becomes rather large when the signal incidents from around $\pm 90°$ (due to the cosine term), in which case, the effective array aperture diminishes, reducing the angular resolution significantly. Furthermore, since the moving area of target UE is in general larger in the horizontal dimension than in the vertical dimension, the SNR level at the azimuth extreme ($\pm 90°$) is normally lower than that at the elevation extreme, therefore, the SNR is most likely not large enough to compensate the negative impact from the cosine term. Consequently, the azimuth AoA in general yields a worse accuracy than the elevation AoA, as given in Fig. 3.5.

3.5.2.2 WCG vs SLAT EKF vs normal EKF

The obtained positioning performance applying the three proposed algorithms is compared when overall one target UE and six anchor UE are considered in the environment. In particular, the horizontal locations of the anchor UE are randomly generated and uniformly distributed over the 3D space shown in Fig. 3.4. In order to avoid extreme cases when all the anchor UE are located rather close to each other, a 8 m horizontal interval among them is ensured in the simulation setup.

For a fair comparison, both ToA and AoA measurements are utilized in both EKF-based solutions. This is due to the fact that WCG applies both types of LRMs to obtain the location estimates. The positioning performance in 3D and vertical plane are obtained based on 500 trials (using random trajectories and locations) and characterized via cumulative density function (CDF) in Fig. 3.6, in which the 1 m

and 0.2 m accuracy threshold are explicitly highlighted using the cyan vertical lines for a better demonstration of the reliability of the location estimates. Such threshold values are employed according to [7, Table 7.3.2.2-1], where positioning performance requirements are envisioned for NR system. Furthermore, the presented performance refers to the target UE location estimation accuracy since both WCG and normal EKF do not estimate the anchor UE's locations.

As shown in Fig. 3.6, the performance of each approach become worse (shift towards right) as the location uncertainty σ_{AT} becomes larger. This phenomenon proves that a higher location uncertainty in general leads to a less accurate location estimation. In terms of the performance difference among different algorithms, it can be seen that at a given σ_{AT} (especially if larger than 0.5 m), the accuracy of SLAT EKF is higher than that of WCG which outperforms the normal EKF in both 3D and vertical plane. That being said, the integration of the location uncertainty of the anchor UE into the measurement covariance by the normal EKF cannot well compensate the resulting negative impact, whereas the SLAT EKF solution can, to a large extent, finish the joint positioning of both target UE and anchor UE with better performance than the normal EKF. In the case of $\sigma_{\mathrm{AT}} = 5$ m that corresponds to an approximate 7.1 m randomness in 3D obtained according to (3.33), the SLAT EKF is able to achieve a 80% 3D sub-meter accuracy as well as vertical sub-0.2 meter accuracy, whereas the WCG and the normal EKF stay at a 75% and 35% sub-0.2 meter accuracy, respectively, and both less than 10% 3D sub-meter accuracy.

Due to the observed disparity in the performance, in the following sections, focus and efforts will be given to the SLAT EKF. The corresponding performance is evaluated under random anchor deployments by utilizing different types of LRMs individually and collectively ('Individually' means the utilization of one type of LRMs e.g., only ToA, and 'collectively' means more than one type of LRMs are applied, e.g., ToA+AoA). Furthermore, the performance of different numbers of target UE and anchor UE is also assessed and presented.

3.5.2.3 Performance under different number of targets and anchors

Finally, the overall positioning performance under different numbers of target UE and anchor UE is characterized. Specifically, uniformly distributed anchor UE are generated within the environment together with the RWP-based trajectories for target UE. The positioning performance of both target UE and anchor UE utilizing

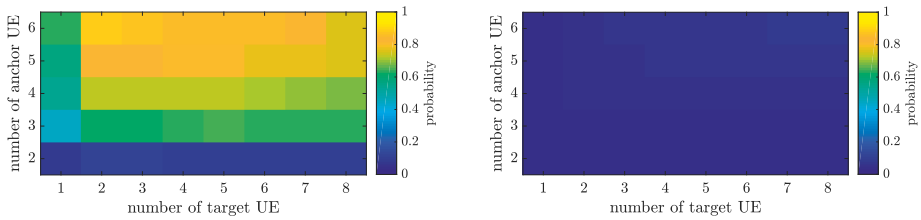

(a) Probability of 2D sub-meter accuracy

(b) Probability of vertical sub-0.2 meter accuracy

Figure 3.7 Positioning performance of *ToA* based SLAT EKF at $\sigma_{\text{AT}} = 4$ m under various number of target UE and anchor UE.

ToA-only, AoA-only and ToA+AoA is given in Fig. 3.7, Fig. 3.8 and Fig. 3.9, respectively, applying the same metrics and initialization approach with $\sigma_{\text{AT}} = 4$ m. Specifically, the vertical performance by ToA in Fig. 3.7b turns out to be constantly poor regardless of the overall number of K or M. However, in terms of the performance in 2D plane, interesting phenomenon is observed. Specifically, when $M = 2$, the varying of K remains indifferent to the final outcome due to the fact that any two anchor UE always form a collinear deployment, yielding bad geometry for ToA based positioning (verified also in Fig. 4 of publication IV). An obvious performance boost is seen at the top left corner where K changes from one to two. However, the continuing growth of K (i.e., $3, \cdots, 8$) does not bring significant performance gain any more for $M = 3, \cdots, 6$. Moreover, given any considered K, more anchor UE in generally returns a better performance.

The performance of AoA shown in Fig. 3.8. In particular, the system with more than one target UE demonstrates a major performance improvement over the one-target system, but the performance gain remains rather stable ever since the number of target UE increases over two. Additionally, more anchor UE brings incremental performance gain in both 2D and vertical plane for $K \geq 2$, and the overall best obtained performance in terms of 2D sub-meter accuracy and vertical sub-0.2 meter accuracy reaches around 50 % and 70%, respectively.

Moving towards Fig. 3.9 (the ToA+AoA based system[5]), it is seen that the performance of both 2D and vertical plane possesses rather similar trend. In particular, the performance remains at a lower level when $M = 2$ regardless of the value of K (be-

[5]The performance of TDoA+AoA based system and TDoA based system are omitted here due to the similar performance. However, the plotted performance and analysis can be found in Fig.5 of publication VI.

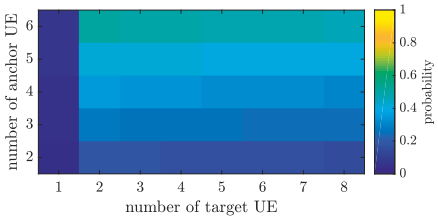

(a) Probability of 2D sub-meter accuracy

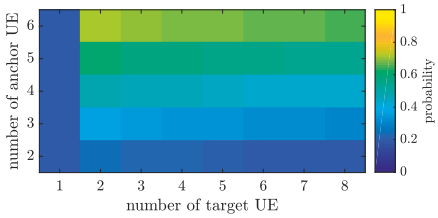

(b) Probability of vertical sub-0.2 meter accuracy

Figure 3.8 Positioning performance of *AoA* based SLAT EKF at $\sigma_{\text{AT}} = 4$ m under various number of target UE and anchor UE.

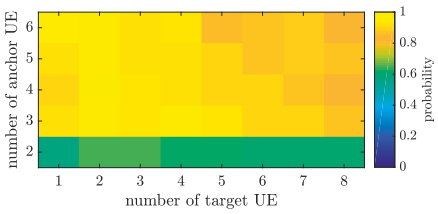

(a) Probability of 2D sub-meter accuracy

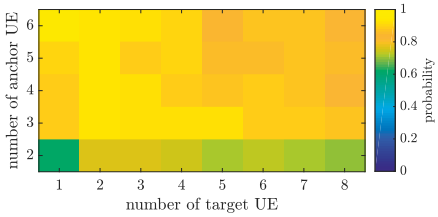

(b) Probability of vertical sub-0.2 meter accuracy

Figure 3.9 Positioning performance of *ToA+AoA* based SLAT EKF at $\sigma_{\text{AT}} = 4$ m under various number of target UE and anchor UE.

tween 60%-70% sub-meter and sub-0.2 meter accuracy) than the rest of the cases. As discussed and seen previously in Fig. 3.7, the presence of two anchor UE inevitably yields the collinear deployment, positioning therefore only relies on the AoA measurements, yielding worse performance compared to other rows. Nevertheless, the corresponding performance is still much better than the performance demonstrated in Fig. 3.7 (utilizing ToA only) and Fig. 3.8 (utilizing AoA only). When there are two anchor UEs in total ($M = 2$), adding more target UE improves the vertical performance more than the 2D performance (see the last row of Fig. 3.9a and Fig. 3.9b). In the cases of $M = 3, \cdots, 6$, the overall performance in both planes significantly improves to approximately 80%-95%. That is to say, the growth of K value (from 1 to more) does not bring much performance gain to ToA+AoA based system as it does to ToA or AoA based system. Therefore, the investigation on the number of target and anchor UE demonstrates that acquiring LRMs from both time-domain and angle-domain plays a vital role in enhancing the achievable positioning accuracy especially under challenging system geometry.

3.6 Summary

In this chapter, several positioning solutions of achieving the location awareness via mmWave D2D communications were presented. Although the air interface has been selected to be the NR sidelink, the positioning solutions can also be applied in other air interfaces and employed in other scenarios with a straightforward extension. In particular, a network-centric positioning engine was adopted, and three positioning approaches were formulated with a focus on addressing the potential challenges in the industrial environment, i.e., the location uncertainty of the anchors. With regard to the positioning performance, it is seen that the SLAT EKF certainly outperforms the other two methods in both horizontal and vertical planes, however, at the expense of a longer state vector that leads to a higher computational complexity. Nevertheless, such challenge on computational power can be alleviated by the utilization of edge computing at the cloud, i.e., the adopted network-centric framework.

In addition, the geometric impact on the achieved positioning accuracy was studied. The positioning outcome becomes significantly more robust when the LRMs from both time and angle domain are available than only one type of LRMs is accessible. In terms of the positioning accuracy with different number of overall UE, the simulation results showed that more anchor UE in the system can in general improve the overall performance because of more available LRMs. However, the growth of the number of target UE does not typically yield a performance improvement, even though two-target system vastly outperforms one-target system when utilizing LRMs individually.

With proper combination of efficient positioning and sensing solutions, it is reasonable to believe that an improved 3D situational awareness can be obtained and utilized in both physical and virtual world use cases, further expanding the proposed wireless solution beyond the considered scenarios.

4 EXPLOITING THE LOCATION AWARENESS — A NETWORK-CENTRIC POSITIONING-AIDED BEAMFORMING STRATEGY

In the previous chapter, several positioning solutions were developed and presented to achieve the location awareness in the context of industrial IoT. In this chapter, a positioning-aided communication framework is introduced and formulated for enhanced communication performance. The achievable benefits in both initial access latency and DL spectral efficiency further demonstrate the applicability of the proposed PA-BF (positioning + BF) to the industrial IoT use cases.

Before a systematic discussion on the proposed framework, let us first introduce the existed BF strategies, which has been so far discussed through the following three representative categories:

- an exhaustive searching strategy, exhaustive beamforming (EX-BF) [30, 53]
- a multi-level searching strategy, hierarchical/genetic BF strategy [43, 131]
- a location-based strategy, context-information (CI)-based BF [13, 31, 37, 40]

The detailed elaborations on each type of BF are omitted herein, interesting readers may refer to publication III for more information.

Aiming at enhancing the communication performance in the DL, a positioning-aided communication framework is proposed to facilitate the location awareness of the UE obtained via UL positioning. All in all, compared with proposed strategies in the literature, the proposed PA-BF operates on a low-complexity analog BF in which only one beam is generated at one time instant, while positioning is carried out in the UL by means of multi-connectivity in a mmWave SCNs.

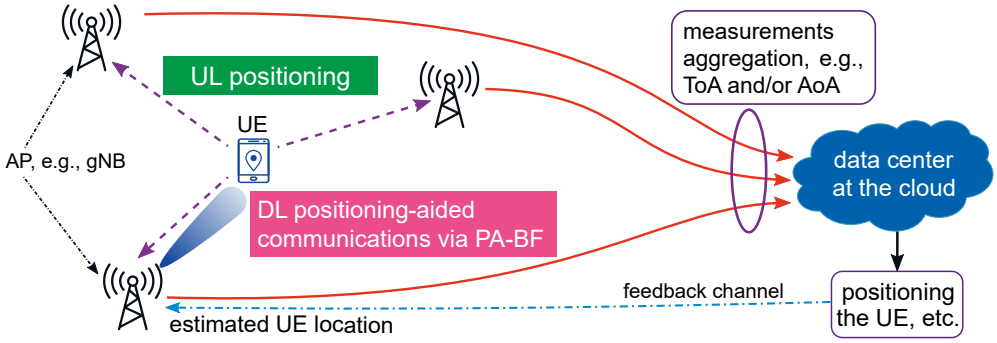

Figure 4.1 A cloud-oriented mmWave mobile network, facilitating the positioning-aided communications.

4.1 A cloud-oriented mmWave mobile network

This section begins with an overview of the considered cloud-oriented network. Thereafter, the UL positioning as well as the DL positioning-aided communications scheme are described and formulated.

4.1.1 System overview

Continuing with the network-centric feature employed for positioning in Chapter 3, a cloud-oriented mmWave network is envisioned and discussed involving both communication and positioning, as depicted in Fig. 4.1. In particular, a TDD-based system is considered with mmWave as the main RAT[1]. Specifically, every UE is assumed to be omni-directional, from which the pilot/reference signals are transmitted to the APs in a periodic manner. Further, orthogonal frequency division multiple access (OFDMA) is employed for multiple access among the UE, and the APs that are in the LoS condition with respect to the UE are denoted as the LoS-APs. At the network side, URA is assumed to be installed on each AP, from which *only one antenna element remains active (omni-directional) in the UL positioning phase, whereas all the antenna elements function in the DL transmission (directional).*

Such configuration is adapted to reduce the positioning overhead in the UL while exploiting directional communications in the DL that is determined by the UL positioning accuracy. Further details will be discussed in Section 4.1.3 and Section 4.2.2.1. Moreover, the LRMs are estimated by the LoS-APs, then sent to the edge/cloud

[1]The work integrates both mmWave and WiFi RATs can be found in publication IV.

server, where the UE locations are estimated based on the collected measurements. The edge/cloud server can be considered as a central unit or data center that is responsible for scheduling, handover predictions, and radio resource management of the overall network. With the estimated UE locations, the positioning-aided DL communications are then implemented, which, as will be demonstrated, yield a shorter initial access latency than a conventional beam alignment process.

It is also important to point out that, since it is a network-centric positioning scheme, the round-trip delay between the cloud and the APs may cause extra delays, namely, the cloud communication latency [134]. However, such latency is typically much smaller than the periodicity of pilot/reference signal transmission, therefore, can be ignored. Nevertheless, the system model and formulation do include the cloud communication latency, which will be presented in Section 4.2.2.1.

4.1.2 UL positioning engine

In the considered multi-connectivity scenario, the UE maintains radio connections with more than one LoS-AP. In particular, the set of LoS-APs indices is denoted as $\mathscr{M}$, where the known location of each AP is denoted as $\mathbf{P}_{\mathrm{AP},m} = [x_m, y_m, z_m]^T$, $\forall m \in \mathscr{M}$. The location of any arbitrary UE is denoted as $\mathbf{p} = [x, y, z]^T$. Since one antenna element remains active at the AP in the UL, the received signal $r_m(t)$ at the mth LoS-AP is

$$r_m(t) = \sqrt{g_r P_{\mathrm{T,UL}}} h_m s(t - \tau_m) + (s * \nu)(t) + n(t), \tag{4.1}$$

where $P_{\mathrm{T,UL}}$ and g_r refer to the linear scale transmit power of the UE and the received antenna gain at the AP, respectively. Moreover, h_m denotes as the corresponding path-loss coefficient with respect to the mth LoS-AP. Additionally, $s(t - \tau_m)$ is the time-domain signals with a duration of T_s and bandwidth B_{w}, and the additive Gaussian noise is denoted as $n(t)$ with a power spectrum density of N_0. The propagation delay is written as $\tau_m = ||\mathbf{p} - \mathbf{P}_{\mathrm{AP},m}||/c$. Moreover, the potential un-correlated scattering in the environment is modeled as the convolution of signal $s(t)$ and *diffuse reflection* components $\nu(t)$ [67]

$$(s * \nu)(t) = \int s(u)\nu(t - u)\,\mathrm{d}u, \tag{4.2}$$

in which $\nu(t)$ represents a zero-mean stochastic process, and the power ratio of h and $\nu(t)$ is decided by the Rician-K in [5, Table 7.5-6]. Since the direct path contains almost the entire energy in the mmWave frequency band [86], the impact to $r_m(t)$ due to either *specular reflection* or diffuse reflection can be disregarded.

4.1.2.1 Utilized LRMs

After the acquisition of UL pilot signals, the LRMs are extracted for positioning. In this chapter, the UL positioning is carried out in a synchronized network considering the TDoA measurements $\Delta\hat{\tau} \in \mathbb{R}^{M-1}$

$$\Delta\hat{\tau} = f_{\Delta\tau}(\mathbf{p}) + \boldsymbol{n}_{\Delta\tau}, \tag{4.3}$$

where $\boldsymbol{f}_{\Delta\tau}(\mathbf{p})$ and $\boldsymbol{n}_{\Delta\tau} \in \mathbb{R}^{M-1}$ represent the TDoA observation function and the measurement noise vector, respectively. In particular, there are in total M LoS-APs. The observation function $\boldsymbol{f}_{\Delta\tau}(\mathbf{p})$ is given as

$$f_{\Delta\tau}(\mathbf{p}) = \left[\frac{d_2 - d_1}{c}, \cdots, \frac{d_M - d_1}{c}\right]^T, \tag{4.4}$$

where the reference LoS-AP is selected to be the one with index 1, and d_m is denoted as the Euclidean distance between the UE and the mth AP

$$d_m = ||\mathbf{p} - \mathbf{P}_{\mathrm{AP},m}|| = \sqrt{\Delta x_m^2 + \Delta y_m^2 + \Delta z_m^2}, \tag{4.5}$$

where $\Delta x_m = x - x_m, \Delta y_m = y - y_m$ and $\Delta z_m = z - z_m$.

Furthermore, under a LoS propagation, the noise vector $\boldsymbol{n}_{\Delta\tau}$ fits a zero-mean Gaussian distribution, that is, $\boldsymbol{n}_{\Delta\tau} \sim \mathcal{N}\left(\mathbf{0}_{M-1}, \mathbf{R}_{\Delta\tau}\right)$, in which the covariance matrix is described as [101, Ch.4]

$$\mathbf{R}_{\Delta\tau} = \begin{bmatrix} \sigma_{\tau,1}^2 + \sigma_{\tau,2}^2 & \sigma_{\tau,1}^2 & \cdots & \sigma_{\tau,1}^2 \\ \sigma_{\tau,1}^2 & \sigma_{\tau,1}^2 + \sigma_{\tau,3}^2 & \cdots & \sigma_{\tau,1}^2 \\ \vdots & \vdots & \ddots & \vdots \\ \sigma_{\tau,1}^2 & \sigma_{\tau,1}^2 & \cdots & \sigma_{\tau,1}^2 + \sigma_{\tau,M}^2 \end{bmatrix}. \tag{4.6}$$

It is worth pointing out that, the covariance (4.6) is assembled based upon the

statistics of ToA measurements since each TDoA measurement is calculated via two ToA measurements one of which refers to the same reference AP. The theoretical characterization (via CRLB) of any individual $\sigma^2_{\tau,m}$ was defined in (3.8).

4.1.2.2 Positioning error bound

PEB can be thought of as the CRLB with respect to the UE location $\mathbf{p} = [x, y, z]^T$. The derivation begins with the Fisher information matrix (FIM) that is the Jacobian matrix based on the utilized data/statistics [58, Ch.3]. In essence, PEB is an unbiased estimator and the FIM with respect to the UE location $\mathbf{p}$ can be computed as [138, Ch.2]

$$\boldsymbol{I}_{\Delta\tau} = \left[\frac{\partial f_{\Delta\tau}(\mathbf{p})}{\partial \mathbf{p}}\right]^T \mathbf{R}^{-1}_{\Delta\tau} \left[\frac{\partial f_{\Delta\tau}(\mathbf{p})}{\partial \mathbf{p}}\right], \tag{4.7}$$

where the derivative w.r.t. $f_{\Delta\tau}(\mathbf{p})$ is calculated in line with (4.4)

$$\frac{\partial f_{\Delta\tau}(\mathbf{p})}{\partial \mathbf{p}} = \begin{bmatrix} \frac{\Delta x_2}{d_2} - \frac{\Delta x_1}{d_1} & \frac{\Delta y_2}{d_2} - \frac{\Delta y_1}{d_1} & \frac{\Delta z_2}{d_2} - \frac{\Delta z_1}{d_1} \\ \vdots & \vdots & \vdots \\ \frac{\Delta x_M}{d_M} - \frac{\Delta x_1}{d_1} & \frac{\Delta y_M}{d_M} - \frac{\Delta y_1}{d_1} & \frac{\Delta z_M}{d_M} - \frac{\Delta z_1}{d_1} \end{bmatrix}. \tag{4.8}$$

Thereafter, the 3D PEB can be computed as

$$\text{PEB} = \text{CRLB}(\mathbf{p}) = \sqrt{\text{trace}\left(\boldsymbol{I}^{-1}_{\Delta\tau}\right)}, \tag{4.9}$$

where 'trace' refers to the sum of the diagonal entries of a matrix. More importantly, the derived PEB (4.9) serves as the prior information on the UE location to implement the proposed PA-BF, which will be described in the next section.

4.1.3 DL positioning-aided communications

After positioning, the estimated UE locations are transmitted back to one or several APs to initialize the positioning-aided communications as demonstrated in Fig. 4.1. In particular, the location awareness of the UE not only facilitates several location-based use cases [2] but also enormously reduces the initial access latency. It is important to note that all the antenna elements of the URA (at the APs) are active in the

DL, therefore, the communication is a multiple-input single-output (MISO) model

$$r(t) = \sqrt{P_{\mathrm{T,DL}}}\boldsymbol{h}_{\mathrm{DL}}^{H}\boldsymbol{f}^{*}s(t-\tau_{\mathrm{DL}}) + (s * \nu_{\mathrm{DL}})(t) + n(t), \tag{4.10}$$

where $\boldsymbol{h}_{\mathrm{DL}}$ can be expressed as the product of channel coefficient h_{DL} and the array response $\boldsymbol{b}_{\mathrm{URA}}$, that is, $\boldsymbol{h}_{\mathrm{DL}} = h_{\mathrm{DL}}\boldsymbol{b}_{\mathrm{URA}}(\phi_{\mathrm{AoD}})$ in which $\phi_{\mathrm{AoD}} \triangleq (\varphi_{\mathrm{AoD}}, \theta_{\mathrm{AoD}})$ is the true angle of departure (AoD) pair and $\boldsymbol{b}_{\mathrm{URA}}$ is the array response described the same way as (3.3) and (3.4).

In addition, the DL transmit power, LoS delay, time-domain transmit signal, additive Gaussian noise and the receive signal are denoted as $P_{\mathrm{T,DL}}$, τ_{DL}, $s(t), n(t)$ and $r(t)$, individually. It is noteworthy that the power of DL diffuse reflection components ν_{DL} is much less than that of UL because of a more directional transmission in the DL than in the UL. Moreover, the selected AP for DL communication is denoted as the primary AP that located at $\mathbf{P}_0 = [x_0, y_0, z_0]^T$. In the considered system, the precoder $\boldsymbol{f}^{*}$ (i.e., the beam-steering vector) is formed based on the predicted angle pair with respect to the primary AP, $\hat{\phi}_{\mathrm{AoD}} \triangleq (\hat{\varphi}_{\mathrm{AoD}}, \hat{\theta}_{\mathrm{AoD}})$, that is obtained according to the estimated UE location, $\hat{\mathbf{p}} = [\hat{x}, \hat{y}, \hat{z}]^T$ as

$$\begin{aligned} \hat{\varphi}_{\mathrm{AoD}} &= \arcsin\left(\frac{\hat{z}-z_0}{||\hat{\mathbf{p}}-\mathbf{P}_0||}\right), \\ \hat{\theta}_{\mathrm{AoD}} &= \operatorname{atan}_2(\hat{y}-y_0, \hat{x}-x_0). \end{aligned} \tag{4.11}$$

Basically, the estimated location of UE is described as $\hat{\mathbf{p}} = \mathbf{p} + \boldsymbol{e}$, in which the covariance of the error vector $\boldsymbol{e}$ is reflected by the FIM (4.7) as

$$\mathbb{E}\left[\boldsymbol{e}\boldsymbol{e}^{T}\right] = \boldsymbol{I}_{\Delta\tau}^{-1}. \tag{4.12}$$

It is to be emphasized that the product of $\boldsymbol{h}_{\mathrm{DL}}^{H}\boldsymbol{f}$ decides the achievable BF gain of the PA-BF, and it attains the maximal value whenever the predicted angle pair $\hat{\phi}_{\mathrm{AoD}}$ are well aligned with the true angle pair ϕ_{AoD}.

4.2 Benchmark strategy and performance metric

In this section, the selected benchmark strategy as well as the considered performance metrics are introduced.

4.2.1 The benchmark strategy

A standardized codebook-based BF [11, 41] is chosen as the benchmark strategy, that is, the EX-BF with a 3D discrete Fourier transform (DFT) [31]. It is noteworthy that codebook other than DFT-based one [43, 131] can also be considered, however, those codebooks normally involve multi-level beam refinement (i.e., a sequential change of the beamwidth) that requires a digital or hybrid BF structure with high power consumption.

4.2.2 Performance metric — Spectral efficiency

Unlike the general spectral efficiency defined and utilized in information theory [118] where reliable communication is guaranteed at the price of infinite latency, the initial access latency caused by beam training has to be included and considered in the final calculation of the spectral efficiency. For a clear illustration, Fig. 4.2 demonstrates the principle of the initial access procedure in a typical scheme and in the proposed positioning-aided communication scheme. In general, the overall frame duration consists of both the initial access latency (for beam training) and the data transmission latency, therefore, a natural trade-off between the throughput and the positioning accuracy [31] needs to be considered for the conventional scheme in Fig. 4.2a, where the positioning performance is determined by the beam resolutions and applied BF strategies during the initial access.

Normally, a narrow beam resolution does return a good AoA estimation (which then transfers into high positioning accuracy), however, at the expense of long beam training latency, resulting in short data transmission time, thus low throughput. Aiming at reducing the latency of beam training for initial access, the positioning-aided communication scheme is proposed and depicted in Fig. 4.2b, where the (quasi) omni-directional transmission (with wide beams) is adopted during the initial access. With such configuration, the UE location can be estimated based on the delay (time)-domain measurements rather than the angle-domain measurements, resulting in a reduced latency for initial access (beam training) as well as an increased duration for data transmission. The performance of such scheme depends on several parameters, at which we will take a look next.

Specifically, the overall frame duration for DL communication is denoted as T_f,

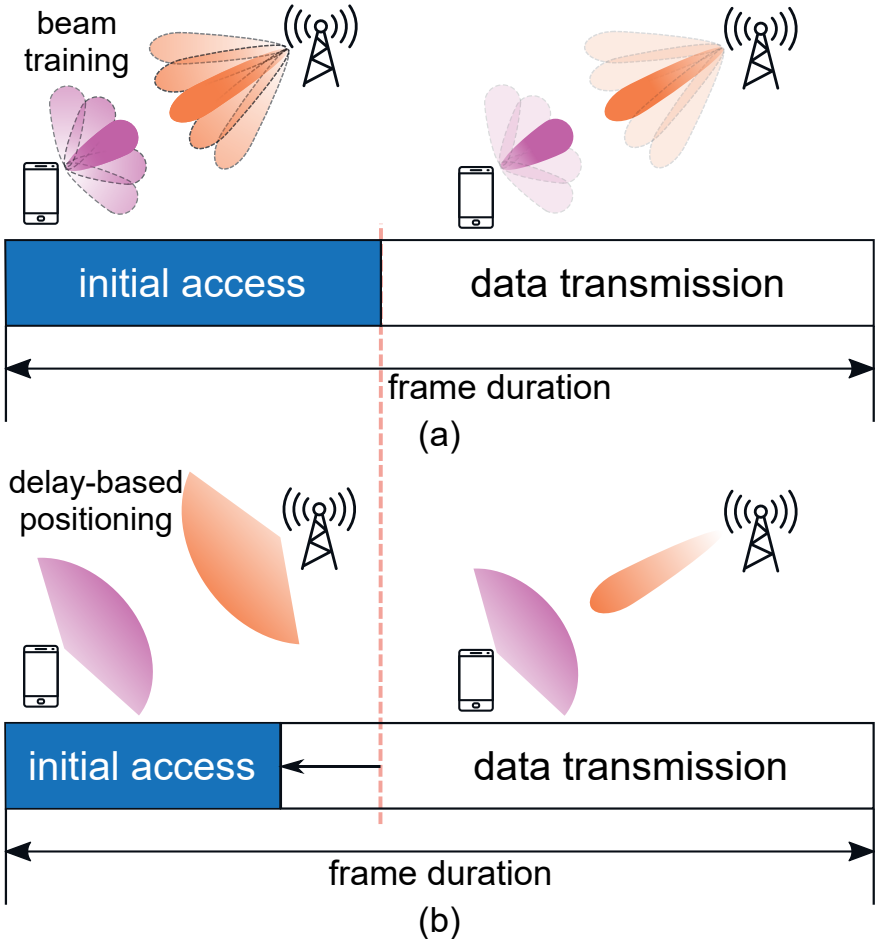

Figure 4.2 Demonstration of two different schemes for initial access and data transmission. (a) A standardized procedure [11] when both Tx & Rx equip directional antennas. (b) The proposed positioning-aided communication scheme.

from which the effective transmit ratio η is defined as

$$\eta = 1 - \frac{T_{\mathrm{IA}}}{T_f}, \tag{4.13}$$

where T_{IA} refers to the initial access latency, a certain amount of time for beam sweeping, beam measurement and beam reporting, the length of which not only decides the positioning accuracy, but also alters the communication performance in terms of the achievable spectral efficiency. For a given channel realization h_{DL}, the

spectral efficiency is expressed as

$$R = \eta \log_2 \left(1 + \frac{P_{\mathrm{T,DL}} |h_{\mathrm{DL}}|^2}{P_n} G_{\mathrm{BF}}(\boldsymbol{f}^*, \phi_{\mathrm{AoD}}) \right), \tag{4.14}$$

where $P_n = N_0 B_{\mathrm{w}}$, defined in (3.8) refer to the noise power over the considered bandwidth. In particular, $\frac{P_{\mathrm{T,DL}} |h_{\mathrm{DL}}|^2}{P_n}$ is denoted as the SNR without BF gain. As expressed in (4.10), $\boldsymbol{f}^* \in \mathbb{C}^{N_R \times 1}$ refers to the chosen codeword (beam-steering vector) in accordance with the applied BF strategy, and N_R refers to the number of antenna elements defined in Section 3.2.1. Last but not least, the resulting BF gain is denoted as G_{BF}, which is a function of $\boldsymbol{f}^*$ and the true AoD pair $\phi_{\mathrm{AoD}} \triangleq (\varphi_{\mathrm{AoD}}, \theta_{\mathrm{AoD}})$.

4.2.2.1 The proposed PA-BF

According to (4.10) and (4.14), PA-BF, the spectral efficiency of PA-BF in the DL can be described as

$$R_{\mathrm{PA}} = \eta_{\mathrm{PA}} \log_2 \left(1 + \frac{P_{\mathrm{T,DL}} |h_{\mathrm{DL}}|^2}{P_n} G_{\mathrm{BF}}(\boldsymbol{f}_{\mathrm{PA}}, \phi_{\mathrm{AoD}}) \right), \tag{4.15}$$

where η_{PA} is the effective transmit ratio (to be defined in (4.17)) and $\boldsymbol{f}_{\mathrm{PA}} \in \mathbb{C}^{N_R \times 1}$ refers to the beam-steering vector designed based upon the acquired location awareness of the UE, that is defined as

$$\boldsymbol{f}_{\mathrm{PA}} = \boldsymbol{a}_{\mathrm{ULA}}(\hat{\varphi}_{\mathrm{AoD}}) \otimes \boldsymbol{a}_{\mathrm{ULA}}(\hat{\theta}_{\mathrm{AoD}} | \hat{\varphi}_{\mathrm{AoD}}), \tag{4.16}$$

where the estimated angle pair $(\hat{\varphi}_{\mathrm{AoD}}, \hat{\theta}_{\mathrm{AoD}})$ was given in (4.11). Moreover, an essential benefit of the proposed PA-BF comes to the temporal effectiveness of obtaining the codeword without the necessity of looking up throughout the whole codebook, thus maintaining a short initial access latency.

Considering that one codeword occupies one OFDM symbol, the effective transmit ratio η_{PA} is

$$\eta_{\mathrm{PA}} = 1 - \frac{T_{\mathrm{IA}}}{T_f} = 1 - \frac{T_s + T_e}{T_f}, \tag{4.17}$$

where $T_{\mathrm{IA}} = T_s + T_e$ in which T_s refers to the positioning overhead, which, according to the proposed scheme, takes one OFDM symbol. Furthermore, the round trip

delay from the APs to the cloud and back to the primary AP is denoted as T_e, i.e., the cloud communication latency [134]. It is noteworthy that T_e is normally negligible given the fact that the data center are generally located in the proximity of the APs which are connected via fiber optics. Additionally, the BF gain is expressed as

$$G_{\mathrm{BF}}(\boldsymbol{f}_{\mathrm{PA}}, \phi_{\mathrm{AoD}}) \triangleq |\boldsymbol{f}_{\mathrm{PA}}^{H}(\hat{\phi}_{\mathrm{AoD}})\boldsymbol{b}_{\mathrm{URA}}(\phi_{\mathrm{AoD}})|^2, \tag{4.18}$$

the numerical measure of which is determined by the precision and the accuracy of the predicted angle pair $\hat{\phi}_{\mathrm{AoD}}$ that depends on the positioning accuracy since (4.18) is maximized whenever $\hat{\phi}_{\mathrm{AoD}} \approx \phi_{\mathrm{AoD}}$. Additionally, the maximal value of (4.18) is scaled according to the $\beta_0(N_R, \phi)$ in (3.3).

4.2.2.2 The benchmark EX-BF

For comparison, a 3D EX-BF is selected as the benchmark strategy. Specifically, by exhaustively searching through the whole codebook, EX-BF applies the beam with the highest BF gain for transmission. Specifically, the applied codebook for EX-BF is organized as a DFT-form matrix, in which each column represents one codeword and is orthogonal to the others. The whole codebook is denoted as $\mathscr{F} \in \mathbb{C}^{N_R \times N_{\mathrm{cw}}}$ that consists of an overall N_{cw} beam-steering vectors $\boldsymbol{f} \in \mathbb{C}^{N_R \times 1}$. Therefore, the spectral efficiency of the EX-BF is expressed as

$$R_{\mathrm{EX}} = \eta_{\mathrm{EX}} \log_2\left(1 + \frac{P_{\mathrm{T,DL}}|h_{\mathrm{DL}}|^2}{P_n} G_{\mathrm{BF}}(\boldsymbol{f}_{\mathrm{EX}}, \phi_{\mathrm{AoD}})\right), \tag{4.19}$$

where the selected beam-steering vector $\boldsymbol{f}_{\mathrm{EX}}$ is the codeword that maximizes the following criterion

$$\boldsymbol{f}_{\mathrm{EX}} = \arg\max_{\boldsymbol{f} \in \mathscr{F}} G_{\mathrm{BF}}(\boldsymbol{f}, \phi_{\mathrm{AoD}}), \tag{4.20}$$

in which the BF gain $G_{\mathrm{BF}}(\boldsymbol{f}, \phi_{\mathrm{AoD}}) \triangleq |\boldsymbol{f}^H \boldsymbol{b}_{\mathrm{URA}}(\phi_{\mathrm{AoD}})|^2$. In terms of the effective transmit ratio of EX-BF

$$\eta_{\mathrm{EX}} = 1 - \frac{T_{\mathrm{IA}}}{T_f} = 1 - \frac{N_{\mathrm{cw}} T_s}{T_f}, \tag{4.21}$$

where the initial access latency consumes overall $N_{\mathrm{cw}} T_s$ seconds for beam training according to (4.20). It is important to note that (4.17) and (4.21) are obtained based

on the same criterion that each codeword utilizes one OFDM symbol.

Judging from $\beta_0(N_R, \phi)$ that is defined in (3.3), one may infer that, on one hand, more antenna elements N_R supports a narrower angular resolution which brings higher BF gain in (4.19). On the other hand, a larger N_R also indicates a larger number of codewords, which leads to a lower effective transmit ratio, thus a less spectral efficiency. Comparing between (4.17) and (4.21), the advantage of PA-BF lies in a larger effective transmit ratio because of the pre-determined AoD obtained through UL positioning. Nevertheless, the performance of PA-BF depends hugely on the positioning accuracy since it significantly affects the achieved BF gain G_{BF} in (4.18). In the mean time, the benefit of EX-BF is the ensured BF gain given a well-designed codebook that provides complete spatial coverage, whereas its shortcoming lies in a longer initial access latency due to the exhaustive search. The performance of EX-BF and PA-BF with different positioning accuracy will be presented and analyzed next.

4.3 Scenarios and simulations

In this section, the considered 3D scenario and network deployment are described. Thereafter, the simulation-based results and discussion are provided.

4.3.1 Scenario deployment

The top view illustration of an indoor/outdoor environment (120 m×90 m) is depicted in Fig. 4.3. In particular, the spatial-correlated RSS from the primary AP is presented to demonstrate the propagation condition. Furthermore, the z-coordinate of all the APs are equally set at 4 m, whereas that of total UE are fixed at 1 m. Specifically, the URA orientations are marked as the red dotted lines separately at each AP location. All the three plotted LoS-APs are involved in the positioning process, forming the multi-connectivity. However, only the red circular marker located at [0, 20] participates in the communication, and it is referred to as the *primary AP*. Essentially, the primary AP can be thought as a macro AP in the coverage layer whereas the secondary APs represent the (remote) radio units that assist positioning.

In the simulation, there are in total ten random AP deployments being generated. As to each deployment, there exists a certain amount of APs, ranging from three to six. It is important to note that, such randomly generated deployment may result in

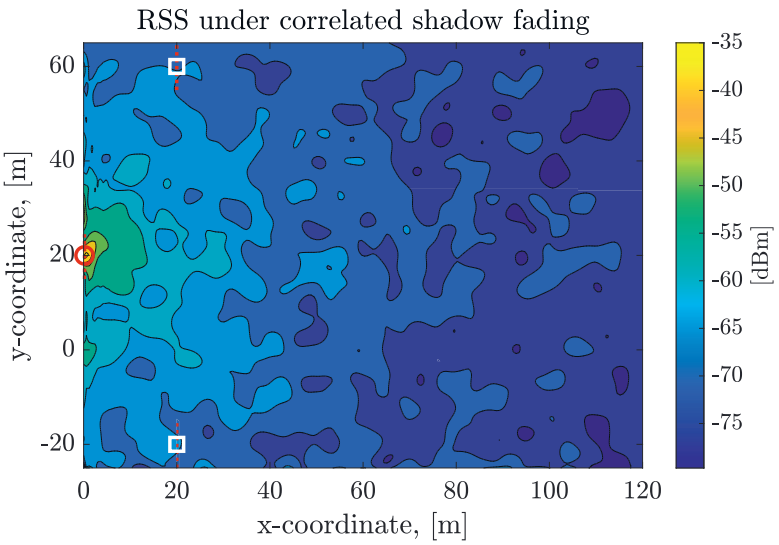

Figure 4.3 The top view illustration of a spatial correlated RSS distribution with respect to the AP in red circle.

an ill-conditioned geometric relationship, as the lesson learnt and demonstrated in Chapter 3. Therefore, all the generated AP deployments are checked before being applied in the simulation, such that the maximal PEB among the whole map is controlled under 2 m for fair comparison. Last but not least, the LoS propagation with respect to at least three APs is assumed throughout the considered area.

4.3.2 Simulation evaluations and analysis

First of all, the overall frame duration T_f is selected with respect to the relative velocity V between the AP and the UE. Basically, the duration of T_f is directly related to the coherence time of the wireless channel, denoted as T_c, the time over which the channel state remains as constant [107], which is expressed as a function of the Doppler shift f_d as [118]

$$T_c = \frac{1}{4f_d}, \tag{4.22}$$

where $f_d = \frac{V_d}{\lambda_c} = \frac{V\cos(\Omega)}{\lambda_c}$, in which $\cos(\Omega)$ represents the directional cosine, and Ω refers to the LoS incidence angle for calculating the projection of the 3D velocity onto the plane formed by the AP and the UE. Therefore, the 3D velocity V is larger

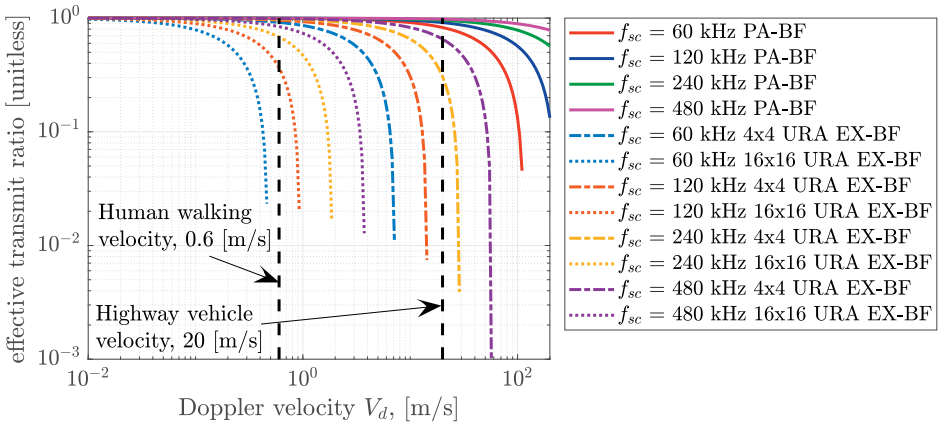

Figure 4.4 The effective transmit ratio $1 - T_{\text{IA}}/T_f$ as a function of Doppler velocity V_d.

than and equal to the Doppler velocity V_d, i.e., $V \geq V_d$.

The considered system operates at 39 GHz with a 100 MHz bandwidth[2]. Moreover, the frame duration T_f is assumed to be as long as the channel coherence time T_c, i.e., $T_f = T_c$. Furthermore, the effective transmit ratio is computed for the considered two BF strategies under N_R =16 (4×4 URA) / 256 (16×16 URA) with different sub-carrier spacing f_{sc}. In essence, the f_{sc} is the beam sweeping rate given the assumption that each training beam (codeword) occupies one OFDM symbol. Based on (4.17) and (4.21), the effective transmit ratio for both EX-BF and PA-BF is calculated and plotted in Fig. 4.4 as a function of V_d. It can be observed that, under the same f_{sc} of EX-BF, a smaller N_R allows for a higher η_{EX} since a smaller N_R in general yields a smaller size of the codebook (less beam training time). Given a certain N_R, a wider f_{sc} leads to a higher η_{EX} for the fact that each codeword uses up shorter duration for a higher f_{sc}, thus yielding longer time for data transmission.

On the other hand, the effective transmit ratio for PA-BF as shown in Fig. 4.4 is independent of antenna configuration since the corresponding codebook involves only one codeword that is constructed based on the estimated UE location. Analogous to the EX-BF, a larger f_{sc} also fulfills a higher η_{PA}. For better discussion, a new metric, *Doppler tolerance* is introduced, which corresponds to the maximum Doppler velocity when the effective transmit ratio is larger than 0. In Fig. 4.4, the Doppler tolerance is reflected by the horizontal axis where the curves halts. This

[2]The same carrier was employed in, e.g., [95] with 200 MHz bandwidth for positioning in a 5G network.

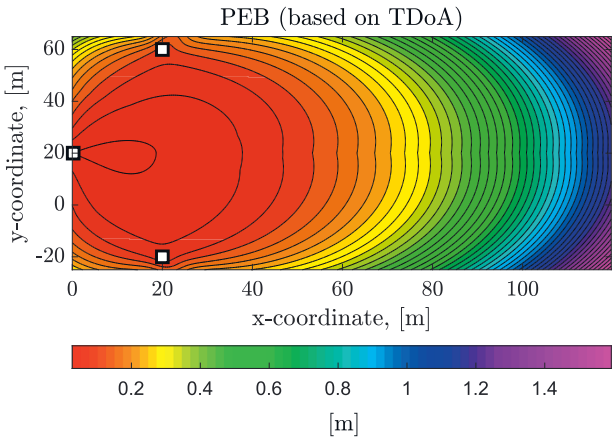

Figure 4.5 The PEB in 3D obtained on the UE height using the TDoA measurements under the same AP deployment of Fig. 4.3.

metric suggests the largest V_d the corresponding BF strategy can sustain without utilizing the whole frame duration for beam sweeping/training only. It is shown that a smaller N_R or a wider f_{sc} (or both) satisfy a higher Doppler tolerance, which in turn, can be utilized for initial access in high speed applications [70] where objects are moving with high speed.

Additionally, the PEB in 3D utilizing the TDoA measurements is plotted in Fig. 4.5 showing the pattern of positioning accuracy as a function of different locations. Inspecting from (4.7) and (4.9), the 3D PEB is principally determined by the measurement covariance $\boldsymbol{R}_{\Delta_\tau}$ that was defined in (3.8). In principle, it is affected by two factors, the signal bandwidth and the received SNR. Thus, given a fixed bandwidth, a farther UE-APs distance leads to a higher PEB. Furthermore, Fig. 4.5 merely manifests the theoretical PEB (4.9) under the specific APs deployment therein. That being said, the PEB varies according to the number and deployment of APs.

Based on the achieved location awareness of the UE, PA-BF is implemented in the DL for enhanced communications. As the reference benchmark, EX-BF is also carried out under the same condition using the simulation numerology that is summarized in Table 4.1. The carrier frequency, sub-carrier spacing as well as the signal bandwidth are selected according to the NR specification [5] with a focus on FR 2 communications. Furthermore, as discussed in Section 4.2.2.1, the BF performance counts on two metrics, the effective transmit ratio η and the BF gain G_{BF}. In partic-

Table 4.1 Simulation parameters

Parameter	Value
carrier frequency f_c	39 GHz
sub-carrier spacing f_{sc}	240 kHz
signal bandwidth B_{w}	100 MHz
UL transmit power $P_{\text{T,UL}}$	10 dBm
DL transmit power $P_{\text{T,DL}}$	27 dBm
max. array gain $\beta_0(4,\phi)$	14 dBi
max. array gain $\beta_0(16,\phi)$	25 dBi
pathloss model	indoor shopping mall [5]

Table 4.2 Considered 3D positioning accuracies based on the positioning accuracy requirement in [2]

3D error [m]	**Error in x** σ_x, [m]	**Error in y** σ_y, [m]	**Error in z** σ_z, [m]
3	2.09	2.09	0.51
10	7	7	1.41
50	35	35	7.07

ular, the G_{BF} of EX-BF is guaranteed to reach the maximum at the cost of long beam training latency, whereas that of PA-BF varies depending on the available location awareness of the UE. Therefore, in order to evaluate the performance variations of PA-BF under good or poor location awareness, different positioning accuracies are considered and summarized in Table 4.2, in which the location uncertainty in each direction (x-, y-, z-) applies a zero mean Gaussian distribution[3].

Considering two feasible UE velocities (0.6m/s and 2m/s) in the indoor environment, the CDF of the spectral efficiency applying EX-BF and PA-BF throughout the whole map are presented in Fig. 4.6 and Fig. 4.7. Specifically, Fig. 4.6 showcases the spectral efficiency distribution of all the locations on the map at 0.6m/s. From Fig. 4.6a where a 4×4 URA is applied, it is observed that the overall performance are quite similar except for the 50m-aided PA-BF. In Fig. 4.6b with a 16×16 URA, the performance gain does become noticeable, smaller positioning error does return better spectral efficiency.

Further, the comparison between Fig. 4.6a and Fig. 4.6b demonstrates that the

[3]The values tabulated in Table 4.2 are selected according to the positioning accuracy requirements defined in [2].

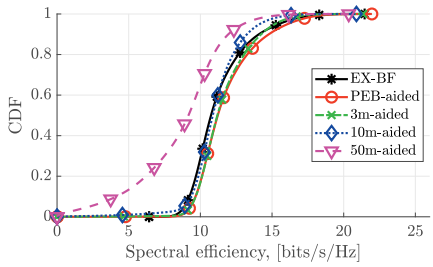

(a) 4×4 URA

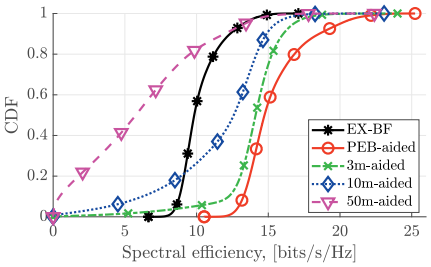

(b) 16×16 URA

Figure 4.6 The spectral efficiency by PA-BF (aided by different positioning accuracy) and EX-BF at **0.6 m/s** Doppler velocity over the considered area.

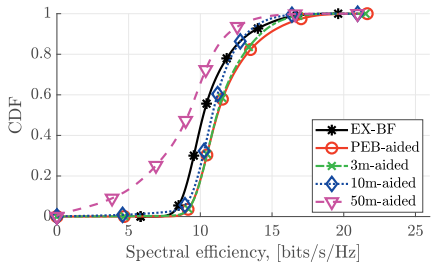

(a) 4×4 URA

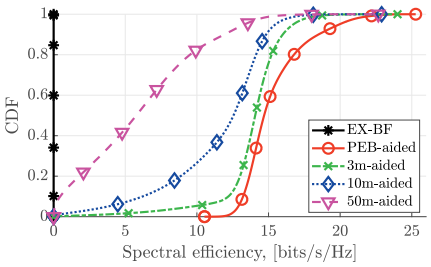

(b) 16×16 URA

Figure 4.7 The spectral efficiency by PA-BF (aided by different positioning accuracy) and EX-BF at **2.0 m/s** Doppler velocity over the considered area.

performance of PEB-aided, 3m-aided PA-BF actually become better with narrow antenna since the corresponding curves move towards the right, whereas the 10m-aided, 50m-aided PA-BF and EX-BF shift to the left reflecting a degraded performance (smaller spectral efficiency) when employing narrow antenna. This result indicates that the PA-BF aided by more reliable location estimation harnesses the higher array gain arising from a larger N_R, such that the narrower beam can be precisely steered towards the right direction, whereas the disparity in terms of positioning accuracy possesses less effects on the communication performance with a wider array beam (smaller N_R). In the meantime, with an increasing N_R, a degradation in performance of EX-BF is observed because narrower array beam leads to a longer beam training time, resulting in a lower effective transmit ratio as well as a smaller spectral efficiency.

Fig. 4.7 demonstrates the CDF of spectral efficiency at a higher velocity, i.e., $V_d = 2$ m/s. Comparing the results obtained at a lower mobility in Fig. 4.6a, the performance in Fig. 4.7a remains roughly similar except that the EX-BF experienced a slight degradation (since the black curve shifts towards left). Moving towards Fig. 4.7b in which the beamwidth becomes narrower and the array gain becomes higher, a similar performance of PA-BFs compared to Fig. 4.6b is achieved since better positioning accuracy in general results in better spectral efficiency. In contrast, the performance of EX-BF in Fig. 4.7b stuck approximately at 0 bits/s/Hz. This is because the Doppler tolerance for 16×16 URA at $f_{\text{sc}} = 240$ kHz is about 1.9 m/s as given in Fig. 4.4, thereafter, the effective transmit ratio of EX-BF become negative (for any V_d larger than 1.9 m/s), which indicates that the beam training for initial access costs the whole period of a frame duration T_f and no time is available for the data transmission.

4.4 Summary

In this chapter, a positioning-aided communication framework (positioning + BF) is presented and evaluated in a cloud-oriented mmWave network, in which the location awareness achieved via UL positioning was utilized to perform the PA-BF in the DL. Albeit possessing a low initial access latency, the simulation evaluation demonstrated that, the overall performance of PA-BF highly depends on the available location awareness (positioning accuracy) as well as the relative geometry between the Tx & Rx. A narrow beam with high array gain is indeed compelling. However, such configuration also comes along with high probability of beam misalignment, resulting in poor communication performance. Therefore, choosing the suitable system configuration according to the available knowledge and the specific environment is of paramount importance to apply the proposed framework in the industrial IoT use cases. In the next chapter, the feasibility of a location-aware handover scheme is studied, further exploring and analyzing the benefits of the location-aware communications scheme in the context of industrial IoT.

5 EXPLOITING THE LOCATION AWARENESS — A DEVICE-CENTRIC LOCATION-AWARE HANDOVER SCHEME

In the preceding chapter, a positioning-aided communication scheme was demonstrated, in which a PA-BF strategy is enabled with reduced initial access latency and augmented DL throughput conditional on the achieved positioning accuracy (i.e., the location awareness). While the data transmission in cellular network is in general DL-dominant, there are use cases where heavy data traffic is created by the industrial robots or vehicles, which requires high UL throughput [113]. In this chapter, a device-centric LHO scheme is presented.

Indeed, the concept of LHO has been recently investigated in [33, 36, 48, 108, 114, 136, 137], our work remains different mainly from two respects,

- instead of assuming perfect known UE locations/trajectories, positioning solutions are integrated to achieve location awareness. The handover performance under different positioning accuracy is evaluated;
- Besides the numerical simulation, a multi-RAT robotic platform is built up and employed also in the experiments to examine the feasibility of the LHO.

This chapter provides a summary of publication IV with a focus on the simulation-based performance. For the experiment setup and results, please refer to Section 3 and Section 5.2 of publication IV.

5.1 System overview

In order to illustrate our technical context, the principle of the proposed LHO scheme is depicted in Fig. 5.1, where a mmWave-enabled multi-RAT robot is moving inside an industrial environment while performing tasks, like video surveillance and/or

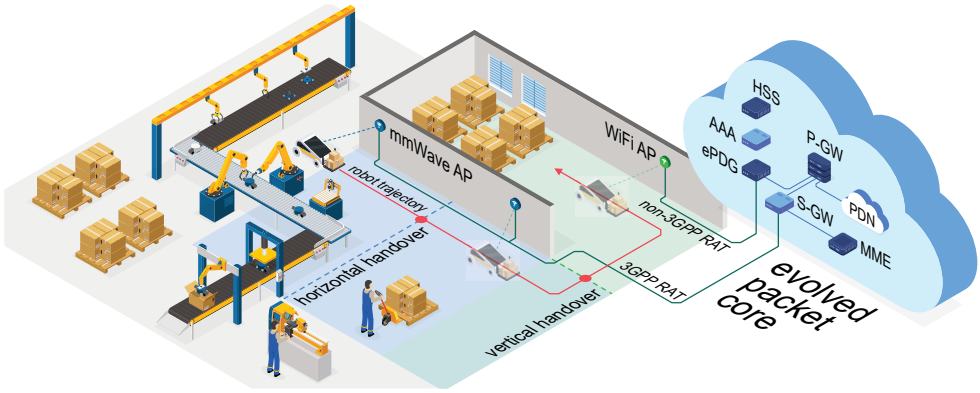

Figure 5.1 A conceptual illustration of the location-aware handover (LHO) scheme in an industrial multi-radio environment.

cargo transportation. Therefore, it is expected that the robot generates a large-volume data for video transmission, thus forming a UL-dominant data transportation. In order to guarantee the quality of the UL connectivity, our key target is to strengthen the link robustness while enhancing the throughput over the entire robot trajectory, in such a way that the robot maintains a connection with the mmWave AP in its LoS coverage, and switches to the cmWave AP whenever moving outside of the LoS coverage by exploiting the available location awareness, i.e., LHO.

5.2 Scenario deployment

The scenario utilized for assessing the LHO is demonstrated in Fig. 5.2 where the office corridor is applied to simulate an industrial multi-radio environment. Overall, one mmWave AP, i.e., wireless Gigabit alliance (WiGig) and one cmWave AP, i.e., WiFi are considered in the environment. The LoS coverage of the mmWave AP is created using Blender, as will be discussed in Section 5.3.1 and depicted in Fig. 5.2a. A WiFi AP that is configured and positioned inside the office, remains in the NLoS state w.r.t. the initial location of the robot.

In this study, the considered environment remains mostly static, which to some extent fosters the feasibility of the proposed handover scheme. However, it should be noted that when the dynamic environment is being dealt with, such as an automated factory, the LoS map of the environment has to be updated accordingly, e.g., through ray-tracing, which would inevitably increases the overall complexity. Overall, the

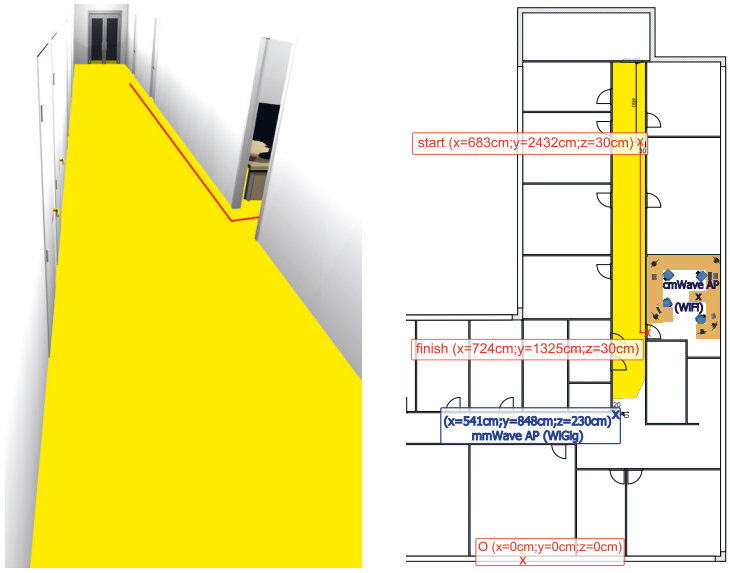

Figure 5.2 Test scenario 3D model and layout. (a) The 3D view of the corridor from the WiGig perspective. The red line represents an exemplified robot trajectory; (b) The top view of floor plan with the coordinates used in simulation. The yellow shadow refers to the LoS coverage of WiGig.

main objective is to guarantee an augmented throughput by maximizing the radio connection with the mmWave AP, while enhancing the link robustness by switching to cmWave-RAT in the non-ideal condition for the industrial IoT use cases.

5.3 Enabling the handover with location awareness

5.3.1 From environmental awareness to mmWave LoS coverage

This section describes a method to convert the 3D map, i.e., the environmental awareness into the LoS coverage for the prediction of the LoS state w.r.t. the mmWave AP at any specific locations within the considered environment. In particular, there are three primary steps:

1. *Building the 3D model and identifying the 2D plane.*
2. *Calculating the mmWave LoS coverage.*

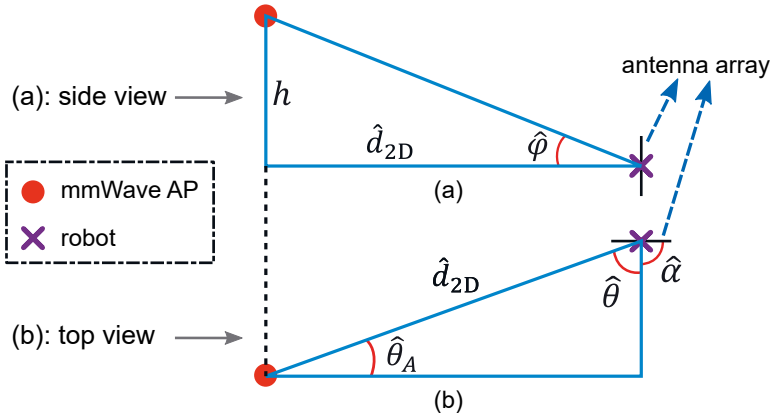

Figure 5.3 The geometric relationships between the robot and mmWave AP from side view and top view.

3. *Affine transform from 3D to 2D.*

More specifically, the considered physical environment is constructed via 3D modeling to provide visual descriptions from the perspective of the mmWave AP. Thereafter, the 2D plane where the robot moves is identified, it is seen as the floor plan. The LoS coverage is then produced based on the identified 2D plane in the previous step, forming a 'warped' map which is shown in Fig. 5.2a. Finally, a geometric transformation from 3D to 2D (called affine transformation) is implemented to acquire the top view of the environment and the LoS coverage.

In the simulation campaign, the red line plotted in both the subplots of Fig. 5.2 is utilized as the ground truth of robot trajectory for the evaluations of the achievable positioning and handover performance. Moreover, the LoS map is integrated in the robot, then applied to determine the LoS relationship between the robot and the mmWave AP for the evaluation of the LHO scheme, which will be discussed in Section 5.3.3.

5.3.2 Proposed positioning solution

As demonstrated in Fig. 5.3, a geometry-based positioning (GBP) solution is designed and constructed based on the geometric relationship between the mmWave AP and the robot. In particular, the purple cross marker denotes the robot, while the red dot represents the mmWave AP. Furthermore, the URA installed on the robot is highlighted by the black solid line on top of the purple markers. It is also notewor-

Algorithm 2: Geometry-based positioning (GBP)

Input: $\hat{\varphi}$, $\hat{\theta}$, $\hat{\alpha}$, x_A, y_A
Output: $\hat{x}$, $\hat{y}$

1 Compute the 2D distance between mmWave AP and the robot based on elevation AoA measurement $\hat{\varphi}$ and the known antenna height difference h

$$\hat{d}_{2\mathrm{D}} = h/\tan(\hat{\varphi})$$

2 Convert the azimuth AoA measurement $\hat{\theta}$ at the robot to the AoD $\hat{\theta}_A$ at the mmWave AP taking into account the array orientation measurement $\hat{\alpha}$ of the robot

$$\hat{\theta}_A = \pi - |\hat{\theta} - \hat{\alpha}|.$$

3 Calculate the robot location based on $\hat{d}_{2\mathrm{D}}$ and $\hat{\theta}_A$

$$\begin{bmatrix} \hat{x} \\ \hat{y} \end{bmatrix} = \begin{bmatrix} x_A + \hat{d}_{2\mathrm{D}} \cos\hat{\theta}_A \\ y_A + \hat{d}_{2\mathrm{D}} \sin\hat{\theta}_A \end{bmatrix}$$

thy that since a device-centric scheme is considered in this chapter, i.e., positioning and handover are implemented at the robot side, the orientation of the antenna array on the mmWave AP is negligible. Further, the noiseless elevation AoA, azimuth AoA, and the true orientation of the antenna array (in the azimuth plane) of the robot after the transformation from the robot coordinates to the local coordinates [56] are denoted as φ, θ, and α, respectively. It is noteworthy that only the azimuth array orientation has to be considered since the elevation array orientation remains unvaried as the robot moves forward. The robot orientation is the same as the antenna orientation. Additionally, the notation $\hat{}$ denotes the noisy measurement of the corresponding noiseless quantity. The time index in Algorithm 2 is not necessary since the proposed algorithm is a snap-shot based solution, and the location estimates of the adjacent time instants is independent.

5.3.3 Proposed handover scheme

The procedures of the proposed handover scheme, LHO is presented in Fig. 5.4. In a nutshell, the decision of LHO is made based on the knowledge of the location

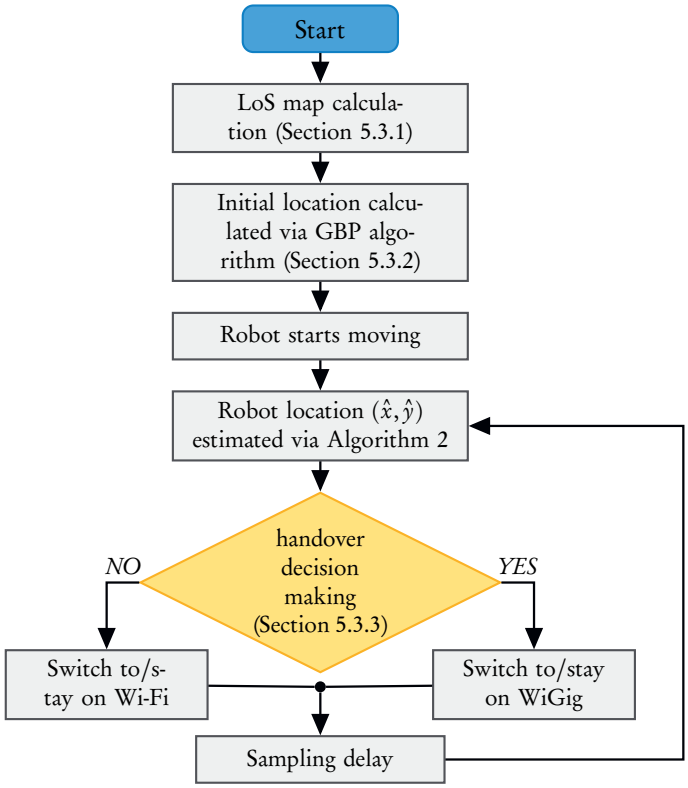

Figure 5.4 Procedures of the proposed LHO scheme.

awareness (i.e., the estimated robot locations) in association with the knowledge of the LoS coverage of the mmWave AP (i.e., the environmental awareness). Therefore, in order to smoothly execute the LHO, a accurately updated/calculated LoS coverage is periodically needed together with a mechanism for switching the packet flow from one RAT to another. Specifically, the LHO is initiated whenever the estimated robot lies inside the handover buffer region that is defined with respect to the LoS–NLoS boundary, such that the handover is preempted and completed in a proactive manner. As a result, the handover decision is in general made and executed a little before the actual LoS–NLoS boundary to avoid connection loss. It is also important to note that the performance of such handover scheme depends on multiple factors including the robot velocity, the available RAT, the positioning accuracy as well as the update frequency especially at the presence of dynamic obstacles. The handover efficiency can in fact be improved by taking into account multiple factors, such as the predefined robot trajectory, the radio environment map and the sensor data.

5.4 Handover performance and analysis

Since a device-centric handover scheme is discussed, both the RSS and the elevation and azimuth AoA at the robot side are plotted in Fig. 5.5. Specifically, the pre-defined robot trajectory is divided into three segments, each is represented by different colors: In light green region – the robot remains static initializing system. In light red region – the robot moves toward the office entrance, where it makes a turn (shown as the black dashed line), then drives into the office (toward the NLoS region with respect to the mmWave AP, i.e., the light blue region). The robot passes the LoS–NLoS border on its way into the office, where the RSS value significantly drops.

The obtained positioning accuracy via GBP is shown in Fig. 5.6a. In particular, the 2D root mean square errors along the considered robot track (the red curve in Fig. 5.2) within the LoS region is characterized to reflect the location awareness. The parameters applied in the simulation are given in Table. 5.1. The RF values therein are chosen based on the WiGig specifications. In this simulation campaign, the CRLB-based LRMs [101, Ch. 3] are applied. That being said, the elevation and azimuth AoA measurements based on the SNR are generated according to (3.14), which are then utilized as the input LRMs $(\hat{\varphi}, \hat{\theta})$ of Algorithm 2 to obtain the location estimates.

Additionally, the uncertainty of orientation $\hat{\alpha}$ is modeled by an un-biased Gaussian error with a standard deviation σ_α that is set to two levels, $\sigma_\alpha = 0.1°$ or $5°$ [143]. Consequently, Fig. 5.6a demonstrates that, the obtained positioning error is small for a low σ_α. More importantly, the positioning accuracy becomes higher when the robot approaches the mmWave AP owing to the fact that for a given AoA error, the robot suffers a smaller positioning error when the relative distance is smaller.

In terms of the handover performance, the cumulative density function of the handover location in time is plotted in Fig. 5.6b. It is observable that when the location awareness is not trustworthy (i.e., AoA error suffers from $\sigma_\alpha = 5°$), the handover is in general performed much earlier than that when the location awareness is reliable ($\sigma_\alpha = 0.1°$). Such early switch to another RAT has negatively impact on the achievable throughput, service latency and jitter, which consequently degrade the QoS and/or the quality of experiences (QoE) of the robot. Therefore, achieving reliable location awareness remains as the key to maintain a satisfactory LHO performance.

Table 5.1 Parameter table for simulation

Parameter	Value
carrier frequency	60.5 GHz
signal bandwidth	2.16 GHz
transmit power @ AP*	21.64 dBm
max. array gain @ AP*	13.48 dBi
max. array gain @ robot	13.48 dBi
robot update interval	0.5 sec
pathloss model	InH-office [5]
fast fading model	Rician distribution

* The "AP"s mentioned in the table refer to the WiGig rather than WiFi since the simulation is carried out to model the communication between the mmWave AP and the robot.

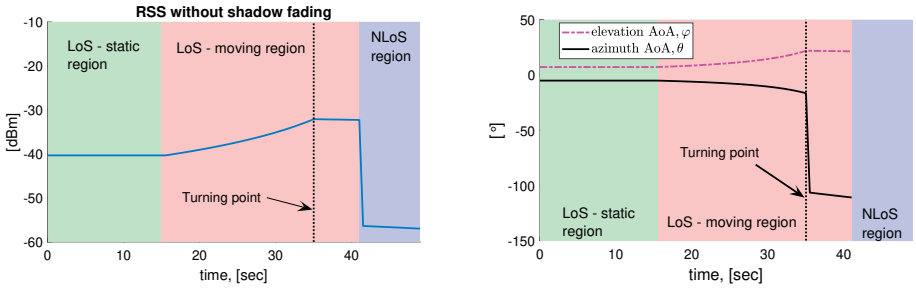

(a) The RSS without shadow fading applying an indoor office pathloss model [5].

(b) Noiseless elevation AoA, φ, and azimuth AoA, θ with respect to mmWave AP.

Figure 5.5 Simulation-based numerical characterization as a function of time along the simulated robot trajectory (see Figure 5.2b)).

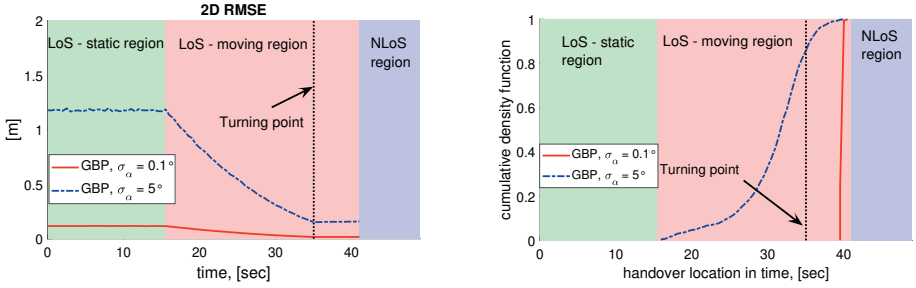

(a) 2D RMSE as a function of time via simulation.

(b) Handover locations via simulation.

Figure 5.6 Positioning and handover performance via simulations.

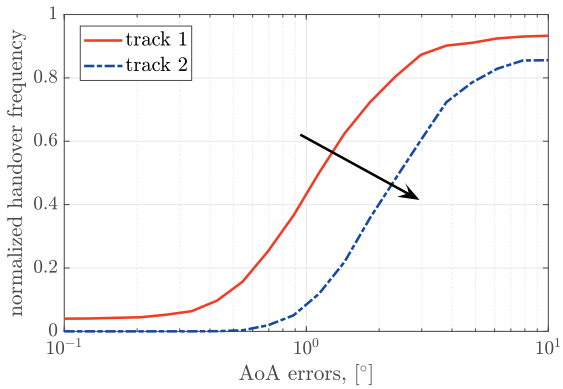

Figure 5.7 The handover frequency as a function of AoA accuracy for two considered tracks.

Last but not least, the handover frequency of LHO is presented as a function of the AoA measurement accuracy at two different tracks. Besides the track in red that shown in Fig. 5.2, another track is considered, which is parallel to the track in red but 0.25 m towards the center of the corridor. For the sake of clear definitions, these two considered tracks are specifically described as:

- track 1: the red track shown in Fig. 5.2, located 40 cm away from the corridor wall;
- track 2: another track that is 65 cm away from the corridor wall, i.e., 25 cm away from track 1 towards the center of corridor.

That being said, track 2 is set slightly further from the sensitive edge, i.e., the LoS-NLoS border than track 1. Consequently, the handover frequency of both tracks increases as the degradation of AoA accuracy as shown in Fig. 5.7, indicating that an unsatisfactory location awareness (positioning accuracy) leads to a poor LHO performance. In particular, under a given AoA accuracy, the handover frequency of track 1 is in general higher than that of track 2. The reason lies in the fact that track 1 is closer to the sensitive edge than track 2, therefore, for a given location awareness, the tracks that are further away from the sensitive edge is able to achieve a more stable performance than the tracks near the sensitive edge. Hence, the performance of LHO depends on not only the achievable location awareness but also the geometric relationship in the considered environment, the situational awareness.

5.5 Summary

In this chapter, the performance of the LHO is analyzed by employing the obtained location awareness together with the available environmental awareness. In particular, the simulation based handover performance is presented. Integrating also the experiment-based outcome, we believe that the considered handover schemes can be exploited for a more efficient handover scheme design enabling a mmWave-ready HetNets with automated guided vehicles [24]. With accurate location estimates, timely environmental knowledge as well as the radio statistics, a hybrid handover scheme can be developed to guarantee the link robustness and to provide sufficient data throughput in any dynamic environments.

6 CONCLUSIONS AND FUTURE PERSPECTIVES

6.1 Conclusions

In this thesis, a set of mathematical models and simulation tools have been formulated and developed to provide accurate 3D positioning solutions and location-aware communication frameworks in the context of 5G-empowered industrial IoT.
From positioning perspective, the following conclusions and contributions were presented:

1. Characterization of different LRMs. As the inputs to the positioning algorithms, the theoretical achievable accuracy of several LRMs, such as ToA, TDoA and AoA were evaluated based on realistic mmWave channel simulated using ray-tracing engine. Such theoretical characterization fundamentally describes the utilized radio resources in closed forms, facilitating improved configurations and design of radio positioning system.
2. Development and evaluation of 3D positioning algorithms. Targeting the industrial IoT scenarios, snapshot and sequential positioning solutions were developed to cope with the location uncertainty of the anchors. Joint positioning and tracking (also named as SLAT-EKF) does in general provide performance with higher accuracy and reliability at the expense of a higher computational complexity than the other considered approaches, such as WCG. Furthermore, approximately 80% 3D sub-meter accuracy can be achieved by SLAT-EKF for all the involved agents when the initial anchor location uncertainty is around 7m (in 3D). Together with other proposed positioning approaches, Chapter 3 provided several practical choices for positioning with anchor location uncertainty being taken into account.

In terms of location-aware communication aspects, the following conclusions and contributions were presented:

1. A positioning-aided communication scheme with reduced initial access latency as well as improved throughput in a cloud-oriented network was proposed. Via a network-centric positioning scheme, the achieved location awareness was exploited to perform an efficient BF, namely, the PA-BF with lower latency than the standardized strategy. The performance in terms of throughput can be significantly improved especially under high mobility scenario on condition that the positioning accuracy is higher than a threshold that is dependent on the AP-UE geometry. Such communication scheme (i.e., positioning+BF) could provide feasible means and useful insights into the design of a joint positioning and communication framework.
2. The feasibility of a LHO scheme in the HetNets was evaluated. Integrating both sub-6 GHz and mmWave radio interface, a user-centric LHO scheme in a multi-radio environment was designed and tested for augmented throughput and reinforced link robustness. Applying a "proof-of-concept" evaluation, an enhanced location awareness has been proved to effectively improve the throughout compared to the RSS-based benchmark strategy, while maintaining the link robustness[1]. The conducted study, therefore, sheds light on the possibility and feasibility for the further development of autonomous vehicles, with wireless technology as an unique and indispensable enabler.

Meanwhile, the potential answers and proposed solutions to all three research questions identified in Chapter 1 were specifically provided throughout Chapter 2 and Chapter 5:

- In terms of research question 1, illustrations and analysis on the challenges and opportunities for communications and positioning from different fundamental perspectives, such as mmWave, SCNs, MIMO and BF were given in Chapter 2, further discussing and highlighting the benefits of the synergy of the considered ingredients (e.g., see the left plot of Fig. 6.1).
- Chapter 3 offered specific solutions to research question 2, where the challenges for positioning in the industrial environment (e.g., anchor location un-

[1]Although the RSS-based handover was not introduced specifically in the introductory part, its performance was evaluated and discussed together with LHO in publication IV.

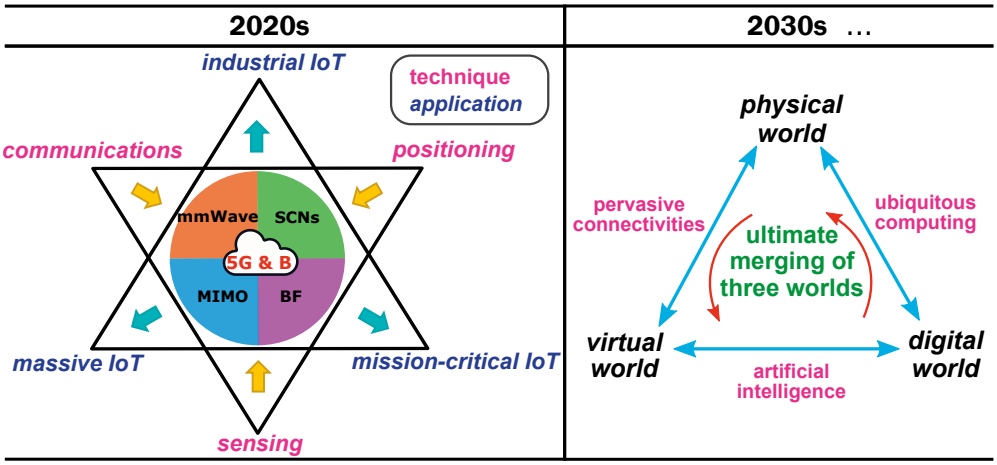

Figure 6.1 From the complement of technologies and use cases towards the ultimate merging of the physical world, the digital world and the virtual world.

certainty and system geometry) were resolved by the proposed joint positioning and tracking approach.

- Regarding research question 3, the benefits and feasibility of location-aware communication scheme were investigated and demonstrated in Chapter 4 and Chapter 5, respectively, enhancing the importance of positioning functionality and achievable location awareness further beyond the industrial IoT use cases.

6.2 Future perspectives

From 3G to 5G, wireless technology has undergone significant transformation over the past two decades, from a one-dimensional mobile communication system to a multi-dimensional computing platform with seamless connectivity. With the advent of novel techniques and immersive digital penetration, it can be foreseen that 5G and beyond wireless shall be fully deployed in the near future, forming a cloud-oriented intelligent communication networks with diverse IoT use cases. Therefore, the Author could courageously predict that the successful merging of physical world, digital world and virtual world (as illustrated in the right plot of Fig. 6.1) will be gradually and eventually realized on our way towards the sixth generation (6G) wireless system. As such, continuous development on the key techniques and radio access

networks from different layers and dimensions call upon further investigations. Particularly, the future research and investigation can start from the following perspectives:

Joint positioning and sensing — fusion of location awareness and environmental awareness towards situational awareness. Positioning is no longer about estimating the UE location only, but also the locations of dynamic APs, such as drone-anchors. In addition to locations, the orientations (as were described in Section 2.4 and Section 3.2) at both Tx & Rx can be estimated jointly with locations to, e.g., improve the efficiency of directional communications. With sensing technique in the picture, a 3D map of the environment can be constructed using the information extracted from the propagation channel. Therefore, a joint positioning and sensing scheme remains to be investigated to achieve the situational awareness for more engaging use cases.

Enhanced reliability via situational awareness, diverse spectrum, and cognitive slicing. Although FR 2 is open for wireless usage, link robustness in front of dynamic mobility and blockage should be dealt with efficiently to reduce the latency and enhance the reliability. Situational awareness that is achieved via positioning and sensing can be exploited to find several candidate paths for efficient routing at the physical layer. Furthermore, smart spectrum management and cognitive network slicing can be applied to increase the network versatility to satisfy heterogeneous verticals and diverse use cases.

Optimization among radio resources, system geometry, and positioning accuracy in dynamic environments. Positioning performance is essentially a function of several parameters, such as the available radio resources, the utilized LRMs, the applied positioning algorithms and the system geometry. As an extension of study in Chapter 3, a smart optimization strategy shall be investigated in a way that the radio resources, e.g., signal bandwidth, transmit power are adapted accordingly to optimize the positioning accuracy while adjusting the geometric relationships within the network.

Unification of communications, positioning, and sensing technologies with artificial intelligence — beyond RF convergence. More data than ever can be and will be collected from wireless system and IoT devices. Ubiquitous mobile edge computing could vastly drive the fusion of channel information and context information (location + environment), which is then intelligently processed via learning-based approaches, further harnessing the knowledge from all wireless dimensions and perspectives.

REFERENCES

[1] 3GPP, TR 22.801 V15.0.0. *Study on management and orchestration of network slicing for next generation network (Release 15)*. Jan. 2018.

[2] 3GPP, TR 22.872 V16.0.0. *Study on positioning use cases (Release 16)*. June 2018.

[3] 3GPP, TR 38.101-3 V16.3.0. *NR; User Equipment (UE) radio transmission and reception; Part 3: Range 1 and Range 2 Interworking operation with other radios (Release 16)*. Mar. 2020.

[4] 3GPP, TR 38.885 V16.0.0. *Study on NR Vehicle-to-Everything (V2X) (Release 16)*. Mar. 2019.

[5] 3GPP, TR 38.900 V15.0.0. *Study on channel model for frequency spectrum above 6 GHz (Release 15)*. June 2018.

[6] 3GPP, TR 38.901 V16.1.0. *Study on channel model for frequencies from 0.5 to 100 GHz (Release 16)*. Dec. 2019.

[7] 3GPP, TS 22.261 V17.3.0. *Service requirements for the 5G system; Stage 1 (Release 17)*. July 2020.

[8] 3GPP, TS 23.271 V15.2.0. *Functional stage 2 decription of Location Services (Release 15)*. Dec. 2019.

[9] 3GPP, TS 37.864 V15.0.0. *Dual Connectivity (EN-DC) of LTE Downlink (DL) / 1 Up Link (UL) and inter-/intra-band NR 2 Down Link (DL) / 2 Up Link (UL) bands (Frequency Range 1 (FR1) + Frequency Range 2 (FR2)) (Release 15)*. June 2018.

[10] 3GPP, TS 38.401 V16.6.0. *NG-RAN; Architecture description (Release 16)*. July 2021.

[11] 3GPP, TS 38.802 V14.2.0. *Study on New Radio Access Technology, Physical Layer Aspects (Release 14)*. Sept. 2017.

[12] N. Abbas, Y. Zhang, A. Taherkordi and T. Skeie. Mobile Edge Computing: A Survey. *IEEE Internet of Things Journal* 5.1 (2018), 450–465.

[13] W. B. Abbas and M. Zorzi. Context information based initial cell search for millimeter wave 5G cellular networks. *2016 European Conference on Networks and Communications (EuCNC)*. 2016, 111–116.

[14] S. Aditya, A. F. Molisch and H. M. Behairy. A Survey on the Impact of Multipath on Wideband Time-of-Arrival Based Localization. *Proceedings of the IEEE* 106.7 (2018), 1183–1203.

[15] S. Akoum, A. Thornburg, X. Wang and A. Ghosh. Robust Beam Management for Mobility in mmWave Systems. *2018 52nd Asilomar Conference on Signals, Systems, and Computers*. 2018, 1269–1273.

[16] J. G. Andrews, S. Buzzi, W. Choi, S. V. Hanly, A. Lozano, A. C. K. Soong and J. C. Zhang. What Will 5G Be?: *IEEE Journal on Selected Areas in Communications* 32.6 (June 2014), 1065–1082.

[17] J. G. Andrews, X. Zhang, G. D. Durgin and A. K. Gupta. Are we approaching the fundamental limits of wireless network densification?: *IEEE Communications Magazine* 54.10 (2016), 184–190.

[18] T. Bag, S. Garg, Z. Shaik and A. Mitschele-Thiel. Multi-Numerology Based Resource Allocation for Reducing Average Scheduling Latencies for 5G NR Wireless Networks. *2019 European Conference on Networks and Communications (EuCNC)*. 2019, 597–602.

[19] A.-S. Bana, E. de Carvalho, B. Soret, T. Abrão, J. C. M. Filho, E. G. Larsson and P. Popovski. Massive MIMO for Internet of Things (IoT) Connectivity. *arXiv* abs/1905.06205 (2019).

[20] J. R. Barry, E. A. Lee and D. G. Messerschmitt. *Digital communication*. Springer Science & Business Media, 2012.

[21] J. M. Batalla, C. X. Mavromoustakis, G. Mastorakis, N. N. Xiong and J. Wozniak. Adaptive Positioning Systems Based on Multiple Wireless Interfaces for Industrial IoT in Harsh Manufacturing Environments. *IEEE Journal on Selected Areas in Communications* 38.5 (2020), 899–914.

[22] E. Björnson, J. Hoydis and L. Sanguinetti. Massive MIMO Networks: Spectral, Energy, and Hardware Efficiency. *Foundations and Trends® in Signal Processing* 11.3-4 (2017), 154–655.

[23] F. Boccardi, R. W. Heath, A. Lozano, T. L. Marzetta and P. Popovski. Five disruptive technology directions for 5G. *IEEE Communications Magazine* 52.2 (2014), 74–80.

[24] D. Bore, A. Rana, N. Kolhare and U. Shinde. Automated Guided Vehicle Using Robot Operating Systems. *2019 3rd International Conference on Trends in Electronics and Informatics (ICOEI)*. 2019, 819–822.

[25] C. Campolo, A. Molinaro, F. Romeo, A. Bazzi and A. O. Berthet. 5G NR V2X: On the Impact of a Flexible Numerology on the Autonomous Sidelink Mode. *2019 IEEE 2nd 5G World Forum (5GWF)*. 2019, 102–107.

[26] X. Cheng, M. Wang and S. Li. Compressive Sensing-Based Beamforming for Millimeter-Wave OFDM Systems. *IEEE Transactions on Communications* 65.1 (Jan. 2017), 371–386.

[27] O. Chukhno, N. Chukhno, O. Galinina, Y. Gaidamaka, S. Andreev and K. Samouylov. Analysis of 3D Deafness Effects in Highly Directional mmWave Communications. *2019 IEEE Global Communications Conference (GLOBECOM)*. 2019, 1–6.

[28] E. Dahlman, S. Parkvall and J. Skold. *5G NR: The Next Generation Wireless Access Technology*. Elsevier Science, 2018. ISBN: 9780128143230.

[29] M. De Ree, G. Mantas, A. Radwan, S. Mumtaz, J. Rodriguez and I. E. Otung. Key Management for Beyond 5G Mobile Small Cells: A Survey. *IEEE Access* 7 (2019), 59200–59236.

[30] V. Desai, L. Krzymien, P. Sartori, W. Xiao, A. Soong and A. Alkhateeb. Initial beamforming for mmWave communications. *Conference Record - Asilomar Conference on Signals, Systems and Computers* 2015 (Apr. 2015), 1926–1930.

[31] G. Destino and H. Wymeersch. On the trade-off between positioning and data rate for mm-wave communication. *2017 IEEE International Conference on Communications Workshops (ICC Workshops)*. May 2017, 797–802.

[32] R. Di Taranto, S. Muppirisetty, R. Raulefs, D. Slock, T. Svensson and H. Wymeersch. Location-Aware Communications for 5G Networks: How location information can improve scalability, latency, and robustness of 5G. *IEEE Signal Processing Magazine* 31.6 (Nov. 2014), 102–112.

[33] X. Dong, L. Zhao, H. Zhao and C. Pan. RAN Slicing-based Handover Scheme in HetNets. *2018 IEEE 23rd International Conference on Digital Signal Processing (DSP)*. 2018, 1–5.

[34] Ericsson. *Critical Capabilities for Private 5G Networks*. White Paper. 2020.

[35] B. Etzlinger, H. Wymeersch and A. Springer. Cooperative Synchronization in Wireless Networks. *IEEE Transactions on Signal Processing* 62.11 (June 2014), 2837–2849.

[36] C. Fiandrino, H. Assasa, P. Casari and J. Widmer. Scaling Millimeter-Wave Networks to Dense Deployments and Dynamic Environments. *Proceedings of the IEEE* 107.4 (Apr. 2019), 732–745.

[37] N. Garcia, H. Wymeersch, E. G. Ström and D. Slock. Location-aided mm-wave channel estimation for vehicular communication. *2016 IEEE 17th International Workshop on Signal Processing Advances in Wireless Communications (SPAWC)*. July 2016, 1–5.

[38] S. Gezici, Zhi Tian, G. B. Giannakis, H. Kobayashi, A. F. Molisch, H. V. Poor and Z. Sahinoglu. Localization via ultra-wideband radios: a look at positioning aspects for future sensor networks. *IEEE Signal Processing Magazine* 22.4 (2005), 70–84.

[39] A. Ghosh, A. Maeder, M. Baker and D. Chandramouli. 5G Evolution: A View on 5G Cellular Technology Beyond 3GPP Release 15. *IEEE Access* 7 (2019), 127639–127651.

[40] M. Giordani, M. Mezzavilla and M. Zorzi. Initial Access in 5G mmWave Cellular Networks. *IEEE Communications Magazine* 54.11 (Nov. 2016), 40–47.

[41] M. Giordani, M. Polese, A. Roy, D. Castor and M. Zorzi. A tutorial on beam management for 3GPP NR at mmWave frequencies. *IEEE Communications Surveys & Tutorials* 21.1 (2018), 173–196.

[42] M. Giordani, M. Polese, A. Roy, D. Castor and M. Zorzi. Standalone and non-standalone beam management for 3GPP NR at mmWaves. *IEEE Communications Magazine* 57.4 (2019), 123–129.

[43] H. Guo, B. Makki and T. Svensson. A genetic algorithm-based beamforming approach for delay-constrained networks. *2017 15th International Symposium on Modeling and Optimization in Mobile, Ad Hoc, and Wireless Networks (WiOpt)*. May 2017, 1–7.

[44] F. Gustafsson and F. Gunnarsson. Mobile positioning using wireless networks: possibilities and fundamental limitations based on available wireless network measurements. *IEEE Signal Processing Magazine* 22.4 (2005), 41–53.

[45] I. Guvenc and C. Chong. A Survey on TOA Based Wireless Localization and NLOS Mitigation Techniques. *IEEE Communications Surveys & Tutorials* 11.3 (2009), 107–124.

[46] R. W. Heath, N. González-Prelcic, S. Rangan, W. Roh and A. M. Sayeed. An Overview of Signal Processing Techniques for Millimeter Wave MIMO Systems. *IEEE Journal of Selected Topics in Signal Processing* 10.3 (2016), 436–453.

[47] H. Holma, A. Toskala and T. Nakamura. *5G Technology: 3GPP New Radio*. 1st. Wiley, 2019. ISBN: 9781119236313.

[48] P. Hsieh, W. Lin, K. Lin and H. Wei. Dual-Connectivity Prevenient Handover Scheme in Control/User-Plane Split Networks. *IEEE Transactions on Vehicular Technology* 67.4 (2018), 3545–3560.

[49] HuaWei Technologies, Inc. *5G Network Architecture*. White Paper. 2016.

[50] E. Hyytiä, H. Koskinen, P. Lassila, A. Penttinen, J. Virtamo and J. Roszik. Random Waypoint Model in Wireless Networks. *Networks and Algorithms: Complexity in physics and Computer Science* (Jan. 2005).

[51] J. Campos. *Understanding of the 5G NR Physical Layer*. Keysight technologies. 2017.

[52] I. K. Jain, R. Kumar and S. S. Panwar. The Impact of Mobile Blockers on Millimeter Wave Cellular Systems. *IEEE Journal on Selected Areas in Communications* 37.4 (2019), 854–868.

[53] C. Jeong, J. Park and H. Yu. Random access in millimeter-wave beamforming cellular networks: issues and approaches. *IEEE Communications Magazine* 53.1 (Jan. 2015), 180–185.

[54] M. Ji, J. Kim, J. Jeon and Y. Cho. Analysis of positioning accuracy corresponding to the number of BLE beacons in indoor positioning system. *2015 17th International Conference on Advanced Communication Technology (ICACT)*. 2015, 92–95.

[55] J. Kang, I. Orikumhi, Y. Park and S. Kim. A Millimeter Wave Beam Tracking in Vehicular Scenario via Particle Filter. *2018 International Conference on Network Infrastructure and Digital Content (IC-NIDC)*. 2018, 234–238.

[56] W. Kang and Y. Han. SmartPDR: Smartphone-Based Pedestrian Dead Reckoning for Indoor Localization. *IEEE Sensors Journal* 15.5 (May 2015), 2906–2916.

[57] A. Karmakar, N. Dey, T. Baral, M. Chowdhury and M. Rehan. Industrial Internet of Things: A Review. *2019 International Conference on Opto-Electronics and Applied Optics (Optronix)*. 2019, 1–6.

[58] S. M. Kay. *Fundamentals of Statistical Signal Processing: Estimation Theory*. Upper Saddle River, NJ, USA: Prentice-Hall, Inc., 1993. ISBN: 0-13-345711-7.

[59] P. Kela, M. Costa, J. Turkka, M. Koivisto, J. Werner, A. Hakkarainen, M. Valkama, R. Jäntti and K. Leppänen. Location Based Beamforming in 5G Ultra-Dense Networks. *2016 IEEE 84th Vehicular Technology Conference (VTC-Fall)*. Sept. 2016, 1–7.

[60] Keysight Technologies. *OTA Setup for 5G TF Beamforming Functional Tests*. White Paper. 2018.

[61] M. W. Khan, N. Salman, A. H. Kemp and L. Mihaylova. Localisation of Sensor Nodes with Hybrid Measurements in Wireless Sensor Networks. *Sensors* 16.7 (2016).

[62] H. Kim, X. Ma and B. R. Hamilton. Tracking Low-Precision Clocks With Time-Varying Drifts Using Kalman Filtering. *IEEE/ACM Transactions on Networking* 20.1 (2012), 257–270.

[63] M. Koivisto, M. Costa, J. Werner, K. Heiska, J. Talvitie, K. Leppänen, V. Koivunen and M. Valkama. Joint Device Positioning and Clock Synchronization in 5G Ultra-Dense Networks. *IEEE Transactions on Wireless Communications* 16.5 (2017), 2866–2881.

[64] M. Koivisto, A. Hakkarainen, M. Costa, P. Kela, K. Leppänen and M. Valkama. High-Efficiency Device Positioning and Location-Aware Communications in Dense 5G Networks. *IEEE Communications Magazine* 55.8 (Aug. 2017), 188–195.

[65] M. Koivisto, J. Talvitie, M. Costa, K. Leppänen and M. Valkama. Joint cmWave-based multiuser positioning and network synchronization in dense 5G networks. *2018 IEEE Wireless Communications and Networking Conference (WCNC)*. Apr. 2018, 1–6.

[66] J. Kulmer, S. Hinteregger, B. Großwindhager, M. Rath, M. S. Bakr, E. Leitinger and K. Witrisal. Using DecaWave UWB transceivers for high-accuracy multipath-assisted indoor positioning. *2017 IEEE International Conference on Communications Workshops (ICC Workshops)*. 2017, 1239–1245.

[67] J. Kulmer, E. Leitinger, S. Grebien and K. Witrisal. Anchorless Cooperative Tracking Using Multipath Channel Information. *IEEE Transactions on Wireless Communications* 17.4 (2018), 2262–2275.

[68] E. G. Larsson, O. Edfors, F. Tufvesson and T. L. Marzetta. Massive MIMO for next generation wireless systems. *IEEE Communications Magazine* 52.2 (Feb. 2014), 186–195.

[69] E. Leitinger, F. Meyer, F. Hlawatsch, K. Witrisal, F. Tufvesson and M. Z. Win. A Belief Propagation Algorithm for Multipath-Based SLAM. *IEEE Transactions on Wireless Communications* 18.12 (2019), 5613–5629.

[70] T. Levanen, J. Talvitie, R. Wichman, V. Syrjälä, M. Renfors and M. Valkama. Location-aware 5G communications and Doppler compensation for high-speed train networks. *2017 European Conference on Networks and Communications (EuCNC)*. June 2017, 1–6.

[71] P. Li and J. Xu. Fundamental Rate Limits of UAV-Enabled Multiple Access Channel With Trajectory Optimization. *IEEE Transactions on Wireless Communications* 19.1 (2020), 458–474.

[72] E. S. Lohan, M. Koivisto, O. Galinina, S. Andreev, A. Tolli, G. Destino, M. Costa, K. Leppanen, Y. Koucheryavy and M. Valkama. Benefits of Positioning-Aided Communication Technology in High-Frequency Industrial IoT. *IEEE Communications Magazine* 56.12 (2018), 142–148.

[73] A. Lozano. Long-Term Transmit Beamforming for Wireless Multicasting. *2007 IEEE International Conference on Acoustics, Speech and Signal Processing - ICASSP '07*. Vol. 3. Apr. 2007, III-417-III–420.

[74] A. Lozano, R. W. Heath and J. G. Andrews. Fundamental Limits of Cooperation. *IEEE Transactions on Information Theory* 59.9 (2013), 5213–5226.

[75] M. Marcus and B. Pattan. Millimeter wave propagation: spectrum management implications. *IEEE Microwave Magazine* 6.2 (June 2005), 54–62.

[76] F. J. Martin-Vega, M. C. Aguayo-Torres, G. Gomez, J. T. Entrambasaguas and T. Q. Duong. Key Technologies, Modeling Approaches, and Challenges for Millimeter-Wave Vehicular Communications. *IEEE Communications Magazine* 56.10 (Oct. 2018), 28–35.

[77] J. Medbo, P. Kyosti, K. Kusume, L. Raschkowski, K. Haneda, T. Jamsa, V. Nurmela, A. Roivainen and J. Meinila. Radio propagation modeling for 5G mobile and wireless communications. *IEEE Communications Magazine* 54.6 (2016), 144–151.

[78] R. Mendrzik, F. Meyer, G. Bauch and M. Z. Win. Enabling Situational Awareness in Millimeter Wave Massive MIMO Systems. *IEEE Journal of Selected Topics in Signal Processing* 13.5 (2019), 1196–1211.

[79] R. Mendrzik, H. Wymeersch, G. Bauch and Z. Abu-Shaban. Harnessing NLOS Components for Position and Orientation Estimation in 5G Millimeter Wave MIMO. *IEEE Transactions on Wireless Communications* 18.1 (2019), 93–107.

[80] E. Y. Menta, N. Malm, R. Jäntti, K. Ruttik, M. Costa and K. Leppänen. On the Performance of AoA–Based Localization in 5G Ultra–Dense Networks. *IEEE Access* 7 (2019), 33870–33880.

[81] M. T. Moayyed, B. Antonescu and S. Basagni. Clustering Algorithms and Validation Indices for mmWave Radio Multipath Propagation. *2019 Wireless Telecommunications Symposium (WTS)*. 2019, 1–7.

[82] E. Mohamed, H. Esmaiel and A. Abdelreheem. Adaptive Location-based Millimeter Wave Beamforming Using Compressive Sensing Based Channel Estimation. *IET Communications* 13 (Feb. 2019).

[83] A. Morsali, S. Norouzi and B. Champagne. Single RF Chain Hybrid Analog/Digital Beamforming for Mmwave Massive-mimo. *2019 IEEE Global Conference on Signal and Information Processing (GlobalSIP)*. 2019, 1–5.

[84] S. Mumtaz, A. Alsohaily, Z. Pang, A. Rayes, K. F. Tsang and J. Rodriguez. Massive Internet of Things for Industrial Applications: Addressing Wireless IIoT Connectivity Challenges and Ecosystem Fragmentation. *IEEE Industrial Electronics Magazine* 11.1 (2017), 28–33.

[85] H. Q. Ngo, A. Ashikhmin, H. Yang, E. G. Larsson and T. L. Marzetta. Cell-Free Massive MIMO Versus Small Cells. *IEEE Transactions on Wireless Communications* 16.3 (2017), 1834–1850.

[86] Y. Niu, Y. Li, D. Jin, L. Su and A. V. Vasilakos. A survey of millimeter wave communications (mmWave) for 5G: opportunities and challenges. *Wireless Networks* 21.8 (Nov. 2015), 2657–2676.

[87] N. Patwari, J. N. Ash, S. Kyperountas, A. O. Hero, R. L. Moses and N. S. Correal. Locating the nodes: cooperative localization in wireless sensor networks. *IEEE Signal Processing Magazine* 22.4 (2005), 54–69.

[88] B. Paul, A. R. Chiriyath and D. W. Bliss. Survey of RF Communications and Sensing Convergence Research. *IEEE Access* 5 (2017), 252–270.

[89] Z. Pi and F. Khan. An introduction to millimeter-wave mobile broadband systems. *IEEE Communications Magazine* 49.6 (June 2011), 101–107.

[90] Qualcomm Technologies, Inc. *How will 5G transform Industrial IoT?* White Paper. 2019.

[91] Qualcomm Technologies, Inc. *Private 5G Networks for Industrial IoT*. White Paper. 2019.

[92] T. S. Rappaport, S. Sun, R. Mayzus, H. Zhao, Y. Azar, K. Wang, G. N. Wong, J. K. Schulz, M. Samimi and F. Gutierrez. Millimeter Wave Mobile Communications for 5G Cellular: It Will Work!: *IEEE Access* 1 (2013), 335–349.

[93] E. Rastorgueva-Foi, M. Costa, M. Koivisto, K. Leppänen and M. Valkama. User Positioning in mmW 5G Networks Using Beam-RSRP Measurements and Kalman Filtering. *2018 21st International Conference on Information Fusion (FUSION)*. 2018, 1–7.

[94] E. Rastorgueva-Foi, M. Costa, M. Koivisto, J. Talvitie, K. Leppäneny and M. Valkama. Beam-based Device Positioning in mmWave 5G Systems under Orientation Uncertainties. *2018 52nd Asilomar Conference on Signals, Systems, and Computers*. 2018, 3–7.

[95] E. Rastorgueva-Foi, M. Koivisto, M. Valkama, M. Costa and K. Leppänen. Localization and Tracking in mmWave Radio Networks using Beam-Based DoD Measurements. *2018 8th International Conference on Localization and GNSS (ICL-GNSS)*. June 2018, 1–6.

[96] F. Rusek, D. Persson, B. K. Lau, E. G. Larsson, T. L. Marzetta, O. Edfors and F. Tufvesson. Scaling Up MIMO: Opportunities and Challenges with Very Large Arrays. *IEEE Signal Processing Magazine* 30.1 (2013), 40–60.

[97] H. Sahota and R. Kumar. Maximum-Likelihood Sensor Node Localization Using Received Signal Strength in Multimedia With Multipath Characteristics. *IEEE Systems Journal* 12.1 (2018), 506–515.

[98] J. Saloranta and G. Destino. On the utilization of MIMO-OFDM channel sparsity for accurate positioning. *2016 24th European Signal Processing Conference (EUSIPCO)*. 2016, 748–752.

[99] S. S. A. Al-Samahi, K. C. Ho and N. E. Islam. Improving Elliptic/Hyperbolic Localization Under Multipath Environment Using Neural Network for Outlier Detection. *IEEE INFOCOM 2019 - IEEE Conference on Computer Communications Workshops (INFOCOM WKSHPS)*. 2019, 933–938.

[100] M. K. Samimi, T. S. Rappaport and G. R. MacCartney. Probabilistic Omnidirectional Path Loss Models for Millimeter-Wave Outdoor Communications. *IEEE Wireless Communications Letters* 4.4 (2015), 357–360.

[101] S. Sand, A. Dammann and C. Mensing. *Positioning in Wireless Communication Systems*. John Wiley & Sons Ltd., June 2014.

[102] K. Senel, E. Björnson and E. G. Larsson. Human and Machine Type Communications Can Coexist in Uplink Massive MIMO Systems. *2018 IEEE International Conference on Acoustics, Speech and Signal Processing (ICASSP)*. 2018, 6613–6617.

[103] M. Sheng, Y. Zheng, J. Liu, S. Valaee and J. Li. Accurate Indoor Localization Assisted With Optimizing Array Orientations and Receiver Positions. *IEEE Transactions on Vehicular Technology* 69.1 (2020), 509–521.

[104] H. Shokri-Ghadikolaei, C. Fischione, G. Fodor, P. Popovski and M. Zorzi. Millimeter wave cellular networks: a MAC layer perspective. *IEEE Transactions on Communications* 63.10 (Oct. 2015), 3437–3458.

[105] D. Simon. *Optimal State Estimation: Kalman, H Infinity, and Nonlinear Approaches*. New York, NY, USA: Wiley-Interscience, 2006. ISBN: 0471708585.

[106] Stephane Teral, IHS Markit. *5G best choice architecture*. White Paper. 2019.

[107] G. L. Stüber. *Principles of Mobile Communication*. 3rd. New York, NY: Springer New York, 2011. ISBN: 978-1461403654.

[108] C. Suarez-Rodriguez, Y. He and E. Dutkiewicz. Theoretical Analysis of REM-Based Handover Algorithm for Heterogeneous Networks. *IEEE Access* 7 (2019), 96719–96731.

[109] S. Sun, T. S. Rappaport, R. W. Heath, A. Nix and S. Rangan. Mimo for millimeter-wave wireless communications: beamforming, spatial multiplexing, or both?: *IEEE Communications Magazine* 52.12 (2014), 110–121.

[110] S. Sun, T. S. Rappaport, M. Shafi, P. Tang, J. Zhang and P. J. Smith. Propagation Models and Performance Evaluation for 5G Millimeter-Wave Bands. *IEEE Transactions on Vehicular Technology* 67.9 (2018), 8422–8439.

[111] S. Sur, V. Venkateswaran, X. Zhang and P. Ramanathan. 60 GHz indoor networking through flexible beams: A link-level profiling. *Proceedings of the 2015 ACM SIGMETRICS International Conference on Measurement and Modeling of Computer Systems*. 2015, 71–84.

[112] K. Swetha and B. N. Subrahmanyam. Interference management and resource allocation for communications underlying downlink/uplink decoupling (DUDe) heterogeneous networks. *2017 International Conference on Multimedia, Signal Processing and Communication Technologies (IMPACT)*. 2017, 60–64.

[113] N. Tafintsev, D. Moltchanov, M. Simsek, S. Yeh, S. Andreev, Y. Koucheryavy and M. Valkama. Reinforcement Learning for Improved UAV-Based Integrated Access and Backhaul Operation. *2020 IEEE International Conference on Communications Workshops (ICC Workshops)*. 2020, 1–7.

[114] M. Tayyab, X. Gelabert and R. Jäntti. A Survey on Handover Management: From LTE to NR. *IEEE Access* 7 (2019), 118907–118930.

[115] X. Tian and W. Jia. Improved clustering and resource allocation for ultra-dense networks. *China Communications* 17.2 (2020), 220–231.

[116] K. T. Truong and R. W. Heath. Effects of channel aging in massive MIMO systems. *Journal of Communications and Networks* 15.4 (2013), 338–351.

[117] K. T. Truong and R. W. Heath Jr. Impact of spatial correlation and distributed antennas for massive MIMO systems. *Proc. AsilomarConf. Signals Syst. Comput.* 2013.

[118] D. Tse and P. Viswanath. *Fundamentals of Wireless Communications*. Cambridge Univ. Press, 2005.

[119] V. Va, J. Choi and R. W. Heath. The Impact of Beamwidth on Temporal Channel Variation in Vehicular Channels and Its Implications. *IEEE Transactions on Vehicular Technology* 66.6 (2017), 5014–5029.

[120] D. Verenzuela, E. Björnson and L. Sanguinetti. Spectral and Energy Efficiency of Superimposed Pilots in Uplink Massive MIMO. *IEEE Transactions on Wireless Communications* 17.11 (2018), 7099–7115.

[121] J. Vieira, F. Rusek, O. Edfors, S. Malkowsky, L. Liu and F. Tufvesson. Reciprocity Calibration for Massive MIMO: Proposal, Modeling, and Validation. *IEEE Transactions on Wireless Communications* 16.5 (2017), 3042–3056.

[122] H. Wang, P. Zhang, J. Li and X. You. Radio propagation and wireless coverage of LSAA-based 5G millimeter-wave mobile communication systems. *China Communications* 16.5 (2019), 1–18.

[123] K. Wang, P. Li, F. Ding, Z. Pan, N. Liu and X. You. Analysis of coverage and area spectrum efficiency of UDN with inter-tier dependence. *China Communications* 16.3 (2019), 154–164.

[124] L. Wei, R. Q. Hu, Y. Qian and G. Wu. Key elements to enable millimeter wave communications for 5G wireless systems. *IEEE Wireless Communications* 21.6 (2014), 136–143.

[125] T. Wei and X. Zhang. mtrack: High-precision passive tracking using millimeter wave radios. *Proceedings of the 21st Annual International Conference on Mobile Computing and Networking*. 2015, 117–129.

[126] T. Wei and X. Zhang. Pose Information Assisted 60 GHz Networks: Towards Seamless Coverage and Mobility Support. *Proceedings of the 23rd Annual International Conference on Mobile Computing and Networking*. MobiCom '17. Snowbird, Utah, USA: ACM, 2017, 42–55. ISBN: 978-1-4503-4916-1.

[127] F. Wen and H. Wymeersch. 5G Synchronization, Positioning, and Mapping From Diffuse Multipath. *IEEE Wireless Communications Letters* 10.1 (2021), 43–47.

[128] Y. Wen, X. Tian, X. Wang and S. Lu. Fundamental limits of RSS fingerprinting based indoor localization. *2015 IEEE Conference on Computer Communications (INFOCOM)*. 2015, 2479–2487.

[129] Wireless Insite. *https://www.remcom.com/wireless-insite-em-propagation-software*. Remcom Corporation.

[130] K. Witrisal, P. Meissner, E. Leitinger, Y. Shen, C. Gustafson, F. Tufvesson, K. Haneda, D. Dardari, A. F. Molisch, A. Conti and M. Z. Win. High-Accuracy Localization for Assisted Living: 5G systems will turn multipath channels from foe to friend. *IEEE Signal Processing Magazine* 33.2 (2016), 59–70.

[131] W. Wu, D. Liu, Z. Li, X. Hou and M. Liu. Two-Stage 3D Codebook Design and Beam Training for Millimeter-Wave Massive MIMO Systems. *2017 IEEE 85th Vehicular Technology Conference (VTC Spring)*. June 2017, 1–7.

[132] X. Wu, N. C. Beaulieu and D. Liu. On Favorable Propagation in Massive MIMO Systems and Different Antenna Configurations. *IEEE Access* 5 (2017), 5578–5593.

[133] S. Wyne, K. Haneda, S. Ranvier, F. Tufvesson and A. F. Molisch. Beamforming Effects on Measured mm-Wave Channel Characteristics. *IEEE Transactions on Wireless Communications* 10.11 (2011), 3553–3559.

[134] K. Xu, K. Wang, R. Amin, J. Martin and R. Izard. A Fast Cloud-Based Network Selection Scheme Using Coalition Formation Games in Vehicular Networks. *IEEE Transactions on Vehicular Technology* 64.11 (Nov. 2015), 5327–5339.

[135] R. Yagoub, M. Benaissa, B. Benadda and M. Merzoug. Low Cost RTL-SDR Based Positioning Solution Based on GSM Cell Id. *2019 6th International Conference on Image and Signal Processing and their Applications (ISPA)*. 2019, 1–6.

[136] L. Yan, H. Ding, L. Zhang, J. Liu, X. Fang, Y. Fang, M. Xiao and X. Huang. Machine Learning-Based Handovers for Sub-6 GHz and mmWave Integrated Vehicular Networks. *IEEE Transactions on Wireless Communications* 18.10 (Oct. 2019), 4873–4885.

[137] S. Zang, W. Bao, P. L. Yeoh, B. Vucetic and Y. Li. Managing Vertical Handovers in Millimeter Wave Heterogeneous Networks. *IEEE Transactions on Communications* 67.2 (Feb. 2019), 1629–1644.

[138] R. Zekavat and R. M. Buehrer. *Handbook of Position Location: Theory, Practice and Advances*. 2nd. Wiley-IEEE Press, 2019. ISBN: 978-1-119-43460-3.

[139] Y. Zeng, Q. Wu and R. Zhang. Accessing From the Sky: A Tutorial on UAV Communications for 5G and Beyond. *Proceedings of the IEEE* 107.12 (2019), 2327–2375.

[140] Y. Zeng, R. Zhang and T. J. Lim. Wireless communications with unmanned aerial vehicles: opportunities and challenges. *IEEE Communications Magazine* 54.5 (2016), 36–42.

[141] W. Zhang and W. Zhang. Beam Training and Tracking Efficiency Analysis for UAV mmWave Communication. *2018 IEEE International Conference on Communication Systems (ICCS)*. 2018, 115–119.

[142] Zhian Deng, Lin Ma and Yubin Xu. Intelligent AP selection for indoor positioning in wireless local area network. *2011 6th International ICST Conference on Communications and Networking in China (CHINACOM)*. 2011, 257–261.

[143] A. Zhou, L. Wu, S. Xu, H. Ma, T. Wei and X. Zhang. Following the Shadow: Agile 3-D Beam-Steering for 60 GHz Wireless Networks. *IEEE INFOCOM 2018 - IEEE Conference on Computer Communications*. Apr. 2018, 2375–2383.

PUBLICATIONS

PUBLICATION

I

Opportunities and Challenges in the Industrial Internet of Things based on 5G Positioning

Y. Lu, P. Richter and E. S. Lohan

*2018 8th International Conference on Localization and GNSS (ICL-GNSS)*2018, 1–6
DOI: 10.1109/ICL-GNSS.2018.8440903

Opportunities and Challenges in the Industrial Internet of Things based on 5G Positioning

Yi Lu, Philipp Richter, Elena Simona Lohan
Tampere University of Technology, Finland
{yi.lu, philipp.richter, elena-simona.lohan}@tut.fi

***Abstract*—This paper discusses several features of 5G positioning in the context of applications for the Industrial Internet of Things (IIoT) which demand high accuracy of position information. The main opportunities to come with 5G networks, such as huge available spectrum, small cell networks, Multiple Input Multiple Output antennas and beamforming are summarized, and the challenges in the context of robot 5G positioning are pointed out. A case study for the localization of an indoor robot in a multi-wall multi-floor scenario is presented, based on various carrier frequencies and access node densities. We find out that sub-meter positioning accuracy required for most of the future industrial applications is theoretically achievable via a combination of small cell networks, mmWave carriers and antenna arrays, but practical issues such as node synchronization, connectivity and ultra dense network deployment costs have to be tackled.**

I. Introduction

With the fast advances of 5G standardization, several new opportunities are brought along, such as Augmented Reality (AR), eHealth, telepresence and Industrial Internet of Things (IIoT). Among those, in our opinion it is the IIoT that can benefit the most from the positioning capabilities of 5G networks, because position information can help to optimize and to automatize the processes in various vertical sectors, ranging from logistics and manufacturing to mining and transportation. It is usually understood that there are three main segments within the IIoT, namely the industrial control, the factory automation, and the process automation. Especially within the industrial control and factory automation segments, the positioning information is highly beneficial at both communication sides: for the (mobile) terminals (or robots) to accomplish their tasks and for the network to allocate and control the resources and to increase the processing efficiency.

IIoT applications are characterized by stringent requirements in terms of the quality, latency and reliability of the communication link as well as of the accuracy and precision of the positioning. These demands need to be met both indoors and outdoors, and typically over large coverage areas. Moreover, additional information about the surroundings, e.g. from sensor networks or maps, might be required such that, for example, the unmanned robots can navigate in a dynamic environment and autonomously accomplish their critical tasks within a manufacturing process. This paper outlines how different features of the 5G networks can improve the 5G positioning and it assesses their trade-off in the context of IIoT robot localization.

The goal of this paper is three-fold: first to present a survey of the opportunities and challenges in the IIoT localization based on 5G positioning; secondly, to present an analytical model for indoor path losses, shadowing, and Time of Arrivals (ToA) under Line of Sight (LoS) and Non Line of Sight (NLoS) conditions; and lastly, to show a case-study based on an indoor multi-floor multi-wall simulator for 3D positioning of a robot within cmWave and mmWave spectra. We will show the impact on the positioning accuracy of the indoor robot if we use mmWave signals, if we increase the AN (Access Node) density, and if we make use of MIMO antenna gains through beamforming.

II. 5G positioning

In this section, we discuss the benefits of various 5G network features in terms of achieving accurate and robust 5G positioning of the robots.

A. mmWave and beyond

The first benefits in 5G networks is the availability of a rich spectrum by utilizing the abundant mmWave band (i.e., spectrum larger than 30 GHz) which is not used in previous wireless communication system (i.e., 2G, 3G and 4G LTE). At mmWave, we have higher path loss and higher sensitivity to the atmosphere (absorption and penetration) [1] than at cmWave. The mmWave spectrum is therefore widely recognized to be used for short distance communications [2]. Certain transformations of the structure of networks have to be made to make use of mmWave at its full potential, and these will be discussed in the next subsections.

In terms of positioning benefits of the mmWave, higher accuracy and lower latency positioning of robots are made possible, due to more available signal bandwidth compared with cmWave spectrum. Specifically, a more accurate ToA (Time of Arrival) estimation in 5G positioning is enabled because of a finer delay domain resolution brought by the larger bandwidth, which at its turns leads to a more precise range estimation. Secondly, by leveraging the sparsity of the mmWave channel, the robot can in theory be localized with only one AN because multipath components can be converted to virtual anchors that contributes to the position estimate [3], [4].

However, a few challenges are incurred at the same time. Firstly, the positioning methods in 5G mmWave systems are quite opportunistic, especially with high mobility, i.e., the

communication quality as well as the positioning accuracy are closely tied to the environment, thus, the link reliability is highly context based. Also, several factors such as a poor geometry w.r.t. the ANs in view or temporary blockage of the LoS can have severe negative impact on the radio link.

Research beyond 5G also focuses on sub-mmWave band or TeraHertz (THz) bands, where the signal bandwidth will become even larger, antenna array size become even smaller (half-wavelength of 1 THz is only $150\,\mu$m which means, e.g., that a 128 elements antenna array only possesses a physical length of 19.2 mm). Therefore, massive MIMO will be enhanced to achieve further larger bandwidth and to reduce the interference. Moreover, the backhaul link of a network can take advantage of THz band in order to provide higher backhaul data rate than fronthaul [5]. Some of the challenges in THz bands (also sometimes referred to as "THz gap") are: extremely high path losses and atmosphere sensitivity, as well as large heat dispersion at antennas.

B. Small cell networks (SCNs)

The advantage brought in by the SCNs concept into the 5G positioning comes mainly from the fact that the SCNs can compensate the mmWave propagation loss. The severe path loss problem of mmWave can be addressed if the maximum distance between AN and robots (or terminals) within a single cell become shorter. Network densification is the key solution as it is much more easier for one AN to track a few (e.g., less than 10) robots than tens or hundreds of robots as in a conventional network (2G-4G). As such, the direct benefit to positioning brought by network densification is the potential to higher accuracy. The frequency reuse factor is also raised by using SCNs, yielding a high spectral efficiency. In addition, SCN can provide better cell-edge communication quality than conventional AN deployment, because the interference coming from adjacent cells is minimized due to high attenuation of mmWave signal.

In terms of positioning, SCNs enhance communication reliability and quality to any robot in indoor and urban areas, because when the mmWave signal from one AN is blocked, the robot can simply switch to a nearby ANs which has a better link quality. Thus, also the LoS probability increases in SCNs, which is considered as crucial in order to achieve sub-meter positioning accuracy. Moreover, SCNs can lead to a better positioning accuracy from the upper bound perspective: the radius of cell coverage defines a upper bound of absolute positioning error, therefore, small cells possess generally smaller radius that yields a smaller upper bound. In our simulator (Section IV), we model LoS probability according to the walls and the floors present in the propagation path and we investigate the average number of LoS connections per robot in a realistic multi-floor multi-wall scenario.

The main challenge coming with SCNs is the cost of backhaul communications and the backhaul routing algorithm among the ANs, further discussion of SCNs can be found in [6].

C. Massive MIMO

A third feature in 5G networks is the concept of massive MIMO, which lays the foundation of a high directional communication system by employing large antenna array techniques at both sides of the transmission chain. Massive MIMO provides a high energy efficiency thanks to a high directivity of the antenna arrays,a high spectrum efficiency due to large multiplexing gain, and a high reliability or robustness due to large diversity gain [7], [8]. The large multiplexing gain between the AN, on one hand, and the robot on the other hand, would enable the ultra high mobile broadband connection that 4G LTE cannot currently provide. Regarding to its benefits to positioning, massive MIMO offers a high directional beam which translates into a high SINR (Signal to interference noise ratio), which at its turn reduces the uncertainty of the ToA estimation. The highly directional link improves further the positioning and communications, by reducing the average number of multipath components received by the robot [8].

A challenge in massive MIMO is the signal processing algorithm complexity, due to the large number of antennas at both sides. Additionally, the acquisition of the channel state information (CSI) at AN on the downlink is rather difficult, as each robot has to estimate an amount of channel responses that is proportional to the number of AN antennas. This can be avoided if location-based beamforming (or geometric beamforming) is used [9].

D. Beamforming

Associated with massive MIMO, the beamforming (BF) technique, which is an array signal processing technique, makes the communications more efficient based on the awareness in the angular domain. Without antenna array and BF, the access nodes and the robots would acquire the signals in an omnidirectional ('blind') manner. This would make the multipaths to be a troublesome. As a result, the ToA measurements would be corrupted by multiple delays and the direction of arrival (DoA) estimation would not be possible. On the other hand, with BF, the high directional beam radiated by antenna array can be steered towards certain directions, forming dedicated transmission and reception at both sides. Not only can the high path loss and the interference coming from inter-cell and intra-cell be minimized, but also the ToAs from different paths become distinguishable. Thus, the DoA can be also estimated. As a consequence, with the ToA and DoA estimates, positioning can be carried out with a lower number of ANs compared to what is required by the RSS-based or ToA-based positioning system.

If also the robot is equipped with a BF capable multi-antenna system, the DoA and the Direction of Departure (DoD) can be estimated, facilitating the estimation of the robot's orientation with respect to the AN. By taking advantage of the sparsity of mmWave propagation channel, compressive sensing theory [4] can be used to efficiently estimate DoD and/or DoA which in turn contribute considerably to the positioning accuracy. Articles regarding BF based positioning application can be found in [9]–[12].

III. Positioning-related requirements and challenges in industrial applications

Table I summarizes the needed positioning-related features in various IIoT applications, according to the authors' view. Sub-m positioning accuracy is expected for the robot to be able to operate safely and reliably. A higher latency in positioning estimation is expected to be tolerated at smaller robot speeds.

The challenges related to positioning in industrial environments include:

- Device heterogeneity: many sensors and robot types available, some supporting only Received Signal Strength (RSS) measurements and some other supporting also ToA or DoA measurements.
- NLoS and multipath propagation: such situations introduce positioning errors in ToA and DoA estimates; solutions are, for example, to combine ToA/DoA information with other available information (e.g., visual reality, building maps, etc.).
- Synchronization issues: ToA-based positioning estimators typically rely on the assumption that the ANs are synchronized. Such synchronization is not always easy to achieve, especially with heterogeneous devices.
- Bandwidth and carrier frequency: the higher the available bandwidth, the more accurate positioning solutions can be found. For carrier frequencies above 30 GHz, currently more than 500 MHz contiguous bandwidths are available, while for carriers around 1–5 GHz, the available bandwidths are typically below 100 MHz. This points towards the advantage of employing mmWave signals for accurate positioning. On the other hand, the path losses are much higher at mmWave than at cmWave, which means that accurate positioning solutions are likely to be achieved only with a high AN density.

TABLE I
Positioning and navigation target requirements in industrial applications

Application	Indoor accuracy (cm)	Outdoor accuracy (cm)	Obstacle detection	Availability (%)	Latency (ms)
Indoor robot control	< 10	–	Yes	100	< 50
Outdoor robot control	–	< 30	Yes	100	< 10
Indoor item tracking	< 50	–	Yes	99	< 200
Outdoor item tracking	–	< 100	Yes	99	< 100
Remote control with AR	< 10	< 10	Yes	100	< 1

IV. Analytical modelling for indoor positioning

In this section, we introduce our indoor multi-floor multi-wall simulator that is based on a real building map with three floors. Two types of measurements are generated based on reasonable parameters and the geometry of the map, followed by a brief summary of the positioning method.

A. RSS-based positioning

The first positioning method is a RSS-based non-linear least square (NLS) estimator. The RSS $P_{a,i}$ from the a-th AN to the i-th robot is modelled according to a frequency-dependent multi-wall multi-floor model as follows,

$$P_{a,i} = \begin{cases} P_{T_a} - 20\log_{10}(f_{\text{c[Hz]}}) \\ \quad - 20\log_{10}(d_{a,i}) \\ \quad - 20\log_{10}\left(\frac{4\pi}{c}\right) + \eta_{\text{LOS}} \qquad \text{if LOS} \\ P_{T_a} - 20\log_{10}(f_{\text{c[Hz]}}) \\ \quad - 20\log_{10}(d_{a,i}) \\ \quad - N_{iw_{a,i}} L_{iw} - N_{f_{a,i}} L_f \\ \quad - 20\log_{10}\left(\frac{4\pi}{c}\right) + \eta_{\text{NLOS}} \quad \text{if NLOS} \end{cases} \tag{1}$$

where P_{T_a} is the "apparent" transmit power of the a-th AN, (i.e., 'apparent' means here that we take into account all the cable losses and antenna gains at both ends), $f_{\text{c[Hz]}}$ is the considered carrier frequency, $L_{iw} = 10$ dB and $L_f = 20$ dB are the losses due to wall and floor attenuation (assumed constant within the building), $d_{a,i}$, $N_{iw_{a,i}}$ and $N_{f_{a,i}}$ are the distance, the number of walls and the number of floors between the a-th AN and the i-th robot, respectively. The speed of light is denoted by c, and η_{LOS} and η_{NLOS} express the shadowing for LoS and NLoS cases. The shadowing was modelled as a Gaussian-distributed variable with zero mean and standard deviation 2 dB for LoS cases and 6 dB for NLoS cases. The LoS cases were identified based on the building map, shown in Fig. 1: if there was no floor and no wall between the AN and robot, then we were in a LoS situation; if there was at least one floor or one wall on the AN–robot path, then we were in a NLoS situation. A receiver sensitivity of -110 dBm was assumed, meaning that signals received below this value are not heard, therefore, measurement from that specific AN will be discarded. We remark that our proposed model in eq. (1) is also similar to the indoor 3GPP channel models proposed for mmWave propagation [13].

B. ToA-based positioning

Here we assume perfectly synchronized ANs and robots and that the channel between ANs and robots is LoS-dominant (i.e., any multipath can be distinguished). Then, the ToA measurements from any arbitrary AN to any given robot (indices a, i have been dropped here for clarity) is modelled as

$$\tau_{\text{obs}} = \tau_{\text{true}} + b + v, \tag{2}$$

where $\tau_{\text{true}} = \|\mathbf{p}_{\text{r}} - \mathbf{p}_{\text{AN}}\|/c$, $\mathbf{p}_{\text{r}}$ and $\mathbf{p}_{\text{AN}}$ are the position vector of the robot and AN and v is a normally distributed random variable, $v \sim \mathcal{N}\left(0, \sigma^2_{\text{ToA}}\right)$. The term b reflects the NLoS bias (see fig. 2), which is related with the thickness of the obstacle, γ, as well as the relative permittivity, ε_r, [15]

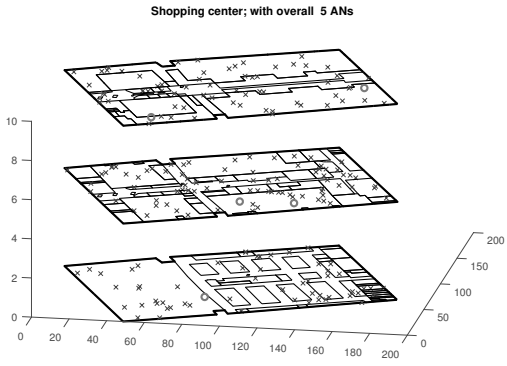

Fig. 1. The building map used in the simulator. Red circles show examples of AN location and blue crosses show examples of robot locations

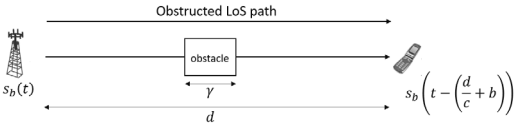

Fig. 2. LoS path blocked by an obstacle

$$b = (\sqrt{\varepsilon_r} - 1)\,\gamma/c. \tag{3}$$

If the signal passes through N_{iw} walls and N_f floors to reach the robot, the whole bias is expressed as

$$b = \sum_{k=1}^{N_{iw}} \left(\sqrt{\varepsilon_{r,k}^{(w)}} - 1\right)\gamma_k/c + \sum_{j=1}^{N_f} \left(\sqrt{\varepsilon_{r,j}^{(f)}} - 1\right)\xi_j/c, \tag{4}$$

where $\varepsilon_{r,k}^{(w)}$ is the relative permittivity of the walls, γ refers to the thickness of the walls, $\varepsilon_{r,j}^{(f)}$ is the relative permittivity of the floors, and ξ refers to the thickness of the floors. The table of relative permittivity of typical construction materials can be found, for example, in [15], [16]. In our case study, the walls are assumed to be made of dry walls and the floors ceilings of solid concrete. It's worth pointing out that different choices of the materials lead to larger or smaller bias b, which affects the final positioning accuracy.

The last term in eq. (2) refers to the uncertainty of the ToA measurement which is caused by the noise v. To model the variance of the ToA, σ^2_{ToA}, we start with a typical multi-tap channel impulse response of a wireless channel, given as

$$h\,(t) = \sum_{i=0}^{L-1} \alpha_i \delta\,(t - \tau_i)\,. \tag{5}$$

Let the transmit passband signal be $s(t) = \text{Re}\left\{s_b(t)e^{j2\pi f_c t}\right\}$, where $s_b(t)$ refers to the baseband signal, the received passband signal $y(t)$ can be expressed as

$$y(t) = \text{Re}\left\{\sum_{i=0}^{L-1} \alpha_i s_b(t-\tau_i) e^{j2\pi f_c (t-\tau_i)}\right\}. \tag{6}$$

The baseband receive signal $y_b(t)$ is therefore [17]

$$y_b(t) = \text{Re}\left\{\sum_{i=0}^{L-1} \alpha_i s_b(t-\tau_i) e^{-j2\pi f_c \tau_i}\right\}. \tag{7}$$

All L taps are resolvable if we have a wide enough bandwidth available; and with known pilot signal and appropriate match filter, the attenuation factors $\alpha_i, i = 1, \ldots, L$ are omitted; therefore, ToA of each path is enveloped in the phase of the channel phasor $e^{-j2\pi f_c \tau_i}$ that is corrupted by AWGN only. The phase noise added on the channel phasor is modelled as a zero mean Gaussian random variable with variance [18]

$$\sigma_\theta^2 = \left[\frac{1}{2SNR}\left(1 + \frac{1}{2SNR}\right)\right] / (2\pi)^2\,. \tag{8}$$

Hence, the noise statistics of the ToA, σ^2_{ToA}, is obtained by dividing eq. (8) by f_c^2, yielding

$$\sigma^2_{\text{ToA}} = \left[\frac{1}{2SNR}\left(1 + \frac{1}{2SNR}\right)\right] / (2\pi f_c)^2 \approx \frac{1}{8\pi^2 f_c^2 SNR}. \tag{9}$$

It's worth pointing out that the approximation in eq. (9) is equal to the CRB (Cramér-Rao Bound) of the variance of ToA estimate [19] if the product BT_s is close to 1. The signal bandwidth is denoted by B and T_s is the signal duration.

The SNR (in log-scale) in eq. (9) was computed as

$$SNR = P_{a,i} - N_0, \tag{10}$$

with $P_{a,i}$ given in eq. (1). The thermal noise power spectral density N_0 is given by $N_0 = -174 + 10\log_{10}(B) + NF$, and NF the receiver noise figure. We assumed that the available bandwidth B was equal at all carrier frequencies for a fair comparison, i.e., $B = 100$ MHz.

C. Positioning method

The positioning method applied here is based on NLS method [14]

$$\hat{\mathbf{p}} = \arg\min_{\mathbf{p}} \|\mathbf{m} - h\,(\mathbf{p})\,\|_2^2, \tag{11}$$

where $\mathbf{m}$ represents the measurements (RSS from eq. (1) or ToA from (2)) received by robots from a set of heard ANs and $\mathbf{p} = [x, y, z]$ is the robot position. The function $h(\cdot)$ refers to the deterministic part (including the corresponding bias) in eq. (1) for RSS measurements and eq. (2) for ToA measurements. Initial values for the NLS algorithm are computed with the centroid localization method [10], i.e. the initial position estimate of each robot is the centroid of all the heard ANs.

V. Simulation results

Fig. 3 shows the average number of LoS connections in function of the total number of ANs in the building, distributed uniformly on each floor of the considered three-floor building. We used 1000 uniformly distributed random robot placements

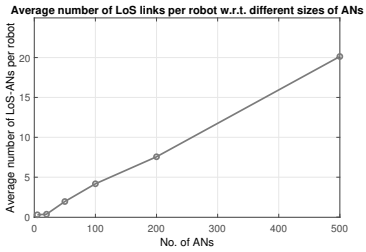

Fig. 3. Average number of LoS connections with different number of ANs

to compute this statistic. A LoS situation was counted when there were no walls and no floors between an AN and a robot. Clearly, if only 5 ANs are available in the whole building (three floors, with a floor surface equal to $183 \times 163 = 29.8 \cdot 10^3\,\mathrm{m}^2$), there are rather few LoS connections. However, if we have 50 or more ANs distributed uniformly in the building, we notice an average of around 2 LoS connections or more for each robot, which is the typical assumption of SCNs.

Fig. 4 shows the RMSE of the RSS-based and the ToA-based positioning methods at different carrier frequencies in cmWave and mmWave spectra and for three AN densities; namely i) when 5 ANs are available in the whole building (i.e., density about 55 ANs per km^2), ii) when 100 ANs are available in the whole building (i.e., density about 1113 ANs per km^2), and iii) when 500 ANs are available in the whole building (i.e., density about 5567 ANs per km^2). RSS-based estimates are rather independent of the carrier frequency and they do not achieve sub-meter accuracy, even with a very high density of ANs. On the other hand, the ToA-based estimators are becoming more accurate, both with an increased carrier frequency (explained by a lower variance in ToA estimates due to a higher root

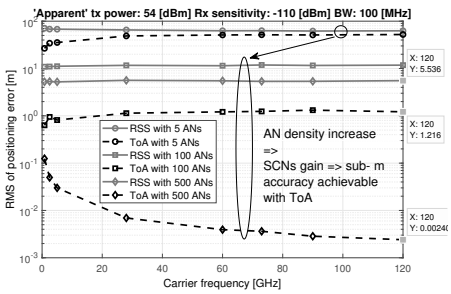

Fig. 4. RSS-based and ToA-based positioning accuracy under different AN densities

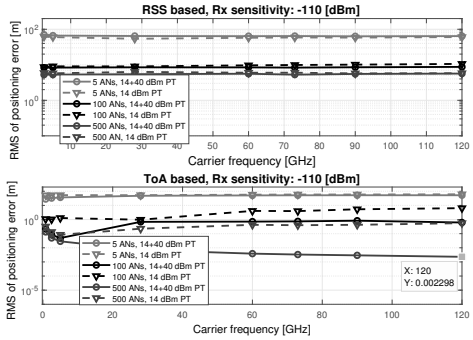

Fig. 5. RSS-based and ToA-based positioning accuracy under different AN densities and different array gains

mean square bandwidth at high carrier frequencies) and with an increased AN density. Nevertheless, in order to achieve a sub-meter accuracy needed for industrial applications, a very high AN density is required. In our case study about 500 ANs are required to yield sub-meter accuracy.

Fig. 5 shows the RMS of the positioning error versus the carrier frequency at two different apparent transmit powers, with RSS-based estimator and ToA-based estimator, respectively. In our study, there were 40 dB difference of apparent Tx power indicating an antenna array gain (i.e., MIMO gain). The obtained result reveals that even under a 40 dB MIMO gain, the accuracy of RSS-based estimates remains unchanged on average; whereas, the ToA-based estimator's accuracy improves, especially in dense network scenarios (i.e., higher than 100 ANs over 3 floors). A positioning accuracy of 2.3 mm, at 120 GHz, proves the benefits of 5G positioning, brought by the rich spectrum, MIMO, and SCNs. As seen in the bottom plot of Fig. 5, with the exception of the case with a very low number of ANs (i.e., 5), the ToA performance is highly improved with an increased antenna gain. We also remark that a similar positioning accuracy is achieved by either applying a high apparent Tx power (e.g., 54 dBm, i.e., high MIMO gain) and a moderate number of ANs (e.g., 100), or by applying a low apparent Tx power (e.g., 14 dBm) but increasing the number of ANs (e.g., 500). The tradeoff between the Tx power and AN density is an interesting future research direction, in order to estimate the overall costs of the network.

Finally, Fig. 6 presents the positioning performance of both RSS-based and ToA-based estimators as a function of the number of ANs deployed in the building. An apparent Tx power of 54 dBm was used (i.e., MIMO gain of 40 dB was included). Fig. 6 shows that, with increasing number of ANs, the error of the RSS-based estimator decreases only slightly, while the error of ToA-based estimator decreases significantly. An error threshold of 50 cm is plotted, in accordance with Table I. We see that in our case study we would need about 200 ANs to achieve 50 cm accuracy at mmWave and 100 ANs

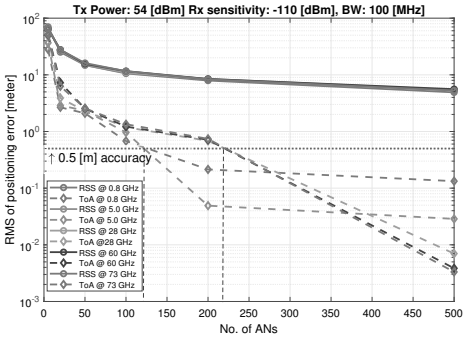

Fig. 6. RSS-based and ToA-based positioning accuracy as a function of the number of ANs

TABLE II
OPPORTUNITIES AND CHALLENGES OF 5G FOR WIRELESS POSITIONING IN INDUSTRIAL APPLICATIONS

5G feature	**Opportunity**	**Challenge**
mmWave	Accurate ToA estimation node synchronization	Link reliability and coverage
SCN	High LoS probability	Deployment cost
Massive MIMO	High SINR, i.e., less ToA uncertainty	Algorithm complexity
Beamforming	Accurate DoA/DoD estimation	Beam alignment cost

to achieve a similar accuracy at cmWave (assuming similar antenna gains, bandwidth and transmit powers). This is due to a higher path loss at higher carrier frequencies. Nevertheless, when SCNs and massive MIMO are exploited, positioning in mmWave spectrum promises higher accuracy than in cmWaves spectrum.

VI. CONCLUSION

In this paper we analyzed the opportunities and challenges for IIoT applications from different specific perspectives of 5G positioning and we presented a case study for 5G positioning of robots placed indoor in a multi-wall multi-floor building. A summary of this analysis is given in table II.

Our case study for indoor robot positioning showed that with SCNs (i.e., high AN density) and MIMO gain, a ToA-based estimator is able to achieve the sub-meter positioning accuracy needed for IIoT; additionally, an accuracy tradeoff between the apparent Tx power and the AN density was pointed out. Several technical challenges remain to be tackled, such as the AN–robot synchronization, attitude determination of robots, connectivity limitation, deployment costs of high density ANs. Future research will focus on ToA/DoA modelling and hybridization approaches for more accurate positioning with a moderate AN density.

ACKNOWLEDGEMENT

The authors express their warm thanks to the Academy of Finland (project 313039) for its financial support for this research work.

REFERENCES

[1] Z. Pi and F. Khan, An introduction to millimeter wave mile broadband system, in *IEEE Communications Magazine*, Vol. 49, no.6, pp. 101–107, June 2011.

[2] M. Marcus and B. Pattan, "Millimeter wave propagation; spectrum management implications," in *IEEE Microwave Magazine*, vol. 6, no. 2, pp. 54–62, June 2005.

[3] Klaus Witrisal, Stefan Hinteregger, Josef Kulmer, Erik Leitinger, Paul Meissner, "High-accuracy positioning for indoor applications: RFID UWB 5G and beyond", RFID (RFID) *2016 IEEE International Conference on*, pp. 1–7, 2016.

[4] J. Talvitie, M. Valkama, G. Destino, Henk Wymeersch, "Novel Algorithms for High-Accuracy Joint Position and Orientation Estimation in 5G mmWave Systems", in Proc. *IEEE Global Communications Conference, WI-UAV Workshop*, Dec. 2017.

[5] T. Narytnik, "The ways of creation and use of telecommunication systems in the terahertz band transport distribution 5G mobile networks", *2016 Third International Scientific-Practical Conf. Problems of Infocomm. Science and Technology (PIC ST)*, Kharkiv, pp. 36–39, 2016.

[6] M. Bennis, M. Simsek, A. Czylwik, W. Saad, S. Valentin and M. Debbah, "When cellular meets WiFi in wireless small cell networks," in *IEEE Comm. Magazine*, vol. 51, no. 6, pp. 44–50, Jun 2013.

[7] F. Rusek et al., "Scaling Up MIMO: Opportunities and Challenges with Very Large Arrays," in *IEEE Signal Processing Magazine*, vol. 30, no. 1, pp. 40–60, Jan. 2013.

[8] E. G. Larsson, O. Edfors, F. Tufvesson and T. L. Marzetta, "Massive MIMO for next generation wireless systems," in *IEEE Communications Magazine*, vol. 52, no. 2, pp. 186–195, February 2014.

[9] P. Kela et al., "Location Based Beamforming in 5G Ultra-Dense Networks," *2016 IEEE 84th Vehicular Technology Conference (VTC-Fall)*, Montreal, QC, 2016, pp. 1–7.

[10] M. Koivisto, A. Hakkarainen, M. Costa, P. Kela, K. Leppanen and M. Valkama, "High-Efficiency Device Positioning and Location-Aware Communications in Dense 5G Networks," in *IEEE Communications Magazine*, vol. 55, no. 8, pp. 188–195, 2017.

[11] G. Destino and H. Wymeersch, "On the trade-off between positioning and data rate for mmWave communication," *2017 IEEE International Conference on Communications Workshops (ICC Workshops)*, Paris, 2017, pp. 797–802.

[12] M. W. Khan, N. Salman and A. H. Kemp, "Cooperative positioning using angle of arrival and time of arrival," *2014 Sensor Signal Processing for Defence (SSPD)*, Edinburgh, 2014, pp. 1–5.

[13] 3rd Generation Partnership Project (3GPP), "Technical Specification Group Radio Access Network - Study on channel model for frequency spectrum above 6 GHz", 3GPP TR 38.900 V14.3.1 (Release 14), Jul 2017.

[14] Dennis, J. E. Jr. Nonlinear Least-Squares. State of the Art in Numerical Analysis, ed. D. Jacobs, Academic Press, pp. 269–312.

[15] C. Thajudeen, A. Hoorfar, F. Ahmad, and T. Dogaru, "Measured complex permittivity of walls with different hydration levels and the effect on power estimation of twri target returns," *Progress In Electromagnetics Research B*, Vol. 30, 177–199, 2011.

[16] J. Lu, D. Steinbach, P. Cabrol, P. Pietraski and R. V. Pragada, "Propagation characterization of an office building in the 60 GHz band," *The 8th European Conference on Antennas and Propagation (EuCAP 2014)*, The Hague, 2014, pp. 809–813.

[17] D. Tse, P. Viswanath, Fundamentals of Wireless Communications., Cambridge Univ. Press, 2005.

[18] Y. Lu, G. Seco-Granados, J.A. Lopez-Salcedo, "Kalman filter-based tracking for GNSS space receivers at high orbits", *Proc. 6th International Colloquium on Scientific and fundamental aspects of GNSS/Galileo*, Oct 2017.

[19] N. Patwari, J. N. Ash, S. Kyperountas, A. O. Hero, R. L. Moses and N. S. Correal, "Locating the nodes: cooperative localization in wireless sensor networks," in *IEEE Signal Processing Magazine*, vol. 22, no. 4, pp. 54–69, July 2005.

PUBLICATION

II

EKF-based and Geometry-based Positioning under Location Uncertainty of Access Nodes in Indoor Environment

Y. Lu, M. Koivisto, J. Talvitie, M. Valkama and E. S. Lohan

*2019 International Conference on Indoor Positioning and Indoor Navigation (IPIN)*2019, 1–7
DOI: 10.1109/IPIN.2019.8911785

EKF-based and Geometry-based Positioning under Location Uncertainty of Access Nodes in Indoor Environment

Yi Lu, Mike Koivisto, Jukka Talvitie, Mikko Valkama, and Elena Simona Lohan
Electrical Engineering, *Tampere University*, *Tampere, Finland*
{yi.lu, mike.koivisto, jukka.talvitie, mikko.valkama, elena-simona.lohan}@tuni.fi

***Abstract*—High accuracy positioning enabled by 5G cellular networks will play a crucial role in the robot-based industrial applications, where the vertical accuracy will be as significant as the 3D accuracy. Aiming at target applications relying on flying robots in industrial environments, this paper presents and formulates two positioning algorithms when the location uncertainty of the access nodes (ANs) is taken into consideration. The first algorithm is a low-complexity geometry-based 3D positioning algorithm that utilizes both time-of-arrival and angle-of-arrival measurements. The second algorithm relies on extended Kalman Filter (EKF)-based positioning, by mapping the ANs' location uncertainty into the measurement noise statistics. The performance of the two proposed method is studied in terms of 3D and vertical positioning accuracy, sensitivity to location uncertainty of the ANs, and computational complexity in indoor scenarios. Based on the conducted complexity analysis, the proposed geometry-based algorithm is computationally more efficient than the EKF-based algorithm. In addition, the proposed geometry-based positioning method demonstrates a higher robustness against a high location uncertainty of ANs than the considered EKF-based method.**

***Index Terms*—robot tracking, 5G networks, indoor positioning, non-linear mapping, location uncertainty of access nodes**

I. Introduction

Several applications of the future Industrial Internet of Things (IIoT) systems empowered by 5G networks are likely to require a flying robot to perform various tasks, such as air quality monitoring, between-floor transportation of goods, worker safety control, problem diagnosis or remote maintenance for high-elevation spaces, which are difficult to access manually. The 3D positioning plays an important role in the use cases where the flying robots must be localized and tracked continuously and reliably, both in the horizontal plane and in the vertical plane [1]. Accurate methods for robot positioning typically rely on location-dependent radio measurements, such as the received signal strength, delay and/or angle measurements coming from access nodes (ANs) with precisely known locations [2]–[7]. However, in the case of mobile or wheel-mounted ANs or industrial environments with assets regularly displaced or moved around, the knowledge of the locations of the ANs might not be precise. In other words, depending on device-centric positioning or network-centric positioning, the location-dependent radio measurements are thought to be transmitted from or received at a location that is not the actual location of the ANs. A classical solution to the problem is to perform the joint estimation of locations of both ANs and robot using Bayesian filters, e.g., the extended Kalman filter (EKF). However, an extremely large state vector due to the joint estimation leads to an increased computational complexity that may be unfeasible for the industrial robots with a limited battery life.

In this work, we study two types of positioning algorithms in order to deal with the location uncertainty of the ANs without increasing the computational complexity. Firstly, we extend the 2D positioning method from [8] into a 3D geometry-based positioning method, named as the weighted centroid geometric (WCG). In the WCG, the location of a robot is estimated by fusing both the time of arrival (ToA) and the angle of arrival (AoA) measurements into the robot positioning algorithms. Secondly, instead of incorporating the location of both the robot and the ANs into the state vector of an EKF algorithm, we derive and formulate the EKF-based positioning algorithm with the location uncertainty of the ANs being mapped to the measurement noise statistics. Besides the 3D positioning accuracy, the vertical accuracy is also employed as a performance metric [7], as the vertical accuracy can be particularly crucial in certain applications that relies on robot-positioning in an indoor environment.

The remaining of this paper is organized as follows. First, the system model is described in Section II where the utilized path-loss model, observation models of the considered measurements as well as the location uncertainty model of the ANs are given separately. Both the geometry-based and the EKF-based positioning algorithms are described and formulated in Section III and IV, respectively. In Section V, the test scenario as well as the simulation-based results are present and examined. The conclusion and future works are summarized in the end.

II. System model

We consider a single-input-multiple-outputs (SIMO) positioning system for robot-based industrial applications where a flying robot transmits uplink (UL) pilot signals to the network edge (ANs) where the location-dependent measurements are acquired. In particular, the transmitted data is assumed to employ the form of an orthogonal frequency division multiplex (OFDM) signal sent periodically from the robot equipped with an omnidirectional antenna, while moving along a pre-designed trajectory. We also assume that the ANs are equipped with uniform rectangular antenna (URA) arrays and support

3D beamforming technique. The network edge estimates and collects ToA and AoA measurements and uploads them to a central unit, where the robot's location is then estimated. In this work, positioning is carried out at the network side in order to keep the computational burden on the robot to a minimum.

A. Path loss model and beamforming gains

The robot's location is denoted as $\mathbf{P}[i] = [x[i], y[i], z[i]]^T$ at the ith time-instant along the trajectory. Furthermore, we assume that there are $M[i]$ line-of-sight (LoS)-ANs at the considered time instant (for the sake of clarity we omit the time index of M for the rest of this paper). Based on the location geometry, the received signal strength (RSS) $P_{R,m}[i]$ in dBm at the ith time-instant from the robot to the mth LoS-AN located at $\mathbf{P}_{\text{AN},m} = [x_m, y_m, z_m]^T$ is written as

$$P_{R,m}[i] = P_T - \text{PL}\left(d_m[i]\right) + S\left(\mathbf{P}[i]\right) + G_T + G_R, \quad (1)$$

where P_T is the transmitted UL signal power in dBm, $\text{PL}\left(d_m[i]\right)$ in dB is the path-loss as a function of the Euclidean distance between the robot and the mth LoS-AN, denoted as $d_m[i] = \|\mathbf{P}[i] - \mathbf{P}_{\text{AN},m}\|$. Meanwhile, $S\left(\mathbf{P}[i]\right)$ represents the shadowing that depends on the robot's location. In this paper, we adopted the 3GPP indoor hotspot (InH) path-loss model with LoS path and a Gaussian distributed shadow fading [9]. Moreover, the beamforming gains at the transmitter and receiver are denoted as G_T and G_R, respectively where G_T is normalized to 0 dBi since the robot is equipped with an omnidirectional antenna, whereas G_R depends on the AoA since beamforming technique is enabled at all ANs. In this work, we assume that the G_R is obtained by an exhaustive 3D beam-training strategy in order to ensure that the UL pilot signals are received within the half-power beamwidth of the antenna at each LoS-AN. Note that the RSS values in (1) are not utilized for positioning as such, but rather applied to quantify the accuracy of both ToA and AoA measurements.

B. Observation model of location-dependent parameters

1) ToA measurements and clock offset model: The ToA observation model reflecting the distances between the LoS-ANs and the robot is expressed as

$$\hat{\boldsymbol{\tau}}[i] = \boldsymbol{b}[i] + \boldsymbol{f}_\tau\left(\mathbf{P}[i]\right) + \boldsymbol{n}_\tau[i], \quad (2)$$

where $\boldsymbol{b}[i] \in \mathbb{R}^{M\times 1}$ refers to the clock offset vector. Here, we model the clock offset as a Gaussian random process [10] that meets the synchronization requirement of 5G network, that is, $\boldsymbol{b}[i] \sim \mathcal{N}\left(\mathbf{0}_M, \boldsymbol{R}_{\text{clk}}\right)$ where $\boldsymbol{R}_{\text{clk}} = \sigma^2_{\text{clk}}\mathbf{I}_{M\times M}$ in which $\mathbf{0}_M$ and $\mathbf{I}_{M\times M}$ are vector containing M zeros and $M\times M$ identity matrix, respectively, and σ_{clk} is set to 10 ns [11]. The ToA observation function $\boldsymbol{f}_\tau\left(\mathbf{P}[i]\right)$ is then expressed as

$$\begin{aligned}\boldsymbol{f}_\tau\left(\mathbf{P}[i]\right) &= [\tau_1[i], \cdots, \tau_M[i]]^T \\ &= \left[\|\mathbf{P}[i] - \mathbf{P}_{\text{AN},1}\|, \cdots, \|\mathbf{P}[i] - \mathbf{P}_{\text{AN},M}\|\right]^T / c,\end{aligned} \quad (3)$$

where c is the speed of light. Furthermore, the variable $\boldsymbol{n}_\tau$ represents an additive Gaussian noise vector with zero-mean under the LoS scenario and non-zero mean under the non-ideal propagation conditions, such as non-line-of-sight (NLoS) propagation. Since the LoS scenario is typical in the future 5G ultra dense networks [12], the noise vector $\boldsymbol{n}_\tau[i]$ is modelled as a zero-mean Gaussian variable, that is, $\mathcal{N}\left(\mathbf{0}_M, \boldsymbol{R}_\tau[i]\right)$ with a diagonal noise covariance matrix $\boldsymbol{R}_\tau[i] = \text{diag}\left(\sigma^2_{\tau,1}, \cdots, \sigma^2_{\tau,M}\right)$. The noise variance of the mth ToA measurement, $\sigma^2_{\tau,m}$ (the time index omitted), is bounded by the following Cramér-Rao lower bound (CRLB) for OFDM signals [5, Ch.3]

$$\sigma^2_{\tau,m} \geq \frac{3P_n}{8\pi^2 f^2_{\text{sc}} P_{r,m}[i] M_u(M_u+1)(2M_u+1)}, \quad (4)$$

where f_{sc} represents the sub-carrier spacing, and $M_u = \frac{N_u-1}{2}$, N_u is the overall number of sub-carriers. Furthermore, $P_{r,m}[i]$ is the linear scale of RSS at the ith time instant of the mth AN calculated from (1) and P_n is the noise power over the entire bandwidth. It is worth noting that (4) applies only for OFDM with *uniformly distributed* energy among all the sub-carriers.

2) AoA measurements: The AoA measurements can also be utilized to estimate the direction of the robot's location based on the LoS propagation between every AN-robot pair [5]. In the considered 3D scenario, AoA observations consists of the elevation AoA as well as the azimuth AoA. Taking the URA's orientation into account, the AoA observation is expressed as

$$\hat{\boldsymbol{\phi}}[i] = \boldsymbol{f}_\phi\left(\mathbf{P}[i]\right) + \boldsymbol{\alpha} + \boldsymbol{n}_\phi[i], \quad (5)$$

where $\hat{\boldsymbol{\phi}}[i] \in \mathbb{R}^{2M\times 1}$ consists of the elevation AoA measurements $\hat{\boldsymbol{\varphi}}[i] \in \mathbb{R}^{M\times 1}$ as well as the azimuth AoA measurements $\hat{\boldsymbol{\theta}}[i] \in \mathbb{R}^{M\times 1}$. Furthermore, we denote the known angular offset due to the specific array orientations as $\boldsymbol{\alpha} \in \mathbb{R}^{2M\times 1}$, where $\boldsymbol{\alpha}$ contains the angular offsets along both elevation domain and azimuth domain denoted as $\boldsymbol{\alpha}_\varphi \in \mathbb{R}^{M\times 1}$ and $\boldsymbol{\alpha}_\theta \in \mathbb{R}^{M\times 1}$, respectively. Moreover, the AoA noise vector is also a zero-mean Gaussian process, that is, $\boldsymbol{n}_\phi[i] \sim \mathcal{N}\left(\mathbf{0}_M, \boldsymbol{R}_\phi[i]\right)$ with a noise covariance matrix $\boldsymbol{R}_\phi[i] = \text{diag}\left(\sigma^2_{\varphi,1}, \cdots, \sigma^2_{\varphi,M}, \sigma^2_{\theta,1}, \cdots, \sigma^2_{\theta,M}\right)$ (Same as with $\sigma^2_{\tau,m}$, we drop the time index here). The non-linear AoA observation function $\boldsymbol{f}_\phi(\cdot)$ in (5) consists of the observation function for elevation angle, denoted as $\boldsymbol{f}_\varphi(\cdot)$, and the observation function for azimuth angle, denoted as $\boldsymbol{f}_\theta(\cdot)$. Altogether, the AoA observation function w.r.t. $\mathbf{P}[i]$ is expressed as $\boldsymbol{f}_\phi\left(\mathbf{P}[i]\right) = \left[\boldsymbol{f}^T_\varphi\left(\mathbf{P}[i]\right), \boldsymbol{f}^T_\theta\left(\mathbf{P}[i]\right)\right]^T$, where

$$\boldsymbol{f}_\varphi\left(\mathbf{P}[i]\right) = \begin{bmatrix} \arcsin\left(\Delta z_1[i]/d_1[i]\right) \\ \vdots \\ \arcsin\left(\Delta z_M[i]/d_M[i]\right) \end{bmatrix}, \quad (6)$$

$$\boldsymbol{f}_\theta\left(\mathbf{P}[i]\right) = \begin{bmatrix} \text{atan}_2\left(\Delta y_1[i], \Delta x_1[i]\right) \\ \vdots \\ \text{atan}_2\left(\Delta y_M[i], \Delta x_M[i]\right) \end{bmatrix}, \quad (7)$$

in which $\Delta x_m[i] = x[i] - x_m$, $\Delta y_m[i] = y[i] - y_m$, and $\Delta z_m[i] = z[i] - z_m$ for all $m = 1, \ldots, M$. Additionally, arcsin and atan_2 denote the inverse sine function and four-quadrant inverse tangent function, respectively.

Assuming that the distance between any two adjacent antenna elements is half of the carrier wavelength c/f_c, and taking the azimuth AoA between the mth LoS-AN and the robot, i.e., θ_m as an example, the measurement noise variance of the mth azimuth AoA measurement, $\sigma^2_{\theta,m}$, is bounded by the CRLB that is derived based on [5, Ch.3] as

$$\sigma^2_{\theta,m} \geq \frac{6P_n}{L\left(L^2-1\right)P_{r,m}[i]\left(\pi\cos\theta_m\right)^2}, \tag{8}$$

where L is the number of antenna elements along the azimuth plane and $P_{r,m}[i]$ and P_n are the same variables as in (4). It is noteworthy that the angular CRLB depends on the geometry between the robot and the AN, because (8) reaches to infinity whenever the azimuth AoA approaches $\pm\pi/2$, and it suggests that for $\theta_m \to \pm\pi/2$, the effective aperture of the array grows smaller which results in the diminishing angular resolution of the array.

Additionally, since an $L \times L$ URA is utilized, we assume the angular resolution in both elevation and azimuth direction are the same, and hence, the noise statistics of the elevation AoA measurement, $\sigma^2_{\varphi,m}$, shares the same expression as (8). In (8), the given noise variance is analysed based on dividing the URA model into two separate uniform linear antenna (ULA) arrays including both azimuth and elevation angles. Thus, when appropriately utilizing measurements jointly from all URA antenna elements, the given AoA measurement noise variance can be even further reduced.

C. Location uncertainty of ANs

We denote the error-bearing locations of ANs as $\tilde{\mathbf{P}}_{\text{AN}} \in \mathbb{R}^{3\times M}$ that are known at the central unit whereas the actual ANs' locations are denoted as $\mathbf{P}_{\text{AN}} \in \mathbb{R}^{3\times M}$. Their relationship is expressed as

$$\tilde{\mathbf{P}}_{\text{AN}} = \mathbf{P}_{\text{AN}} + \boldsymbol{e}_{\text{AN}}, \tag{9}$$

where the uncertainty of ANs' locations is denoted as $\boldsymbol{e}_{\text{AN}} = [\boldsymbol{e}_{\text{AN},1}, \cdots, \boldsymbol{e}_{\text{AN},M}]$, in which $\boldsymbol{e}_{\text{AN},m}$ is defined as

$$\boldsymbol{e}_{\text{AN},m} \sim \mathcal{N}\left(\mathbf{0}_3, \text{diag}\left(\sigma^2_{\text{AN}}, \sigma^2_{\text{AN}}, \frac{\sigma^2_{\text{AN}}}{\beta^2}\right)\right). \tag{10}$$

In particular, since the horizontal plane in general occupies a much larger size than that of the vertical plane, we assume that the ANs' locations uncertainty in the z-direction is β times smaller than the uncertainty in x-direction (we use $\beta = 10$ in our simulations), while both x- and y- directions share the same uncertainty σ_{AN}. Note that σ^2_{AN} is not indexed as in this paper we assume that all the ANs suffer from the same level of location uncertainty. In order to obtain the statistics for the ANs' locations, e.g., a training database containing fingerprints can be employed. However, due to several error sources in estimating ANs' locations, the value of σ_{AN} is varied in the simulations to characterize different levels of such uncertainty.

III. Weighted Centroid Geometric Positioning

As the main contribution of this work, we now derive the proposed WCG approach based on the fusion of information from ToA and AoA measurements and the geometry relation between the LoS-AN and the robot as shown in Fig. 1. Throughout this section, *the time index is omitted for the sake of clarity*. With a perfect knowledge on the mth LoS-AN where $m = 1, \ldots, M$ and the corresponding noise-free ToA/AoA measurements, the robot location $\mathbf{P}$ can be acquired as

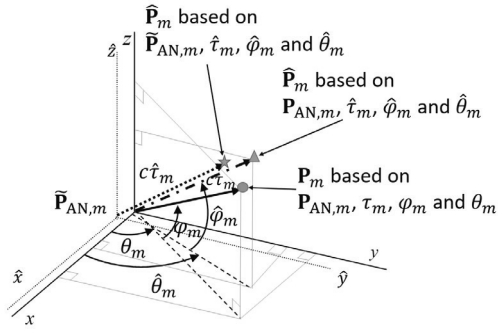

Fig. 1: 3D Geometry between the mth pair of LoS-AN-robot in the presence of measurements and AN location uncertainty.

$$\mathbf{P} = \begin{bmatrix} x \\ y \\ z \end{bmatrix} = \begin{bmatrix} x_m + c\tau_m\cos\varphi_m\cos\theta_m \\ y_m + c\tau_m\cos\varphi_m\sin\theta_m \\ z_m + c\tau_m\sin\varphi_m \end{bmatrix}. \tag{11}$$

However, in practical scenarios, especially in the industrial environments, not only the measurements are corrupted by noise, but also there might be errors in the assumed ANs' locations. By taking into account both measurement noise and the location uncertainty of the ANs, (11) is expressed as

$$\hat{\mathbf{P}}_m = \begin{bmatrix} \hat{x}_m \\ \hat{y}_m \\ \hat{z}_m \end{bmatrix} = \begin{bmatrix} \tilde{x}_m + c\hat{\tau}_m\cos\hat{\varphi}_m\cos\hat{\theta}_m \\ \tilde{y}_m + c\hat{\tau}_m\cos\hat{\varphi}_m\sin\hat{\theta}_m \\ \tilde{z}_m + c\hat{\tau}_m\sin\hat{\varphi}_m \end{bmatrix}, \tag{12}$$

where the location of the mth LoS-AN known to the central unit is denoted as $\tilde{\mathbf{P}}_{\text{AN},m} = [\tilde{x}_m, \tilde{y}_m, \tilde{z}_m]^T$. The (green) star marker in Fig. 1, that is acquired by applying (12), is the position estimate based on imperfect AN location knowledge as well as the noisy measurements between the mth pair of LoS-AN and robot. Therefore, we obtain in total M position estimates from overall M pairs of LoS-ANs and robot, denoted in a matrix form as $\hat{\mathbf{P}} = \left[\hat{\mathbf{P}}_1, \cdots, \hat{\mathbf{P}}_M\right]$. In order to combine the obtained M position estimates into a single robot position estimate, a weight vector is designed by considering the quality of measurements and available clock statistics, such that

$$\begin{aligned} \boldsymbol{w} &= [w_1, \cdots, w_M]^T \\ &= \left[\left(\sigma^2_{\tau,1} + \sigma^2_{\text{clk}}\right)^{-1}, \cdots, \left(\sigma^2_{\tau,M} + \sigma^2_{\text{clk}}\right)^{-1}\right]^T. \end{aligned} \tag{13}$$

Finally, the position estimate obtained by the WCG is the product of the estimate UE location matrix $\hat{\mathbf{P}}$ and the normalized weight vector $\tilde{\boldsymbol{w}}$ such that

$$\hat{\mathbf{P}}_{\text{WCG}} = \hat{\mathbf{P}}\tilde{\boldsymbol{w}}, \tag{14}$$

where $\tilde{\boldsymbol{w}} = \boldsymbol{w}/\sum_{m=1}^{M} w_m$.

IV. Extended Kalman filter based positioning

As a comparison method for the proposed WCG positioning method that only relies on the available measurements at the current state and no prior information is needed, we present a well-known tracking algorithm for robot positioning that is, an EKF. Several works such as [6], [7], [13] have presented the positioning performance achieved by the EKF under 5G mobile networks. Given the available measurements, we consider two EKF-based methods, one utilizes both ToA and AoA measurements, denoted as 'EKF T+A', while the other utilizes only AoA measurements, denoted as 'EKF A'. By considering the location, velocity and acceleration of the robot, the state vector at the ith time instant is given as

$$\mathbf{s}[i] = [x[i], y[i], z[i], v_x[i], v_y[i], v_z[i], a_x[i], a_y[i], a_z[i]]^T, \tag{15}$$

where $x[i], y[i], z[i]$ refers to the location of the robot in x-, y- and z-coordinate, and $v_x[i], v_y[i], v_z[i]$ are the velocity components in terms of x-axis, y-axis and z-axis. Similarly, we have the acceleration components in all three directions, denoted as $a_x[i], a_y[i], a_z[i]$. Furthermore, we assume that the state transition between any two adjacent states follows a linear model and the observation model that connects the state vector with the measurements obeys a non-linear model, which are described in a general form as [14]

$$\begin{aligned} \mathbf{s}[i] &= \mathbf{F}\mathbf{s}[i-1] + \mathbf{v}[i] \\ \mathbf{y}[i] &= \mathbf{h}\left(\mathbf{s}[i]\right) + \mathbf{w}[i], \end{aligned} \tag{16}$$

where $\mathbf{F}$ and $\mathbf{h}$ are the linear state transition matrix and non-linear observation function, respectively, $\mathbf{v}[i] \sim \mathcal{N}(0, \mathbf{Q})$ is the state process noise vector, and $\mathbf{w}[i] \sim \mathcal{N}(0, \mathbf{R})$ refers to as the measurement noise vector. Throughout this paper, we denote $\mathbf{y}[i]$ as the measurement vector that contains the available measurements at the ith time step. Assuming the models in (16) and the statistics of the initial state, the predicted state $\hat{\mathbf{s}}^-[i]$ and state covariance matrix $\hat{\mathbf{\Sigma}}^-[i]$ can be evaluated as

$$\begin{aligned} \hat{\mathbf{s}}^-[i] &= \mathbf{F}\hat{\mathbf{s}}[i-1] \\ \hat{\mathbf{\Sigma}}^-[i] &= \mathbf{F}\hat{\mathbf{\Sigma}}[i-1]\mathbf{F}^T + \mathbf{Q}. \end{aligned} \tag{17}$$

Both a priori mean and covariance estimates in (17) are to be corrected by incorporating the incoming measurements at the specific time instant using the following steps

$$\begin{aligned} \mathbf{K}[i] &= \hat{\mathbf{\Sigma}}^-[i]\mathbf{H}^T[i]\left(\mathbf{H}[i]\hat{\mathbf{\Sigma}}^-[i]\mathbf{H}^T[i] + \mathbf{R}\right)^{-1} \\ \hat{\mathbf{s}}[i] &= \hat{\mathbf{s}}^-[i] + \mathbf{K}[i]\left(\mathbf{y}[i] - \mathbf{h}\left(\hat{\mathbf{s}}^-[i]\right)\right) \\ \hat{\mathbf{\Sigma}}[i] &= \left(\mathbf{I} - \mathbf{K}[i]\mathbf{H}[i]\right)\hat{\mathbf{\Sigma}}^-[i], \end{aligned} \tag{18}$$

where $\hat{\mathbf{s}}[i]$ and $\hat{\mathbf{\Sigma}}[i]$ are the a posteriori estimate of the state vector and state covariance matrix, respectively. In addition, the state-dependent Kalman gain matrix is denoted as $\mathbf{K}[i]$, and $\mathbf{H}[i]$ refers to the Jacobian matrix of the observation function $\mathbf{h}(\cdot)$ evaluated at the predicted state $\hat{\mathbf{s}}^-[i]$.

Since an indoor industrial environment is under consideration, the robot is assumed to move with a constant acceleration which indicates that the acceleration remains almost constant between consecutive states. Hence, the state transition matrix $\mathbf{F}$ and state noise covariance matrix $\mathbf{Q}$ can be described as [6], [15]

$$\begin{aligned} \mathbf{F} &= \begin{bmatrix} \mathbf{I}_{3\times3} & \Delta t\mathbf{I}_{3\times3} & \frac{\Delta t^2}{2}\mathbf{I}_{3\times3} \\ \mathbf{0}_{3\times3} & \mathbf{I}_{3\times3} & \Delta t\mathbf{I}_{3\times3} \\ \mathbf{0}_{3\times3} & \mathbf{0}_{3\times3} & \mathbf{I}_{3\times3} \end{bmatrix} \\ \mathbf{Q} &= \begin{bmatrix} \frac{\Delta t^5\mathbf{I}_{3\times3}}{20} & \frac{\Delta t^4\mathbf{I}_{3\times3}}{8} & \frac{\Delta t^3\mathbf{I}_{3\times3}}{6} \\ \frac{\Delta t^4\mathbf{I}_{3\times3}}{8} & \frac{\Delta t^3\mathbf{I}_{3\times3}}{3} & \frac{\Delta t^2\mathbf{I}_{3\times3}}{2} \\ \frac{\Delta t^3\mathbf{I}_{3\times3}}{6} & \frac{\Delta t^2\mathbf{I}_{3\times3}}{2} & \Delta t\mathbf{I}_{3\times3} \end{bmatrix}\sigma_q^2, \end{aligned} \tag{19}$$

where Δt represents the time-interval between two adjacent states, and σ_q^2 denotes the uncertainty in the acceleration, that is, the variance of the acceleration noise. The 3×3 identity matrix is denoted as $\mathbf{I}_{3\times3}$. In terms of tuning the process noise covariance matrix $\mathbf{Q}$ for both EKFs, σ_q^2 has been adjusted such that a centimeter-level 3D RMSE is achieved when $\sigma_{\text{AN}} = 0$. Thereafter, the same $\mathbf{Q}$ matrix has been applied for $\sigma_{\text{AN}} > 0$.

When both ToA and AoA measurements are considered for positioning, the measurement vector $\mathbf{y}_{\text{T+A}}[i] \in \mathbb{R}^{3M+1}$ is essentially the fusion of (2) and (5) which is written as $\mathbf{y}_{\text{T+A}}[i] = \left[\hat{\boldsymbol{\tau}}^T[i], \hat{\boldsymbol{\phi}}^T[i]\right]^T$. Similarly, the observation function of the EKF T+A can be stacked as $\mathbf{h}_{\text{T+A}}\left(\mathbf{s}^-[i]\right) = \left[\boldsymbol{f}_\tau^T, \boldsymbol{f}_\phi^T\right]^T$. Moreover, the Jacobian matrix of $\mathbf{h}_{\text{T+A}}\left(\mathbf{s}^-[i]\right)$ is denoted as $\mathbf{H}_{\text{T+A}}[i] \in \mathbb{R}^{3M\times9}$ and it is given as $\mathbf{H}_{\text{T+A}}[i] = \left[\mathbf{H}_\tau^T[i], \mathbf{H}_\phi^T[i]\right]^T$, in which $\mathbf{H}_\tau^T[i]$ and $\mathbf{H}_\phi^T[i]$ denote the Jacobian matrix of the ToA measurements and AoA measurements as

$$\mathbf{H}_\tau[i] = \begin{bmatrix} \frac{\Delta\hat{x}_1[i]}{c\hat{d}_1[i]} & \frac{\Delta\hat{y}_1[i]}{c\hat{d}_1[i]} & \frac{\Delta\hat{z}_1[i]}{c\hat{d}_1[i]} & \mathbf{0}_{1\times6} \\ \vdots & \vdots & \vdots & \vdots \\ \frac{\Delta\hat{x}_M[i]}{c\hat{d}_M[i]} & \frac{\Delta\hat{y}_M[i]}{c\hat{d}_M[i]} & \frac{\Delta\hat{z}_M[i]}{c\hat{d}_M[i]} & \mathbf{0}_{1\times6} \end{bmatrix}, \tag{20}$$

$$\mathbf{H}_\phi[i] = \begin{bmatrix} -\frac{\Delta\hat{x}_1[i]\Delta\hat{z}_1[i]}{\hat{d}_1^2[i]\hat{d}_{\text{2D},1}[i]} & -\frac{\Delta\hat{y}_1[i]\Delta\hat{z}_1[i]}{\hat{d}_1^2[i]\hat{d}_{\text{2D},1}[i]} & \frac{\hat{d}_{\text{2D},1}[i]}{\hat{d}_1^2[i]} & \mathbf{0}_{1\times6} \\ \vdots & \vdots & \vdots & \vdots \\ -\frac{\Delta\hat{x}_M[i]\Delta\hat{z}_M[i]}{\hat{d}_M^2[i]\hat{d}_{\text{2D},M}[i]} & -\frac{\Delta\hat{y}_M[i]\Delta\hat{z}_M[i]}{\hat{d}_M^2[i]\hat{d}_{\text{2D,M}}[i]} & \frac{\hat{d}_{\text{2D},M}[i]}{\hat{d}_M^2[i]} & \mathbf{0}_{1\times6} \\ -\frac{\Delta\hat{y}_1[i]}{\hat{d}_{\text{2D},1}[i]} & \frac{\Delta\hat{x}_1[i]}{\hat{d}_{\text{2D},1}[i]} & 0 & \mathbf{0}_{1\times6} \\ \vdots & \vdots & \vdots & \vdots \\ -\frac{\Delta\hat{y}_M[i]}{\hat{d}_{\text{2D},M}[i]} & \frac{\Delta\hat{x}_M[i]}{\hat{d}_{\text{2D},M}[i]} & 0 & \mathbf{0}_{1\times6} \end{bmatrix}, \tag{21}$$

where $\Delta\hat{x}_m[i] = \hat{x}[i] - \tilde{x}_m$, $\Delta\hat{y}_m[i] = \hat{y}[i] - \tilde{y}_m$, $\Delta\hat{z}_m[i] = \hat{z}[i] - \tilde{z}_m$, $\hat{d}_m[i] = \sqrt{\Delta\hat{x}_m^2[i] + \Delta\hat{y}_m^2[i] + \Delta\hat{z}_m^2[i]}$ and the 2D distance between the predicted robot's location and the mth AN is denoted as $\hat{d}_{\text{2D},m}[i] = \sqrt{\Delta\hat{x}_m^2[i] + \Delta\hat{y}_m^2[i]}$, where $m = 1, \ldots, M$.

In general, without the uncertainty of ANs' location, the measurement noise covariance matrix is denoted as $\boldsymbol{R}_{\text{T+A}}[i] = \text{blkdiag}\{\boldsymbol{R}_\tau[i], \boldsymbol{R}_\phi[i]\}$ for EKF T+A, and $\boldsymbol{R}_{\text{A}}[i] = \boldsymbol{R}_\phi[i]$ for EKF A. However, in the considered scenario and application, the error statistics that incurred due to the assumed ANs'

location uncertainty and clock bias have to be incorporated in the observation model and reflected by the measurement noise covariance matrix. That being said, the uncertainty in the location of the ANs must be mapped to the measurement noise statistics. A linearization is therefore implemented for each AN-robot pair in order to perform the nonlinear mapping from multi-dimension AN location error to a single dimension measurement error. Hence, the resulting $\boldsymbol{R}_{\text{T+A}}[i]$ is given as

$$\boldsymbol{R}_{\text{T+A}}[i] = \text{blkdiag}\left\{\boldsymbol{R}_{\tau}[i] + \tilde{\boldsymbol{R}}_{\tau}[i] + \boldsymbol{R}_{\text{clk}}, \boldsymbol{R}_{\phi}[i] + \tilde{\boldsymbol{R}}_{\phi}[i]\right\}, \tag{22}$$

where $\tilde{\boldsymbol{R}}_{\tau}[i] \in \mathbb{R}^{M\times M}$ and $\tilde{\boldsymbol{R}}_{\phi}[i] \in \mathbb{R}^{2M\times 2M}$. The $\tilde{}$-sign is used to represent the extra noise statistics to ToA and AoA measurements caused by the location uncertainty of ANs.

Since all the ANs are assumed to suffer from the same location uncertainty as discussed in II-C, we express $\tilde{\boldsymbol{R}}_{\tau}[i]$ and $\tilde{\boldsymbol{R}}_{\phi}[i]$ as

$$\tilde{\boldsymbol{R}}_{\tau}[i] = \left[\frac{\partial \boldsymbol{f}_{\tau}}{\partial \tilde{\mathbf{P}}_{\text{AN}}}\bigg|_{\hat{\mathbf{s}}^-[i]}\right] \boldsymbol{R}_{\text{AN}} \left[\frac{\partial \boldsymbol{f}_{\tau}}{\partial \tilde{\mathbf{P}}_{\text{AN}}}\bigg|_{\hat{\mathbf{s}}^-[i]}\right]^T \tag{23}$$

$$\tilde{\boldsymbol{R}}_{\phi}[i] = \left[\frac{\partial \boldsymbol{f}_{\phi}}{\partial \tilde{\mathbf{P}}_{\text{AN}}}\bigg|_{\hat{\mathbf{s}}^-[i]}\right] \boldsymbol{R}_{\text{AN}} \left[\frac{\partial \boldsymbol{f}_{\phi}}{\partial \tilde{\mathbf{P}}_{\text{AN}}}\bigg|_{\hat{\mathbf{s}}^-[i]}\right]^T, \tag{24}$$

where $\boldsymbol{R}_{\text{AN}} = \text{diag}\left(\sigma^2_{\text{AN}}, \sigma^2_{\text{AN}}, \frac{\sigma^2_{\text{AN}}}{\beta^2}\right)$ denotes the covariance matrix of ANs' location uncertainty defined in (10). Moreover, the Jacobian matrix w.r.t. the ANs can be obtained by simply taking the opposite sign of the non-zero terms in (20) and (21) yielding

$$\frac{\partial \boldsymbol{f}_{\tau}}{\partial \tilde{\mathbf{P}}_{\text{AN}}}\bigg|_{\hat{\mathbf{s}}^-[i]} = \begin{bmatrix} \frac{-\Delta\hat{x}_1[i]}{c\hat{d}_1[i]} & \frac{-\Delta\hat{y}_1[i]}{c\hat{d}_1[i]} & \frac{-\Delta\hat{z}_1[i]}{c\hat{d}_1[i]} \\ \vdots & \vdots & \vdots \\ \frac{-\Delta\hat{x}_M[i]}{c\hat{d}_M[i]} & \frac{-\Delta\hat{y}_M[i]}{c\hat{d}_M[i]} & \frac{-\Delta\hat{z}_M[i]}{c\hat{d}_M[i]} \end{bmatrix} \tag{25}$$

$$\frac{\partial \boldsymbol{f}_{\phi}}{\partial \tilde{\mathbf{P}}_{\text{AN}}}\bigg|_{\hat{\mathbf{s}}^-[i]} = \begin{bmatrix} \frac{\Delta\hat{x}_1[i]\Delta\hat{z}_1[i]}{\hat{d}^2_1[i]\hat{d}_{\text{2D},1}[i]} & \frac{\Delta\hat{y}_1[i]\Delta\hat{z}_1[i]}{\hat{d}^2_1[i]\hat{d}_{\text{2D},1}[i]} & -\frac{\hat{d}_{\text{2D},1}[i]}{\hat{d}^2_1[i]} \\ \vdots & \vdots & \vdots \\ \frac{\Delta\hat{x}_M[i]\Delta\hat{z}_M[i]}{\hat{d}^2_M[i]\hat{d}_{\text{2D},M}[i]} & \frac{\Delta\hat{y}_M[i]\Delta\hat{z}_M[i]}{\hat{d}^2_M[i]\hat{d}_{\text{2D},M}[i]} & -\frac{\hat{d}_{\text{2D},M}[i]}{\hat{d}^2_M[i]} \\ \frac{\Delta\hat{y}_1[i]}{\hat{d}_{\text{2D},1}[i]} & -\frac{\Delta\hat{x}_1[i]}{\hat{d}_{\text{2D},1}[i]} & 0 \\ \vdots & \vdots & \vdots \\ \frac{\Delta\hat{y}_M[i]}{\hat{d}_{\text{2D},M}[i]} & -\frac{\Delta\hat{x}_M[i]}{\hat{d}_{\text{2D},M}[i]} & 0 \end{bmatrix}, \tag{26}$$

where $\Delta\hat{x}_m[i]$, $\Delta\hat{y}_m[i]$, $\Delta\hat{z}_m[i]$, $\hat{d}_m[i]$ and $\hat{d}_{\text{2D},m}[i]$ for $m = 1,\ldots,M$ refer to the same notations as (21).

V. Test scenario and simulation-based results

A. Scenario deployment

The positioning performance of the studied positioning algorithms (i.e., WCG, EKF A and EKF T+A) is tested with a realistic wall-divided indoor map with a length of 150 m, width of 112 m, and height of 4 m as shown in the left plot of Fig. 2. The overall trajectory is plotted in the blue curve along which the robot is moving at nearly constant velocities, around 1.1 m/s (human walking speed is around 0.6 m/s), and at a linearly varying height between 1 m and 2 m given in the right plot of Fig. 2. In particular, the corners of the trajectory are smoothed in order to reflect a practical trajectory of a moving robot. Moreover, we design the ANs to be installed on the walls at 3m height shown in red circle markers, and the corresponding array orientations of the ANs, i.e., the angular offsets $\boldsymbol{\alpha}$ are assumed to be known. In particular, we set $\boldsymbol{\alpha}_{\varphi} = \mathbf{0}_M$, whereas the values of $\boldsymbol{\alpha}_{\theta}$, i.e., the orientations in the azimuth domain, are initialized so that the arrays are parallel to the corresponding wall. Furthermore, there are at least four LoS-ANs available along the studied trajectory, and the AN density is around 1.24/25m^2. Finally, we summarize the UL pilot signal parameters used in our simulations in Table I. Note that the carrier frequency is chosen at the millimetre wave (mmWave) band at 39 GHz with an approximate of 123 MHz signal bandwidth. In order to enhance the received signal strength at the ANs, the transmit power is set at 27 dBm which can be further reduced in a multi-robot scenario in order to ease the interference level.

TABLE I: Configuration of the UL OFDM pilot signal

Parameter	Value
Carrier frequency f_c	39 GHz
Sub-carrier spacing f_{sc}	120 kHz
No. of sub-carrier N_u	1024
Signal bandwidth B_w	123 MHz
Transmit power P_T	27 dBm
Receive beamforming gain G_R	20 dBi

B. Performance evaluation

The cumulative distribution function of the ToA measurement error as well as the AoA measurement error are shown in Fig. 3 where the values of the horizontal axis are described in meters for ToA measurement error, and in degrees for the AoA measurement error. Based on the results, it can be seen that the ToA errors are generally below $\pm$10m while the AoA errors rarely reaches beyond $\pm 0.5^{\circ}$. The behavior of the ToA measurement errors can be explained based on the ToA observation model (2) where the considered error sources consists of the thermal noise as well as the synchronization error with a 10ns standard deviation that corresponds to 3m error in distance. We point out here that the thermal noise error is dominated by the synchronization error as the former returns a ToA error in the magnitude of 0.1 - 8 cm owing to the wide signal bandwidth B_w. Compared to the ToA measurements, the AoA measurements seem to be more accurate as 95% of the errors for both the elevation and azimuth angle are within $\pm 0.5^{\circ}$. However, the small values in degrees does not necessarily indicate a better positioning accuracy since even a small error in the AoA measurements may lead to significant positioning errors when the distance between the robot and a given AN is large.

Both the 3D and vertical RMSE as a function of the location uncertainty of the ANs σ_{AN} (along the x-direction)

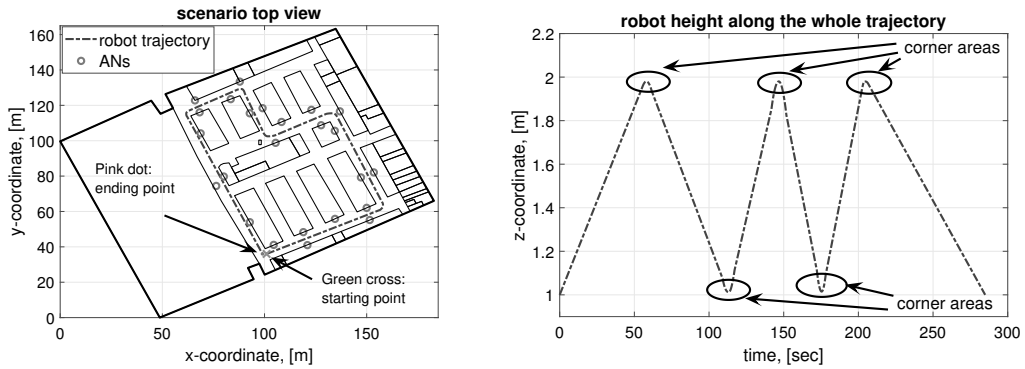

Fig. 2: Left plot: The top view of the deployed indoor scenario, where the walls are illustrated with a black color. The robot starts from the green cross and ends in the pink dot. Blue line represents the robot trajectory and red markers denote the locations of the ANs. Right plot: The robot trajectory in z-coordinate. To reflect a dynamic movement also in the vertical direction, a linear behavior is adopted.

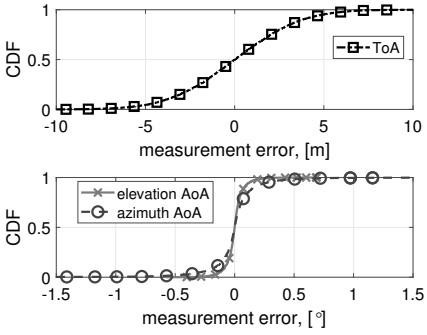

Fig. 3: The cumulative distribution function (CDF) of the ToA measurement error (in meters) and AoA measurement error (in degrees) that were utilized as the inputs of the considered positioning algorithms.

are given in Fig. 4. Note that the results is obtained based on 2000 simulation trials through the whole trajectory. The ANs' locations $\bar{\mathbf{P}}_{\text{AN}}$, known at the central unit are initialized based on (9) in the beginning of each trial. Moreover, the location estimates of both considered EKFs are initialized around the reference location using the standard deviations of 1 m and 0.1 m in horizontal and vertical direction, respectively. Based on the obtained results, the EKF-based approaches outperform the WCG in terms of both 3D and vertical RMSE whenever the uncertainty in ANs' locations remains small enough i.e., $\sigma_{\text{AN}} \leq$ 0.5m, in which case, the EKFs are seen as better positioning solutions. On the other hand, the positioning performance of the EKFs degrades more severely than the WCG when σ_{AN} raises beyond 0.5m although a worse performance is seen to all the algorithms. One possible reason for the vast drop in terms of positioning performance of the EKFs especially at relative high σ_{AN} lies in the un-fulfillment of linearization of the nonlinear observation functions $\boldsymbol{f}_\tau$, $\boldsymbol{f}_\varphi$ and $\boldsymbol{f}_\theta$ w.r.t. the $\hat{\mathbf{s}}^-$ due to the highly un-precise location of the ANs contained in all the nonlinear observation functions. Numerically, the 3D/vertical RMSE of EKF T+A and EKF A raise to about 19m/5.2m and 29m/7.5m respectively whereas that of the WCG are kept roughly at 7m/0.6m at the highest considered uncertainty of ANs' locations, i.e., $\sigma_{\text{AN}} = 5$m. It has been observed that the WCG distinctly demonstrates a better robustness to higher location uncertainty of the ANs than the EKFs under the considered scenario and assumptions.

TABLE II: Computational complexity of positioning algorithms

Algorithm	Computational Complexity
EKFs	$\mathcal{O}(MN_s^2)$+$\mathcal{O}(M^2N_s)$
WCG	$\mathcal{O}(M)$

In addition to the positioning accuracy, we analyze and compare the computational complexity of all the algorithms in terms of the overall number of the involved real multiplications at *a single time instant*. According to [16], there are $21MN_s^2 + 144M^2N_s + 3MN_s$ and $14MN_s^2 + 64M^2N_s + 2MN_s$ real multiplications for EKF T+A and EKF A, respectively where M is denoted as the number of LoS-ANs and N_s refers to the number of entries in the state vector (15). Meanwhile, we computed that there are in total $11M$ real multiplications involved for WCG. Finally, the computational complexity in terms of $\mathcal{O}$ of EKFs and WCG are summarized in Table II.

VI. Conclusions and Future Work

In this paper, we developed and formulated two types of positioning algorithms with the location uncertainty of the ANs being considered and modelled statistically. The first method is a 3D geometry-based positioning approach utilizing both the ToA and AoA measurements. The second one is based on the Bayesian frame work, i.e., the EKF-based approach with the ANs' location uncertainty being mapped into the measurement error statistic. Additionally, the clock errors were

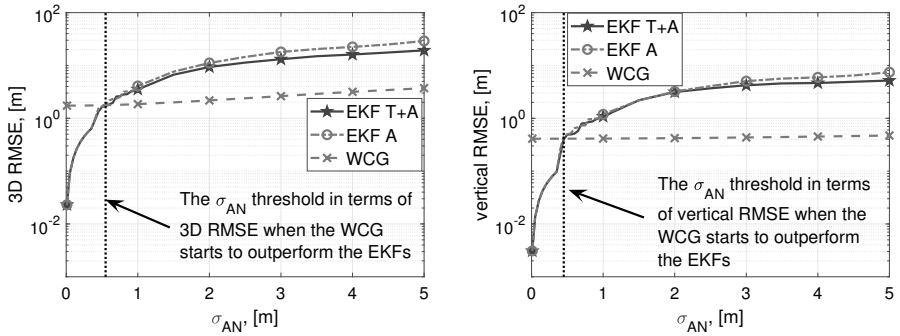

Fig. 4: Left plot: 3D RMSE of different positioning methods as a function of AN uncertainty σ_{AN}. Right plot: Vertical RMSE of different positioning methods as a function of AN uncertainty σ_{AN}.

also taken into consideration. The 3D and vertical RMSE as well as the number of operations needed to implement the considered algorithms (at one time instant) were utilized as the metrics for comparison. The numerical results showed that the utilized EKF-based algorithms remain as a better choice in terms of both 3D and vertical RMSE performances as long as the error contained in the location of ANs was kept at less than 0.5m (i.e., standard deviation along the x-direction). On the other hand, the proposed geometry-based approach, namely the WCG, was capable of maintaining a higher positioning accuracy than EKF-based approaches when exposed to the ANs locations uncertainty larger than 0.5m (standard deviation error), thus yielding a higher robustness. Nevertheless, we point out that the performance threshold (the σ_{AN} where RMSE curves of both EKFs and WCG cross) may vary for a different assumption/scenarios. The main advantage of the proposed WCG approach comes from the huge reduction in the computational complexity compared with considered EKFs, which makes it a very promising candidate for sensor and robot positioning in industrial environments where the ANs are not precisely known or located. Future work will concentrate on the simultaneously estimation of both the robots and ANs locations, as well as on mapping the uncontrolled environment through simultaneous localization and mapping (SLAM) algorithms.

ACKNOWLEDGEMENTS

The authors express their warm thanks to the Academy of Finland (project 313039) for its financial support on this work.

REFERENCES

[1] 3GPP TR 22.872 V16.0.0 Technical Specification Group Services and System Aspects, "Study on positioning use cases (Release 16)," Jun 2018.

[2] J. Yin, Q. Wan, S. Yang, and K. C. Ho, "A simple and accurate tdoa-aoa localization method using two stations," *IEEE Signal Processing Letters*, vol. 23, no. 1, pp. 144–148, Jan 2016.

[3] H. Naseri and V. Koivunen, "A Bayesian algorithm for distributed network localization using distance and direction data," *IEEE Transactions on Wireless Communications*, Aug 2017.

[4] S. Tomic, M. Beko, R. Dinis, and P. Montezuma, "A Closed-Form Solution for RSS/AoA Target Localization by Spherical Coordinates Conversion," *IEEE Wireless Communications Letters*, vol. 5, no. 6, pp. 680–683, Dec 2016.

[5] S. Sand, A. Dammann, and C. Mensing, *Positioning in Wireless Communication Systems, John Wiley & Sons Ltd.*, Jun 2014.

[6] J. Talvitie, T. Levanen, M. Koivisto, K. Pajukoski, M. Renfors, and M. Valkama, "Positioning of high-speed trains using 5G new radio synchronization signals," in *2018 IEEE Wireless Communications and Networking Conference (WCNC)*, April 2018, pp. 1–6.

[7] M. Koivisto, M. Costa, A. Hakkarainen, K. Leppänen, and M. Valkama, "Joint 3D positioning and network synchronization in 5G ultra-dense networks using UKF and EKF," in *2016 IEEE Globecom Workshops (GC Wkshps)*, Dec 2016, pp. 1–7.

[8] M. W. Khan, N. Salman, A. H. Kemp, and L. Mihaylova, "Localisation of sensor nodes with hybrid measurements in wireless sensor networks," *Sensors*, vol. 16, no. 7, 2016. [Online]. Available: http://www.mdpi.com/1424-8220/16/7/1143

[9] 3GPP TR 38.900 V15.0.0 Technical Specification Group Radio Access Network, "Study on channel model for frequency spectrum above 6 GHz (Release 15)," Jun 2018.

[10] L. Moody, "Sensors, measurement fusion and missile trajectory optimisation," PhD thesis, Cranfield University, July 2003.

[11] H. Li, L. Han, R. Duan, and G. M. Garner, "Analysis of the synchronization requirements of 5G and corresponding solutions," *IEEE Communications Standards Magazine*, vol. 1, no. 1, pp. 52–58, March 2017.

[12] J. G. Andrews, S. Buzzi, W. Choi, S. V. Hanly, A. Lozano, A. C. K. Soong, and J. C. Zhang, "What will 5G be?" *IEEE Journal on Selected Areas in Communications*, vol. 32, no. 6, pp. 1065–1082, June 2014.

[13] E. Rastorgueva-Foi, M. Koivisto, M. Valkama, M. Costa, and K. Leppänen, "Localization and tracking in mmwave radio networks using beam-based DoD measurements," in *2018 8th International Conference on Localization and GNSS (ICL-GNSS)*, June 2018, pp. 1–6.

[14] D. Simon, *Optimal State Estimation: Kalman, H Infinity, and Nonlinear Approaches*. New York, NY, USA: Wiley-Interscience, 2006.

[15] M. Koivisto, J. Talvitie, M. Costa, K. Leppänen, and M. Valkama, "Joint cmwave-based multiuser positioning and network synchronization in dense 5G networks," in *2018 IEEE Wireless Communications and Networking Conference (WCNC)*, April 2018, pp. 1–6.

[16] S.-Y. Hou, S.-H. Chang, and H.-S. Hung, "Predictive Angle Tracking Algorithm Based on Extended Kalman Filter," in *Sensor Array*, W. Yang, Ed. IntechOpen, 2012. [Online]. Available: https://doi.org/10.5772/35507

PUBLICATION

III

Positioning-Aided 3D Beamforming for Enhanced Communications in mmWave Mobile Networks

Y. Lu, M. Koivisto, J. Talvitie, M. Valkama and E. S. Lohan

IEEE Access 8.(2020), 55513–55525
DOI: 10.1109/ACCESS.2020.2981815

IEEE Access
Multidisciplinary ⋮ Rapid Review ⋮ Open Access Journal

Received February 25, 2020, accepted March 11, 2020, date of publication March 18, 2020, date of current version March 30, 2020.

Digital Object Identifier 10.1109/ACCESS.2020.2981815

Positioning-Aided 3D Beamforming for Enhanced Communications in mmWave Mobile Networks

YI LU, (Student Member, IEEE), MIKE KOIVISTO, (Student Member, IEEE), JUKKA TALVITIE, (Member, IEEE), MIKKO VALKAMA, (Senior Member, IEEE), AND ELENA SIMONA LOHAN, (Senior Member, IEEE)
Department of Electrical Engineering, Tampere University, 33720 Tampere, Finland

Corresponding author: Yi Lu (yi.lu@tuni.fi)

This work was supported in part by the Academy of Finland through PRISMA under Project 313039 and in part by the Finnish Funding Agency for Innovation under Project 5G VIIMA.

ABSTRACT The extension from centimeter wave frequencies to millimeter wave (mmWave) frequencies has triggered an enormous transformation in terms of radio access architecture for future wireless networks, and it has therefore empowered unlimited opportunities for the user-oriented services and applications. Besides mmWave as a driving element, beamforming (BF) will be incorporated as a key enabling technology for the future wireless networks. In this paper, we propose a positioning-aided beamforming (PA-BF) framework for enhanced downlink communications in a cloud-oriented mmWave mobile networks. We show that the proposed PA-BF achieves a higher effective transmit ratio that is equivalent to a lower initial access latency than the conventional codebook-based BF, which in turn manifests its capability to support high-velocity mobile users. We also analyze the impact of positioning accuracies on the performance of PA-BF and discuss the trade-offs between different BF strategies with varied system parameters. Our simulation results demonstrate that, with a narrow beam phased array and reasonably good positioning accuracy, the PA-BF framework is capable of achieving higher spectral efficiency than the considered codebook-based BF especially at higher velocities.

INDEX TERMS Exhaustive beamforming, millimeter wave mobile networks, positioning-aided beamforming, positioning-aided communications.

I. INTRODUCTION

Without a doubt, upcoming wireless communication systems will extend the radio channels towards a higher frequency range, namely the millimeter wave (mmWave) band, in order to enable various user-driven services that require ultra-high channel capacity in both uplink (UL) and downlink (DL), such as virtual reality and video conference. Although the abundance in the available signal bandwidth is ensured, a considerable challenge of mmWave lies in the fact that the mmWave signals have a higher path-loss and a higher penetration/absorption loss than centimeter wave signals, depending on the materials and structures within the propagation environment [1]. Consequently, in order to overcome the severe propagation losses, the future wireless communication systems incorporate several other features such as the small cell networks (SCNs) and beamforming (BF) as the ingredient technologies [2] that empower a multi-function wireless mmWave mobile network. In general, SCNs, also known as ultra dense networks (UDNs), bring various benefits to both communications [3] and radio positioning [4] due to a high probability of having a line-of-sight (LoS) connection between the transmitter and receiver, for instance. From the communications perspective, SCNs alleviate the significant path-loss and reflection/diffraction loss thanks to a shorter end-to-end propagation distance.

Apart from SCNs, the mmWave mobile networks will incorporate the BF functionalities as another enabling technology to overcome the severe path-loss and to better optimize the interference level at both UL and DL. Together with a massive multiple-input multiple-output (MIMO) antenna technology [5], transmission towards the desired direction is enabled. Therefore, BF not only alleviates the significant path-loss by taking advantage of the MIMO antenna gain, but it also reduces both the potential intra-cell and inter-cell interference via the elegant spatial reuse [6, Ch.1].

The associate editor coordinating the review of this manuscript and approving it for publication was Ahmed Mohamed Ahmed Almradi.

Nevertheless, an optimal spatial reuse requires a sophisticated BF strategy in terms of the beam management [7]. In other words, an optimized BF ensures better spatial multiplexing and better receive signal-to-noise ratio (SNR) but it yields a longer latency of the initial access (IA) especially when narrow beams are utilized at both ends of the communication link. However, a long IA latency is not acceptable for the mission-critical applications such as the autonomous driving and robotics that require a ultra reliable low latency communication (URLLC) [8]. Herein, we adapt the semi-directional communication mode [9] where an omni-directional user equipment (UE) and an analog BF enabled access point (AP) are assumed throughout this paper.

In order to enhance the DL communication quality, we propose a positioning-aided beamforming (PA-BF) framework that exploits the location information of the UE via network-centric UL positioning, thus leading to a lower IA latency and a higher throughput than utilizing the codebook-based BF strategies [7]. The contributions of this paper include the demonstration, formulation, and simulation of the PA-BF strategy leveraging a cloud-oriented mobile network, and we summarized the key contributions as follows:

- Introducing a PA-BF strategy tailored for mmWave mobile network that is operating on an envisioned cloud-oriented radio access architecture;
- Presenting a theoretical formulation of the system model for performing the PA-BF in the DL, showing that a better spectral efficiency and lower IA latency can be achieved compared to the codebook-based BF;
- Deriving the positioning-error bound (PEB) based on the time difference of flight measurements by assuming LoS-dominant connections among each pair of AP and the UEs.
- Demonstrating that the proposed PA-BF framework can support much higher UE velocities than the codebook-based BF, while maintaining the same communication quality in terms of the achievable spectral efficiency.

II. RELATED WORKS

The intuitive trade-off between the IA latency and achievable communication quality has been previously addressed in the literature through three main BF strategies for IA in 5G mmWave networks: i) an exhaustive beamforming (EX-BF) strategy [10], [11], ii) a hierarchical/genetic BF strategy [12]–[14] and iii) a context-information (CI)-based BF strategy [15]–[18] which is also known as location-based BF. Generally speaking, EX-BF and hierarchical BF strategies rely on a pre-defined single/multi-level codebook, thus they can be regarded as belonging to the same family of codebook-based BF. For the CI-based BF strategy, its advantage comes mainly from the reduced IA latency compared to the codebook-based strategies, due to the pre-defined spatial direction indicated by the context information of the user location typically acquired via available positioning technology on the UE, which must be then informed to the APs [16]. The usefulness of the location information in the context of BF was analyzed in [17], where the authors focused on the benefits in terms of channel estimation duration and in the received SNR level when exploiting location information of targets with different location accuracies. Moreover, the authors in [18] analyzed the connection between positioning accuracy and the effective data rate as a function of different training overheads such as the number of beams.

Additional related studies on the CI-based BF and location-aware communications can be found in [4], [19]–[23]. In [19], the authors have proposed a location-aware BF strategy for multi-user (MU) massive MIMO system for the high speed train (HST) scenario, where the location information has been exploited to reduce the complexity of BF. However, the impact of the positioning error on the BF performance has not been examined therein. Regarding the CI-based BF strategy, a compressive sensing (CS) based BF with CI was proposed in [20] where the location-uncertainty of mobile users is exploited to reduce the sweeping range in the angle domain. Assuming a symmetric positioning error, the CS based multi-level BF has been applied to find the optimal beam for mmWave communications and a performance in terms of spectral efficiency close to the EX-BF has been achieved. Additionally, the authors in [21] have studied the benefits of the location-based BF over the codebook-based BF in a 2D scenario where the location estimate comes from a global navigation satellite system (GNSS). However, neither the impact of positioning accuracy on the considered location-based BF nor the way that the AP acquires the location estimate of UE[1] before the BF were clearly investigated therein. Moreover, a network-centric system is proposed to enable the location-based BF in the DL in [22], [23]. Via the tracking of directional parameters (elevation and azimuth angles) by an extended Kalman filter at the network side, the precoder for DL communication is designed for location-based BF, and the results shown that, despite a closer performance, the matched filter (MF) based precoder has achieved a better signal-to-interference-plus-noise ratio (SINR) and user throughput than the zero-force (ZF) based precoder. While considering a network-centric system, the authors in [4] presented the positioning performance in a dense 5G network, and compared the location-based BF with the channel state information (CSI)-based BF in terms of the user throughput. In particular, the location-based BF manifested a certain advantage over the CSI-based BF because of a reduced pilot overhead owing to the available location information.

In this work, the CSI-based BF is not considered mainly due to the short effective duration of the CSI [9] as well as due to the high cost of acquiring the perfect CSI of each antenna element especially in large-scale mmWave systems [12], [24]. Furthermore, the other strategy, CS-based BF,

[1] Since a GNSS-based positioning was applied, it implies that only the UE knows its estimated location but AP does not before the BF.

is not chosen as the benchmark here for several reasons. We elaborate our rationale from two major perspectives: i) the realization of CS-based BF strategy such as [20], [25] is normally conditional on the acquisition of the CSI at both the transmitter and the receiver sides, which yields a higher algorithm complexity and a longer latency [26]; ii) the CS-based BF in general requires the utilization of fully digital beamforming or hybrid beamforming in order to change the beamwidth which remains as a high-demand on the device hardware. All in all, compared with aforementioned works, our proposed PA-BF framework operates on a low-complexity analog BF, where the positioning is done via multi-connectivity in the UL within a cloud-oriented network architecture.

Besides the simulation-based study on BF for the mmWave networks, experimental work has been conducted in [27], [28], where different specific model-driven 3D beam-steering mechanisms were applied to achieve high communication performances in terms of several micro-benchmarks in 60 GHz wireless networks. Assisted by the measurement campaign, the authors in [27] analyze the impact of 3D motion and rotation to the link performance of the 60 GHz connection. The discovery revealed a ''deformed-cross'' pattern of the channel quality distribution applying 3D beams, which leads to an optimal beam-steering mechanism, the OScan. Based on the evaluations, the designed OScan outperforms existed mechanisms in terms of convergence, accuracy and overhead, therefore providing higher throughput gain for different applications, environments and users. In [28], the authors proposed a robust 60 GHz network architecture for seamless room-scale coverage with multi-Gbps throughput. In the context of multiple APs and UEs, the proposed method maximizes the spatial reuse as well as reduces the overwhelming IA latency in the mmWave networks by exploiting the UE's pose information (location and orientation) and predicting the best beam pattern of each AP among several UEs.

These two works have devoted tremendous contributions towards 3D beam-steering by the means of theoretical analysis, algorithm development and experimental measurements. It is noteworthy that in the aforementioned works, the UE positioning was carried out by utilizing, e.g., the motion sensors in a device-centric manner, after which BF is carried out to select optimal AP and harvest a higher throughput via mmWave communication. However, our proposed framework is essentially a combination of both positioning and BF. That is, the UE location is first estimated via an UL positioning at the network side, and the PA-BF is performed thereafter to take advantage of the obtained location awareness yielding a lower IA latency as well as a better communication quality. We provide a simulation-based performance characterization under various positioning errors, while considering the impact of geometric relations on the system level performance.

Throughout this paper, the EX-BF is chosen as the benchmark for the performance comparison with the proposed PA-BF. The choice of this benchmark was motivated by two main factors: i) neither EX-BF nor PA-BF require the change of beamwidth yielding a similar mechanism complexity. Therefore, it makes the comparison fair; ii) EX-BF was shown to give better performance than other strategies in terms of detection probability [16] as well as the spectral efficiency [20] which serves as another factor. Finally, we point out that all BF strategies considered herein refer to the analog BF, i.e., only one beam can be generated at one time.

III. THE PROPOSED CLOUD-ORIENTED SYSTEM

In this section, an overview of the cloud-oriented mobile network is given, followed by a systematic description of UL positioning as well as DL positioning-aided communications.

A. SYSTEM OVERVIEW

Our envisaged radio access architecture is depicted in Fig.1, where a cloud-oriented mobile network is proposed for a mmWave-based communication and positioning system in which the signals for both UL and DL employ orthogonal frequency division multiplexing (OFDM) waveforms. In addition, a time-division duplex (TDD) protocol is considered in the system with a focus on mmWave-enabled radio access technology (RAT), and a multi-RAT-enabled heterogeneous network (HetNet) was proposed and analyzed in [29]. Moreover, each UE within the network is assumed to be equipped with an omni-directional antenna from which the UL pilot signals[2] are transmitted to the network (i.e., to the APs) in a periodic manner. The APs that are in the LoS condition with respect to the UEs are referred to as the LoS-APs. At the network edge, we assume that a uniform rectangular array (URA) is installed on each AP, from which only one antenna element is assumed to be active in the UL positioning phase whereas all the elements function during the DL communication phase.

Such a system is tailored to minimize the positioning overhead in the UL whereas taking advantage of array gain in the DL that is conditional on the UL positioning performance, as will be discussed in Section III-C and V-A. Furthermore, we assume that the location-dependent measurements such as time of flight (ToF) and/or angle of arrival (AoA) are measured by the APs and sent to the *cloud*, where the UE location is estimated based on the aggregated measurements. In terms of functionality, the cloud can be considered as a data center (entity) that operates the radio resource management, the scheduling and the handover decisions for the entire network. After the cloud-based UE location estimation, this estimated location is transmitted from the cloud back to the network.[3] With this estimated UE location, the positioning-aided DL communications are implemented, which, as we

[2]The UL pilot signals can be, for instance, the sounding reference signals (SRS) [30].

[3]Herein, the cloud communication latency, i.e., the round-trip delay between the cloud and the APs is assumed to be much smaller than the periodicity of UL pilot signal, and therefore, the cloud communication latency can be ignored [31].

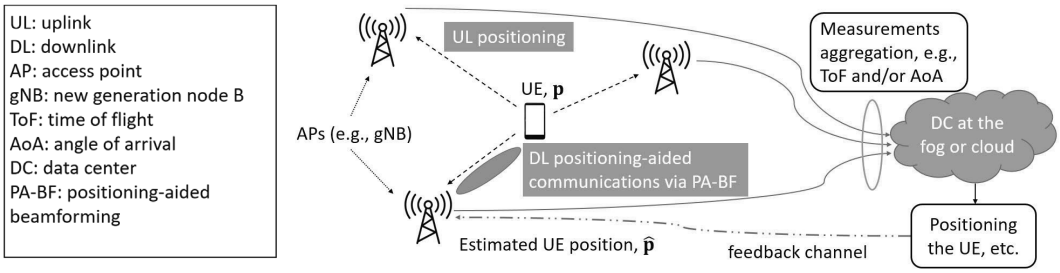

FIGURE 1. The envisioned radio access architecture — a cloud-oriented mobile network.

will show, will yield a shorter IA latency compared with a conventional IA-BF procedure.

B. UL POSITIONING

This subsection presents the UL positioning system in which the location of a UE is estimated. In general, the positioning solution that utilizes UL pilot signals in a network-centric manner has several advantages over a device-centric positioning approach, such as

1. No knowledge or estimation on the orientation of the UE array is needed. Although an omni-directional antenna is assumed for the UE in this work, UL positioning arguments the aforementioned advantage especially for multi-antenna UEs.
2. Since the positioning algorithms are not evaluated at the UE side, the power consumption of the UE battery is kept to a minimum, thus it can highly benefit power-sensitive applications such as industrial robotics.
3. The estimated UE location can be directly utilized by the network to enable any location-based services, therefore, no additional links are needed for the UE to report its location back to the network.
4. The location awareness of the UE at the network side is beneficial to beam tracking as the beam-steering vector can be continuously pointed towards the UE.

For positioning, we consider a multi-connectivity scenario where the UL pilot signal from the UE reaches more than one LoS-AP, which is a reasonable assumption in the light of future SCNs/UDNs. We further denote the set of LoS-APs indices as $\mathcal{M}$, where each AP is located at a known location $\mathbf{P}_{\mathrm{AP},m} = [x_m, y_m, z_m]^T, \forall m \in \mathcal{M}$. The UE location vector is denoted as $\mathbf{p} = [x, y, z]^T$. Assuming a $L \times L$ URA with one active antenna element in the UL, the received signal $r_m(t)$ at the mth LoS-AP is

$$r_m(t) = \sqrt{g_r P_{\mathrm{T,UL}}} h_m s(t - \tau_m) + (s * \nu)(t) + n(t), \quad (1)$$

where $P_{\mathrm{T,UL}}$ and g_r refer to the UL transmit power in a linear scale and the received antenna gain at the AP, respectively. Moreover, h_m denotes as the corresponding channel coefficient w.r.t. the mth LoS-AP. In this work, h_m has been modeled according to the 3GPP indoor hotspot (InH) shopping mall channel model [32]. In addition, $s(t - \tau_m)$ is the continuous time-domain transmit signals with a duration of T_s and bandwidth B_w, and $n(t)$ denotes the additive Gaussian noise with a power spectrum density of N_0. The LoS delay τ_m is the quotient of the Euclidean distance between the UE and mth AP and the speed of light, $\tau_m = \|\mathbf{p} - \mathbf{P}_{\mathrm{AP},m}\|/c$. Also, the Hermitian transpose is denoted as ^{H}. Last but not least, the convolution of signal $s(t)$ and *diffuse reflection* components $\nu(t)$ is applied to model the un-correlated scattering with the un-planar surfaces/obstacles of the environment [33], [34]

$$(s * \nu)(t) = \int s(u)\, \nu(t - u)\, \mathrm{d}u, \quad (2)$$

where $\nu(t)$ is a zero-mean Gaussian process, and the power ratio of h and $\nu(t)$ is determined and calculated by the Rician-K factor in [32, Table 7.5-6]. However, given the fact that the direct path contains nearly all the energy in the mmWave communications [35], the effect to $r_m(t)$ from both the *specular reflection* and diffuse reflection can be overlooked.

1) MEASUREMENT MODEL

Once the UL pilot signal is acquired, location-dependent measurements needs to be extracted for positioning. Typically, the positioning related measurements consists of ToF and AoA that offer the information in terms of distance and spatial direction w.r.t. the location of APs. However, due to the disparate nature of the clock offsets among the APs and the UE, the ToF measurements remain useless until the synchronization is achieved or otherwise compensated [36]–[38]. Therefore, by assuming a network with synchronized APs, the UL positioning in this work is carried out considering the time difference of flight (TDoF) measurements $\Delta\hat{\boldsymbol{\tau}} \in \mathbb{R}^{M-1}$ that are observed according to

$$\Delta\hat{\boldsymbol{\tau}} = \boldsymbol{f}_{\Delta\tau}(\mathbf{p}) + \boldsymbol{n}_{\Delta\tau}, \quad (3)$$

where $\boldsymbol{f}_{\Delta\tau}(\mathbf{p})$ refers to the TDoF observation function and $\boldsymbol{n}_{\Delta\tau} \in \mathbb{R}^{M-1}$ is the measurement noise vector. Note that M represents the overall number of the LoS-APs. Specifically, the non-linear function $\boldsymbol{f}_{\Delta\tau}(\mathbf{p})$ is expressed as

$$\boldsymbol{f}_{\Delta\tau}(\mathbf{p}) = \left[\frac{d_2 - d_1}{c}, \cdots, \frac{d_M - d_1}{c}\right]^T, \quad (4)$$

where the reference LoS-AP is selected to be the one with index 1, and d_m is denoted as the Euclidean distance between the UE and the mth AP, that is given as

$$d_m = \|\mathbf{p} - \mathbf{P}_{\mathrm{AP},m}\| = \sqrt{\Delta x_m^2 + \Delta y_m^2 + \Delta z_m^2}. \quad (5)$$

where $\Delta x_m = x - x_m$, $\Delta y_m = y - y_m$ and $\Delta z_m = z - z_m$.

Moreover, since the LoS propagation is assumed, the noise vector $\boldsymbol{n}_{\Delta\tau}$ is modelled as a zero-mean Gaussian process, such that $\boldsymbol{n}_{\Delta\tau} \sim \mathcal{N}(\mathbf{0}_{M-1}, \boldsymbol{R}_{\Delta\tau})$ with the noise covariance matrix being described as [39, Ch.4]

$$\boldsymbol{R}_{\Delta\tau} = \begin{bmatrix} \sigma_{\tau_1}^2 + \sigma_{\tau_2}^2 & \sigma_{\tau_1}^2 & \cdots & \sigma_{\tau_1}^2 \\ \sigma_{\tau_1}^2 & \sigma_{\tau_1}^2 + \sigma_{\tau_3}^2 & \cdots & \sigma_{\tau_1}^2 \\ \vdots & \vdots & \ddots & \vdots \\ \sigma_{\tau_1}^2 & \sigma_{\tau_1}^2 & \cdots & \sigma_{\tau_1}^2 + \sigma_{\tau_M}^2 \end{bmatrix}. \quad (6)$$

In essence, the noise covariance matrix (6) is constructed based on the Cramér-Rao lower bound (CRLB) of the ToF measurement, and that is in fact the reason why (6) is non-diagonal (i.e., more correlated) as each TDoF measurement is calculated based on two ToF measurements one of which comes from the same reference AP. Taking the noise variance of the ToF measurement between the mth LoS-AP and the UE as an example, we have [39, Ch.3]

$$\sigma_{\tau,m}^2 \geq \frac{3}{8\pi^2 f_{\text{sc}}^2 \text{SNR}_m M_u (M_u+1)(2M_u+1)}, \quad (7)$$

where the CRLB of ToF lies on the right side of the equation, and the received SNR at the mth LoS-AP is denoted as $\text{SNR}_m = \text{EIRP}_{\text{UL}}|h_m|^2/N_0 B_w$, in which $\text{EIRP}_{\text{UL}} = P_{\text{T,UL}} g_r$ is the equivalent isotropic radiated power [40, Ch.4]. Since only one active antenna element is assumed in the UL, the received antenna gain g_r in (1) is set to be 0 dBi. Furthermore, f_{sc} is the sub-carrier spacing, and $M_u = \frac{N_u-1}{2}$, N_u is the overall number of sub-carriers. With a fixed signal bandwidth B_w, the following numerical condition is satisfied

$$B_w = f_{\text{sc}} N_u = f_{\text{sc}} (2M_u - 1). \quad (8)$$

Therefore, beside the received SNR, the ToF measurement noise variance is also inversely proportional to the overall bandwidth B_w.

2) POSITIONING ERROR BOUND (PEB)

PEB, which is essentially the CRLB when the parameters of interest refer to each component of the UE location vector $\mathbf{p} = [x, y, z]^T$, normally starts with the calculation of Fisher information matrix (FIM) based on the available measurements [41, Ch.3]. Since only TDoF measurements are considered and its measurement noise is zero-mean Gaussian distributed under LoS, the FIM of location $\mathbf{p}$ can be computed as [42, Ch.2]

$$\boldsymbol{I}_{\Delta\tau} = \left[\frac{\partial \boldsymbol{f}_{\Delta\tau}(\mathbf{p})}{\partial \mathbf{p}}\right]^T \boldsymbol{R}_{\Delta\tau}^{-1} \left[\frac{\partial \boldsymbol{f}_{\Delta\tau}(\mathbf{p})}{\partial \mathbf{p}}\right], \quad (9)$$

where the derivative w.r.t. $\boldsymbol{f}_{\Delta\tau}(\mathbf{p})$ is calculated in line with (4)

$$\frac{\partial \boldsymbol{f}_{\Delta\tau}(\mathbf{p})}{\partial \mathbf{p}} = \begin{bmatrix} \frac{\Delta x_2}{d_2} - \frac{\Delta x_1}{d_1} & \frac{\Delta y_2}{d_2} - \frac{\Delta y_1}{d_1} & \frac{\Delta z_2}{d_2} - \frac{\Delta z_1}{d_1} \\ \vdots & \vdots & \vdots \\ \frac{\Delta x_M}{d_M} - \frac{\Delta x_1}{d_1} & \frac{\Delta y_M}{d_M} - \frac{\Delta y_1}{d_1} & \frac{\Delta z_M}{d_M} - \frac{\Delta z_1}{d_1} \end{bmatrix}. \quad (10)$$

Given the FIM in (9), the 3D PEB is then calculated as

$$\text{PEB} = \text{CRLB}(\mathbf{p}) = \sqrt{\text{trace}\left(\boldsymbol{I}_{\Delta\tau}^{-1}\right)}, \quad (11)$$

where 'trace' denotes the summation of the diagonal values of the matrix. In particular, the derived PEB (11) serves as a prior information to implement the proposed PA-BF. Hence, in the next sub-section, we describe how this information can be exploited to enhance the DL communications.

C. DL POSITIONING-AIDED COMMUNICATIONS

Once positioning is done at the data center, the estimated UE location is sent to one or several APs via the feedback channel shown in Fig.1. The knowledge of the UE location not only enables various location-based services [43] but also vastly reduces the latency caused at IA process. It is to note that in the DL, all the antenna elements of the URA at the AP is active, as such, the multiple-input single-output (MISO) model is applied to describe the DL communication model at the receiver side as

$$r(t) = \sqrt{P_{\text{T,DL}}} \boldsymbol{h}_{\text{DL}}^H \boldsymbol{f}^* s(t - \tau_{\text{DL}}) + (s * \nu_{\text{DL}})(t) + n(t), \quad (12)$$

where the DL channel vector $\boldsymbol{h}_{\text{DL}}$ is the product of channel coefficient h_{DL} and the array response $\boldsymbol{b}_{\text{URA}}$, that is, $\boldsymbol{h}_{\text{DL}} = h_{\text{DL}} \boldsymbol{b}_{\text{URA}}(\phi_{\text{AoD}})$, in which, $\phi_{\text{AoD}} \triangleq (\varphi_{\text{AoD}}, \theta_{\text{AoD}})$ is the true angle of departure (AoD) pair and $\boldsymbol{b}_{\text{URA}}$ can be understood as a combination of several uniform linear arrays (ULAs), which is therefore obtained as [44]

$$\begin{aligned} \boldsymbol{b}_{\text{URA}}(\phi_m) &= \sqrt{\beta_0(L, \phi_m)} \boldsymbol{a}_{\text{URA}}(\phi_m), \\ \boldsymbol{a}_{\text{URA}}(\phi_m) &= \boldsymbol{a}_{\text{ULA}}(\varphi_m) \otimes \boldsymbol{a}_{\text{ULA}}(\theta_m|\varphi_m), \end{aligned} \quad (13)$$

where $\beta_0(L, \phi_m)$ represents the antenna gain that depends on the overall number of antenna elements L^2 as well as the AoA pair, $\phi_m \triangleq (\varphi_m, \theta_m)$ w.r.t. the mth LoS-AP. Note that $\boldsymbol{a}_{\text{ULA}}(\theta_m|\varphi_m)$ refers to the ULA response at θ_m given φ_m. Meanwhile, we assume that the URA consists of identical isotropic antenna elements, and all adjacent elements are $\lambda/2$ apart in both elevation and azimuth plane, where λ is the wavelength of carrier frequency f_c. Hence, both the ULA response $\boldsymbol{a}_{\text{ULA}}(\varphi_m)$ and $\boldsymbol{a}_{\text{ULA}}(\theta_m|\varphi_m)$ for the kth antenna element are expressed as

$$\begin{aligned} [\boldsymbol{a}_{\text{ULA}}(\varphi_m)]_k &= e^{-jk\pi \sin(\varphi_m)}/L, \\ [\boldsymbol{a}_{\text{ULA}}(\theta_m|\varphi_m)]_k &= e^{-jk\pi \cos(\varphi_m)\sin(\theta_m)}/L, \end{aligned} \quad (14)$$

where $k = [-\frac{L-1}{2}, \frac{L-1}{2}]$. The normalized array response $\boldsymbol{a}_{\text{URA}} \in \mathbb{C}^{L^2 \times 1}$ can be calculated by the kronecker product, denoted as $\otimes$, of the two ULA responses as in (13).

Additionally, $P_{\text{T,DL}}$ and τ_{DL} refer to the linear scale transmit power and the LoS delay in the DL, respectively, and the transmit signal, the additive Gaussian noise and the receive signal in the time domain are denoted as $s(t)$, $n(t)$ and $r(t)$, individually. Similar to the UL (1), the diffuse reflection components are considered in the DL (12) as well. However, due to a more directional transmission,[4] the

[4]Herein, we present a single-input single-output (SISO) model in the UL, and a MISO model in the DL.

power of DL diffuse reflection components ν_{DL} is much less than that of UL which can therefore be ignored as well. Furthermore, we denote the selected AP for DL communication as the primary AP that located at $P_0 = [x_0, y_0, z_0]^T$. More importantly, in positioning-aided communication system, the beam-steering vector $\boldsymbol{f}^*$ (the precoder) is constructed based on the predicted angle pair w.r.t. the primary AP that is defined as $\hat{\phi}_{\mathrm{AoD}} \triangleq (\hat{\varphi}_{\mathrm{AoD}}, \hat{\theta}_{\mathrm{AoD}})$, that is obtained in accordance with the estimated UE location, $\hat{\mathbf{p}} = [\hat{x}, \hat{y}, \hat{z}]^T$ as

$$\hat{\varphi}_{\mathrm{AoD}} = \arcsin\left(\frac{\hat{z} - z_0}{\|\hat{p} - P_0\|}\right),$$
$$\hat{\theta}_{\mathrm{AoD}} = \operatorname{atan}_2\left(\hat{y} - y_0, \hat{x} - x_0\right). \tag{15}$$

Here, it is to note that the considered UE location estimate is given as $\hat{\mathbf{p}} = \mathbf{p} + \boldsymbol{e}$, where the covariance of the zero-mean error vector $\boldsymbol{e}$ is related with the FIM (9) as

$$\mathbb{E}\left[\boldsymbol{e}\boldsymbol{e}^T\right] = \boldsymbol{I}_{\Delta\tau}^{-1}. \tag{16}$$

That is, we consider an unbiased location estimator $\hat{\mathbf{p}}$ [39, Ch. 4]. Moreover, we point out that the product of $\boldsymbol{h}_{\mathrm{DL}}^H \boldsymbol{f}$ reflects the beamforming gain of the PA-BF, and it reaches the maximum whenever the predicted angle pair $\hat{\phi}_{\mathrm{AoD}}$ matches with the true angle pair ϕ_{AoD}. And the way on choosing and/or constructing the codewords for both considered beamforming strategies is given in the next section.

IV. UTILIZED 3D CODEBOOK FOR EX-BF AND PA-BF

In essence, the codebook acts as a dictionary that consists of a group of codewords (beam-steering vectors) in order to find the optimal path in the spatial domain to establish the best possible communication link based on the current channel conditions and environments. In this section, we demonstrate the codebook utilized for both considered BF strategies.

A. THE 3D DFT CODEBOOK FOR EX-BF

The codebook we consider for the EX-BF herein is the discrete Fourier transform (DFT) codebook [18] due to its orthogonality among all codewords. And a 3D DFT codebook is needed for BF in a 3D environment. As described in (1), each codeword is essentially a function of an angle in 2D or an angle pair for 3D case [45]. Therefore, the 3D codebook for EX-BF consists of a set of angle pairs, each of which is applied for constructing one specific codeword to cover one spatial direction. Furthermore, the angular coverage of the 3D codebook should be the whole spatial direction on a sphere, which is fully described by the angle pairs that consists of the azimuth and elevation angles that specify the phase shift for each antenna element (14). Particularly in the 3D scenario, it is noteworthy that the circumference of the longitude remains constant with respect to all azimuth angles whereas that of the latitude becomes smaller as the elevation angle approaches $\pm\pi/2$ (the North pole or South pole). Therefore, the sampled azimuth angles at higher elevation plane should be less dense than at lower elevation plane to avoid the oversampling.

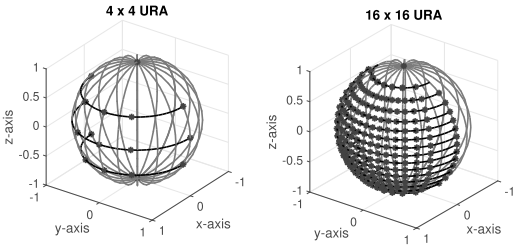

FIGURE 2. A demonstration of the selected angle pairs based on the DFT codebook for 4 × 4 and 16 × 16 URA for half a sphere.

TABLE 1. The total number of codewords within the 3D DFT codebook of different URA configuration for the EX-BF.

URA configuration $L \times L$	No. of codewords N_{cw}
4×4	16
16×16	244

The selected angle pairs that mapped onto the sphere surface are demonstrated in Fig. 2 yielding less samples at higher elevation level for both 4×4 and 16×16 URA. If we denote the resulting codebook as $\mathcal{B}$, any individual codeword $\boldsymbol{g} \in \mathcal{B}$ can be expressed as

$$\boldsymbol{g} = \boldsymbol{a}_{\mathrm{URA}}\left(\phi_{i,j}\right) = \boldsymbol{a}_{\mathrm{ULA}}\left(\varphi_i\right) \otimes \boldsymbol{a}_{\mathrm{ULA}}\left(\theta_{i,j}|\varphi_i\right), \tag{17}$$

where $\boldsymbol{g} \in \mathbb{C}^{L^2 \times 1}$ and $\phi_{i,j} \triangleq \left(\varphi_i, \theta_{i,j}\right)$ represent one of the selected angle pairs. The total number of codewords of half the sphere for 2 specific URA configuration is tabulated in Table 1.

B. THE 3D CODEBOOK FOR PA-BF

Unlike any typical codebooks for EX-BF or hierarchical BF [14], which contains several codewords, the 3D codebook for PA-BF is essentially a single codeword, constructed based on the spatial knowledge acquired from the UL positioning. Therefore, the codeword $\boldsymbol{f}_{\mathrm{PA}}$ for PA-BF is obtained as

$$\boldsymbol{f}_{\mathrm{PA}} = \boldsymbol{a}_{\mathrm{ULA}}(\hat{\varphi}_{\mathrm{AoD}}) \otimes \boldsymbol{a}_{\mathrm{ULA}}(\hat{\theta}_{\mathrm{AoD}}|\hat{\varphi}_{\mathrm{AoD}}), \tag{18}$$

where the estimated angle pair $(\hat{\varphi}_{\mathrm{AoD}}, \hat{\theta}_{\mathrm{AoD}})$ was given in (15). One of the key advantages of applying the PA-BF lies in the effectiveness of acquiring the final codeword without consuming extra time on searching throughout the whole codebook exhaustively or hierarchically, therefore enjoying a short IA latency. We further elaborate the performance metrics of PA-BF and EX-BF in the next section.

V. PERFORMANCE METRICS

One of the most relevant performance metrics in wireless communications is the spectral efficiency [46], which is therefore chosen herein to characterize the performance of studied BF strategies. The achievable spectral efficiency is examined under varying parameters, such as the effective transmit ratio, the transmit power, channel realization and the BF gain. The *effective transmit ratio* is a indirect measure of the IA latency and it depends on the codebook size, which at

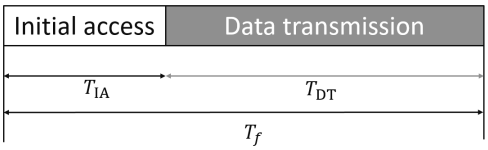

FIGURE 3. The overall frame duration T_f that consists of both IA duration T_{IA} and data transmission duration T_{DT}.

its turn is determined by the applied BF strategy. For illustration purposes, the overall frame time that contains both IA and data transmission is depicted in Fig. 3. Herein, we define that the DL communication occurs over the duration of the whole frame period T_f from which the effective transmit ratio η is defined as

$$\eta = 1 - \frac{T_{\mathrm{IA}}}{T_f}, \tag{19}$$

where T_{IA} refers to the IA latency that typically used for beam alignment, the length of which largely depends on the BF strategy and codebook size. For any given DL channel realization h_{DL}, the spectral efficiency is given as

$$R = \eta \log_2 \left(1 + \frac{P_{\mathrm{T,DL}}|h_{\mathrm{DL}}|^2}{P_n} G_{\mathrm{BF}}(\boldsymbol{f}^*, \phi_{\mathrm{AoD}})\right), \tag{20}$$

where $P_n = N_0 B_w$ refer to the thermal noise power over the entire signal bandwidth. Note that $\frac{P_{\mathrm{T,DL}}|h_{\mathrm{DL}}|^2}{P_n}$ is denoted as the SNR without BF gain. Additionally, $\boldsymbol{f}^* \in \mathbb{C}^{L^2 \times 1}$ refers to the selected beam-steering vector subject to the applied BF strategy. Furthermore, G_{BF} is defined as the achieved BF gain that is a function of $\boldsymbol{f}^*$ and the true AoD pair $\phi_{\mathrm{AoD}} \triangleq (\varphi_{\mathrm{AoD}}, \theta_{\mathrm{AoD}})$.

A. SPECTRAL EFFICIENCY OF THE PROPOSED PA-BF

When utilizing the PA-BF, the achieved DL spectral efficiency according to (12) and (20) can be described as

$$R_{\mathrm{PA}} = \eta_{\mathrm{PA}} \log_2 \left(1 + \frac{P_{\mathrm{T,DL}}|h_{\mathrm{DL}}|^2}{P_n} G_{\mathrm{BF}}(\boldsymbol{f}_{\mathrm{PA}}, \phi_{\mathrm{AoD}})\right), \tag{21}$$

where $\boldsymbol{f}_{\mathrm{PA}}$, defined in (18), is the normalized beam-steering vector designed according to the acquired knowledge on the UE location via UL positioning. By assuming that one codeword takes up one OFDM symbol duration, the effective transmit ratio η_{PA} is

$$\eta_{\mathrm{PA}} = 1 - \frac{T_{\mathrm{IA}}}{T_f} = 1 - \frac{T_s + T_e}{T_f}, \tag{22}$$

where $T_{\mathrm{IA}} = T_s + T_e$, in which, T_s refers to the UL positioning overhead that takes one OFDM symbol[5] and T_e is the cloud communication latency [31] that is attributed to the round trip delay from the APs to the cloud and back to the primary AP. It is noteworthy that T_e is generally negligible due to the fact that the cloud servers are normally distributed in the proximity of the APs which are connected via fiber optics. In addition, the BF gain is acquired as

$$G_{\mathrm{BF}}\left(\boldsymbol{f}_{\mathrm{PA}}, \phi_{\mathrm{AoD}}\right) \triangleq |\boldsymbol{f}_{\mathrm{PA}}^H(\hat{\phi}_{\mathrm{AoD}}) \boldsymbol{b}_{\mathrm{URA}}(\phi_{\mathrm{AoD}})|^2. \tag{23}$$

Note that the BF gain of PA-BF is decided by the precision of the predicted angle pair $\hat{\phi}_{\mathrm{AoD}}$ that relies on the positioning accuracy because (23) is maximized whenever $\hat{\phi}_{\mathrm{AoD}} \approx \phi_{\mathrm{AoD}}$. And the maximum achievable value of (23) is decided by the $\beta_0(L, \phi)$ in (13).

B. SPECTRAL EFFICIENCY OF THE EX-BF

The EX-BF [18] extended to 3D case is employed herein as a benchmark for the comparison of the performance. Specifically, EX-BF applies the best beam for communication via searching through the whole codebook in an exhaustive manner. In particular, the applied codebook for EX-BF is designed in Section. IV-A in a form of the DFT matrix in which each column is orthogonal to the others and we denote it as $\mathcal{F} \in \mathbb{C}^{L^2 \times N_{\mathrm{cw}}}$ that consists of N_{cw} beam-steering vectors $\boldsymbol{f} \in \mathbb{C}^{L^2 \times 1}$ in total, in which the N_{cw} depends on the codebook design algorithm and array configuration. As such, the spectral efficiency of the EX-BF for a given DL channel realization is expressed as

$$R_{\mathrm{EX}} = \eta_{\mathrm{EX}} \log_2 \left(1 + \frac{P_{\mathrm{T,DL}}|h_{\mathrm{DL}}|^2}{P_n} G_{\mathrm{BF}}(\boldsymbol{f}_{\mathrm{EX}}, \phi_{\mathrm{AoD}})\right), \tag{24}$$

where $\boldsymbol{f}_{\mathrm{EX}}$ is the selected beam-steering vector, that is, the codeword that maximizes the following

$$\boldsymbol{f}_{\mathrm{EX}} = \arg\max_{\boldsymbol{f} \in \mathcal{F}} G_{\mathrm{BF}}(\boldsymbol{f}, \phi_{\mathrm{AoD}}), \tag{25}$$

where $G_{\mathrm{BF}}(\boldsymbol{f}, \phi_{\mathrm{AoD}}) \triangleq |\boldsymbol{f}^H \boldsymbol{b}_{\mathrm{URA}}(\phi_{\mathrm{AoD}})|^2$. Moreover, the effective transmit ratio of EX-BF η_{EX} is

$$\eta_{\mathrm{EX}} = 1 - \frac{T_{\mathrm{IA}}}{T_f} = 1 - \frac{N_{\mathrm{cw}} T_s}{T_f}, \tag{26}$$

where the IA latency consumes $N_{\mathrm{cw}} T_s$ seconds in total for beam training and selecting the best codeword according to (25). Note that (22) and (26) are obtained based on the same assumption that each codeword takes up one OFDM symbol.[6]

Together with $\beta_0(L, \phi)$, we can infer that, on one hand, a larger number of antenna elements yields a finer angular resolution which in turn leads to better BF gain in (24). On the other hand, a larger number of antenna elements L suggests a larger number of codewords, which conversely causes a lower effective transmit ratio and therefore a smaller spectral efficiency than with smaller L. Via the inspection of (22) and (26), the advantage of PA-BF is that η_{PA} will be mostly higher than η_{EX} by virtue of the pre-determined AoD obtained through the UL positioning. Nevertheless, the performance of PA-BF is directly determined by the positioning accuracy which highly affects the BF gain G_{BF} in (23).

[5]Recall that a SISO communication was assumed in the UL, therefore, the positioning overhead of PA-BF within the IA latency T_{IA} takes up one OFDM symbol, i.e., one beam.

[6]We clarify that even if, in 5G NR, 4 OFDM symbols take up one training beam (one codeword) in the synchronization signal (SS)-block for IA [47, Ch. 16], the UL SRS that spans one OFDM symbol [7] is utilized in the PA-BF. Thus, we assume the same numerology for EX-BF for a fair comparison.

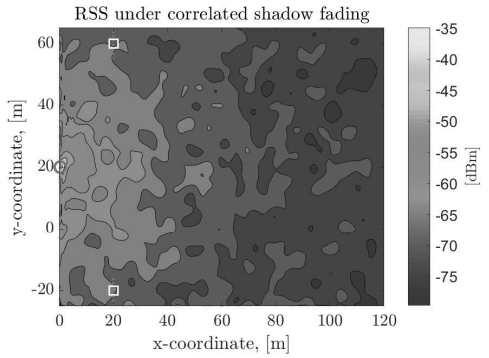

FIGURE 4. An illustration of the top view of a specific AP deployment with the RSS distribution. The red circular marker and white squared markers represent the primary AP and secondary APs, respectively. The red dotted lines refer to the array orientation of each AP. The colormap is used to reflect the RSS w.r.t. the primary AP under spatial correlated shadow fading that is generated with a 10m correlation distance and 2dB (initialized) shadow fading [32, Table 7.5-6 part 2].

Meanwhile, the advantage of EX-BF is a guaranteed BF gain given a complete spatial coverage of the applied codebook whereas its disadvantage lies in the exhaustive search which will return a lower η_{EX}. The spectral efficiency of EX-BF and PA-BF with different positioning accuracy will be given and analyzed in the next section.

VI. SCENARIO DEPLOYMENT AND SIMULATION RESULTS

In this section, we first describe and discuss about the considered scenario and network deployment, after which we provide simulation-based results with detailed analysis.

A. SCENARIO DEPLOYMENT AND DISCUSSION

An illustration of the top view of the scenario deployment of an indoor space with a physical size of 120m×90m (with a 0.5m resolution in both x- and y- directions) is presented in Fig. 4 together with the received signal strength (RSS) considering a spatial correlated shadow fading that is generated via the Gaussian process [42, Ch. 11] for which the applied parameters are found in [32]. In order to model a 3D indoor environment, the z-coordinate of UE is fixed at 1m whereas that of APs are all equally set at 4m. Moreover, the URA orientation is marked as the red dotted line at each AP location. Furthermore, for the 3 illustrated LoS-APs in Fig. 4, we refer to the red circular marker located at [0, 20] as the *primary AP* which is capable of both UL positioning and DL communication whereas the other two APs (marked as the white square markers) located at [20, -20] and [20, 60] respectively as the *secondary APs* that only receive and process the UL pilot signals. Basically, the primary AP can be considered as the AP in the coverage layer whereas the secondary APs are seen as the remote radio heads (RRHs) that assist the UL positioning.

Without the loss of the generality, we generated 10 random layouts (each with random locations of several APs, and only one of them serves as the primary AP) for simulation purposes, and each layout consists of a limited number of APs (from minimum 3 to maximum 6 APs), whereas in practice, the density of APs can be much higher considering the SCNs. Finally, the LoS propagation is assumed throughout the considered area.

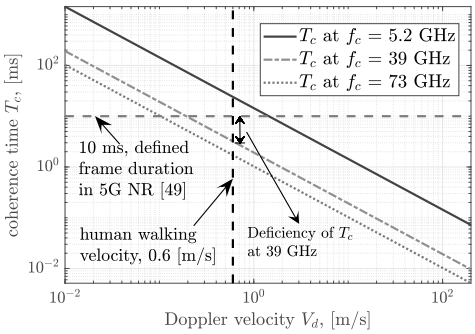

FIGURE 5. Coherence time T_c as a function of Doppler velocity V_d at various carrier frequencies.

B. SIMULATIONS RESULTS AND PERFORMANCE ANALYSIS

We start the analysis with our approach to select the overall frame duration T_f w.r.t. a physical quantity, the relative velocity between the AP and the UE. Since all the APs are static, the relative velocity is reflected by the UE mobility only. Basically, the connection is established based on the coherence time of the wireless channel, denoted as T_c, that is the time over which the channel condition remains as constant [48]. In particular, the coherence time T_c can be expressed as a function of the Doppler shift f_d as [46]

$$T_c = \frac{1}{4f_d}, \tag{27}$$

in which the Doppler shift is inversely proportional to the carrier wavelength as $f_d = \frac{V_d}{\lambda_c} = \frac{V\cos(\Omega)}{\lambda_c}$, where $\cos(\Omega)$ is normally known as the directional cosine, and Ω is the LoS incidence angle that can be used to calculate the projection of the 3D velocity onto the connection between the AP and the UE. As a result the actual mobility V is lower bounded by the Doppler velocity V_d, i.e., $V \geq V_d$. For any given directional cosine $\cos(\Omega)$, and carrier frequency f_c, a larger velocity lead to higher Doppler shift f_d, which in return yields a shorter coherence time T_c.

Considering different carrier frequencies, the coherence time as a function of Doppler velocity is illustrated in Fig. 5. It is worth pointing out that the horizontal axis refers to the Doppler velocity V_d rather than the 3D velocity V. It is observed that the coherence time T_c at 5.2 GHz (the WiFi band) shows a clear longer duration compared with that at higher mmWave band which matches the fact that a high carrier is more sensitive to a higher mobility. In particular, the channel coherence time T_c at $V_d = 0.6$ m/s drops to roughly 3 ms at 39 GHz and 2 ms at 73 GHz, both are much shorter than the 10 ms benchmark (red dashed line) defined

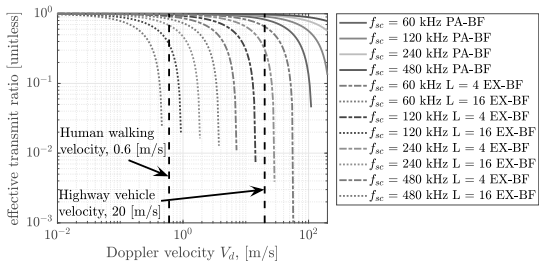

FIGURE 6. The effective transmit ratio $1 - T_{IA}/T_f$ as a function of Doppler velocity V_d for the considered BF strategies.

as the frame duration of 5G NR [49]. We mark this difference in Fig. 5 enhancing the importance of reducing the IA latency which can be achieved by the proposed PA-BF, as is discussed and demonstrated next.

Herein, the cloud-oriented mobile networks are operating at a carrier of 39 GHz with 100 MHz bandwidth. The same carrier was adopted in, e.g., [50] with double bandwidth for positioning in 5G network. Furthermore, we assume the frame duration T_f has the same length as the channel coherence time T_c, $T_f = T_c$. Thereafter, we first present the effective transmit ratio of the considered two beamforming strategies over different number of antenna elements L and the sub-carrier spacing f_{sc} used in the UL OFDM signal. It is noteworthy that the f_{sc} is essentially the beam-switching rate since we assume that each training beam (codeword) occupies one OFDM symbol. Based on (22) and (26), the effective transmit ratio for both EX-BF and PA-BF is presented in Fig. 6 as a function of the Doppler velocity. It is observed that for EX-BF, under the same f_{sc} (the same colored curves), a smaller L in general yields a higher η_{EX} as smaller L yields a smaller size of the codebook. Furthermore, for a given the number of antenna elements L, the larger the f_{sc} in general leads to the higher the η_{EX} due to the fact that each codeword takes up less time for a higher f_{sc}, which in return, leaves more time for data transmission.

Meanwhile, the effective transmit ratio of the PA-BF that is independent of antenna configuration since the codebook of PA-BF consists of only one codeword that is constructed based on the estimated UE location is also depicted in Fig. 6. Similar to the EX-BF case, a larger f_{sc} fulfills a higher η_{PA}. Moreover, we introduce a new metric, the *Doppler tolerance* that corresponds to the maximum Doppler velocity that the effective transmit ratio remains positive, that is, the horizontal coordinate where the curves ends in Fig. 6. In particular, the metric indicates the largest velocity that the corresponding BF strategy can support without using the whole frame duration only for beam training. We see that a lower L or a higher f_{sc} or both yield a higher Doppler tolerance which can be employed to the IA for high velocity applications. Comparing the EX-BF with the PA-BF, it is seen that under the same f_{sc}, the PA-BF not only achieves a higher effective transmit ratio for the most of the tested velocities, but more significantly, a much higher Doppler tolerance than the EX-BF. Hence, for the HST applications [51], [52] where objects are moving around 100 m/s, the PA-BF is clearly a better candidate.

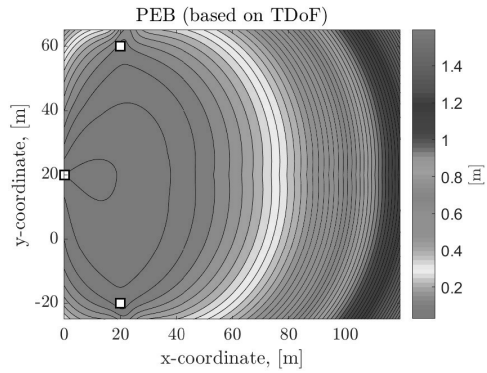

FIGURE 7. The 3D PEB acquired via TDoF measurements in the UL on the UE height under the same AP deployment of Fig. 4 for a consistent demonstration.

TABLE 2. Simulation parameters.

Parameter	Value
Carrier frequency f_c	39 GHz
Sub-carrier spacing f_{sc}	240 kHz
Signal bandwidth B_w	100 MHz
UL transmit power $P_{\text{T,UL}}$	10 dBm
DL transmit power $P_{\text{T,DL}}$	27 dBm
Max. array gain $\beta_0\,(4, \phi)$	14 dBi
Max. array gain $\beta_0\,(16, \phi)$	25 dBi
Pathloss model	InH shopping mall

In addition, the 3D PEB based on the TDoF measurements in the UL is given in Fig. 7 showing how the positioning accuracy varies at different locations. It is noted from (9) and (11) that the PEB is mainly affected by the measurement noise statistics $\boldsymbol{R}_{\Delta\tau}$ which is characterized in (7) that is determined by two factors. In particular, the first one refers to the signal bandwidth which is fixed[7] in the considered scenario. The second one is the received SNR that is mainly inversely proportional to the distance. Therefore, it is seen that the farther the UE goes from the LoS-APs, the higher the resulting PEB for that location. More importantly, Fig. 7 demonstrates the theoretical PEB (11) under the APs deployment therein. As expected, when the number and deployment of APs changes (see Section. VI-A), the PEB varies accordingly.

Once the location accuracy of the UE is acquired, the PA-BF is to be carried out to enhance the DL communications. For comparison, the EX-BF strategy is applied under the same scenario and the same set of parameters summarized in Table 2. According to the discussion in Section V-A, the performance of BF mainly depends on two metrics, the effective transmit ratio η and the BF

[7]Even though the signal bandwidth is fixed herein, it is noteworthy that a wider bandwidth suggests a smaller determinant of $\boldsymbol{R}_{\Delta\tau}$, which in turn, yields a larger FIM and therefore a smaller PEB.

TABLE 3. Considered 3D positioning accuracies based on the positioning accuracy requirement in [43] where the Gaussian distribution is assumed in all the directions.

3D error [m]	**Error in x** σ_x, [m]	**Error in y** σ_y, [m]	**Error in z** σ_z, [m]
3	2.09	2.09	0.51
10	7	7	1.41
50	35	35	7.07

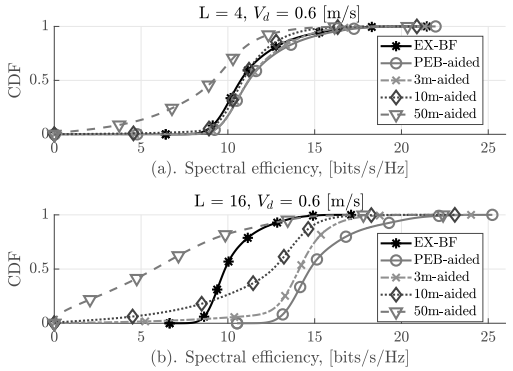

FIGURE 8. The CDF of spectral efficiency obtained via EX-BF and PA-BF aided by different positioning accuracy with UEs at 0.6 m/s Doppler velocity over the whole map.

gain G_{BF}. Due to the natural attributes of the studied BF strategies, the G_{BF} for EX-BF can always be guaranteed to reach the maximum whereas that for PA-BF varies based on the available a prior of the UEs' locations. Hence, to evaluate the performance of PA-BF under different positioning accuracies, we summarize considered (UL) positioning accuracies in Table 3 where the 3D error as well as the error along each direction (x-, y-, z-) are specified, in which the error along each direction fits a zero mean Gaussian distribution. Note that the values tabulated in Table 3 are selected according to the positioning accuracy requirements defined in [43].

Taking two feasible UE mobilities in the indoor environment into account, we present the cumulative distribution function (CDF) of the spectral efficiency achieved by the EX-BF and all the considered PA-BF throughout the whole map in Fig. 8 and Fig. 9. Note that the results are obtained based on 1000 simulation trials over all the 10 randomly generated AP deployments. The CDF of spectral efficiency for all the considered locations on the map at normal UE speed (0.6m/s) is given in Fig. 8. From Fig. 8a where each AP is equipped with a 4×4 URA, we see that the performance of EX-BF together with all the tested PA-BF except the 50m-aided are quite similar. In Fig. 8b where the 16×16 URA is considered, the performance of all considered beamforming techniques becomes distinguishable, and higher positioning accuracy does return higher spectral efficiency. It is also noteworthy that, the comparison between Fig. 8a and Fig. 8b demonstrates that the curves for PEB-aided, 3m-aided and 10m-aided PA-BF actually shift towards the right yielding a better performance whereas the

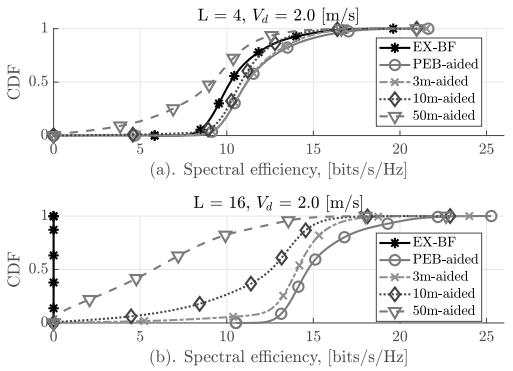

FIGURE 9. The CDF of spectral efficiency obtained via EX-BF and PA-BF aided by different positioning accuracy with UEs at 2 m/s Doppler velocity over the whole map.

behaviors for 50m-aided PA-BF and EX-BF shift to the left manifesting a worse performance. This result suggests that the PA-BF aided by higher positioning accuracy can actually take advantage of a higher array gain coming from a larger L, such that the narrower beam is accurately pointed towards the UE, whereas the difference in terms of positioning accuracy plays a less significant role for a wider array beam (smaller L). However, the considered 50m positioning accuracy is simply too high for PA-BF to ensure a stable spectral efficiency under the considered scenario. Meanwhile, when the number of antenna elements L increases, the worse performance of EX-BF is mainly due to the fact that narrower array beam leads to more codewords to cover the entire spatial domain, which leads to a lower effective transmit ratio and worse overall performance.

In Fig. 9, we further compare the performance at a higher mobility where the Doppler velocity $V_d = 2$ m/s. Specifically, the performance at 4×4 URA case in Fig. 9a for all considered methods remains comparable with the results in Fig. 8a although the EX-BF suffered a little degradation in performance as the black curve shifts towards left. On the other hand, in Fig. 9b where the array gain becomes higher and the beamwidth becomes narrower, a similar performance of PA-BFs compared to Fig. 8b is seen as better positioning accuracy yields better spectral efficiency. A major difference compared to Fig. 8b lies in the performance of EX-BF which stuck roughly at 0 bits/s/Hz. The numerical reason is given in Fig. 6 which demonstrates that the Doppler tolerance at $f_{\text{sc}} = 240$ kHz and $L = 16$ is about 1.9 m/s, therefore, the effective transmit ratio of EX-BF is negative for a 16×16 URA at 2 m/s Doppler velocity, which means that there is no time for data transmission as the beam training takes up the whole frame duration T_f.

Finally, we present the average spectral efficiency μ_R as a function of 2D distance $d_{\text{2D},1}$[8] (from the UEs to the primary AP) together with the ± 1 standard deviation of the spectral efficiency σ_R interval in Fig. 10. Although the CDF in Fig. 8

[8]Thereafter, we denote $d_{\text{2D},1}$ as d_{2D} for simplicity.

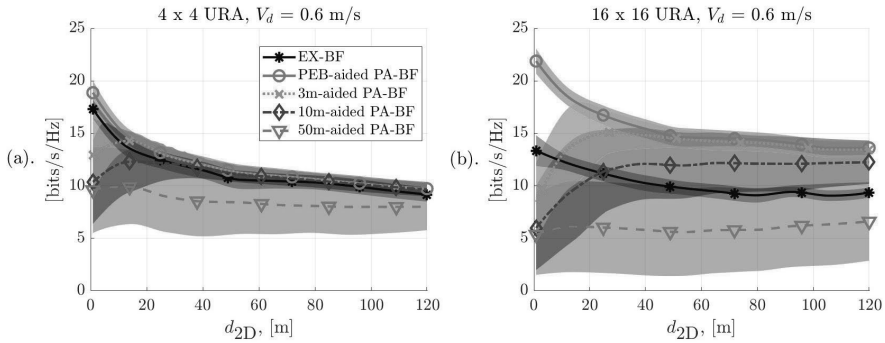

FIGURE 10. The $\mu_R \pm \sigma_R$ interval plot of the spectral efficiency as a function of 2D distance d_{2D} from the primary AP applying the PA-BF with various positioning accuracies and EX-BF.

and Fig. 9 present the global performance through the entire map, the $\mu_R \pm \sigma_R$ as a function of d_{2D} provides insights on the performance dependency of both PA-BF and EX-BF w.r.t. the distance. It can be seen that the average spectral efficiency μ_R of EX-BF and PEB-aided PA-BF decrease when d_{2D} increases (mainly due to a larger path-loss), whereas non-PEB-aided PA-BFs have the worst performance at very small and very large d_{2D}. The worse performance at smaller d_{2D} implies that positioning accuracy has a bigger impact on PA-BF when AP and UE are close to than they are far away from each other. Furthermore, it is noteworthy that the performance of some non PEB-aided PA-BFs does converge[9] to the performance of PEB-aided PA-BF when d_{2D} reaches beyond a certain threshold that is dependent on the array beamwidth.

Specifically, for the 4×4 URA that is shown in Fig. 10a, the performance of 10m-aided and 3m-aided converges to PEB-aided performance at $d_{2D} = 10$m and $d_{2D} = 38$m, respectively. The performance of 50m-aided PA-BF remains as the worst on account of a low μ_R and a larger σ_R over the whole d_{2D}. For the 16×16 URA presented in Fig. 10b, only 3m-aided PA-BF converges towards the PEB-aided performance at approximately $d_{2D} = 50$m. Meanwhile, the performance gap in terms of μ_R between the 10m-aided and PEB-aided PA-BF gradually gets smaller as the 2D distance increases, but suffered a bigger σ_R. Similar to the 50m-aided PA-BF under 4×4 URA, the corresponding performance of 16×16 URA remains at a much lower level with $\sigma_R = 5$ bits/s/Hz throughout the whole tested d_{2D}.

Based on the results and analysis, we conclude that, i) for a given array beamwidth, the farther the UE is from the primary AP, the less accurate positioning is needed for the PA-BF to achieve the same spectral efficiency; ii) a wider array beamwidth (smaller L) yields a shorter d_{2D} at which the communication performance of PA-BFs (aided by different positioning accuracies) converges. On the other hand, the EX-BF has demonstrated a extreme-close performance to the PEB-aided PA-BF when $L = 4$ and a much worse performance if the number of antenna elements L raises to 16.

[9]The performance convergence includes both μ_R and σ_R.

It is worth pointing out that under both URA configurations, EX-BF demonstrates a comparable or even better performance than the non PEB-aided PA-BF especially at a closer distance. Furthermore, the EX-BF has manifested a distance independent σ_R throughout the whole considered d_{2D} which means that EX-BF provides a stable communication quality that might be favored for certain applications that the reliability outweighs the throughput.

VII. CONCLUSION AND DISCUSSION

In this paper, we proposed and examined a cloud-oriented communication system where the achieved location-awareness via UL positioning was exploited to carry out efficient BF in the DL (i.e., the PA-BF), which, as a result, enhanced the communication performance in a mmWave mobile networks. In terms of the positioning accuracy, we considered and analyzed the theoretical PEB obtained based on the TDoF measurements in the context of multi-connectivity. We further evaluated the dependency of such PEB on the received SNR, on the array size, as well as on the geometric relations. For comparison, the EX-BF strategy was employed as a benchmark, based on a 3D DFT-codebook. We showed that, with the knowledge of the UE location, the proposed PA-BF achieved a much higher effective transmit ratio than the EX-BF which in turn leaded to a longer time for data transmission. The PA-BF is therefore inherently much more suitable for applications that require high velocity, such as HST.

In terms of communication performance, we assessed the spectral efficiency of EX-BF and PA-BF under various positioning accuracy assumptions besides the PEB. Our simulation results showed that, with reasonably small positioning error and narrow beam antenna configurations, the PA-BF in general achieved a higher spectral efficiency than the EX-BF especially at higher velocities. Although a larger positioning error in general leaded to a worse performance, the degradation of performance became less significant as the distance between UE and the primary AP reached beyond a certain threshold that is dependent on the antenna beamwidth. In other words, the aforementioned threshold is farther for a narrower array beamwidth (more antenna elements) than a wider array beamwidth (less antenna elements). Additionally, under a certain UE-to-AP distance, the wider

the array beamwidth is, the less accurate the positioning has to be for achieving the same communication performance. Therefore, a wide array beamwidth shall be favored if positioning uncertainty is large, whereas the narrow-beam array is preferred when positioning accuracy is high. Additionally, it is observed that the EX-BF, which does not rely on UL positioning, maintained a stable performance that was mainly affected by the path-loss, but was unable to support high velocity UEs.

As such, the insight obtained via our results serves as a look-up table (see results in Fig. 8, Fig. 9 and Fig. 10) on selecting the BF strategy with a better performance in terms of spectral efficiency under specific array sizes according to the uncertainty of UEs' location. For future investigation, we propose a *hybrid-BF* strategy that integrates the advantage of both codebook-based BF and PA-BF in order to cope with the joint LoS/NLoS conditions in a more practical environment.

ACKNOWLEDGMENT

The authors appreciate Dr. G. Destino (from the University of Oulu, Finland) for his insightful comments on improving the quality of this paper. In addition, they express their sincere gratitude towards the Finnish Foundation for Technology Promotion. Finally, they sincerely thank the Editor and anonymous reviewers for the encouraged advice and constructive comments that improved the contribution of this work.

REFERENCES

[1] M. Marcus and B. Pattan, "Millimeter wave propagation: Spectrum management implications," *IEEE Microw. Mag.*, vol. 6, no. 2, pp. 54–62, Jun. 2005.

[2] Y. Lu, P. Richter, and E. S. Lohan, "Opportunities and challenges in the industrial Internet of Things based on 5G positioning," in *Proc. 8th Int. Conf. Localization GNSS (ICL-GNSS)*, Jun. 2018, pp. 1–6.

[3] M. Kamel, W. Hamouda, and A. Youssef, "Ultra-dense networks: A survey," *IEEE Commun. Surveys Tuts.*, vol. 18, no. 4, pp. 2522–2545, 4th Quart., 2016.

[4] M. Koivisto, A. Hakkarainen, M. Costa, P. Kela, K. Leppanen, and M. Valkama, "High-efficiency device positioning and location-aware communications in dense 5G networks," *IEEE Commun. Mag.*, vol. 55, no. 8, pp. 188–195, Aug. 2017.

[5] E. G. Larsson, O. Edfors, F. Tufvesson, and T. L. Marzetta, "Massive MIMO for next generation wireless systems," *IEEE Commun. Mag.*, vol. 52, no. 2, pp. 186–195, Feb. 2014.

[6] E. Björnson, J. Hoydis, and L. Sanguinetti, "Massive MIMO networks: Spectral, energy, and hardware efficiency," *Found. Trends Signal Process.*, vol. 11, nos. 3–4, pp. 154–655, 2017, doi: 10.1561/2000000093.

[7] M. Giordani, M. Polese, A. Roy, D. Castor, and M. Zorzi, "A tutorial on beam management for 3GPP NR at mmWave frequencies," *IEEE Commun. Surveys Tuts.*, vol. 21, no. 1, pp. 173–196, 1st Quart., 2019.

[8] P. Popovski, J. J. Nielsen, C. Stefanovic, E. D. Carvalho, E. Strom, K. F. Trillingsgaard, A.-S. Bana, D. M. Kim, R. Kotaba, J. Park, and R. B. Sorensen, "Wireless access for ultra-reliable low-latency communication: Principles and building blocks," *IEEE Netw.*, vol. 32, no. 2, pp. 16–23, Mar. 2018.

[9] H. Shokri-Ghadikolaei, C. Fischione, G. Fodor, P. Popovski, and M. Zorzi, "Millimeter wave cellular networks: A MAC layer perspective," *IEEE Trans. Commun.*, vol. 63, no. 10, pp. 3437–3458, Oct. 2015.

[10] C. Jeong, J. Park, and H. Yu, "Random access in millimeter-wave beamforming cellular networks: Issues and approaches," *IEEE Commun. Mag.*, vol. 53, no. 1, pp. 180–185, Jan. 2015.

[11] V. Desai, L. Krzymien, P. Sartori, W. Xiao, A. Soong, and A. Alkhateeb, "Initial beamforming for mmWave communications," in *Proc. 48th Asilomar Conf. Signals, Syst. Comput.*, Nov. 2014, pp. 1926–1930.

[12] H. Guo, B. Makki, and T. Svensson, "A genetic algorithm-based beamforming approach for delay-constrained networks," in *Proc. 15th Int. Symp. Modeling Optim. Mobile, Ad Hoc, Wireless Netw. (WiOpt)*, May 2017, pp. 1–7.

[13] Z. Xiao, T. He, P. Xia, and X.-G. Xia, "Hierarchical codebook design for beamforming training in millimeter-wave communication," *IEEE Trans. Wireless Commun.*, vol. 15, no. 5, pp. 3380–3392, May 2016.

[14] W. Wu, D. Liu, Z. Li, X. Hou, and M. Liu, "Two-stage 3D codebook design and beam training for millimeter-wave massive MIMO systems," in *Proc. IEEE 85th Veh. Technol. Conf. (VTC Spring)*, Jun. 2017, pp. 1–7.

[15] A. Capone, I. Filippini, and V. Sciancalepore, "Context-based cell search in millimeter wave 5G networks," in *Proc. 21th Eur. Wireless conf.*, May 2015, pp. 1–5. [Online]. Available: http://arxiv.org/abs/1501.02223

[16] M. Giordani, M. Mezzavilla, and M. Zorzi, "Initial access in 5G mmWave cellular networks," *IEEE Commun. Mag.*, vol. 54, no. 11, pp. 40–47, Nov. 2016.

[17] N. Garcia, H. Wymeersch, E. G. Strom, and D. Slock, "Location-aided mm-wave channel estimation for vehicular communication," in *Proc. IEEE 17th Int. Workshop Signal Process. Adv. Wireless Commun. (SPAWC)*, Jul. 2016, pp. 1–5.

[18] G. Destino and H. Wymeersch, "On the trade-off between positioning and data rate for mm-wave communication," in *Proc. IEEE Int. Conf. Commun. Workshops (ICC Workshops)*, May 2017, pp. 797–802.

[19] X. Chen and P. Fan, "Low-complexity location-aware multi-user massive MIMO beamforming for high speed train communications," in *Proc. IEEE 85th Veh. Technol. Conf. (VTC Spring)*, Jun. 2017, pp. 1–6.

[20] E. Mohamed, H. Esmaiel, and A. Abdelreheem, "Adaptive location-based millimetre wave beamforming using compressive sensing based channel estimation," *IET Commun.*, vol. 13, no. 9, pp. 1287–1296, Feb. 2019.

[21] R. Maiberger, D. Ezri, and M. Erlihson, "Location based beamforming," in *Proc. IEEE 26th Conv. Elect. Electron. Eng. Israel*, Nov. 2010, pp. 184–187.

[22] P. Kela, M. Costa, J. Turkka, M. Koivisto, J. Werner, A. Hakkarainen, M. Valkama, R. Jantti, and K. Leppanen, "Location based beamforming in 5G ultra-dense networks," in *Proc. IEEE 84th Veh. Technol. Conf. (VTC-Fall)*, Sep. 2016, pp. 1–7.

[23] P. Kela, M. Costa, K. Leppanen, and R. Jantti, "Location-aware beamformed downlink control channel for ultra-dense networks," in *Proc. IEEE Conf. Standards Commun. Netw. (CSCN)*, Sep. 2017, pp. 7–11.

[24] X. Cheng, M. Wang, and S. Li, "Compressive sensing-based beamforming for millimeter-wave OFDM systems," *IEEE Trans. Commun.*, vol. 65, no. 1, pp. 371–386, Jan. 2017.

[25] A. Alkhateeb, O. El Ayach, G. Leus, and R. W. Heath, Jr., "Channel estimation and hybrid precoding for millimeter wave cellular systems," *IEEE J. Sel. Topics Signal Process.*, vol. 8, no. 5, pp. 831–846, Oct. 2014.

[26] A.-S. Bana, E. de Carvalho, B. Soret, T. Abrão, J. C. Marinello, E. G. Larsson, and P. Popovski, "Massive MIMO for Internet of Things (IoT) connectivity," 2019, *arXiv:1905.06205*. [Online]. Available: http://arxiv.org/abs/1905.06205

[27] A. Zhou, L. Wu, S. Xu, H. Ma, T. Wei, and X. Zhang, "Following the shadow: Agile 3-D beam-steering for 60 GHz wireless networks," in *Proc. IEEE Conf. Comput. Commun. (INFOCOM)*, Apr. 2018, pp. 2375–2383.

[28] T. Wei and X. Zhang, "Pose information assisted 60 GHz networks: Towards seamless coverage and mobility support," in *Proc. 23rd Annu. Int. Conf. Mobile Comput. Netw. (MobiCom)*, New York, NY, USA, 2017, pp. 42–55. [Online]. Available: http://doi.acm.org/10.1145/3117811.3117832

[29] A. S. Mubarak, H. Esmaiel, and E. M. Mohamed, "LTE/Wi-Fi/mmWave RAN-level interworking using 2C/U plane splitting for future 5G networks," *IEEE Access*, vol. 6, pp. 53473–53488, 2018.

[30] *NR; Radio Resource Control (RRC) Protocol Specification (Release 15)*, document TS 38.331 V15.6.0, 3GPP, Jun. 2018.

[31] K. Xu, K.-C. Wang, R. Amin, J. Martin, and R. Izard, "A fast cloud-based network selection scheme using coalition formation games in vehicular networks," *IEEE Trans. Veh. Technol.*, vol. 64, no. 11, pp. 5327–5339, Nov. 2015.

[32] *Study on Channel Model for Frequency Spectrumb Above 6 GHz (Release 15)*, document TR 38.900 V15.0.0, 3GPP, Jun. 2018.

[33] J. Kulmer, E. Leitinger, P. Meissner, S. Hinteregger, and K. Witrisal, "Cooperative localization and tracking using multipath channel information," in *Proc. Int. Conf. Localization GNSS (ICL-GNSS)*, Jun. 2016, pp. 1–6.

[34] J. Kulmer, E. Leitinger, S. Grebien, and K. Witrisal, "Anchorless cooperative tracking using multipath channel information," *IEEE Trans. Wireless Commun.*, vol. 17, no. 4, pp. 2262–2275, Apr. 2018.
[35] Y. Niu, Y. Li, D. Jin, L. Su, and A. V. Vasilakos, "A survey of millimeter wave communications (mmWave) for 5G: Opportunities and challenges," *Wireless Netw.*, vol. 21, no. 8, pp. 2657–2676, Nov. 2015, doi: 10.1007/s11276-015-0942-z.
[36] B. Etzlinger, H. Wymeersch, and A. Springer, "Cooperative synchronization in wireless networks," *IEEE Trans. Signal Process.*, vol. 62, no. 11, pp. 2837–2849, Jun. 2014.
[37] M. Koivisto, J. Talvitie, M. Costa, K. Leppänen, and M. Valkama, "Joint cmWave-based multiuser positioning and network synchronization in dense 5G networks," in *Proc. IEEE Wireless Commun. Netw. Conf. (WCNC)*, Apr. 2018, pp. 1–6.
[38] J. Medbo, I. Siomina, A. Kangas, and J. Furuskog, "Propagation channel impact on LTE positioning accuracy: A study based on real measurements of observed time difference of arrival," in *Proc. IEEE 20th Int. Symp. Pers., Indoor Mobile Radio Commun.*, Sep. 2009, pp. 2213–2217.
[39] S. Sand, A. Dammann, and C. Mensing, *Positioning in Wireless Communications Systems*. Hoboken, NJ, USA: Wiley, Jun. 2014.
[40] Y. Huang and K. Boyle, *Antennas: From Theory to Practice*. Hoboken, NJ, USA: Wiley, 2008.
[41] S. M. Kay, *Fundamentals of Statistical Signal Processing: Estimation Theory*. Upper Saddle River, NJ, USA: Prentice-Hall, 1993.
[42] R. Zekavat and R. M. Buehrer, *Handbook of Position Location: Theory, Practice and Advances*, 1st ed. Hoboken, NJ, USA: Wiley, 2011.
[43] *Study on Positioning Use Cases: Stage 1 (Release 16)*, document TR 22.872 V16.0.0, 3GPP, Jun. 2018.
[44] A. Richter, "Estimation of radio channel parameters: Models and algorithms," Ph.D. dissertation, Ilmenau Univ. Technol., Ilmenau, Germany, 2005.
[45] J. Wang, Z. Lan, C.-S. Sum, C.-W. Pyo, J. Gao, T. Baykas, A. Rahman, R. Funada, F. Kojima, I. Lakkis, H. Harada, and S. Kato, "Beamforming codebook design and performance evaluation for 60 GHz wideband WPANs," in *Proc. IEEE 70th Veh. Technol. Conf. Fall*, Sep. 2009, pp. 1–6.
[46] D. Tse and P. Viswanath, *Fundamentals of Wireless Communications*. Cambridge, U.K.: Cambridge Univ. Press, 2005.
[47] E. Dahlman, S. Parkvall, and J. Skold. (2018). *5G NR: The Next Generation Wireless Access Technology*. Elsevier Science. [Online]. Available: https://books.google.fi/books?id=lcSLswEACAAJ
[48] G. L. Stüber, *Principles of Mobile Communication*, 3rd ed. New York, NY, USA: Springer, 2011.
[49] *NR: Physical Layer; General Description (Release 15)*, document TS 38.201 V15.0.0, 3GPP, Jan 2018.
[50] E. Rastorgueva-Foi, M. Koivisto, M. Valkama, M. Costa, and K. Leppänen, "Localization and tracking in mmWave radio networks using beam-based DoD measurements," in *Proc. 8th Int. Conf. Localization GNSS (ICL-GNSS)*, Jun. 2018, pp. 1–6.
[51] J. Talvitie, T. Levanen, M. Koivisto, K. Pajukoski, M. Renfors, and M. Valkama, "Positioning of high-speed trains using 5G new radio synchronization signals," in *Proc. IEEE Wireless Commun. Netw. Conf. (WCNC)*, Apr. 2018, pp. 1–6.
[52] T. Levanen, J. Talvitie, R. Wichman, V. Syrjälä, M. Renfors, and M. Valkama, "Location-aware 5G communications and Doppler compensation for high-speed train networks," in *Proc. Eur. Conf. Netw. Commun. (EuCNC)*, Jun. 2017, pp. 1–6.

YI LU (Student Member, IEEE) was born in Tianjin, China, in 1988. He received the M.Sc. degree (Hons.) in mobile communications from Heriot-Watt University, U.K., in 2012. From 2014 to 2017, he was working as a Research Assistant with the Universitat Autonoma de Barcelona (UAB), Spain, on several different projects that cover topics from the phase-shift holography for electrically large antenna measurement to statistical signal processing for GNSS-oriented applications. Since March 2018, he has been employed with the Electrical Engineering Unit, Tampere University, as a Doctoral Researcher. His research interests include network-centric positioning system and positioning-aided communications in mmWave mobile networks.

MIKE KOIVISTO (Student Member, IEEE) was born in Rauma, Finland, in 1989. He received the M.Sc. degree in applied mathematics from the Tampere University of Technology (TUT), Finland, in 2015. He is currently pursuing the Ph.D. degree with the Electrical Engineering Unit, Tampere University. His research interests include cellular networks and network-based positioning with an emphasis on positioning algorithm development and the utilization of location information in future mobile networks.

JUKKA TALVITIE (Member, IEEE) was born in Hyvinkää, Finland, in 1981. He received the M.Sc. degree in automation engineering and the Ph.D. degree in computing and electrical engineering from the Tampere University of Technology (TUT), Finland, in 2008 and 2016, respectively. He is currently a University Lecturer with Tampere University, Finland. In addition to academic research, he has involved several years in industry-based research and development projects on a wide variety of research topics, including radio signal waveform design, network-based positioning and next generation WLAN, and cellular system design. His main research interests include signal processing for communications, wireless locations techniques, radio signal waveform design, and radio network system level development.

MIKKO VALKAMA (Senior Member, IEEE) was born in Pirkkala, Finland, in 1975. He received the M.Sc. and Ph.D. degrees (Hons.) in electrical engineering from the Tampere University of Technology (TUT), Finland, in 2000 and 2001, respectively. In 2002, he received the Best Ph.D. Thesis Award from the Finnish Academy of Science and Letters for his dissertation entitled Advanced I/Q Signal Processing for Wideband Receivers: Models and Algorithms. In 2003, he was a Visiting Postdoctoral Researcher with the Communications Systems and Signal Processing Institute, SDSU, San Diego, CA, USA. He is currently a Full Professor and the Laboratory Head of the Electrical Engineering Unit, Tampere University. His general research interests include communications signal processing, estimation and detection techniques, signal processing algorithms for flexible radios, cognitive radios, full-duplex radios, radio localization, 5G mobile cellular radio networks, digital transmission techniques such as different variants of multicarrier modulation methods and OFDM, and radio resource management for ad-hoc and mobile networks.

ELENA SIMONA LOHAN (Senior Member, IEEE) received the M.Sc. degree in electrical engineering from the Polytechnic University of Bucharest, in 1997, the D.E.A. degree in econometrics from Ecole Polytechnique, Paris, in 1998, and the Ph.D. degree in telecommunications from the Tampere University of Technology, in 2003. She is currently an Associate Professor with the Electrical Engineering Unit, Tampere University (formerly known as the Tampere University of Technology), and a Visiting Professor with the Universitat Autonoma de Barcelona (UAB), Spain. She is leading a research group on signal processing for wireless positioning. She is a Co-Editor of the first book on Galileo satellite system *Galileo Positioning Technology* (Springer), the Co-Editor of a book *Multi-Technology Positioning* (Springer), and the author or coauthor of more than 185 international peer-reviewed publications, and holds six patents and inventions.

PUBLICATION

IV

Feasibility of Location-Aware Handover for Autonomous Vehicles in Industrial Multi-Radio Environments

Y. Lu, M. Gerasimenko, R. Kovalchukov, M. Stusek, J. Urama, J. Hosek, M. Valkama and E. Lohan

Sensors 20.21 (2020)
DOI: 10.3390/s20216290

sensors

MDPI

Article

Feasibility of Location-Aware Handover for Autonomous Vehicles in Industrial Multi-Radio Environments

Yi Lu [1,*], Mikhail Gerasimenko [1,2], Roman Kovalchukov [1], Martin Stusek [1,2], Jani Urama [1], Jiri Hosek [2], Mikko Valkama [1] and Elena Simona Lohan [1]

[1] Department of Electrial Engineering, Tampere University, 33720 Tampere, Finland; gerasimenkoma89@gmail.com (M.G.); roman.kovalchukov@tuni.fi (R.K.); xstuse01@vutbr.cz (M.S.); jani.urama@tuni.fi (J.U.); mikko.valkama@tuni.fi (M.V.); elena-simona.lohan@tuni.fi (E.S.L.)

[2] Department of Telecommunications, Brno University of Technology, 616 00 Brno, Czech Republic; hosek@feec.vutbr.cz

* Correspondence: yi.lu@tuni.fi

Received: 28 August 2020; Accepted: 2 November 2020; Published: 5 November 2020

Abstract: The integration of millimeter wave (mmWave) and low frequency interfaces brings an unique opportunity to unify the communications and positioning technologies in the future wireless heterogeneous networks (HetNets), which offer great potential for efficient handover using location awareness, hence a location-aware handover (LHO). Targeting a self-organized communication system with autonomous vehicles, we conduct and describe an experimental and analytical study on the LHO using a mmWave-enabled robotic platform in a multi-radio environment. Compared to the conventional received signal strength indicator (RSSI)-based handover, the studied LHO not only improves the achievable throughput, but also enhances the wireless link robustness for the industrial Internet-of-things (IIoT)-oriented applications. In terms of acquiring location awareness, a geometry-based positioning (GBP) algorithm is proposed and implemented in both simulation and experiments, where its achievable accuracy is assessed and tested. Based on the performed experiments, the location-related measurements acquired by the robot are not accurate enough for the standalone-GBP algorithm to provide an accurate location awareness to perform a reliable handover. Nevertheless, we demonstrate that by combining the GBP with the dead reckoning, more accurate location awareness becomes achievable, the LHO can therefore be performed in a more optimized manner compared to the conventional RSSI-based handover scheme, and is therefore able to achieve approximately twice as high average throughput in certain scenarios. Our study confirms that the achieved location awareness, if accurate enough, could enable an efficient handover scheme, further enhancing the autonomous features in the HetNets.

Keywords: dead reckoning; geometry-based positioning; indoor industrial environments; location-aware handover; mmWave communications; multi-radio access; radio positioning

1. Introduction

Wireless communications and mobile networks are inherently integrated into the daily activities of every business sector, ranging from academic events to industrial operations. With the paradigm introduced by ITU, known as "Always Best Connected" (ABC) [1], the 3rd generation partnership project (3GPP) has proposed the coordinated multi-point (CoMP) operation in [2], where coordinated transmission and reception applies between macro cell(s) and micro cell(s) of heterogeneous networks (HetNets) to provide seamless, quality of service (QoS)-aware media services to the active user equipment (UE), including Internet of Things (IoT) devices and/or mobile vehicles therein.

Furthermore, dual connectivity (DC) has been proposed in [3], where any arbitrary UE enjoys radio resources provided by access point (AP) with the same/different radio access technology (RAT) under non-ideal backhaul. To further exploit the benefits of DC from the perspectives of user throughput and mobility enhancement within small cell networks (SCNs), multi-radio dual connectivity (MR-DC) [4] grows to become a feasible solution for the cooperation/co-existence of 4G long term evolution (LTE) and 5G new radio (NR), facilitating the convergence of communications and positioning solutions as well as enabling the autonomous function for the connected vehicles. As an extension of DC, MR-DC suggests that the UE can be configured to maintain multiple connections [5] and utilize resources of multi-RAT enabled networks, i.e., the HetNets.

In the context of multi-RATs and SCNs, seamlessly handing over to or selecting a network/RAT, which provides the best possible QoS to the UE, remains a crucial enabler of a self-organized communication system, in which the connected vehicles/robots are capable of performing efficient handover in a self-organized manner via the obtained location awareness, such that the throughput as well as the link quality are jointly optimized. Apart from the IEEE 802.21 multimedia-independent handover (MIH) standard that supports a QoS-based handover within the HetNets, several works [6–18] investigated the location-aware handover (LHO) and/or location-aware network selection (LNS) strategy ensuring that the mobile users have access to the required media service via the best available network. The objective of our work is therefore to investigate the feasibility and benefits of such efficient handover decision making schemes (i.e., the LHO) when integrating the positioning solutions. Furthermore, as a result of the proliferation of industrial vehicles [19], we believe that the LHO algorithm will not only be beneficial to the conventional mobile users, but also it will be desirable for vehicle/robot-based industrial Internet of things (IIoT) applications where multi-Gbps throughput is required for data offloading/exchange (e.g., virtual reality [20]) with one or several millimeter wave (mmWave) APs.

In this paper, we describe an efficient LHO scheme for a multi-RAT robotic platform in an indoor multi-radio environment. Thereafter, an experimental study is performed to evaluate the concept feasibility and demonstrate the achievable performance. In our measurement setup, one mmWave AP and one centimeter wave (cmWave) AP (WiFi at 2.5 GHz) are deployed and utilized. Furthermore, we construct a 3D line-of-sight (LoS) map for the area of interest where the LHO algorithm is tested. This map indicates the area where the robot has the LoS communications with the mmWave AP. Then, by considering the available location-related measurements (LRMs) (to be discussed in Section 2.2) at the robot side, we formulate a geometry-based positioning (GBP) algorithm and evaluate the corresponding achievable positioning accuracy in theory.

Although the theoretical positioning accuracy is shown to be promising, the experimental outcomes with a standalone GBP are hardly satisfactory due to the inaccuracy and instability of LRMs, as we discuss in Section 5.2. However, by combining the GBP and the dead reckoning (DR) methods, the experimental results corroborate that with the LHO scheme a handover can be performed right before the robot loses its LoS connection with respect to (w.r.t.) the mmWave AP. Hence, the LHO scheme guarantees higher throughput for the robot than the conventional received signal strength indicator (RSSI)-based handover approach. The key contributions of our paper are summarized as follows:

- we formulate and analyze a positioning algorithm, GBP, based on the angle measurements from one mmWave AP enabling 2D positioning in the 3D environment;
- we propose an efficient LHO handover scheme that utilizes both the GBP positioning algorithm as well as the DR method;
- we study and test the proposed handover scheme using a multi-RAT prototype robot developed by our group, and we assess the statistics of RSSI, latency, and estimated robot locations.

The rest of the paper is organized as follows. In Section 2, we systematically review the state-of-the-art in LHO/LNS, which is followed by the introduction of the problem formulation. Section 3 outlines the utilized multi-RAT robotic platform as well as the scenario of interest for

conducting the LHO. In Section 4, we describe the constructed 3D map for our simulation campaign together with the proposed positioning algorithm and handover scheme. Section 5 provides a discussion on the simulation results of the theoretical positioning accuracy and the experimental results related to the handover schemes. Finally, Section 6 wraps up this paper with a conclusion.

2. State-of-the-Art Overview and Problem Formulation

Here, an overview of both the handover schemes and the positioning techniques is given followed by the state-of-the-art and the problem formulation.

2.1. Overview of Handover Schemes

The implementation of a handover procedure is necessary in any wireless network because of the mobility of the users within. However, such implementation depends on various factors including the average coverage of the serving entities e.g., AP or base station (BS), the trajectory and the velocity of the users, the multiple access scheme (orthogonal or non-orthogonal multiple access), carrier frequency and the type of the network (mmWave based or cmWave based, Homogeneous Networks or HetNets, etc.). Handovers are also classified based on the decision entity, decision criteria, and performance metrics. A comprehensive overview of handover schemes can be found in [21,22], where the authors paid particular attention to the so-called vertical handover. The latter is a switch between different RATs or standards, which is a key mechanism to enable the HetNets. In cellular networks, handover decisions are usually made in a centralized manner. In other words, the handover is in general carried out based on the downlink RSSI measurements together with the corresponding hysteresis and timer, during which the RSSI of the target cell should be higher than the RSSI of the original cell. However, in vertical handover it is not always efficient to use traditional metrics [23].

In addition, handovers can be classified based on the target performance. For example, a handover scheme allowing to switch the cell without a service interruption (minimized packet loss) is called "seamless" handover, while in "fast" handover the latency of packets is minimized. In the case of mmWave access, additional issues arise: due to high channel penetration loss, the zone where a handover may be performed without session interruption is usually very small [24]. This problem also appears in the case of LoS–non line-of-sight (NLoS) boundary crossing, where mmWave signal level drops significantly and rapidly, and the traditional RSSI-based handover schemes cannot react fast enough.

2.2. Overview of Positioning Techniques

In general, positioning techniques are categorized in several different ways [25,26], wherein each category may differ in terms of various physical media signal used (e.g., sound, light, or radio signal), or different principles of obtaining the location of the target of interest (e.g., proximity, fingerprinting, or multilateration). Alternatively, the positioning techniques stem from a specific positioning system, which can be classified into two groups: self-positioning systems and remote-positioning systems ([27] Ch. 1). While the former is essentially a DR system [28], as it computes the current location based on the previous location by fusing the heading and the distance measurements obtained from the inertial measurement unit (IMU) sensors, the remote-positioning system is referred to as a radio-positioning system, as it relies on the LRMs wherein the relative location information is embedded. Typical LRMs consists of RSSI, time of arrival (ToA), and/or angle of arrival (AoA).

For a radio-positioning system, the acquisition of the LRMs relies on different equipment and/or methods. Owing to the simplicity of acquisition and low-complexity in terms of the needed hardware, RSSI-based positioning remains an attractive approach especially for indoor scenarios ([27] Ch. 11). However, several error sources, such as multi-path and NLoS, impair the stability and prediction quality of the RSSI measurements and therefore may keep the positioning accuracy away from being acceptable by the requirements specified for certain use cases [29]. In addition, the ToA measurements can also be employed for positioning by using a multilateration principle ([27] Ch. 6), such as the global

navigation satellite system (GNSS)-based positioning. Conditional on a perfect synchronized clock among the UE and AP, the ToA-based positioning is capable of achieving much higher accuracy than the RSSI-based positioning especially at higher carrier frequencies and over wider bandwidths [30]. However, due to inherent clock offset among transmitters and receivers, certain approaches are required to compensate for the synchronization errors [31,32]. Last but not least, there is also the AoA-based positioning enabled by antenna arrays or directional antennas ([27] Ch. 9), such that the direction from which the signal arrives at the receiver (i.e., the AP in a network-centric positioning system) is known. Hence, a location estimation is obtained by applying the multi-angulation principle ([33] Ch. 2). Under both LoS and NLoS propagation, the antenna orientation at the receiver side must be known or estimated to make the AoA measurements reasonable for positioning.

Besides the positioning principles for different LRMs, various algorithms can be applied to learn the location estimates based on one or multiple LRMs ([27] Ch. 2, [34,35]). In this work, the robot location is acquired by combining the radio-positioning techniques (for the estimation of initial location of the robot) and the self-positioning (for subsequent positioning) by utilizing the outputs of the on-board sensors to predict the moving distance and the direction of the robot at each time instant.

2.3. State-of-the-Art in the Location-Aware Communications and Handover Schemes

A location-aware adaptive communication system has been investigated in ([33] Ch. 9), where adaptive modulation and coding (AMC) together with location information was cooperatively combined in order to achieve macro diversity. It was suggested in [33] that wireless communications can benefit from a proactively updated location information of the UEs. This is because location-aware communication systems are capable of predicting more precisely the channel state information (CSI) at the transmitter for adaptive beamforming as compared to location-unaware communication systems. With a perfect knowledge of location and a fingerprint database, a location-aware system showed decent improvements in terms of the mean capacity over pure CSI-based systems especially for the applications with long feedback delays and large channel variations. However, the advantage of a location-aware system may not hold when positioning error increases above a certain threshold. In practical situations, it is likely that positioning errors may be excessive for the UE to benefit from a location-aware communication mechanism.

As an indispensable component of the handover process, network selection algorithms have been studied with location awareness, i.e., LNS. In [6], a TCP/IP based LNS architecture was proposed on top of IEEE 802.21 MIH standard. Specifically, location awareness of mobile users as well as the available network information were monitored periodically by a location & network monitor (LNM). The former was then exploited to predict the distances to the currently available networks, user trajectory, as well as the mobility patterns, for designing the LNS algorithms. Despite better handover performance than without location awareness, the impact of location errors of the mobile users towards the LNS was not considered therein. Additionally, cloud-based network selection for vehicular networks was proposed in [7] for leveraging the rich computing power and data storage of a cloud computing server. The efficiency of the aforementioned network selection algorithms stemmed from offloading complex computations to a geographically distributed cloud server, which in turn provided better decision-making in the network selection, based on a broader network information. Moreover, a fast convergence algorithm for solving a coalition formation game was proposed in [7] to enable optimization over larger scale networks and practical implementation.

Works on LHO under different scenarios can be found in [8–10] and the references therein. Taking into account the information of both user location and network load, the authors in [8] studied the LHO scheme in multi-cell networks. Two metrics have been utilized to optimize the handover process, namely, the angle of handover and the load-balancing index. The former suggests that the moving direction of the UEs can be computed based on the previous location estimates by the GNSS, which is then exploited to predict the most likely target cell that the UE will connect to. Further, the consideration of the load balancing index is to ensure that the QoS of the UEs does not drop if the

target cell is already heavily loaded. The simulation results in [8] showed that the proposed LHO algorithm outperforms the conventional one, especially for UEs with high-but-constant velocity and UEs that make turns less frequently.

Similarly, relying on the location estimation provided by GNSS, authors of [9] proposed an efficient network selection scheme based on not only the estimated location of the users (via GNSS technique) but also maps reflecting the channel quality information (i.e., the average of signal strength) as well as the traffic load. Due to the rapid changes of traffic load, frequent updates of such information are therefore necessary which poses a stringent requirement in terms of the latency and throughput of back-haul link of the HetNets. However, the proposed schemes may suffer severe degradation when GNSS-based positioning is disabled or provides low-accuracy location estimates, which can be the practical cases especially in the urban macro scenario.

With the proxy mobile IPv6 (PMIPv6) in mind, the authors of [10] investigated several handover schemes, such as fast handover for PMIPv6 (FPMIPv6), smart buffering, and low-latency handover, and compared the corresponding handover performance with the proposed location-aware fast PMIPv6 (LA-FPMIPv6). In particular, the FPMIPv6 aims at reducing the packet loss by scanning and detecting the network status of all APs around the source AP. The handover is thus prepared once the RSSI of the source AP falls below a certain threshold. Similarly, the smart-buffering scheme, which also predicts the handover based on the RSSI, was proposed in [10] to reduce the packet loss. The main difference between smart-buffering scheme and FPMIPv6 lies in the fact that in the FPMIPv6 the UE scans the surrounding APs once handover decision is made, whereas for the smart-buffering scheme, the target AP, with which the UE is connected, searches for the source AP to retrieve the buffered packets. The resulting handover latency is the same as with the PMIPv6, but smart buffering enjoys a lower packet loss. Furthermore, by omitting the UE's authentication procedure, low-latency handover was also proposed in [10] to reduce the packet loss. However, due to the fact that only RSSI has been considered as the parameter, the handover cannot be predicted precisely whenever the measured RSSI is considerably different from the actual values. Hence, the LA-FPMIPv6 was proposed to perform a handover based on both the location information of the UE as well as the RSSI. Hence, both the handover timings and the next AP to which the UE will connect can be predicted more precisely than in the aforementioned algorithms, and therefore it achieves enhanced performance in terms of the reduced signaling cost, buffering cost, and handover latency.

As key components in reducing the network latency and increasing the link robustness, control/user plane separation (CUPS) [36] together with MR-DC have been employed to improve the handover performance in mmWave HetNets. The authors of [11] proposed a prevenient handover scheme with radio resource control signalling duplication and master-secondary switch in order to reduce the handover failure rate and service interruption time. Similarly, for a CUPS network, the authors of [12] presented a seamless handover scheme by introducing a handover-assisted micro evolved NodeB (HO A-eNB) in the overlapping area. Such HO A-eNB maintains a continuous connectivity with the UE throughout the handover process, resulting in improved success probability of handover. However, deploying such HO A-eNBs in all the possible overlapping areas may incur prohibitive costs as well as posing a stringent requirement on the backhaul link capacity of the network.

By integrating the mmWave networks with the sub-6GHz networks for better link robustness and higher throughput, the benefit of performing handover with location awareness of the UE has been investigated in [13–15]. In [13], the location and velocity information (mobility information) of the UE was exploited to optimize the overall network performance, such as reducing the number of handovers as well as enhancing the user QoS. However, similar to the aforementioned works, the way of acquiring a perfect knowledge of the mobility information of the UE was not clearly specified. Moreover, the importance of location information has been investigated in [14,15]. By exploiting the available CSI at sub-6 GHz bands, the authors in [14] proposed to apply a machine learning method to predict the location information of the UE, which is then utilized to achieve faster handover. The results showed that with location awareness, the UEs enjoy higher spectral efficiency than with the conventional

handover scheme. Furthermore, with the objective of allowing the mmWave networks to operate at scale, the authors in [15] shared their thoughts on the scalability challenges in mmWave networks and also presented positioning algorithms (network-based and device-based) for achieving high accuracy of location awareness. Such positioning algorithms can be not only employed to enable location-based services, but also help reduce the handover costs and make optimized handover decisions.

In addition to the handover schemes based on location- and mobility-awareness, other contextual information, such as quality of experience (QoE) and radio environment map (REM), has also been employed and exploited to improve the handover performance. Targeting at improved UE's QoE, the authors in [16] have presented a Q-learning based algorithm for vertical handoff in the HetNets. Via continuous interaction with the environment, an optimized handoff strategy is achieved, i.e., the QoE is maximized based on created mappings between QoS metrics and achieved subjective experience on the side of UEs). Meanwhile, in [17], the REM as well as the UE trajectories are considered to predict the quality of network connectivity that is then exploited for handover process. It is seen that the handover performance improves when the time-to-trigger, the UE velocity, and the location error are low. However, the addressed carrier lies in sub-6 GHz band, and REM of mmWave APs was not considered.

Further work using REM for handover can be found in [18], where positioning and radio maps have been combined together for intra-frequency handover. Applying two location prediction methods, the handover decision was made by determining the BS that may offer the highest reference signal received power (RSRP) based on the radio map. However, unconditionally switching to the BS with the highest RSRP might result in frequent handovers and a high ping-pong rate [11]. Contrary to the handover that chooses the BS with the highest RSRP, the authors of [37] proposed to perform a handover only if the signal-to-interference-plus-noise ratio (SINR) at the UE side is lower than a certain threshold over the entire time-to-trigger period. Accordingly, a handover is not triggered even if the RSSI from the serving BS is not the highest, thus, reducing the unnecessary handovers. However, the impact produced by the prediction error of the RSSI was not considered therein, which is the case in practical HetNets.

In addition to service-based architecture (SBA) and CUPS, both the core network and the radio access network (RAN) of 5G NR support network slicing (NS) [38] as another enhancement compared to evolved packet core (EPC) ([39] Ch. 6). Essentially, NS serves as the key enabler for the deployment of multiple virtual networks operating on a shared physical network/infrastructure, and each virtual network can therefore be configured to support different specific network functions indicated by the SBA. Consequently, a RAN slicing-based handover scheme was proposed to provide better UE QoS during a handover [40]. Based on the envisioned hierarchical control model, a handover was triggered based on the current link quality as well as the network condition. More importantly, the handover decision not only indicated the target BS, but also suggested a target RAN slice that better satisfied the UE QoS. Given a highly virtualized network, such a handover scheme is capable of more flexible resource utilization and allocation. However, the performance of such scheme is limited by the available bandwidth/resources of the corresponding RAN as well as the respective propagation condition. In the case of realistic situation, such as, blockage/NLoS, a vertical handover between cmWave and mmWave RATs remains crucial to ensure the reception/decoding of signals from both control and user planes, thus, is more efficient than NS-based handover.

More related works using similar RATs and addressing industrial use cases can be found in [41–43]. Specifically, the authors of [41] presented a proactive handover method based on an assessment of the RSSI, the procedure of which remains rather similar to one of the handover methods considered in our work. However, the handover was considered between APs of the same RAT instead of a multi-RAT situation. In the conclusion, the authors also mention that such RSSI-based handover can be improved by considering the user mobility, which is another measure of the location awareness being considered in our work as well. Additionally, the authors of [42] have presented a WiFi/WiGig handover based on the RSSI, no other handover schemes were studied nor investigated therein. Furthermore, the authors

of [43] proposed handoff schemes for applications involving the mobility of robots and devices in a real industrial environment. By considering multiple metrics, such as the mobility awareness, RSSI and packet delivery condition, the study showed that the handoff can be triggered with high accuracy and reduced ping-pong effect. Admittedly, handover considering one metric may lead to inaccurate and frequent triggering, therefore, integrating various metrics results in accurate decision making for the handover. In our work, we demonstrate that when location awareness is accurate and reliable enough, the trigger timing for handover can be computed with high accuracy. It is noteworthy that integrating several metrics undoubtedly increases the algorithm complexity and latency in the overall handover process.

Compared with the aforementioned works, our work differs in two major aspects, (i) instead of assuming perfect knowledge of the UE locations/trajectories, we develop a dedicated positioning algorithm (i.e., GBP) to achieve location awareness. In addition, the positioning results and their impact on the handover performance are analyzed and assessed by our simulations as well as practical experiments; (ii) unlike the works supported only by numerical simulation, a multi-RAT robotic platform is employed in our experiments to justify and assess the real-world feasibility of the LHO algorithm.

2.4. Problem Formulation

Based on the HetNets structure that is featured with the MR-DC (multi-connectivity [5]), the main objectives of our work are to experimentally assess the feasibility of performing an efficient handover scheme, i.e., the LHO in a multi-radio environment, to evaluate the benefits of such handover over the conventional RSSI-based approaches, and to understand the key factors of maintaining such improvements. Essentially, the LHO benefits from the advantages of both cmWave and mmWave APs within the HetNets that we summarize in Table 1. In particular, the throughput of the robot is augmented by connecting it with the mmWave AP as long as the robot is in the LoS state w.r.t. the mmWave AP. Meanwhile, more robust connectivity can be ensured by handing over to the cmWave AP before the robot loses the LoS connection w.r.t. the mmWave AP. Therefore, the key performance indicators of the LHO are the reliability of the achieved location awareness and the corresponding positioning accuracy.

To illustrate our technical context, a conceptual figure of the principle pf the proposed handover scheme is developed in Figure 1, where a robot (i.e., a mobile vehicle) is moving within an industrial multi-radio environment while performing certain tasks, such as cargo transportation or video surveillance. To ensure the service quality of the tasks that require wireless connectivity, our objective is to enhance the link robustness while augmenting the throughput throughout the whole robot trajectory. As illustrated by Figure 1, the robot is communicating with the mmWave AP, wherever there is LoS radio connection between them (with a potential horizontal handover, i.e., a switch between the networks of the same RAT in the light blue region), and switches to WiFi (i.e., a vertical handover) before entering the NLoS region of the mmWave AP (see the light green region) based on the available location awareness of the robot, i.e., LHO.

Table 1. Advantage and disadvantage of different RATs.

RAT	Advantages	Disadvantages
cmWave (WiFi)	High robustness to blockage; low diffraction loss	Low throughput due to limited bandwidth
mmWave (WiGig)	High throughput at LoS owing to large bandwidth	Low robustness to blockage; high diffraction loss

WiFi standard: IEEE 802.11n. WiGig standard: IEEE 802.11ad.

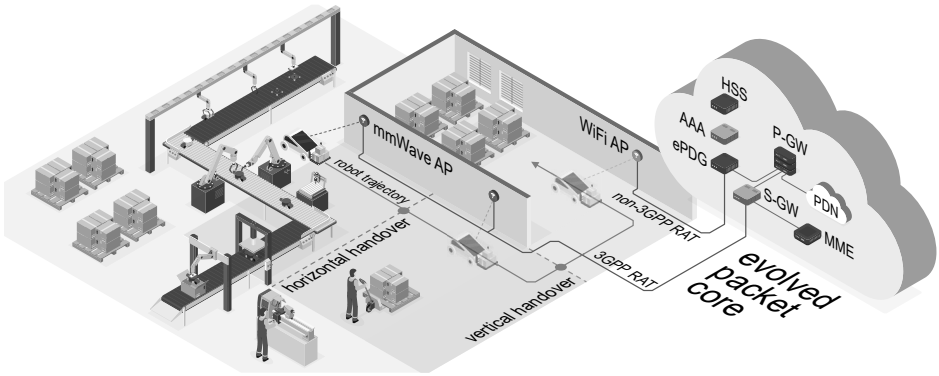

Figure 1. A conceptual figure of the principle of the location-aware handover (LHO) scheme in an industrial multi-radio environment.

Even though a related topic was investigated in several past works as discussed in Section 2, most of the existing papers report enhanced communication performance by assuming ideal location information for all the UEs/vehicles within the network. In our work, the location information is not assumed to be known perfectly, but rather is estimated via the positioning solutions. Exploiting a laboratory setup, we implement and evaluate the positioning algorithms as well as the LHO scheme utilizing a multi-RAT robotic platform. From the network-level perspective, all data are transferred by the evolved packet core (EPC) with 3GPP RAT (mmWave) stream routed via the serving gateway (S-GW) and packet data network gateway (PGW) to the Internet, represented by the packet data network (PDN). The non-3GPP data is served in the same manner utilizing the evolved packet data gateway (ePDG). At the same time, inter-networking is ensured by the mobility management entity (MME), which communicates with both the home subscriber server (HSS) and the authentication, authorization, and accounting (AAA) unit. Further details on the handover procedure implementation between 3GPP and non-3GPP networks are given in [44].

3. Equipment and Scenario Description

This section describes the multi-RAT robotic platform and the scenario of interest for LHO evaluation.

3.1. Multi-RAT Robotic Platform

Here, the multi-RAT robotic platform used to evaluate our LHO scheme is presented. It can carry up to four kilograms of payload and reach 7 km/h speed. It is currently capable of performing remote operations in indoor environments for approximately two hours without recharging. The installed hardware allows us to detect obstacles located half-a-meter away from the vehicle, which in combination with the data obtained from the on-board camera makes it possible to implement capabilities for autonomous driving.

Our vehicular platform is equipped with cmWave (WiFi) and mmWave (WiGig) interfaces in order to provide multi-connectivity features. Wi-Fi interface is SL-1506 dongle working on RT5370N chip and implementing the standard 802.11n. The module uses closed-loop power control with an output power range between 2 and 18 dBm conveyed via a single 2 dBi omnidirectional antenna. As we used a Linux-based operating system, the communication rate adaptation was driven by the Minstrel algorithm, which is part of the mac80211 kernel subsystem [45]. In the case of mmWave connection, the vehicular platform is equipped with a Mikrotik wAP 60G client station based on the Qualcomm QCA6320 WiGig module with maximum Tx power of 21.67 dBm. The module is further provided with a 6×6 phased array antenna with a maximum gain of 13.5 dBi.

At the core of the platform is an UDOO x86 single-board computer. In particular, the two motors of the vehicular platform are controlled via a RoboClaw motor controller connected to the UDOO board. Further, the RoboClaw has a power connection to external battery packs and a voltage regulator. A photo detailing the components of the platform is shown in Figure 2 and the technical details and features of the platform are summarized in Table 2. The platform can also operate in manual mode, where the vehicle is controlled by the operator remotely. Hence, the operator is monitoring the video stream provided by the camera installed on the front of the vehicle.

The platform allows us to collect various types of statistics. First, we monitor the communication performance by analyzing signal strength, end-to-end packet latency, and throughput data. For the installed WiGig transceiver, we also collect antenna array configuration statistics provided by the application programming interface (API) of the device. On top of that, UDOO board has an integrated six-axis sensor, which allows us to monitor the heading of the vehicle. Further, the motors of the driving wheels have magnetic encoders, which make it possible to estimate the location of the vehicle in relation to the starting position.

Table 2. Technical specifications and features of multi-RAT robotic platform.

Framework	**Dagu Wild Thumper Chassis with 6 Wheels and 2 Motors**
Computing unit	UDOO ×86
Operating system	Debian Jessie
Radio access technologies	MikroTik wAP 60G (mmWave) and 802.11n Wi-Fi transceiver
Battery	2 × 8000 mAh LiPo
Camera	Logitech C270 HD
Sensors	SEN-13959 distance meters and 2× quadrature wheel encoders and BMI160 six-axis sensor

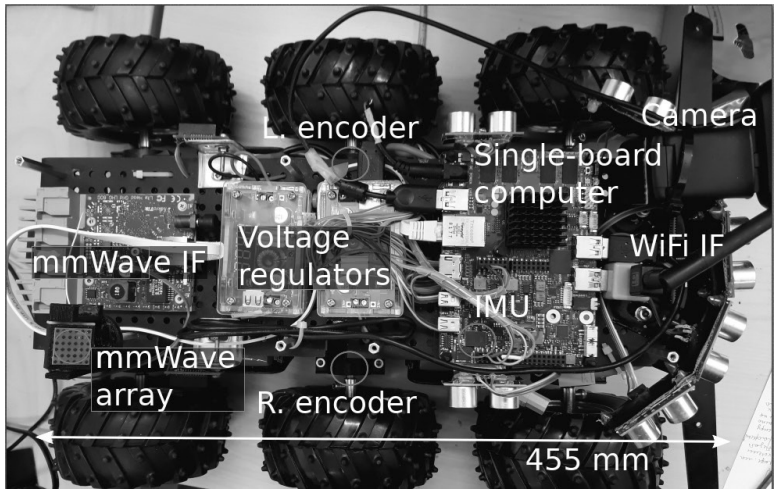

Figure 2. Prototype photo (disassembled) with notes.

3.2. *Scenario of Interest*

The scenario for evaluating the LHO scheme is presented in Figure 3 where a typical office setting is employed to mimic an industrial environment. The corridor, where the test was held is 3×2.5 m wide/high. The offices are separated from the corridor with 10 cm wide partition walls. Inside the office, the WiFi AP is installed on a 1.5 m height (see Figure 3). Along the office walls there are installed

three wooden tables, four metal chairs and two cupboards, which do not obstruct the LoS condition between robot and WiFi nor robot trajectory during the test.

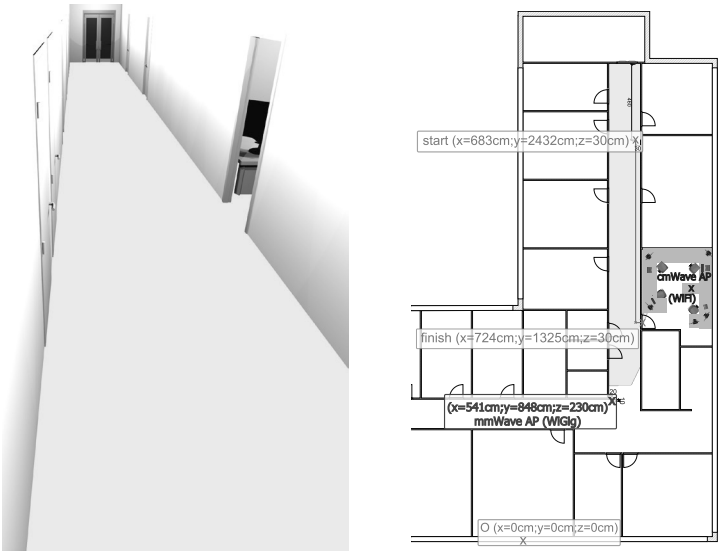

(**a**) (**b**)

Figure 3. Test scenario 3D model and layout. (**a**) The 3D model of the corridor. (**b**) Test scenario layout combined with LoS map.

In terms of the robot trajectory, the starting location was 15 m away from the mmWave AP that is attached to the ceiling and tilted 15 degrees down, to provide stable coverage to the robot in the LoS conditions. The LoS coverage of the mmWave AP is modeled in Blender, as is discussed in Section 4.1 and shown in Figure 3a with the viewing angles corresponding to the location of the AP and its antenna array configuration span. The WiFi is located inside the office, in the NLoS state w.r.t. the initial location of the robot. It is noteworthy that there exists only one mmWave AP (WiGig) and one cmWave AP (WiFi) within the considered environment, and we tried to minimize the existing interference from other WiFi APs operating in the same area by choosing the least used frequency channel. The overall robot trajectory is as follows. After the first 10 s of initialization (when the vehicle remains stationary), the robot starts moving along the corridor with the constant velocity of approximately 0.5 m/s, until it reaches the entrance to the office, in which the WiFi is located, see Figure 3b. Further, it turns left and moves into the office (entering the mmWave NLoS area). In the end, the robot drives one meter inside the office and stops. All in all, the core objective of this work is to maximize the radio connection with the mmWave AP for an augmented throughput, while switching to the WiFi in the non-ideal condition for enhanced link robustness in the industrial environment.

Last but not least, we emphasize that the proposed handover scheme works the best in static environments, where the scenario layout either changes rarely, or changes are periodic and predictable. If there is a need to consider dynamic scenario reconfiguration, the LoS map of the environment should be modified accordingly, which certainly increases the overall complexity. An example of an environment with predictable geometry dynamics could be a fully automated factory or storage/production hall.

4. Enabling Multi-RAT Indoor Handover

In this section, the method of constructing the 3D indoor environment as well as the LoS map w.r.t. the mmWave AP is provided. Inheriting the ideas from [35,46], the developed GBP algorithm is then presented and formulated. Finally, the proposed handover scheme is described and discussed.

4.1. Determining mmWave LoS

Here, we describe the method [47] of building the LoS map of the mmWave AP within the considered environment. The main purpose of this method is to construct a 3D model of a particular environment in order to predict the LoS state w.r.t. the mmWave AP at any specific locations. In particular, the necessary steps are given as follows.

1. Building 3D model. The first step is to obtain a considered environment in the 3D modeling software that provides sufficient details to reflect all the objects that obstruct the LoS path between the objects of interest (e.g., the mmWave AP and the robot).
2. Identifying 2D plane. In the 3D model, we add a plane on the height corresponding to the device antenna. The surface of the plane in the 3D environment represents the set of all possible points where the device antenna can be situated. For further image processing simplification, the plane is uniformly colored, while the choice of its material results in the absence of shadows and reflections (illustrated in Figure 3a).
3. AP point of view (PoV) LoS map. A 2D render from the AP's point of view is used to produce a "warped" map (shown as Figure 3a). The viewing angles are set to the antenna parameters of the AP.
4. Affine transform. The final step is to perform a geometric transformation to the projected PoV map in order to eliminate the z-coordinate as well as restore the proportions such that the orthogonal coordinate system (top view) of the LoS map of the area is obtained. In particular, the transform is carried out by applying three anchor points, which have been marked with the red cross shown in Figure 3b. It is important to note that the red line shown therein is employed as the ground truth of the robot trajectory in the simulation campaign (see Section 5.1), which is different from the ground truth of the robot trajectory in the experiments that is not measured and therefore remains unknown.

The red line plotted in Figure 3b is applied as the robot trajectory for simulation-based study on the RSSI, AoA and proposed positioning algorithm. The information provided by the LoS map (such as the LoS–NLoS border) is first integrated in the robot, and then utilized to decide whether the robot resides in the LoS region w.r.t. the mmWave AP for the experimental evaluation of the proposed handover scheme, which will be discussed in Section 4.3.

4.2. Proposed Positioning Algorithm

Since the proposed positioning algorithm is geometry-based, we provide an illustration of the geometry relation between the mmWave AP and the robot in terms of the side view and top view in Figure 4, in which the GBP algorithm is constructed. Specifically, the mmWave AP is represented by the red dot, while the purple cross marker denotes the robot. Further, the antenna array deployed on the robot is highlighted by the black solid line on top of the purple markers. It is important to note that since the positioning is implemented at the robot side, the antenna array of the mmWave AP is therefore omitted. In addition, we denote the noiseless elevation and azimuth AoA at the robot side as φ and θ, and the true orientation of the antenna array (in the azimuth plane) on the robot after the transformation from the robot coordinates to the local 3D Cartesian coordinates [28] is α. In this work, only the array orientation in the azimuth plane (horizontal plane) has to be considered because the elevation orientation of the array remains vertical to the ground as the robot moves along the trajectory. Further, $\hat{}$ denotes the noisy measurement of the corresponding noiseless quantity. By solving the geometrical relationship between the mmWave AP and the robot shown in Figure 4, the GBP algorithm is described in Algorithm 1, where the inputs contain the AoA measurements, $\hat{\varphi}$ and $\hat{\theta}$,

and the orientation measurements $\hat{\alpha}$. Additionally, the GBP requires the location information of the mmWave AP to complete the radio-positioning for the robot. It is noteworthy that the time index is omitted in Algorithm 1 due to the independence between the location estimates of the adjacent time instants.

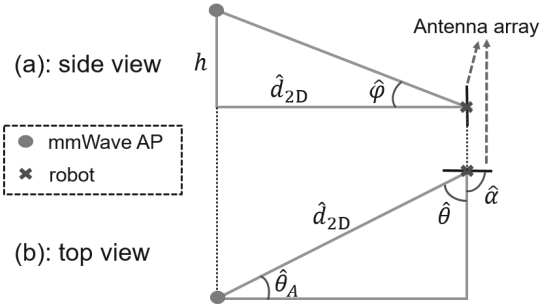

Figure 4. Illustration of geometric relationships between the robot and mmWave AP from two points of view.

Today, there are various methods to estimate the robot location, e.g., the extended Kalman filter (EKF) [31,34,35,48] or the theoretical positioning error bound [27,49]. Here, we propose and apply the GBP for robot positioning due to three major reasons. The first one is the limited availability of LRMs. Given the considered scenario, there is only one mmWave AP available for acquiring the LRMs. For positioning with two unknowns (i.e., $x-, y-$ components of a 3D coordinate), most of the existing algorithms require at least three APs. The second reason is the algorithm complexity. In order to reduce battery usage during positioning, the applied positioning algorithm needs to be less computationally complex. Comparing with the EKF, the GBP algorithm was shown to have much lower computational complexity while providing reasonable positioning accuracy [35]. Third, the main target of this work is not to compare different positioning algorithms but to acquire location awareness for better handover performance. Generally, a better positioning performance is directly related to a better LHO performance; however, as we discuss in Section 5.2, the LRMs obtained by the robot is too coarse to be used for accurate positioning by any positioning algorithms.

Algorithm 1: Geometry-based positioning (GBP)

Input: $\hat{\varphi}$, $\hat{\theta}$, $\hat{\alpha}$, x_A, y_A

Output: $\hat{x}$, $\hat{y}$

1 Compute the 2D distance between mmWave AP and the robot based on elevation AoA measurement $\hat{\varphi}$ and the known antenna height difference h

$$\hat{d}_{2D} = h/\tan(\hat{\varphi})$$

2 Convert the azimuth AoA measurement $\hat{\theta}$ at the robot to the angle of departure (AoD) $\hat{\theta}_A$ at the mmWave AP taking into account the array orientation measurement $\hat{\alpha}$ of the robot

$$\hat{\theta}_A = \pi - |\hat{\theta} - \hat{\alpha}|.$$

3 Calculate the robot location based on $\hat{d}_{2D}$ and $\hat{\theta}_A$

$$\begin{bmatrix} \hat{x} \\ \hat{y} \end{bmatrix} = \begin{bmatrix} x_A + \hat{d}_{2D}\cos\hat{\theta}_A \\ y_A + \hat{d}_{2D}\sin\hat{\theta}_A \end{bmatrix}$$

4.3. Proposed Handover Scheme

The proposed handover scheme, LHO that is illustrated and described in Figure 5, is in general based on the knowledge of estimated robot locations and the potential LoS zone w.r.t. the mmWave AP location. In particular, the LHO is initiated whenever the robot enters/exits the mmWave NLoS area. To predict and execute the handover, the robot compares its current estimated location with the handover location on the LoS map of the environment that is shown in Figure 3. For instance, if the robot starts off in the LoS area, the LHO is triggered only if the estimated robot location no longer lies on the LoS map, in which case, a switch from mmWave RAT to WiFi shall occur. The performance of this scheme depends on multiple factors including the positioning accuracy, the presence of moving obstacles, and the robot speed. To improve the handover efficiency, one can take into account the robot trajectory, the channel statistics (measured signal level) and the sensor data (e.g., images/video, pseudo-range measurements).

In addition, traditional RSSI hysteresis and time triggers may be used to eliminate possible ping-pong effects [10]. However, in this paper we use a "proof of concept" scheme, which only takes into account the current estimated location of the robot, and triggers a handover when the robot crosses the LoS-NLoS border. Assuming that we know the map of the building and the LoS border, together with the current location of the robot, the task of predicting if the robot is in the LoS area becomes in checking if it is located inside the polygon of an arbitrary shape, i.e., points in polygon (PiP). Since the observed polygon can be non-convex, the most efficient way to solve the problem is via a ray intersection method with the complexity of $O(N)$, where N represents the number of edges in the considered polygon [50]. In order to decrease the computing power requirements, the LoS area polygon should be calculated separately (using e.g., Blender) for each mmWave AP in the deployment scenario, while the checking algorithm should be applied only for the currently used AP.

The complexity and the feasibility of our scheme, therefore, depend on the complexity and the accuracy of the employed location estimation algorithm together with the complexity of the chosen PiP algorithm. As in the conventional schemes, the resultant computation intensity of the location-aware solution depends on the status (location) updates frequency. The implementation of the LHO scheme requires the storing of pre-calculated LoS maps and the realization of a mechanism to switch the packet flow from one RAT to another. In the paper, we compare the performance of the proposed handover scheme with a traditional RSSI-based approach. The RSSI-based handover is triggered when the WiFi RSSI is higher than the mmWave RSSI plus a 3 dB margin, for the duration of three consecutive measurements. Herein, the 3 dB hysteresis margin is set according to the recommendation made in [11]. It serves as the handover threshold throughout the overall handover process. Furthermore, the handover is implemented in a network-layer using "soft handover" approach—the data flow switching is enabled by changing the destination IP address, which triggers the routing table update and changes the physical interface (WiGig or WiFi TX) used for the transmission. In other words, the association (signaling) with appropriate AP (WiGig or WiFi) is not discontinued in order to record the appropriate statistics since it is connected to both APs at the same time. However, the implementation of the proposed algorithm could be realized using "hard handover" approach as well.

In terms of the fairness of the comparison between the two considered handover scheme, we provide the following elaborations: in general, both the RSSI-based handover and the LHO belong to the context-aware handover scheme. Therefore, the two handover schemes are different in terms of the utilized context for handover prediction and triggering. In [23], various context-aware handover schemes are discussed and compared. In particular, some works utilized the positioning system, such GNSS as the context parameter, whereas others measured the RSSI values and used them as the context parameter. In a way, the comparison between RSSI-based handover and LHO (in the same environment) is fair enough, since they merely utilized different context parameters for triggering the handover procedure. Nevertheless, LHO is in general more difficult to implement than the RSSI-based handover since it requires more information about the environment. Our contribution in this work is to demonstrate the potential performance gain when utilizing the estimated location

information for the handover, hence the LHO, further enhancing the unification of positioning and communication technologies in the HetNets.

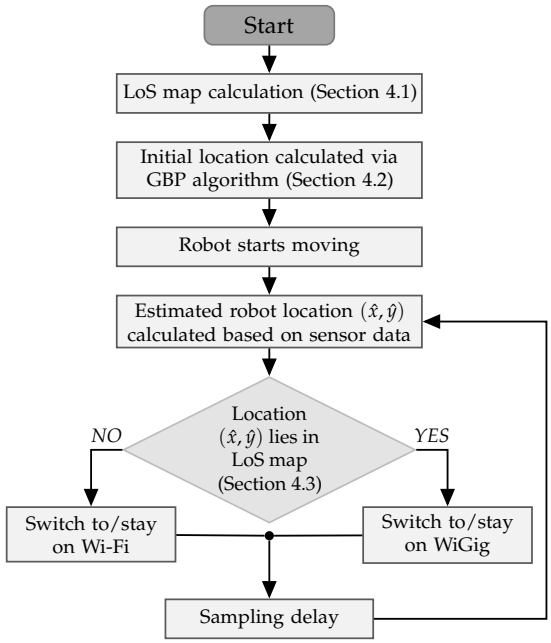

Figure 5. Procedures of the roposed LHO scheme.

5. Obtained Results and Evaluation

In this section, the performance of both the simulation-based positioning algorithm and the experiment-based handover scheme is presented and discussed.

5.1. Simulation-Based Positioning Accuracy

First, noiseless elevation and azimuth AoA with respect to the mmWave AP together with the RSSI (at the robot) without shadow fading are plotted in Figure 6 for the comparison with the acquired experimental results, as will be shown in the next subsection. Specifically, the robot trajectory is divided into three segments, which are marked with different colors: first, the robot remains static in the light green region performing operational system initialization. Thereafter, it moves toward the office entrance (the light red region), where the robot makes a turn (black dashed line), and drives inside the office (toward the NLoS region w.r.t. the mmWave AP, i.e., the light blue region). On its way into the office, the robot passes the LoS-NLoS border, where the RSSI value significantly drops.

The positioning accuracy via a numerical simulation shown in Figure 7 is characterized by the 2D root mean square error (RMSE) and the corresponding cummulative distribution function (CDF) of the 2D positioning error along the considered robot track within the LoS region (see the red curve in Figure 3b). Further, the applied parameters of the simulation are summarized in Table 3, where the utilized pathloss model refers to the 3GPP indoor hotspot (InH)-office LoS scenario. In our simulation campaign, the Cramér-Rao lower bound (CRLB)-based LRMs ([33] Ch. 3), i.e., the elevation and azimuth AoA measurements based on the RSSI (see Figure 6a) are generated according to the methods in [35], which are then utilized as the input LRMs $(\hat{\varphi}, \hat{\theta})$ of Algorithm 1 to obtain the corresponding theoretical accuracy in Figure 7. It is worth pointing out that, in Figure 7a, the positioning performance gradually becomes better in the light red region before the turning point, this is due to the fact that

the robot is moving towards the mmWave AP, the RSSI level becomes higher (as shown in Figure 6a) which leads to more accurate AoA measurements that yields lower positioning errors.

The array orientation measurement $\hat{\alpha}$ is assumed to be corrupted by an un-biased Gaussian error with the standard deviation of σ_{α} that is set to two different values in the simulation campaign. Specifically, the curves in Figure 7 manifest the difference in terms of the obtained positioning accuracy at two different orientation error statistics ($\sigma_{\alpha} = 0.1^{\circ}$or 5° [51]), which reflects the impact to the LRMs that stems from the stable or coarse orientation measurements obtained from a six-axis sensor on the robot. As it is observed in Figure 7, the positioning accuracy by GBP is generally higher for a smaller orientation error statistics σ_{α}, as well as when the robot approaches the mmWave AP owing to the fact that for a given AoA measurement error, the robot suffers a smaller positioning error when it is closer to the mmWave AP. In other words, the AoA measurement error is translated into a larger/smaller positioning error at a larger/smaller UE-AP distance. It is also worth noting that the RMSE curve stops when the robot enters the NLoS region, thus indicating the fact that the communication with the mmWave AP is discontinued when the LoS is blocked.

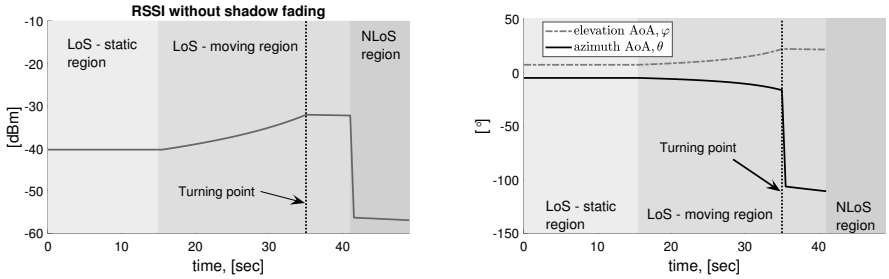

(**a**) (**b**)

Figure 6. Simulation-based numerical characterization as a function of time along the simulated robot trajectory (see Figure 3b). (**a**) The received signal strength indicator (RSSI) applying InH office pathloss model ([52] Table 7.4.1-1); (**b**) Noiseless AoA with respect to mmWave AP.

Table 3. Utilized simulation parameters.

Parameter	Value
Carrier frequency	60.5 GHz
Signal bandwidth	2.16 GHz
Transmit power @ AP *	21.64 dBm
Max. array gain @ AP *	13.48 dBi
Max. array gain @ robot	13.48 dBi
Robot update interval	0.5 s
Pathloss model	InH-office [52]
Fast fading model	Rician distribution

* The "AP"s mentioned in the table refer to the mmWave AP rather than WiFi since the simulation is carried out to model the communication between the mmWave AP and the robot.

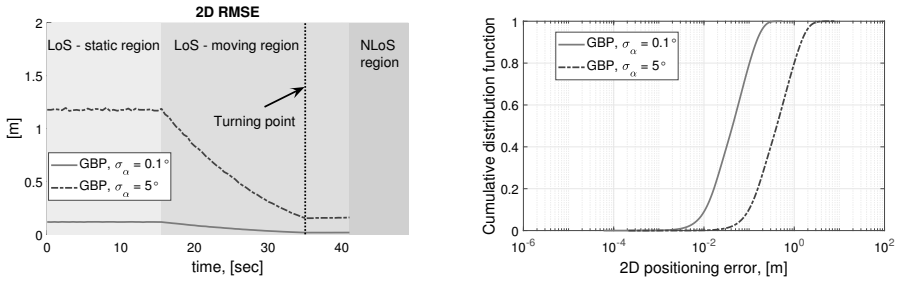

(**a**) (**b**)

Figure 7. Positioning performance via GBP along the robot trajectory in Figure 3b over 2000 trials in the simulation campaign. It is noteworthy that the timeline of Figure 6a is slightly different than that of Figures 8 and 9, which are obtained from the experiment. The reason lies in the fact that the ground truth of the robot trajectory is unknown in the experiment but is defined in the simulation campaign. (**a**) 2D RMSE as a function of time via simulation. (**b**) CDF of positioning error via simulation.

5.2. Experiment-Based Handover Performance

In this experiment, we considered a user-centric handover procedure; hence, the serving entities (mmWave and cmWave APs) are used only to provide the necessary data for the robot to make a handover decision. While on a network-scale, the experiment may be envisioned as simply providing WiFi accessibility, handover targeting the preservation of appropriate data session continuity is carried out on the user side.

The connection-related performance is displayed in Figure 8, where the horizontal axis represents the timeline of the handover experiment starting from 0 s. With the black, yellow and red vertical lines, the time of the RSSI-based (1), location-aware (2) and preferred (3) handover schemes are indicated, respectively. It is noteworthy that the handover (3) does not correspond to any practical handover schemes, it indicates the preferred handover location that maximizes the throughput while maintaining the link robustness throughout the whole considered robot trajectory in the experiment. Specifically, the RSSI measurements are shown in Figure 8a. It can be observed that the RSSI-based handover scheme switches to mmWave too early, while the location-based scheme is triggered just before the signal strength from the mmWave AP drops. Here, it should be mentioned that the RSSI-based handover performance is displayed for a particular measurement set and is limited by high variations of the WiFi RSSI in the NLoS environment. While adjustment of the hysteresis and time margins might improve the efficiency of the scheme in question, it is more complicated to achieve optimized performance due to the multi-RAT nature of the considered scenario. Similarly, in Figure 8b it is visible that the location-based scheme makes a switch just before the latency issues begin on the mmWave link; hence, it offers better performance than with the RSSI-based handover, which provides higher average throughput.

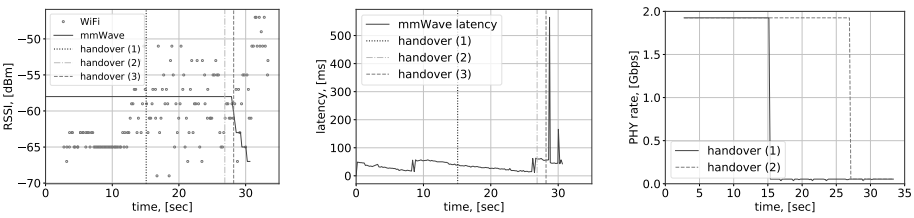

(**a**) (**b**) (**c**)

Figure 8. Measurements collected by the robot at the test scenario, (**a**) RSSI measurements; (**b**) WiGig latency measurements; (**c**) physical layer (PHY) rate.

For a clear demonstration of the performance difference, we summarize the achieved physical layer (PHY) rate of the robot by both of the considered handover schemes in Figure 8c, in which, we refer to handover (1) as the RSSI-based scheme and handover (2) as the LHO scheme, respectively. It is evident that the maximum rate is achieved when the robot is connected to the mmWave AP, whereas the minimum case is acquired by the WiFi connection. More importantly, our experimental results indicate that over the considered time duration, the handover (2), i.e., the LHO, achieves nearly twice as high average rate (1.523 Gbits/s against 0.806 Gbits/s) than the handover (1) owing to location awareness that maximizes the connected time to the mmWave AP that provides a higher bandwidth, hence a higher throughput. Meanwhile, the link robustness is satisfactory as well since the vertical handover to WiFi was performed before the robot entered the NLoS region w.r.t. the mmWave AP.

Ideally, the robot should keep using the mmWave technology as long as possible, due to its higher throughput and lower latency. An early switch to WiFi affects not only the achieved throughput but also delay and jitter, which may become unsatisfactory for delay-sensitive applications, such as telemetry or high-resolution video streaming. Even though the performance of location-aware handover is better than a particular realization of the RSSI-based scheme, it is still not as efficient as the performance of handover scheme (3), the "preferred" option (illustrated as the red line in Figure 8a,b). However, delaying a handover may lead to high packet losses and potential disconnections due to small LoS–NLoS region on the border of the mmWave coverage areas. For example, it is observed in Figure 8a that after approximately 30 s the mmWave data are not collected due to a connection loss.

Further, the performance of the LHO algorithm can be improved or degraded largely depending on the accuracy of the location awareness. In other words, when the positioning accuracy is high and reliable enough according to the environment and requirement, the LHO in general can achieve higher throughput than the RSSI-based handover. In the experiment, we apply the proposed GBP algorithm to compute only the initial location of the robot, thereafter, DR is applied for the location estimation of the rest of the trajectory. This is done because of the large errors of the measured AoA at the output of the antenna array, as shown in Figure 9a. By comparing Figure 9a,b, it is clear that the AoA measurements acquired by the robot do not reflect the changes of the AoA with a sufficient accuracy. Hence, standalone-GBP cannot provide adequate AoA accuracy for a reliable positioning accuracy and is therefore applied only to calculate the initial robot location. In terms of the reasons for the large errors of measured AoA, we provide the following elaborations. First, the employed mmWave equipment does not allow for continuous and "smooth" control over the array directivity. Instead, the used array has several fixed configurations, each corresponding to a particular vertical and horizontal direction of the main lobe. Each configuration covers approximately 10 degrees in the horizontal and vertical planes, which significantly decreases the accuracy of the LRMs, i.e., the AoAs. Second, we do not have access to the beam-searching algorithm, which makes it difficult to evaluate if the utilized configuration corresponds to a direct link or to a reflection from the wall or another object.

In Figure 9b, the estimated robot locations along the trajectory are plotted. For the DR-only case, we manually measure the true initial location of the robot, and the subsequent locations are measured by using robot IMU and wheel encoders data, i.e., the DR. In the "GBP+DR" case, the GBP (see Algorithm 1) is utilized to calculate the initial location, while the rest of the algorithm operates in the same way as in the DR-only case. The array configuration data received from the mmWave AP allows us to estimate the initial location of the robot with approximately one meter precision, which is sufficient to make adequate handover decisions in our case. However, we did not use the standalone-GBP method to estimate the location due to the precision-related issues as discussed above. It should also be noted that the precision requirements depend on the building layout and the robot dimensions.

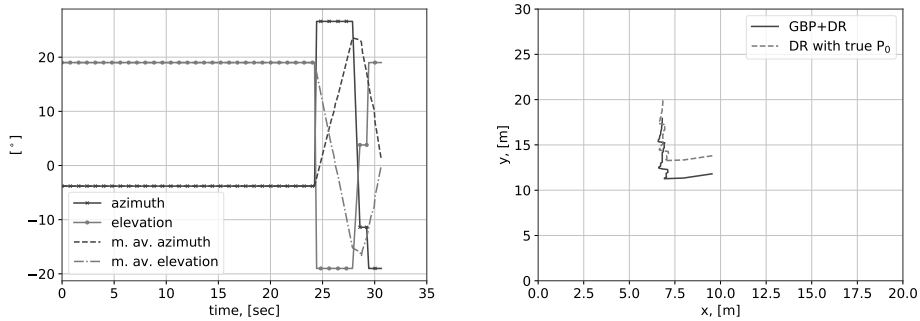

(**a**) (**b**)

Figure 9. Practical implementation of location estimation algorithm, (**a**) WiGig beamforming variation; (**b**) Estimated and measured location.

In summary, our experiments and the corresponding results validate the feasibility of the LHO for mobile communications in a multi-radio environment, the observed performance gap of the considered handover schemes can be exploited for a more efficient handover scheme design enabling a self-organized communication system with autonomous vehicles in mmWave-ready HetNets, where both the link robustness and data throughput can be reliably guaranteed and sufficiently provided.

6. Conclusions

In this paper, we presented the enabling methods and the experimentally-oriented feasibility study on the LHO utilizing a multi-RAT robotic platform in an indoor HetNets environment with the target to achieve enhanced link robustness as well as augmented throughput, thus enabling a self-organized communication system with autonomous vehicles. In terms of location awareness, we developed and presented the GBP algorithm for positioning the constructed robot. The corresponding positioning accuracy has been tested via simulations by utilizing the CRLB-level AoA measurements with the array orientation uncertainty taken into account.

In addition to the numerical analysis, an experimental measurement campaign was conducted with the multi-RAT robotic platform in order to justify the feasibility of the proposed positioning algorithm as well as the LHO algorithm. Despite the coarse AoA measurements, our experimental results confirmed that the “GBP+DR" method is capable of providing sufficient positioning accuracy, which is essential to perform the LHO. With the obtained location awareness, the handover was carried out more precisely before the robot entered the NLoS region. Owing to a longer LoS connection with the mmWave AP, the LHO can achieve twice higher throughput than the conventional RSSI-based handover scheme. During the experiments, two independent data streams were maintained: one to control the telemetry connection and another one to provide video feedback between the robot and its remote operator. In both cases, session continuity targeted by the handover procedure was preserved, although a noticeable lag was observed in the video stream.

Even though the performance of the LHO scheme is bounded by the practical limitations of the employed equipment, it was shown via simulations that the applied positioning approach is capable of offering accurate enough location estimates in realistic indoor environments, thus further improving the performance of the discussed LHO in a multi-radio environment. Four directions of future work are currently envisioned: (i) development of advanced algorithms for more accurate AoA estimation based on the received signals at the mmWave array on the robot; (ii) assessment of practical performance levels in different types of environments and under varying densities of multi-radio network deployments considering potential interference; (iii) study and investigation of a hybrid

handover scheme integrating various metrics, such as RSSI and location awareness under different environments and scenarios; (iv) together with positioning, the sensing techniques will also be applied to produce a simulated environment for multi-RAT handover with efficient beamforming strategy, expanding the proposed algorithm well beyond the considered scenario.

Author Contributions: The main idea and objective of this research were identified by Y.L., M.G., R.K. M.S. and J.U., and supervised by J.H., M.V. and E.S.L.; Y.L. provided the state-of-the-art review, proposed and validated the positioning algorithm using simulation; M.G. implemented the two considered handover schemes experimentally; Y.L. and M.G. wrote the major part of the original draft; R.K. modelled the office environment and provided the key coordinates for simulation study; A video was prepared by Y.L. and J.U.; J.H., M.V. and E.S.L. reviewed the original manuscript and acquired the research funding. All authors have read and agreed to the published version of the manuscript.

Funding: This research was financially supported by the Academy of Finland, projects PRISMA (313039) and ULTRA (328226 and 328214), the Finnish Foundation for Technology Promotion, the Finnish Funding Agency for Innovation under the project 5G VIIMA as well as the international mobility project MeMoV, No. CZ.02.2.69/0.0/0.0/16_027/00083710 funded by European Union, Ministry of Education, Youth and Sports, Czech Republic and Brno University of Technology. For the research, the infrastructure of the SIX Center at Brno University of Technology was used.

Conflicts of Interest: The authors declare no conflict of interest.

References

1. ITU-R M.1645. Framework and Overall Objectives of the Future Development of IMT-2000 and System Beyond IMT-2000. 2015. Available online: https://www.itu.int/dms_pubrec/itu-r/rec/m/R-REC-M2083-0-201509-I!!PDF-E.pdf (accessed on 1 September 2015).
2. 3GPP, TR 36.819 V11.2.0. Coordinated Multi-Point Operation for LTE Physical Layer Aspects (Release 11). 2013. Available online: https://portal.3gpp.org/desktopmodules/Specifications/SpecificationDetails.aspx?specificationId=2498 (accessed on 1 September 2013).
3. 3GPP, TR 36.842 V12.0.0. Study on Small Cell Enhancements for E-UTRA and E-UTRAN; Higher Layer aspects (Release 12). 2014. Available online: https://portal.3gpp.org/desktopmodules/Specifications/SpecificationDetails.aspx?specificationId=2543 (accessed on 1 January 2014).
4. 3GPP, TR 37.340 V15.5.0. NR; Multi-Connecitivty; Overall Description; Stage 2 (Release 15). 2019. Available online: https://portal.3gpp.org/desktopmodules/Specifications/SpecificationDetails.aspx?specificationId=3198 (accessed on 1 October 2020).
5. Giordani, M.; Mezzavilla, M.; Rangan, S.; Zorzi, M. Multi-connectivity in 5G mmWave cellular networks. In Proceedings of the 2016 Mediterranean Ad Hoc Networking Workshop (Med-Hoc-Net), Vilanova i la Geltru, Spain, 20–22 June 2016; pp. 1–7. [CrossRef]
6. Bi, T.; Muntean, G. Location-aware network selection mechanism in heterogeneous wireless networks. In Proceedings of the 2017 IEEE Conference on Computer Communications Workshops (INFOCOM WKSHPS), Atlanta, GA, USA, 1–4 May 2017; pp. 583–588. [CrossRef]
7. Xu, K.; Wang, K.; Amin, R.; Martin, J.; Izard, R. A Fast Cloud-Based Network Selection Scheme Using Coalition Formation Games in Vehicular Networks. *IEEE Trans. Veh. Technol.* **2015**, *64*, 5327–5339. [CrossRef]
8. Liu, C.; Xia, W.; Chen, G.; Shen, L. Location-aware handover decision algorithm in multi-cell networks. In Proceedings of the 2013 International Conference on Wireless Communications and Signal Processing, Hangzhou, China, 24–26 October 2013; pp. 1–6. [CrossRef]
9. Kuboniwa, J.; Miyake, Y.; Kameda, S.; Taira, A.; Oguma, H.; Suematsu, N.; Takagi, T.; Tsubouchi, K. High efficient network selection scheme using location information for heterogeneous wireless system. In Proceedings of the 2015 IEEE Wireless Communications and Networking Conference Workshops (WCNCW), New Orleans, LA, USA, 9–12 March 2015; pp. 391–396. [CrossRef]
10. Kang, B.; Park, C.; Choo, H. A Location Aware Fast PMIPv6 for Low Latency Wireless Sensor Networks. *IEEE Sens. J.* **2019**, *19*, 9456–9467. [CrossRef]
11. Hsieh, P.; Lin, W.; Lin, K.; Wei, H. Dual-Connectivity Prevenient Handover Scheme in Control/User-Plane Split Networks. *IEEE Trans. Veh. Technol.* **2018**, *67*, 3545–3560. [CrossRef]
12. Zhang, Z.; Zhao, J.; Ni, S.; Gong, Y. A Seamless Handover Scheme With Assisted eNB for 5G C/U Plane Split Heterogeneous Network. *IEEE Access* **2019**, *7*, 164256–164264. [CrossRef]

13. Zang, S.; Bao, W.; Yeoh, P.L.; Vucetic, B.; Li, Y. Managing Vertical Handovers in Millimeter Wave Heterogeneous Networks. *IEEE Trans. Commun.* **2019**, *67*, 1629–1644. [CrossRef]
14. Yan, L.; Ding, H.; Zhang, L.; Liu, J.; Fang, X.; Fang, Y.; Xiao, M.; Huang, X. Machine Learning-Based Handovers for Sub-6 GHz and mmWave Integrated Vehicular Networks. *IEEE Trans. Wirel. Commun.* **2019**, *18*, 4873–4885. [CrossRef]
15. Fiandrino, C.; Assasa, H.; Casari, P.; Widmer, J. Scaling Millimeter-Wave Networks to Dense Deployments and Dynamic Environments. *Proc. IEEE* **2019**, *107*, 732–745. [CrossRef]
16. Chen, J.; Wang, Y.; Li, Y.; Wang, E. QoE-Aware Intelligent Vertical Handoff Scheme Over Heterogeneous Wireless Access Networks. *IEEE Access* **2018**, *6*, 38285–38293. [CrossRef]
17. Suarez-Rodriguez, C.; He, Y.; Dutkiewicz, E. Theoretical Analysis of REM-Based Handover Algorithm for Heterogeneous Networks. *IEEE Access* **2019**, *7*, 96719–96731. [CrossRef]
18. Lembo, S.; Horsmanheimo, S.; Laukkanen, M. Positioning Based Intra-Frequency Handover in Indoor Cellular Network for Ultra Reliable Communications Assisted by Radio Maps. In Proceedings of the 2019 11th International Congress on Ultra Modern Telecommunications and Control Systems and Workshops (ICUMT), Dublin, Ireland, 28–30 October 2019; pp. 1–9.
19. Erisson. *Cellular IoT Evolution for Industry Digitalization*; White Paper; Erisson: Stockholm, Sweden, 2019.
20. Abari, O.; Bharadia, D.; Duffield, A.; Katabi, D. Cutting the cord in virtual reality. In Proceedings of the 15th ACM Workshop on Hot Topics in Networks, Atlanta, GA, USA, 9 November 2016; ACM: New York, NY, USA, 2016; pp. 162–168. [CrossRef]
21. Ahmed, A.; Boulahia, L.M.; Gaïti, D. Enabling Vertical Handover Decisions in Heterogeneous Wireless Networks: A State-of-the-Art and A Classification. *IEEE Commun. Surv. Tutor.* **2014**, *16*, 776–811. [CrossRef]
22. Tayyab, M.; Gelabert, X.; Jäntti, R. A Survey on Handover Management: From LTE to NR. *IEEE Access* **2019**, *7*, 118907–118930. [CrossRef]
23. Khan, M.; Han, X. A Survey of Context Aware Vertical Handover Management Schemes in Heterogeneous Wireless Networks. *Wirel. Pers. Commun.* **2015**, *85*, 2273–2293. [CrossRef]
24. Prasad, R.V.; Niemieeger, I.; Nguyen, T.V.H. A study on handoff issues in radio over fiber network at 60 GHz. In Proceedings of the International Conference on Communications and Electronics 2010, Nha Trang, Vietnam, 11–13 August 2010; pp. 50–54.
25. Al-Ammar, M.A.; Alhadhrami, S.; Al-Salman, A.; Alarifi, A.; Al-Khalifa, H.; Alnafessah, A.; Alsaleh, M. Comparative Survey of Indoor Positioning Technologies, Techniques, and Algorithms. In Proceedings of the 2014 International Conference on Cyberworlds (CW), Santander, Spain, 6–8 October 2014; pp. 245–252. [CrossRef]
26. Brena, R.F.; García-Vázquez, J.P.; Galván-Tejada, C.E.; Muñoz-Rodriguez, D.; Vargas-Rosales, C.; Fangmeyer, J. Evolution of indoor positioning technologies: A survey. *J. Sens.* **2017**, *2017*. [CrossRef]
27. Zekavat, R.; Buehrer, R.M. *Handbook of Position Location: Theory, Practice and Advances*, 2nd ed.; Wiley-IEEE Press: New York, NY, USA, 2019.
28. Kang, W.; Han, Y. SmartPDR: Smartphone-Based Pedestrian Dead Reckoning for Indoor Localization. *IEEE Sens. J.* **2015**, *15*, 2906–2916. [CrossRef]
29. 3GPP, TR 22.872 V16.0.0. Study on Positioning Use Cases (Release 16). 2018. Available online: https://portal.3gpp.org/desktopmodules/Specifications/SpecificationDetails.aspx?specificationId=3280 (accessed on 1 September 2018).
30. Lu, Y.; Richter, P.; Lohan, E.S. Opportunities and Challenges in the Industrial Internet of Things based on 5G Positioning. In Proceedings of the 2018 8th International Conference on Localization and GNSS (ICL-GNSS), Guimaraes, Portugal, 26–28 June 2018; pp. 1–6. [CrossRef]
31. Koivisto, M.; Talvitie, J.; Costa, M.; Leppänen, K.; Valkama, M. Joint cmWave-based multiuser positioning and network synchronization in dense 5G networks. In Proceedings of the 2018 IEEE Wireless Communications and Networking Conference (WCNC), Barcelona, Spain, 15–18 April 2018; pp. 1–6. [CrossRef]
32. Etzlinger, B.; Wymeersch, H.; Springer, A. Cooperative Synchronization in Wireless Networks. *IEEE Trans. Signal Process.* **2014**, *62*, 2837–2849. [CrossRef]
33. Sand, S.; Dammann, A.; Mensing, C. *Positioning in Wireless Communication Systems*; John Wiley & Sons Ltd.: Hoboken, NJ, USA, 2014.

34. Talvitie, J.; Levanen, T.; Koivisto, M.; Pajukoski, K.; Renfors, M.; Valkama, M. Positioning of high-speed trains using 5G new radio synchronization signals. In Proceedings of the 2018 IEEE Wireless Communications and Networking Conference (WCNC), Barcelona, Spain, 15–18 April 2018; pp. 1–6. [CrossRef]
35. Lu, Y.; Koivisto, M.; Talvitie, J.; Valkama, M.; Lohan, E.S. EKF-based and Geometry-based Positioning under Location Uncertainty of Access Nodes in Indoor Environment. In Proceedings of the 2019 International Conference on Indoor Positioning and Indoor Navigation (IPIN), Pisa, Italy, 30 September–3 October 2019; pp. 1–7. [CrossRef]
36. 3GPP, TR 23.714 V14.0.0. Study on Control and User Plane Separation of EPC Nodes (Release 14). 2016. Available online: https://portal.3gpp.org/desktopmodules/Specifications/SpecificationDetails.aspx?specificationId=2963 (accessed on 1 June 2016).
37. Zhao, F.; Tian, H.; Nie, G.; Wu, H. Received Signal Strength Prediction Based Multi-Connectivity Handover Scheme for Ultra-Dense Networks. In Proceedings of the 2018 24th Asia-Pacific Conference on Communications (APCC), Ningbo, China, 12–14 November 2018; pp. 233–238.
38. 3GPP, TR 28.801 V15.0.0. Study on Management and Orchestration of Network Slicing for Next Generation Network (Release 15). 2018. Available online: https://portal.3gpp.org/desktopmodules/Specifications/SpecificationDetails.aspx?specificationId=3091 (accessed on 1 January 2018).
39. Dahlman, E.; Parkvall, S.; Skold, J. *5G NR: The Next Generation Wireless Access Technology*; Elsevier Science: Amsterdam, The Netherlands, 2018.
40. Dong, X.; Zhao, L.; Zhao, H.; Pan, C. RAN Slicing-based Handover Scheme in HetNetss. In Proceedings of the 2018 IEEE 23rd International Conference on Digital Signal Processing (DSP), Shanghai, China, 19–21 November 2018; pp. 1–5.
41. Feirer, S.; Sauter, T. Seamless handover in industrial WLAN using IEEE 802.11k. In Proceedings of the 2017 IEEE 26th International Symposium on Industrial Electronics (ISIE), Edinburgh, UK, 19–21 June 2017; pp. 1234–1239.
42. Li, Y.; Li, C.; Chen, W.; Yeh, C.; Wang, K. Enabling seamless WiGig/WiFi handovers in tri-band wireless systems. In Proceedings of the 2017 IEEE 25th International Conference on Network Protocols (ICNP), Toronto, ON, Canada, 10–13 October 2017; pp. 1–2.
43. Ma, J.; Yang, D.; Zhang, H.; Gidlund, M. A Reliable Handoff Mechniasm for Mobile Industrial Wireless Sensor Networks. *Sensors* **2017**, *17*, 1797. [CrossRef]
44. 3GPP, TS 23.402 V16.0.0. Architecture Enhancements for Non-3GPP Accesses (Release 16). 2019. Available online: https://portal.3gpp.org/desktopmodules/Specifications/SpecificationDetails.aspx?specificationId=850 (accessed on 1 June 2019).
45. Sammour, I.; Chalhoub, G. Evaluation of Rate Adaptation Algorithms in IEEE 802.11 Networks. *Electronics* **2020**, *9*, 1436. [CrossRef]
46. Khan, M.W.; Salman, N.; Kemp, A.H.; Mihaylova, L. Localisation of Sensor Nodes with Hybrid Measurements in Wireless Sensor Networks. *Sensors* **2016**, *16*, 1143. [CrossRef] [PubMed]
47. Orsino, A.; Kovalchukov, R.; Samuylov, A.; Moltchanov, D.; Andreev, S.; Koucheryavy, Y.; Valkama, M. Caching-aided collaborative D2D operation for predictive data dissemination in industrial IoT. *IEEE Wirel. Commun.* **2018**, *25*, 50–57. [CrossRef]
48. Rastorgueva-Foi, E.; Koivisto, M.; Valkama, M.; Costa, M.; Leppänen, K. Localization and Tracking in mmWave Radio Networks using Beam-Based DoD Measurements. In Proceedings of the 2018 8th International Conference on Localization and GNSS (ICL-GNSS), Guimaraes, Portugal, 26–28 June 2018; pp. 1–6. [CrossRef]
49. Lu, Y.; Koivisto, M.; Talvitie, J.; Valkama, M.; Lohan, E.S. Positioning-Aided 3D Beamforming for Enhanced Communications in mmWave Mobile Networks. *IEEE Access* **2020**, *8*, 55513–55525. [CrossRef]
50. Hormann, K.; Agathos, A. The point in polygon problem for arbitrary polygons. *Comput. Geom.* **2001**, *20*, 131–144. [CrossRef]

51. Zhou, A.; Wu, L.; Xu, S.; Ma, H.; Wei, T.; Zhang, X. Following the Shadow: Agile 3-D Beam-Steering for 60 GHz Wireless Networks. In Proceedings of the IEEE INFOCOM 2018-IEEE Conference on Computer Communications, Honolulu, HI, USA, 16–19 April 2018; pp. 2375–2383. [CrossRef]
52. 3GPP, TR 38.900 V15.0.0. Study on Channel Model for Frequency Spectrum above 6 GHz (Release 15). 2018. Available online: https://portal.3gpp.org/desktopmodules/Specifications/SpecificationDetails.aspx?specificationId=2991 (accessed on 1 June 2018).

PUBLICATION

V

Cooperative Positioning System for Industrial IoT via mmWave Device-to-Device Communications

Y. Lu, M. Koivisto, J. Talvitie, E. Rastorgueva-Foi, M. Valkama and E. S. Lohan

*2021 IEEE 93rd Vehicular Technology Conference (VTC2021-Spring)*2021, 1–7
DOI: 10.1109/VTC2021-Spring51267.2021.9448644

Cooperative Positioning System for Industrial IoT via mmWave Device-to-Device Communications

Yi Lu, Mike Koivisto, Jukka Talvitie, Elizaveta Rastorgueva-Foi, Mikko Valkama, and Elena Simona Lohan
Department of Electrical Engineering, Tampere University, Finland
{yi.lu, mike.koivisto, jukka.talvitie, elizaveta.rastorgueva-foi, mikko.valkama, elena-simona.lohan}@tuni.fi

***Abstract*—The millimeter wave (mmWave) device-to-device air interface not only supports a direct wireless connectivity among devices, but it also offers an improved beamforming capability to obtain the direction information among the vehicles and devices for positioning. Both features serve as the key physical layer components for communications and positioning in the industrial Internet of things (IIoT) systems. Exploiting both accurate beamforming and wide bandwidth in a mmWave network, high-accuracy positioning is achievable, which can be then facilitated for location-aware communications, for instance. However, the uncertainty of anchors' locations in the industrial environment highly degrades the achievable positioning accuracy if left without proper consideration. In order to resolve such challenge, this paper presents a cooperative positioning system (CPS), where the locations of all the vehicles and anchors can be jointly estimated based on acquired location-related measurements (LRMs). Furthermore, the positioning performance is evaluated under random trajectories and different geometric relationships between the vehicles and the anchors. We show that, the proposed positioning solution is capable of resolving the aforementioned challenge by simultaneously tracking the mobile vehicles while mapping the locations of the static anchors. Utilizing the LRMs from both time and angular domains, the achieved positioning accuracy in both 2D and vertical plane is demonstrated based on extensive numerical simulations. Last but not least, the impact of different numbers of the mobile vehicles on the overall positioning performance is also investigated.**

***Index Terms*—Cooperative positioning, extended Kalman filter, industrial IoT, millimeter wave device-to-device communications, NR sidelink, simultaneous localization and mapping**

I. Introduction

With the growing employment of Internet of things (IoT) technology in various industry verticals [1], an increasing amount of wireless-enabled vehicles and sensors are to be deployed in the typical industrial environments, such as harbor area and warehouses for tasks like data collection and environment monitoring. Therefore, an enhanced inter-connectivity among the vehicles via the device-to-device (D2D) air interface, i.e., the sidelink, is required for seamless communications and data exchange. As studied in [2], the new radio (NR) sidelink, not only facilitates such inter-connectivity that can be exploited for both communications and positioning, but it also plays an important role in ultimately enabling a wireless-controlled industrial Internet of things (IIoT) system with connected vehicles especially in the context of the proximity-based services (ProSe) and the vehicle-to-everything (V2X) services [3].

Although the advantages of the sidelink for communications were studied, for instance, in [4], its potential benefits for positioning have not been widely investigated especially in the millimeter wave (mmWave) networks featured with beamforming capability. In contrast to a typical cellular scenario [5], a potential and crucial challenge from the positioning perspective remains, i.e., the location uncertainty of the anchors. Indeed, the location information of the anchors may not be precisely known as usual due to a frequent deployment and re-deployment of the anchors in order to enable wireless communications in certain area of the industrial environment. In such context, we propose a cooperative positioning system (CPS) that builds on a Bayesian framework, in which, the locations of all the vehicles and anchors can be jointly estimated based on the acquired location-related measurements (LRMs) via signaling through NR sidelink. The corresponding performance in both 2D and vertical plane is evaluated via extensive ray-tracing based numerical simulations.

In terms of the related works on cooperative positioning, the authors in [6] derived the positioning error bound for mobile agents based on a single type of LRMs, such as received signal strength (RSS), time of arrival (ToA) and angle of arrival (AoA), and discussed the feasibility of acquiring LRMs by utilizing different technologies, such ultra-wideband (UWB) and acoustic media. However, the achievable positioning accuracy by collectively utilizing different types of LRMs (e.g., RSS+AoA) were not discussed therein. Due to the high temporal resolution, the authors in both [7] and [8] adopted the UWB to verify the positioning performance experimentally. In particular, the authors in [7] proposed a robust algorithm by mapping the graphical model into the network topology, yielding small communication overhead and good positioning accuracy. Moreover, an anchorless and cooperative tracking algorithm was proposed in [8] where the multi-path components were utilized for positioning with an available 2D floorplan. Nevertheless, the vertical accuracy which is crucial for certain industrial use cases was not characterized therein. Last but not least, the cooperative positioning was addressed using the set-theoretic estimation methods in [9].

Finally, the main contributions of the proposed positioning framework in this paper are summarized as:

1) By categorizing the involved vehicles and devices into

This work was financially supported by the Academy of Finland, under the projects ULTRA (328226, 328214) and FUWIRI (319994), and the Finnish Funding Agency for Innovation under the project 5G VIIMA. Online videos are available at: https://research.tuni.fi/wireless/research/positioning/cps-d2d/

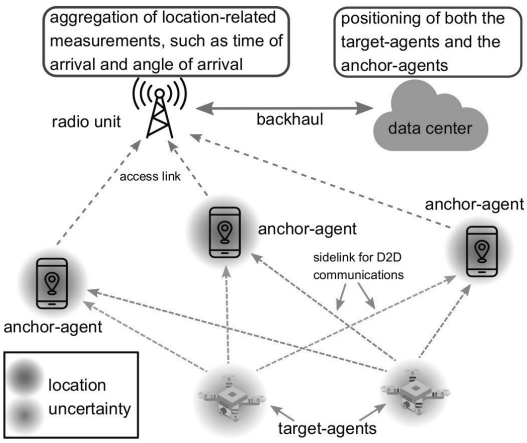

Fig. 1: In the considered positioning framework, the anchor-agents first estimate the location-related measurements (LRMs) based on the received pilot signal from the target-agents via the established sidelink (shown as green and orange dashed lines), after which these LRMs are first communicated to and aggregated at the radio unit (RU), and then fused into the location estimates of both anchor-agents and target-agents at the data center (or locally at the RU [10]) in a sequential manner by employing the proposed extended Kalman filter (EKF)-based approach. The locations of neither the target-agents nor the anchor-agents are perfectly known, the uncertainty is indicated by the blue and magenta shaded circles.

two kinds (targets and anchors) depending on their mobility and functionality, the LRMs are needed only over a subset of the overall D2D connections (i.e., less data) compared to aforementioned works;

2) By fusing the acquired LRMs individually and collectively[1], we provide an extended Kalman filter (EKF)-based formulation that enables the positioning and tracking of both the targets and the anchors in 3D;
3) With two sets of anchor deployment, we evaluate the impact on positioning due to different geometric relationships between the targets and the anchors;
4) Last but not least, we investigate the positioning performance of the proposed algorithm when considering different number of targets.

II. System models and descriptions

A. The cooperative positioning system (CPS)

In this paper, the considered wireless IIoT system is composed of various aerial or ground vehicles and sensor devices, which we refer to as *agents* that are capable of transmitting and receiving radio signals. As illustrated in Fig. 1, two types of agents are considered herein, one refers to the target-agent (T-agent), e.g., unmanned aerial vehicles, which possesses high mobility in order to perform certain tasks, such as environment monitoring and video surveillance. Another type of an agent is the anchor-agent (A-agent), such as the sensor device, which maintains a low mobility for most of the time serving as anchors. Under such context, the core objective of the proposed CPS is to track the moving T-agents while mapping the locations of the static A-agents, thus establishing the simultaneous localization and tracking (SLAT) approach.

In terms of beamforming capability, we assume that all the A-agents are equipped with a directional antenna, such as a uniform rectangle array (URA) in order to estimate the angle-domain LRMs (i.e., the AoA) when periodically receiving the transmitted pilot signals (e.g., the sidelink synchronization signals [11]) from the T-agents. In particular, the pilot signals employ the orthogonal frequency division multiplex (OFDM) waveforms, and the othogonal frequency division multiple access (OFDMA) is adopted as the resource assignment scheme among the T-agents and A-agents. Thereafter, the estimated LRMs at each A-agent are sent to the radio unit (RU) and finally received via backhaul at the data center of the network (i.e., the edge or cloud server) for cooperative positioning.

B. Radio signal and channel models

We continue with the theoretical characterization of the considered signal and channel models. Specifically, at an arbitrary time instant i, the kth T-agent, where $k \in \mathcal{K} = \{1, 2, \cdots, K\}$, transmits sidelink physical signals [11] by means of OFDM. In this particular work, all the T-agents are equipped with omni-directional antennas (an array with a single antenna element). Hence, we have a $N_R \times 1$ channel matrix for each pair of T-agent and A-agent, where N_R refers to the number of antenna elements at the receiver side (A-agent). Furthermore, we denote the transmitted OFDM symbol at the pth sub-carrier as $s_k[p,i] \in \mathbb{C}$. After passing through a line-of-sight (LoS)-dominant mmWave multi-path channel, the transmitted signals are received at the A-agents via a beam sweeping process[2].

The received frequency-domain complex symbol $r_m^{(q,k)}[p,i]$ at the mth A-agent, where $m \in \mathcal{M} = \{1, 2, \cdots, M\}$ from the kth T-agent at the ith time instant and the pth sub-carrier through the qth analog beamformer is expressed as

$$r_m^{(q,k)}[p,i] = \left(\boldsymbol{w}_m^{(q)}[i]\right)^{\mathrm{H}} \left(\boldsymbol{\Lambda}_m[p] s_k[p,i] + \boldsymbol{n}[p,i]\right), \qquad (1)$$

where $\boldsymbol{n}[p,i] \sim \mathcal{CN}\left(\mathbf{0}, \sigma_n^2 \mathbf{I}_{N_R}\right)$ refers to the complex-Gaussian noise with a power density of σ_n^2 imposed on overall N_R antenna elements. Furthermore, the qth beamformer $\boldsymbol{w}_m^{(q)}[i] \in \mathbb{C}^{N_R \times 1}$ can be constructed, but not limited to, via phase-shifters according to certain spatial angles in the utilized codebook. In addition, the identity matrix and Hermitian operation are denoted as $\mathbf{I}$ and $(\cdot)^{\mathrm{H}}$, respectively.

The channel matrix of each sub-carrier, denoted as $\boldsymbol{\Lambda}_m[p] \in \mathbb{C}^{N_R \times N_T}$ (note that $N_T = 1$ in this work) can be written as

$$\begin{aligned} \boldsymbol{\Lambda}_m[p] &= \boldsymbol{A}\boldsymbol{\Gamma}[p] \\ &= \sum_{l=0}^{L-1} \boldsymbol{b}_{\mathrm{URA}}\left(\phi_l\right) \gamma_l e^{-j2\pi f_{\mathrm{sc}} p \tau_l}, \end{aligned} \qquad (2)$$

[1]'Individually' means utilizing of one type of LRMs, e.g., only ToA; 'Collectively' means more than one type of LRMs are applied, e.g., ToA+AoA.

[2]The beam sweeping refers to one beam management process [12], where multiple beamformers, i.e., beam steering vectors are applied to acquire the received signals from different directions.

where L is the overall number of propagation paths and the channel state vector $\mathbf{\Gamma}[p] \in \mathbb{C}^{L\times 1}$ is described as

$$\mathbf{\Gamma}[p] = \left[\gamma_0 e^{-j2\pi f_{\text{sc}} p\tau_0}, \cdots, \gamma_{L-1} e^{-j2\pi f_{\text{sc}} p\tau_{L-1}}\right]^T, \quad (3)$$

where the index of active sub-carrier $p \in \mathcal{P} = \{1, \cdots, P\}$ and f_{sc} is the sub-carrier spacing. The array response matrix in (2) is represented as $\boldsymbol{A} \in \mathbb{C}^{N_R\times L} = [\boldsymbol{b}_{\text{URA}}(\phi_0), \cdots, \boldsymbol{b}_{\text{URA}}(\phi_{L-1})]$. Specifically, $\boldsymbol{b}_{\text{URA}}(\phi_l) \in \mathbb{C}^{N_R\times 1}$ refers to the URA response at the spatial angle $\phi_l \triangleq (\theta_l, \varphi_l)$, and γ_l is the complex channel coefficient including the pathloss of the lth path with a propagation delay of τ_l. Moreover, $\boldsymbol{b}_{\text{URA}}(\phi_l)$ is a combination of two uniform linear array (ULA) responses

$$\boldsymbol{b}_{\text{URA}}(\phi_l) = \sqrt{\beta_0(N_R, \phi_l)}\boldsymbol{a}_{\text{ULA}}(\varphi_l) \otimes \boldsymbol{a}_{\text{ULA}}(\theta_l|\varphi_l), \quad (4)$$

where $\otimes$ denotes the Kronecker product and the scaling factor $\beta_0(N_R, \phi_l)$ represents the array gain as a function of the overall number of antenna elements N_R as well as the spatial angle pair ϕ_l. As defined previously, the angle pair ϕ_l consists of the azimuth angle θ_l as well as the elevation angle φ_l, and together, they define a spatial direction in a 3D environment. Hence, the individual normalized ULA responses are given as

$$\begin{aligned}\boldsymbol{a}_{\text{ULA}}(\varphi_l) &= \frac{e^{-j\pi\sin(\varphi_l)\left[-\frac{N_{\text{el}}-1}{2}, \cdots, \frac{N_{\text{el}}-1}{2}\right]^T}}{\sqrt{N_{\text{el}}}},\\ \boldsymbol{a}_{\text{ULA}}(\theta_l|\varphi_l) &= \frac{e^{-j\pi\cos(\varphi_l)\sin(\theta_l)\left[-\frac{N_{\text{az}}-1}{2}, \cdots, \frac{N_{\text{az}}-1}{2}\right]^T}}{\sqrt{N_{\text{az}}}},\end{aligned} \quad (5)$$

where N_{el} and N_{az} represent the dimensions of the URA, such that $N_R = N_{\text{el}}N_{\text{az}}$. In case of a 8×8 URA, $N_{\text{el}} = N_{\text{az}} = 8$.

C. The location-related measurements (LRMs)

Denoting the locations of the kth T-agent and the mth A-agent as $\mathbf{P}_{\text{T},k}[i] = [x_{\text{T},k}, y_{\text{T},k}, z_{\text{T},k}]^T$ and $\mathbf{P}_{\text{A},m}[i] = [x_{\text{A},m}, y_{\text{A},m}, z_{\text{A},m}]^T$, respectively, we formulate all the desired time-domain and the angle-domain LRMs as

$$\begin{aligned}\hat{\tau}_m^{(k)} &= \tau_m^{(k)} + n_{\tau,m}^{(k)} = \|\mathbf{P}_{\text{T},k} - \mathbf{P}_{\text{A},m}\|/c + n_{\tau,m}^{(k)},\\ \hat{\Delta\tau}_m^{(k)} &= \Delta\tau_m^{(k)} + n_{\Delta\tau,m}^{(k)}\\ &= \|\mathbf{P}_{\text{T},k} - \mathbf{P}_{\text{A},m}\|/c - \|\mathbf{P}_{\text{T},k} - \mathbf{P}_{\text{A},1}\|/c + n_{\Delta\tau,m}^{(k)},\\ \hat{\varphi}_m^{(k)} &= \varphi_m^{(k)} + n_{\varphi,m}^{(k)}\\ &= \arcsin\left(\Delta z_m^{(k)}/\|\mathbf{P}_{\text{T},k} - \mathbf{P}_{\text{A},m}\|\right) + n_{\varphi,m}^{(k)},\\ \hat{\theta}_m^{(k)} &= \theta_m^{(k)} + n_{\theta,m}^{(k)}\\ &= \text{atan}_2\left(\Delta y_m^{(k)}, \Delta x_m^{(k)}\right) + n_{\theta,m}^{(k)},\end{aligned} \quad (6)$$

where the considered LRMs consist of ToA $\hat{\tau}_m^{(k)}[i]$, time difference of arrival (TDoA) $\hat{\Delta\tau}_m^{(k)}[i]$, elevation AoA $\hat{\varphi}_m^{(k)}[i]$ and azimuth AoA $\hat{\theta}_m^{(k)}[i]$, and the time index in (6) are omitted for simplicity. Furthermore, c is the speed of light, $\Delta x_m^{(k)} = x_{\text{T},k} - x_{\text{A},m}$, $\Delta y_m^{(k)} = y_{\text{T},k} - y_{\text{A},m}$, $\Delta z_m^{(k)} = z_{\text{T},k} - z_{\text{A},m}$. Additionally, the inverse sine function and four-quadrant inverse tangent function are denoted as arcsin and atan_2, respectively.

More importantly, we model all the LRMs noises in (6) as unbiased additive Gaussian white noise having the variance that is bounded by the established Cramér-Rao lower bound (CRLB) [13, Ch. 3]. For instance, we express the CRLB of ToA and elevation AoA as follows

$$\sigma_{\tau,m,k}^2[i] \geq \frac{3}{8\pi^2 f_{\text{sc}}^2 \text{SNR}_m^{(k)}[i] M_p(M_p+1)(2M_p+1)}, \quad (7)$$

$$\sigma_{\varphi,m,k}^2[i] \geq \frac{6}{N_{\text{el}}\left(N_{\text{el}}^2-1\right)\text{SNR}_m^{(k)}[i]\ \pi^2\cos^2\left(\varphi_m^{(k)}[i]\right)}, \quad (8)$$

where $M_p = \frac{P-1}{2}$, P is the overall number of active sub-carriers. We see that both CRLB are a function of several parameters, such as the signal bandwidth, $B_w = f_{\text{sc}}P$, the signal-to-noise ratio (SNR), $\text{SNR}_m^{(k)}[i]$, the number of antenna elements, N_{el} and the true AoA, φ_m. Additionally, the TDoA noise model can be computed as $\sigma_{\Delta\tau,m}^2[i] = \sigma_{\tau,m}^2[i] - \sigma_{\tau,1}^2[i]$[3], whereas the azimuth AoA shares the same formulation as (8) except that the term N_{el} shall be swapped to N_{az}.

Of all the parameters, the SNR remains significant since it is a time-variant variable due to the movement of all the T-agents and its value determines the ultimate LRMs' accuracy. After beam sweeping, the obtained SNR is expressed as

$$\text{SNR}_m^{(k)}[i] = \frac{\max\left(\mathbf{B}_m^{(k)}[i]\right)}{P_n}, \quad (9)$$

where P_n refers to the noise power over the total signal bandwidth, and the obtained beam reference signal received power (B-RSRP) vector is denoted as $\mathbf{B}_m^{(k)}[i] \in \mathbb{R}^{Q\times 1}$ where Q is the overall number of the beamformers in the codebook, and the qth B-RSRP $\text{B}_m^{(q,k)}[i]$ is calculated based on (1)

$$\text{B}_m^{(q,k)}[i] = \frac{1}{P}\sum_{p=1}^{P}|r_m^{(q,k)}[p,i]|^2, \quad (10)$$

that is essentially the average power over all the active sub-carriers.

III. Cooperative positioning via EKF

The proposed CPS for positioning of T-agents and A-agents are building on an EKF that is widely applied for positioning in works such as [8]. The choice of an EKF is determined by its flexibility in dealing with the non-linear state transition or measurement models. The proposed EKF is formulated according to [14] as

$$\begin{aligned}\text{state transition model}: \mathbf{s}[i] &= \mathbf{F}\mathbf{s}[i-1] + \mathbf{u}[i]\\ \text{measurement model}: \mathbf{y}[i] &= \mathbf{h}\left(\mathbf{s}[i]\right) + \mathbf{w}[i],\end{aligned} \quad (11)$$

where $\mathbf{y}[i]$ represents the LRMs which are facilitated as the measurements in the EKF, and $\mathbf{s}[i]$ refers to the time-varying state vector[4] that contains the information of both T-agents and A-agents such as

$$\mathbf{s} = \left[\mathbf{s}_{\text{T},1}^T, \cdots, \mathbf{s}_{\text{T},K}^T, \mathbf{P}_{\text{A},1}^T, \cdots, \mathbf{P}_{\text{A},M}^T\right]^T, \quad (12)$$

[3]The ToA noise statistics of reference A-agent is denoted as $\sigma_{\tau,1}^2[i]$.

[4]Thereafter, we drop the involved time index i for simplicity of the notation.

Algorithm 1: EKF-based cooperative positioning

At time index $i = 0$, initialize the state $\mathbf{s}$, covariance $\mathbf{\Sigma}$, process noise covariance $\mathbf{Q}$ according to Section IV-A

for $i = 1, \cdots, T$ **do**

Generate the LRMs vector $\mathbf{y}[i]$ and compute the corresponding measurement noise covariance matrix $\mathbf{R}[i]$

Calculate the Jacobian matrix according to, e.g., (16)

Implement the EKF equations [14]

Prediction:

state $\hat{\mathbf{s}}^{-}[i] = \mathbf{F}\hat{\mathbf{s}}[i-1]$

state covariance $\hat{\mathbf{\Sigma}}^{-}[i] = \mathbf{F}\hat{\mathbf{\Sigma}}[i-1]\mathbf{F}^{T} + \mathbf{Q}[i]$

Kalman gain:

$\mathbf{K}[i] = \hat{\mathbf{\Sigma}}^{-}[i]\mathbf{H}^{T}[i]\left(\mathbf{H}[i]\hat{\mathbf{\Sigma}}^{-}[i]\mathbf{H}^{T}[i] + \mathbf{R}[i]\right)^{-1}$

Correction/update:

$\hat{\mathbf{s}}[i] = \hat{\mathbf{s}}^{-}[i] + \mathbf{K}[i]\left(\mathbf{y}[i] - \mathbf{h}\left(\hat{\mathbf{s}}^{-}[i]\right)\right)$

$\hat{\mathbf{\Sigma}}[i] = \left(\mathbf{I} - \mathbf{K}[i]\mathbf{H}[i]\right)\hat{\mathbf{\Sigma}}^{-}[i]$

end

TABLE I: The number of available LRMs as a function of the number of T-agents K and A-agents M for each considered measurement type

Measurement type	Number of available LRMs, N
ToA, τ	MK
TDoA, $\Delta\tau$	$(M-1)K$
AoA, ϕ	$2MK$
ToA+AoA, τ+ϕ	$3MK$
TDoA+AoA, $\Delta\tau$+ϕ	$(3M-1)K$

in which, the state vector of the kth T-agent is given as

$$\mathbf{s}_{\mathrm{T},k} = \left[\mathbf{p}_{\mathrm{T},k}^{T}, \mathbf{v}_{\mathrm{T},k}^{T}, \mathbf{a}_{\mathrm{T},k}^{T}\right]^{T}, \tag{13}$$

where $\mathbf{v}_{\mathrm{T},k}^{T} = \left[v_x^{\mathrm{T},k}, v_y^{\mathrm{T},k}, v_z^{\mathrm{T},k}\right]$ and $\mathbf{a}_{\mathrm{T},k}^{T} = \left[a_x^{\mathrm{T},k}, a_y^{\mathrm{T},k}, a_z^{\mathrm{T},k}\right]$ denote the state of target velocity and acceleration, respectively. Although only the locations of the A-agents are considered in the state vector, their velocity and acceleration can also be included to enable the tracking of certain movements.

Moreover, the process noise vector is denoted as $\mathbf{u} \sim \mathcal{N}\left(\mathbf{0}_{9K+3M}, \mathbf{Q}\right)$ where $\mathbf{0}_{9K+3M}$ is a zero-vector with a dimension of $9K+3M$. Together with the linear state transition matrix $\mathbf{F}$ and the state covariance matrix $\mathbf{\Sigma}$, we have

$$\mathbf{Q} = \begin{bmatrix} \mathbf{Q}_{\mathrm{T}} & \mathbf{0} \\ \mathbf{0} & \mathbf{Q}_{\mathrm{A}} \end{bmatrix}, \mathbf{F} = \begin{bmatrix} \mathbf{F}_{\mathrm{T}} & \mathbf{0} \\ \mathbf{0} & \mathbf{F}_{\mathrm{A}} \end{bmatrix}, \mathbf{\Sigma} = \begin{bmatrix} \mathbf{\Sigma}_{\mathrm{T}} & \mathbf{0} \\ \mathbf{0} & \mathbf{\Sigma}_{\mathrm{A}} \end{bmatrix}, \tag{14}$$

where $\mathbf{Q}_{\mathrm{T}} \in \mathbb{R}^{9K\times 9K}$, $\mathbf{Q}_{\mathrm{A}} \in \mathbb{R}^{3M\times 3M}$, $\mathbf{F}_{\mathrm{T}} \in \mathbb{R}^{9K\times 9K}$, $\mathbf{F}_{\mathrm{A}} \in \mathbb{R}^{3M\times 3M}$, $\mathbf{\Sigma}_{\mathrm{T}} \in \mathbb{R}^{9K\times 9K}$ and $\mathbf{\Sigma}_{\mathrm{A}} \in \mathbb{R}^{3M\times 3M}$ are the process noise covariance matrix, the linear state transition matrix and state covariance matrix of the considered T-agents and A-agents, respectively. In particular, both $\mathbf{Q}_{\mathrm{T}}$ and $\mathbf{F}_{\mathrm{T}}$ are block diagonal matrices that consist of the corresponding matrix of each individual T-agent, i.e., $\mathbf{Q}_{\mathrm{T}} = \mathrm{blkdiag}\left(\mathbf{Q}_{\mathrm{T},1}, \cdots, \mathbf{Q}_{\mathrm{T},K}\right)$ and $\mathbf{F}_{\mathrm{T}} = \mathrm{blkdiag}\left(\mathbf{F}_{\mathrm{T},1}, \cdots, \mathbf{F}_{\mathrm{T},K}\right)$. Assuming a constant acceleration between consecutive states, we have [15]

$$\begin{aligned} \mathbf{F}_{\mathrm{T},k} &= \begin{bmatrix} 1 & \Delta t & \frac{\Delta t^2}{2} \\ 0 & 1 & \Delta t \\ 0 & 0 & 1 \end{bmatrix} \otimes \mathbf{I}_{3\times 3}, \\ \mathbf{Q}_{\mathrm{T},k} &= \sigma_{q,k}^2 \begin{bmatrix} \frac{\Delta t^5}{20} & \frac{\Delta t^4}{8} & \frac{\Delta t^3}{6} \\ \frac{\Delta t^4}{8} & \frac{\Delta t^3}{3} & \frac{\Delta t^2}{2} \\ \frac{\Delta t^3}{6} & \frac{\Delta t^2}{2} & \Delta t \end{bmatrix} \otimes \mathbf{I}_{3\times 3}, \end{aligned} \tag{15}$$

where Δt denotes the time interval between two consecutive time steps, and $\sigma_{q,k}^2$ refers to the process noise variance of the acceleration of the kth T-agent. For the A-agents, $\mathbf{F}_{\mathrm{A}} = \mathbf{I}_{3M\times 3M}$ and $\mathbf{Q}_{\mathrm{A}} = \mathbf{I}_{3M\times 3M}\sigma_{q,\mathrm{A}}^2$. Similarly, we have the initial state covariance of both agents as the block diagonal matrices as well where $\mathbf{\Sigma}_{\mathrm{T}} = \mathrm{blkdiag}\left(\mathbf{\Sigma}_{\mathrm{T},1}, \cdots, \mathbf{\Sigma}_{\mathrm{T},K}\right)$, where $\mathbf{\Sigma}_{\mathrm{T},k} = \mathrm{blkdiag}\left(\mathbf{\Sigma}_{\mathrm{p},k}, \mathbf{\Sigma}_{\mathrm{v},k}, \mathbf{\Sigma}_{\mathrm{a},k}\right)$ and for the A-agents $\mathbf{\Sigma}_{\mathrm{A}} = \mathrm{blkdiag}\left(\mathbf{\Sigma}_{\mathrm{A},1}, \cdots, \mathbf{\Sigma}_{\mathrm{A},M}\right)$ in which $\mathbf{\Sigma}_{\mathrm{A},m} = \mathrm{diag}\left(\sigma_x^2, \sigma_y^2, \sigma_z^2\right)$.

Furthermore, we denote the measurement noise vector as $\mathbf{w} \sim \mathcal{N}\left(\mathbf{0}_N, \mathbf{R}\right)$ where N is the overall number of available LRMs. In the case where only the ToA measurements are available, the number of LRMs is equal to the number of A-agents, i.e., $N = M$. Therefore, the measurement noise covariance matrix $\mathbf{R}_\tau \in \mathbb{R}^{MK\times MK} = \mathrm{blkdiag}\left(\mathbf{R}_\tau^{(1)}, \cdots, \mathbf{R}_\tau^{(K)}\right)$ in which, $\mathbf{R}_\tau^{(k)} = \mathrm{diag}\left(\sigma_{\tau,1,k}^2, \cdots, \sigma_{\tau,M,k}^2\right)$. The overall number of LRMs as a function of the number of T-agents and A-agents is given in Table I, from which, we see that the overall number of LRMs is larger when utilizing both time- and angle-domain LRMs, which would be beneficial to the performance of CPS, as will be shown in Section IV-D. Furthermore, the measurement function $\mathbf{h}\left(\cdot\right)$ in (11) for all types of LRMs has been explicitly given in (6) from which the Jacobian matrix is computed. Taking as a concrete example the case when only ToA measurement are utilized, the Jacobian matrix $\mathbf{H}_\tau \in \mathbb{R}^{MK\times(9K+3M)}$ can be written as

$$\mathbf{H}_\tau = \begin{bmatrix} \mathbf{H}_{\tau,\mathrm{T}}^{(1)} & \mathbf{0} & \cdots & \mathbf{0} & \mathbf{H}_{\tau,\mathrm{A}}^{(1)} \\ \mathbf{0} & \mathbf{H}_{\tau,\mathrm{T}}^{(2)} & & \vdots & \mathbf{H}_{\tau,\mathrm{A}}^{(2)} \\ \vdots & & \ddots & \mathbf{0} & \vdots \\ \mathbf{0} & \cdots & \mathbf{0} & \mathbf{H}_{\tau,\mathrm{T}}^{(K)} & \mathbf{H}_{\tau,\mathrm{A}}^{(K)} \end{bmatrix}, \tag{16}$$

where $\mathbf{H}_{\tau,\mathrm{T}}^{(k)} \in \mathbb{R}^{M\times 9}$ and $\mathbf{H}_{\tau,\mathrm{A}}^{(k)} \in \mathbb{R}^{M\times 3M}$ refer to the Jacobian matrix of the kth T-agent, where the partial derivatives are taken with respect to (w.r.t.) the variables of T-agent and A-agent, respectively. Additionally, $\mathbf{H}_{\Delta\tau}$, $\mathbf{H}_{\phi}$, $\mathbf{H}_{\tau+\phi}$ and $\mathbf{H}_{\Delta\tau+\phi}$ are constructed in the same manner as (16), and they are evaluated at the a prior mean $\hat{\mathbf{s}}^{-}$ which is shown in Algorithm 1 where the proposed cooperative positioning EKF is briefly summarized. Moreover, the specific Jacobian matrices of $\mathbf{H}_{\tau,\mathrm{T}}^{(k)}$ and $\mathbf{H}_{\phi,\mathrm{T}}^{(k)}$ can be found in [15, Section IV].

IV. Numerical simulations and results analysis

A. Initialization

For the numerical evaluation of the proposed positioning algorithm, the EKF state $\mathbf{s}$ was initialized with random

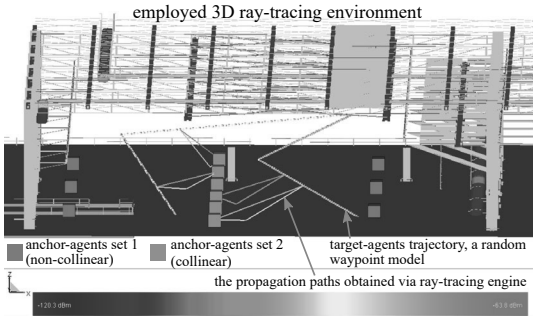

Fig. 2: The ray-tracing enabled 3D industrial environment [16] with two practical A-agents sets, i.e., non-collinear (set 1) deployment in red and collinear (set 2) deployment in green. An example of T-agent trajectory based on a 3D random waypoint (RWP) model in plotted in light yellow.

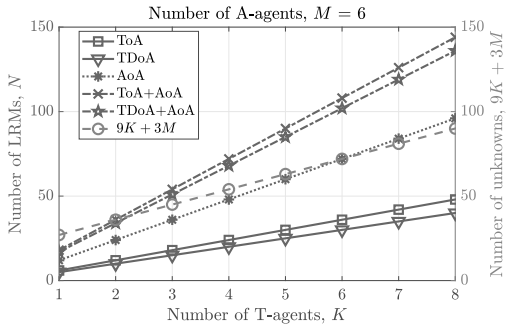

Fig. 3: The overall number of LRMs (left y-axis) and the overall number of unknowns (right y-axis) as a function of the number of considered T-agents with the number of considered A-agents fixed at $M = 6$. The formula of calculating the number of LRMs are given in Table I.

T-agent locations that are normally distributed w.r.t. the true locations and with standard deviation of one meter in all directions, whereas the velocities and accelerations are set to zeros. Consequently, the initial state covariance matrix is given as $\mathbf{\Sigma}_{\mathrm{T},k} = \mathrm{blkdiag}\left(\mathbf{I}_{3\times 3}, \mathbf{\Sigma}_{\mathrm{v},k}, \mathbf{\Sigma}_{\mathrm{a},k}\right)$ in which $\mathbf{\Sigma}_{\mathrm{v},k} = \mathrm{diag}\left(\left(v_x^{\mathrm{T},k}\Delta t\right)^2, \left(v_y^{\mathrm{T},k}\Delta t\right)^2, \left(v_z^{\mathrm{T},k}\Delta t\right)^2\right)$ and $\mathbf{\Sigma}_{\mathrm{a},k} = \mathrm{diag}\left(\left(a_x^{\mathrm{T},k}\Delta t^2\right)^2, \left(a_y^{\mathrm{T},k}\Delta t^2\right)^2, \left(a_z^{\mathrm{T},k}\Delta t^2\right)^2\right), \forall k \in \mathcal{K}$. In addition, the locations of all the A-agents are also initialized around their true locations with a covariance $\mathbf{\Sigma}_{\mathrm{A},m} = \mathrm{diag}\left(\sigma_{\mathrm{AT}}^2, \sigma_{\mathrm{AT}}^2, \frac{\sigma_{\mathrm{AT}}^2}{\beta^2}\right)$, where σ_{AT} refers to the location uncertainty in the horizontal plane and $\beta = 10,\ \forall m \in \mathcal{M}$. Moreover, the process noise variance $\sigma_{q,k}^2$ (of T-agents) is tuned according to the maximum acceleration $|a_{\max}|$ such that $\sigma_{q,k}^2 = \left(|a_{\max}|/(6\Delta t)\right)^2$. Since the A-agents are assumed to be static in this work, the $\sigma_{q,\mathrm{A}}^2$ is set to 0.

B. Test scenarios

The performance of the proposed CPS is evaluated using ray-tracing simulations [16] and numerical evaluations in a mmWave D2D network. In particular, six static A-agents were deployed in a 60m $\times$ 60m area according to two different sets (as depicted in Fig. 2) to evaluate the effect of different geometric relationships. Furthermore, we design the trajectories of all T-agents based on the 3D random waypoint (RWP) model [17] within the considered area, the height of each trajectory is controlled from 0.5m to 8m range, whereas the horizontal range is bounded by the borders of the warehouse. In particular, there are approximately 25 paths (including the LoS path) being generated for each pair of target-anchor at each time instant using ray-tracing simulations. For the purpose of demonstration, the LoS path together with one first-order reflection path are given as examples in Fig. 2. In addition, all the T-agents move independently along their individual trajectories. Subsequently, we summarize the relevant parameters utilized in the simulation in Table II. It is also noteworthy that with the considered parameter configurations, the theoretical maximum D2D distance in the LoS condition is more than 500m, which is enough to ensure the full radio coverage within the environment.

TABLE II: Utilized parameters in the simulation

Parameter	Value
Carrier frequency	26 GHz
Sub-carrier spacing	60 kHz
Signal bandwidth	10 MHz
Transmit power	10 dBm
Receive beamforming gain	18 dBi
EKF update time-interval	100 ms
A-agents antenna	8×8 URA
T-agents antenna	Omni-directional
A-agents height	1.5 m
T-agents height	0.5 – 8 m
Avg. T-agents velocity	1.1 m/s

C. The number of LRMs vs the number of unknowns

Given the number of T-agents, K, and the number of A-agents, M, the number of unknowns in the estimation problem is $9K + 3M$. In particular, Fig. 3 demonstrates the number of available LRMs, N, as a function of K in the case of six A-agents[5] when utilizing different types of LRMs. It is observed that with the increasing value of K, the number of both the unknowns and the LRMs increases. Nevertheless, for the considered number of T-agents, the problem is under-determined ($N < 9K + 3M$) for CPS that applies the time-domain LRMs (ToA, TDoA) and angle-domain LRMs (AoA) individually, and become over-determined ($N > 9K + 3M$) for CPS collectively utilizing the LRMs from both time- and angle-domain (ToA+AoA and TDoA+AoA). A critical case occurs when $K = 2$ and both ToA and AoA measurements are utilized, in which case, $N = 9K + 3M$. In the following subsections, we will present positioning performance under different K and M values.

D. The impact of different numbers of T-agents and A-agents

To assess if the presence of more T-agents could bring practical benefits to the CPS, we first test and present the

[5]We emphasize that M can be any positive integer number, and $M = 6$ is chosen here such that there is one A-agent every 25m$\times$25m area approximately.

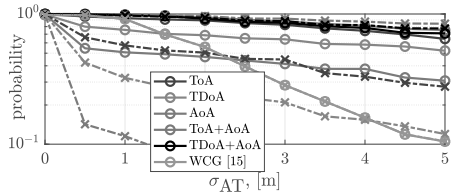

(a) Probability of 2D sub-meter accuracy in set 1 (non-collinear A-agents).

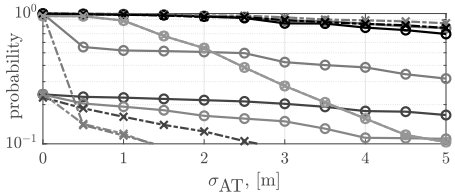

(b) Probability of 2D sub-meter accuracy in set 2 (collinear A-agents).

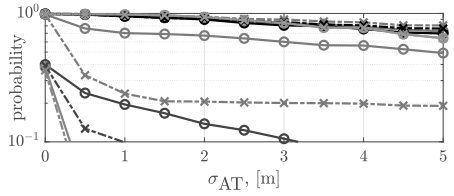

(c) Probability of vertical sub-0.2 meter accuracy in set 1 (non-collinear A-agents).

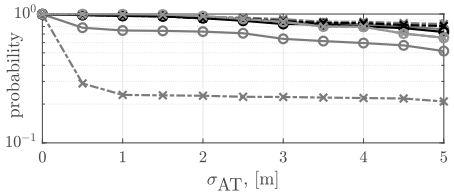

(d) Probability of vertical sub-0.2 meter accuracy in set 2 (collinear A-agents).

Fig. 4: Positioning performance of T-agents. Circle solid lines denote the positioning performance with two T-agents (two-target CPS); Cross dashed lines denote the positioning performance with one T-agent (one-target CPS).

positioning performance at $K = 1$ (one-target CPS) and $K = 2$ (two-target CPS). Moreover, we adopt the probability of sub-meter accuracy in 2D (the horizontal plane) and probability of sub-0.2 meter accuracy [18, Table 7.3.2.2-1] in vertical plane as the performance metrics. Furthermore, we perform in total 500 simulation trials with overall 1000 independent RWP trajectories generated, thus implying that two independent trajectories are generated in each simulation trial[6]. In particular, the length of each RWP trajectory is set to 2000 points with 100 ms interval.

The positioning performance of T-agents is given in Fig. 4. In terms of the performance difference between two-target CPS and one-target CPS[7], it is noticeable that when utilizing the time- and angle-domain LRMs individually, the two-target CPS outperforms the one-target CPS in both (anchor) sets and both 2D and vertical planes. However, the performance gap between two-target and one-target CPS becomes nearly invisible when collectively utilizing the LRMs from both time- and angle-domains. As expected, when utilizing different LRMs[8], both 2D and vertical positioning accuracy of the CPS that collectively utilizes the LRMs is in general higher than that of the CPS that utilizes the LRMs from a single domain. Nevertheless, it is important to note that the ToA-based two-target CPS achieves nearly equivalent 2D performance as the CPS that collectively utilizes LRMs from both domains. For both $K = 1, 2$ cases, the AoA-based CPS demonstrates a rather similar performance in both A-agents sets and both 2D and vertical planes, whereas the time-based CPS suffers a huge performance loss in set 2 (when A-agents are collinear deployed), in which a roughly 20% 2D sub-meter accuracy (in Fig. 4b) and a nearly 3% vertical sub-0.2 meter accuracy (invisible in Fig. 4d) are achieved.

The above observed behavior shows that the time-based CPS suffers severely from the collinear deployment (set 2), which further proves the impact on the positioning performance due to the different geometric relationships between the T-agents and the A-agents when utilizing different LRMs. Moreover, the results in Fig. 4c and Fig. 4d demonstrates that the angle-based CPS offers a much better vertical accuracy in both sets than the time-based CPS over the entire considered σ_{AT} values. Additionally, the weighted centroid geometry (WCG) [15] that utilizes ToA+AoA is applied herein for comparison. It is seen that over the entire considered σ_{AT} values, the WCG in general achieves a comparable vertical performance, whereas its 2D accuracy becomes much worse than the (ToA+AoA)-based CPS when $\sigma_{\mathrm{AT}} > 1$m.

In addition to the T-agents, the positioning performance of A-agents is also obtained and presented in Fig. 5. It is to note that WCG is not included therein due to the fact that WCG is only capable of positioning the T-agents. Moreover, a comparison between Fig. 4 and Fig. 5 reveals the fact that despite slight numerical differences, the obtained performance of the A-agents is rather similar to that of the T-agents except two differences. One is that in set 2 (collinear deployment set), the A-agents (Fig. 5b and Fig. 5d) do not suffer huge accuracy loss as the T-agents (Fig. 4b and Fig. 4d) when utilizing the time-domain LRMs. The reason lies in the fact that for each A-agent in set 2, the geometric relationships between itself and other agents (i.e., the T-agents and other A-agents) are not collinear anymore. Another difference lies in the fact that the vertical performance of A-agents (Fig. 5c and Fig. 5d) is much better than that of T-agents (Fig. 4c and Fig. 4d) when utilizing time-domain LRMs.

The CPS performance is visualized and available online at: https://research.tuni.fi/wireless/research/positioning/cps-d2d/

V. Conclusion

In this paper, we proposed and evaluated a cooperative positioning solution operating on the mmWave D2D air

[6]One out of the two RWP trajectories is selected as the trajectory of the T-agent for one-target CPS.

[7]Comparison between curves in the same colors but with different markers.

[8]Comparison between curves with the same markers but in different colors.

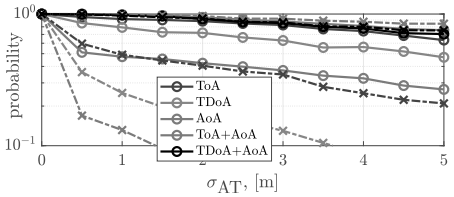

(a) Probability of 2D sub-meter accuracy in set 1 (non-collinear A-agents).

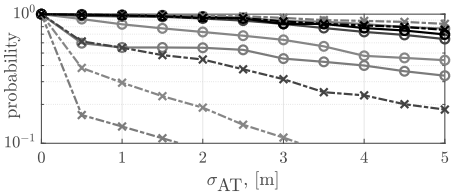

(b) Probability of 2D sub-meter accuracy in set 2 (collinear A-agents).

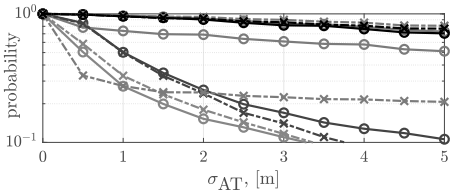

(c) Probability of vertical sub-0.2 meter accuracy in set 1 (non-collinear A-agents).

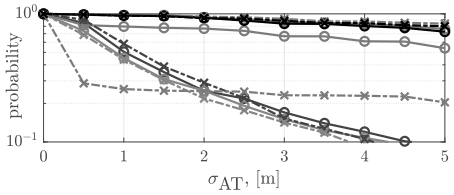

(d) Probability of vertical sub-0.2 meter accuracy in set 2 (collinear A-agents).

Fig. 5: Positioning performance of A-agents. Same as Fig. 4, circle solid lines: two-target CPS; Cross dashed lines: one-target CPS.

interface for the IIoT. The locations of all the agents (including mobile vehicles and anchor devices) can be jointly estimated, forming a SLAT-sense framework. Employing the CRLB-based LRMs from both time- and angle-domains, numerical simulations were carried out with two sets of A-agents under different geometric relationships. Our results demonstrated that the performance in both 2D and vertical plane was boosted when utilizing the LRMs collectively (i.e., time- and angle-domain LRMs together) rather than individually (i.e., either time- or angle-domain LRMs). Furthermore, compared with angle-based positioning, time-based positioning in general performed better in 2D plane and worse in vertical plane. The results also showed that the collinear geometry could severely degrade the 2D positioning performance of the T-agents rather than that of the A-agents of the CPS that utilized only time-domain LRMs.

Last but not least, we found that although with more unknowns than the LRMs, system with one more target (two-target CPS) in general obtain a better positioning performance than that with less target (one-target CPS) especially when utilizing the LRMs individually rather than collectively. Therefore, when only one type of LRMs (e.g., only ToA or only AoA) is available, a multi-target system can reduce the hardware requirement of the A-agents without much performance loss. This key observation can be considered to guarantee certain positioning performance for device with complexity limitations, since acquiring LRMs from both domain requires a more challenged hardware design. Future work will focus on the performance evaluation at various numbers of both T-agents and moving A-agents.

REFERENCES

[1] Erisson, "Cellular IoT Evolution for Industry Digitalization," White paper, 2019.

[2] S. Lien, D. Deng, C. Lin, H. Tsai, T. Chen, C. Guo, and S. Cheng, "3GPP NR Sidelink Transmissions Toward 5G V2X," *IEEE Access*, vol. 8, pp. 35 368–35 382, 2020.

[3] 3GPP, TR 38.885 V16.0.0, "Study on NR Vehicle-to-Everything (V2X) (Release 16)," March 2019.

[4] M. Mikami, K. Serizawa, Y. Ishida, H. Nishiyori, K. Moto, and H. Yoshino, "Field Experimental Evaluation on Latency and Reliability Performance of 5G NR V2V Direct Communication in Real Express Highway Environment," in *2020 IEEE 91st Vehicular Technology Conference (VTC2020-Spring)*, 2020, pp. 1–5.

[5] Y. Lu, P. Richter, and E. S. Lohan, "Opportunities and Challenges in the Industrial Internet of Things based on 5G Positioning," in *2018 8th International Conference on Localization and GNSS (ICL-GNSS)*, June 2018, pp. 1–6.

[6] N. Patwari, J. N. Ash, S. Kyperountas, A. O. Hero, R. L. Moses, and N. S. Correal, "Locating the nodes: Cooperative Localization in Wireless Sensor Networks," *IEEE Signal Processing Magazine*, vol. 22, no. 4, pp. 54–69, July 2005.

[7] H. Wymeersch, J. Lien, and M. Z. Win, "Cooperative Localization in Wireless Networks," *Proceedings of the IEEE*, vol. 97, no. 2, pp. 427–450, Feb. 2009.

[8] J. Kulmer, E. Leitinger, S. Grebien, and K. Witrisal, "Anchorless Cooperative Tracking Using Multipath Channel Information," *IEEE Transactions on Wireless Communications*, vol. 17, no. 4, pp. 2262–2275, April 2018.

[9] J. Fink, D. Schaeufele, M. Kasparick, R. L. G. Cavalcante, and S. Stanczak, "Cooperative Localization by Set-theoretic Estimation," in *WSA 2019; 23rd International ITG Workshop on Smart Antennas*, April 2019, pp. 1–8.

[10] 3GPP, TR 38.856 V16.0.0, "Study on local NR positioning in NG-RAN (Release 16)," Dec. 2019.

[11] 3GPP, TS 38.211 V16.1.0, "NR; Physical channels and modulation (Release 16)," March 2020.

[12] 3GPP, TS 38.802 V14.2.0, "Study on New Radio Access Technology, Physical Layer Aspects (Release 14) ," Sep. 2017.

[13] S. Sand, A. Dammann, and C. Mensing, *Positioning in Wireless Communication Systems*. John Wiley & Sons Ltd., June 2014.

[14] D. Simon, *Optimal State Estimation: Kalman, H Infinity, and Nonlinear Approaches*. New York, NY, USA: Wiley-Interscience, 2006.

[15] Y. Lu, M. Koivisto, J. Talvitie, M. Valkama, and E. S. Lohan, "EKF-based and geometry-based positioning under location uncertainty of access nodes in indoor environment," in *2019 International Conference on Indoor Positioning and Indoor Navigation (IPIN)*, Sep. 2019, pp. 1–7.

[16] Wireless Insite, "https://www.remcom.com/wireless-insite-em-propagation-software," Remcom Incooperation.

[17] E. Hyytiä, H. Koskinen, P. Lassila, A. Penttinen, J. Virtamo, and J. Roszik, "Random Waypoint Model in Wireless Networks," *Networks and Algorithms: Complexity in physics and Computer Science*, Jan. 2005.

[18] 3GPP, TS 22.261 V17.2.0, "Service requirements for the 5G system; Stage 1 (Release 17)," March 2020.

PUBLICATION

VI

Joint Positioning and Tracking via NR sidelink in 5G-Empowered Industrial IoT

Y. Lu, M. Koivisto, J. Talvitie, E. Rastorgueva-Foi, T. Levanen, E. S. Lohan and M. Valkama

Submitted to IEEE Internet of Things Magazine (2021)
DOI: arxiv.org/abs/2101.06003